MTL TR 91-2

AD

AN EXPERIMENTAL AND FINITE ELEMENT INVESTIGATION INTO THE NONLINEAR MATERIAL BEHAVIOR OF PIN-LOADED COMPOSITE LAMINATES

STEVEN M. SERABIAN
MECHANICS AND STRUCTURES BRANCH

January 1991

US ARMY
LABORATORY COMMAND
MATERIALS TECHNOLOGY LABORATORY

U.S. ARMY MATERIALS TECHNOLOGY LABORATORY
Watertown, Massachusetts 02172-0001

The findings in this report are not to be construed as an official Department of the Army position, unless so designated by other authorized documents.

Mention of any trade names or manufacturers in this report shall not be construed as advertising nor as an official indorsement or approval of such products or companies by the United States Government.

DISPOSITION INSTRUCTIONS

Destroy this report when it is no longer needed.
Do not return it to the originator.

UNCLASSIFIED

SECURITY CLASSIFICATION OF THIS PAGE (When Data Entered)

REPORT DOCUMENTATION PAGE		READ INSTRUCTIONS BEFORE COMPLETING FORM
1. REPORT NUMBER MTL TR 91-2	2. GOVT ACCESSION NO.	3. RECIPIENT'S CATALOG NUMBER
4. TITLE (and Subtitle) AN EXPERIMENTAL AND FINITE ELEMENT INVESTIGATION INTO THE NONLINEAR MATERIAL BEHAVIOR OF PIN-LOADED COMPOSITE LAMINATES		5. TYPE OF REPORT & PERIOD COVERED Final Report 6. PERFORMING ORG. REPORT NUMBER
7. AUTHOR(s) Steven M. Serabian		8. CONTRACT OR GRANT NUMBER(s)
9. PERFORMING ORGANIZATION NAME AND ADDRESS U.S. Army Materials Technology Laboratory Watertown, Massachusetts 02172-0001 ATTN: SLCMT-MRS		10. PROGRAM ELEMENT, PROJECT, TASK AREA & WORK UNIT NUMBERS D/A Project: 1L162105AH84 AMCMS Code: 612105.AH840011 Agency Accession: DA 312774
11. CONTROLLING OFFICE NAME AND ADDRESS U.S. Army Laboratory Command 2800 Powder Mill Road Adelphi, Maryland 20783-1145		12. REPORT DATE January 1991 13. NUMBER OF PAGES 272
14. MONITORING AGENCY NAME & ADDRESS(if different from Controlling Office)		15. SECURITY CLASS. (of this report) Unclassified 15a. DECLASSIFICATION/DOWNGRADING SCHEDULE

16. DISTRIBUTION STATEMENT (of this Report)

Approved for public release; distribution unlimited.

17. DISTRIBUTION STATEMENT (of the abstract entered in Block 20, if different from Report)

18. SUPPLEMENTARY NOTES

Thesis submitted to the University of Lowell, Lowell, Massachusetts, in partial fulfillment of the requirements for the Degree of Doctor of Engineering in Mechanical Engineering, October 26, 1989.

19. KEY WORDS (Continue on reverse side if necessary and identify by block number)

Composite materials	Moire analysis	Nonlinear analysis
Bolted joints	Stress analysis	Optical methods
Finite element analysis	Failure	Laminates

20. ABSTRACT (Continue on reverse side if necessary and identify by block number)

(SEE REVERSE SIDE)

DD FORM 1 JAN 73 1473 EDITION OF 1 NOV 65 IS OBSOLETE

UNCLASSIFIED

SECURITY CLASSIFICATION OF THIS PAGE (When Data Entered)

Block No. 20

ABSTRACT

The effect of crossply nonlinear intralaminar shear behavior on the modeling accuracy of pin-loaded [(0/90)n]s and [(+45/-45)n]s composite laminates was quantitatively investigated. Both linear and nonlinear elastic three dimensional finite element approximations that included pin elasticity and contact angle formation were generated. These approximations were compared to both front surface in-plane and out-of-plane experimental moire displacement contours generated from geometric and projection shadow moire techniques.

A modified three point bend test was used to obtain values of laminate transverse shear moduli while through thickness contraction measurements on laminate tension tests were employed to obtain estimates of the Poisson ratio values. Nonlinear crossply intralaminar shear behavior was determined from the ASTM D3518-76 specification.

Three dimensional constitutive equations for the [(0/90)n]s laminate were developed from effective and actual lamina mechanical properties. A material axis transformation of these constitutive equations was employed to produce [(+45/-45)n]s laminate constitutive equations. The validity of these constitutive equations and the effects of nonlinear intralaminar shear behavior were experimentally investigated by a comparison with uniaxial tension tests of both laminates. A sensitivity analysis of through thickness modulus was also done in this comparison in hope of providing insight into the selection of its magnitude.

Comparisons of linear and nonlinear elastic finite element results show significant stress level reductions and increased strain values in [(+45/-45)3]s laminate net and bearing sections. Similar results were observed in the [(0/90)3,0]s laminate shearout section. Both pin proximity and load level intensified these effects. Net section [(+45/-45)3]s experimental strains agreed well with nonlinear elastic finite element results at low pin load levels, but surpassed them at higher pin load levels. Closer pin proximity and increases load level intensified these results. Similar trends were observed in [(+45/-45)3]s bearing and [(0/90)3,0]s shearout sections, but were affected by unsymmetric experimental pin boundary conditions.

A qualitative determination of material damage within the pin-loaded laminates indicated material failure in those regions where experimental and nonlinear elastic finite element results diverged.

PREFACE

The research presented in this report was carried out at the Army Materials Technology Center in Watertown Massachusetts and the University of Lowell in Lowell, Massachusetts.

The report is excerpted fron the D. Eng. thesis of the author that was completed in October, 1989 in the Department of Mechanical Engineering at the University of Lowell. The thesis was supervised in its infancy by the late Professor John McElman and in its completion by Professor Struan Robertson of the Mechanical Engineering Department at the University of Lowell. Also serving on the advisory committee were Professors Craig Douglas, and William Kyros of the University of Lowell and Arthur R. Johnson of AMTL.

TABLE OF CONTENTS

CHAPTER 1. INTRODUCTION

1.1 COMPOSITE MATERIALS

Composite materials were born out of the ideology that a material with improved properties could be created through the combination of two or more constituent materials. Materials consisting of continuous, unidirectional, load carrying fibers imbedded in a homogeneous, load distributing support matrix is one such example of this. Known as a lamina and possessing orthotropic material properties, it may be stacked to construct what is known as a laminate whose anisotropic material properties are dictated by laminae stacking sequence and fiber angle orientation. The use of high strength high modulus fibers such as boron or graphite can create a composite of tailored material properties with a high strength to weight ratio.

This group of materials was widely used by the aerospace industries during the late sixties and early seventies. Their high strength to weight ratio allowed the design engineer to solve many stringent structural criteria in both space and military vehicles. Structures fabricated from composites improved craft mission capability through enhanced performance and increased payload capacity.

Hand in hand with this new capability came the different task of understanding and characterizing the material's mechanical behavior to obtain design confidence. Past design philosophies for isotropic materials proved to be far to inadequate. Extensive research and development efforts and cautious structural applications provided for learning experiences. Many of these initial applications were in space and missile systems with subsequent applications in aircraft, helicopter, and propulsion systems. Cost effective consumer applications based on the early applications may be seen in the automotive, boating, sporting goods, and commercial aircraft industries.

Recent trends have placed composite materials in primary load

carrying structures as opposed to earlier secondary structures. Better characterization of mechanical response and failure behavior is needed to insure higher design confidence levels.

1.2 Mechanical Fastening of Composite Structures

The joining of composite structures by mechanical fastening methods is one area where higher design confidence levels are needed. Although the use of bonding procedures inherent in composite fabrication techniques can reduce the use of mechanically fastened joints, bonded joint strength limitations and structural disassembly necessitate their use. Examples of mechanically fastened joints include riveted, pinned, or bolted arrangements in single and multiple joint configurations. Figure 1.1 shows some examples of single bolted joint configurations while Figure 1.2 illustrates some of their typical failure modes.[1]

Increased structural performance requirements for composite material systems translate into higher stresses in and around the vicinity of bolted joints. The anisotropic character of composites can be utilized to reduce joint stress concentrations while maintaining joint strength. Laminae ply orientation and stacking sequence as well as joint geometric parameters have been shown to greatly affect these performance characteristics.

Analysis of bolted joints in composite structures generally begins with an overall structural assessment to predict the approximate loads appied to the joint as a whole. Individual bolt loads within these joints are then determined by a bolt load distribution analysis [1]. The effects of material type and laminate orientation upon structural integrity are iteratively investigated and a preliminary material system and laminate orientation is selected. A detailed stress analysis of those critical individual bolts is then undertaken in which a material failure criterion is applied to predict joint strength. This complete analysis technique is shown in Figure 1.3.

It is in this detailed stress analysis that modeling assumptions must be made. Material constitutive equations, bolt/material interactions, and material failure behavior are exemplary details that must be understood thoroughly before being incorporated into the stress analysis. Verification

of assumptions regarding these details can only be acheived by rigorous experimental testing.

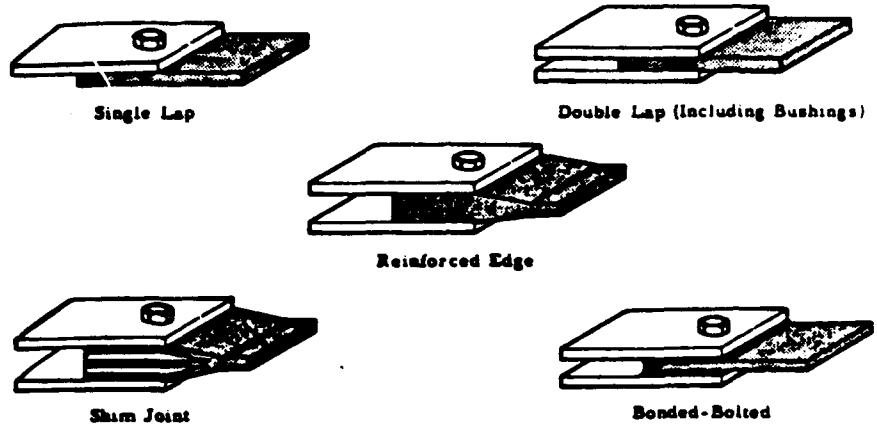

Figure 1.1 Examples of Mecahnically Fastened Joints [ref. 1]

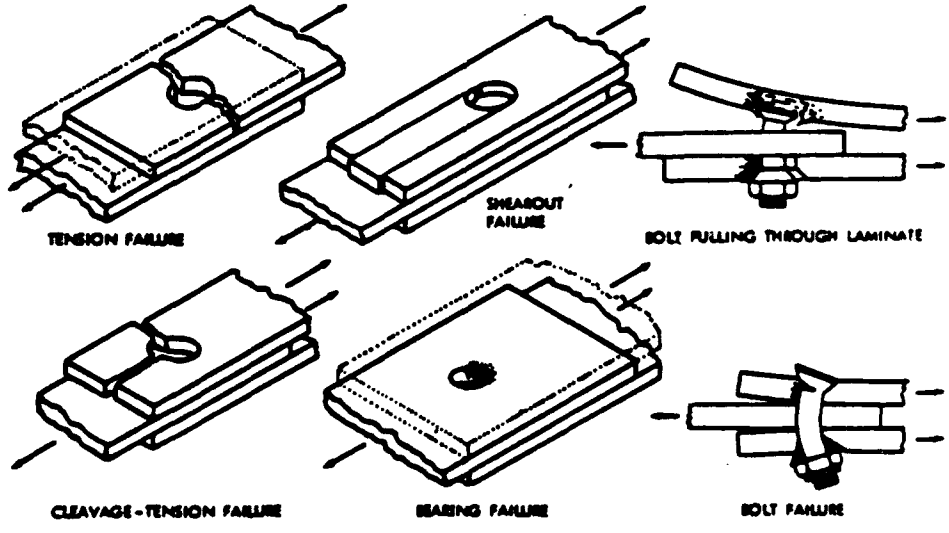

Figure 1.2 Typical Failure Modes of Mechanically Fastened Joints [ref. 1]

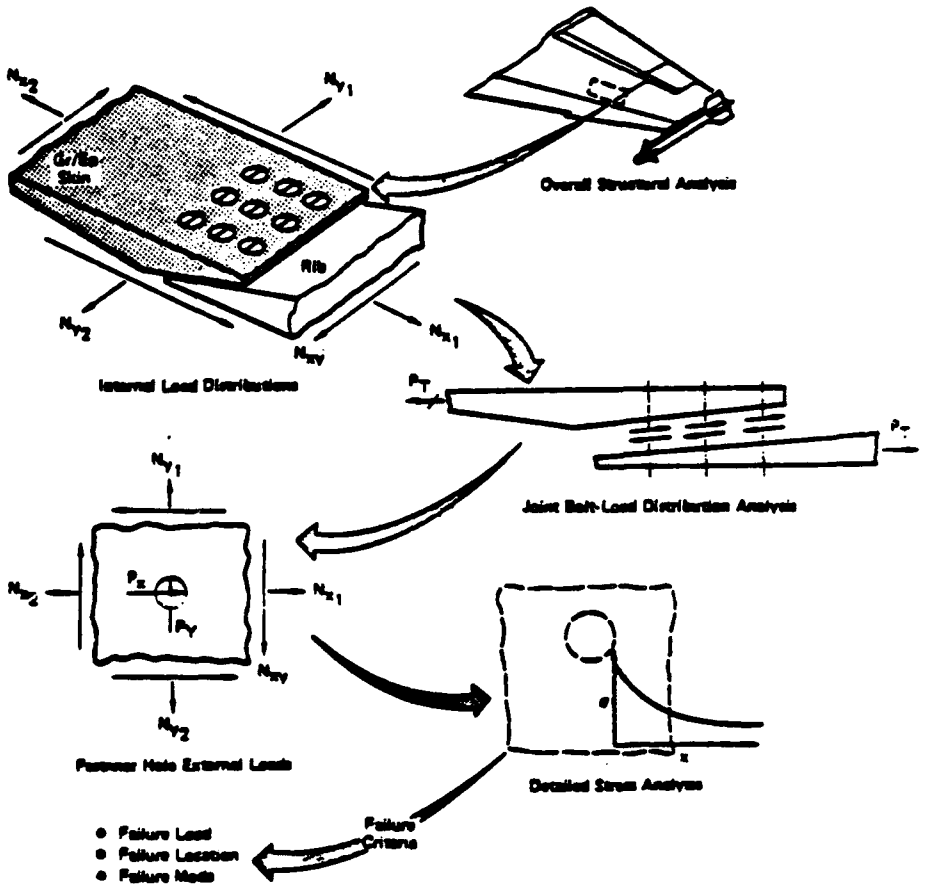

Figure 1.3 Analysis of Bolted Joints in Composite Structures [ref. 1]

CHAPTER 2. RELATED PAST WORK EFFORTS

There have been numerous studies of the mechanical response of bolted joints in composite structures. Some of these have been analytical or numerical in nature while others have been experimental. Nearly all the analytical and numerical studies have relied on a planar treatment of the problem. Experimental approaches range from ultimate failure testing to the application of highly sophisticated experimental stress analysis techniques . A limited number of studies have attempted to verify analytical assumptions experimentally . Both single and multiple connector configurations have been investigated. While this section is an attempt to review these efforts, it does so only as they apply to the present research work and may thus be noninclusive.

2.1 ANALYTICAL/NUMERICAL APPROACHES

Perhaps one of the earliest analytical efforts was the planar approach of Bickley[2] that attempted to find the stresses in an infinite plate with a hole subjected to point, pressure, and shear traction loading. Stress functions were employed and the effects of nonuniform loading conditions around the hole were investigated. In this work, the pin forces acting on the isotropic plate were approximated by a cosinusoidal radial loading around the upper half of the pin. Effects of plate finiteness in this type of approach were studied by Howland,[3] Knight[4], and Theocaris[5], by the superposition of analytic solutions. The effects of plasticity in an isotropic pin-loaded plate was investigated by Howland[6].

The use of composite structures with bolted joints requires the knowledge not only of the complex stress distributions around the hole, but also the ultimate strength of the joint itself. Elasticity approaches have

been employed by many researchers to this avail. Oplinger and Gandhi[7] used a least squares boundary collocation method in conjunction with a complex variable formulation to model the two dimensional elastic response of single and periodic array fasteners with rigidly pinned arrangements. Friction-less contact, linear elastic material conditions, and an assumed cosinusoidal radial pin displacement were used to investigate the effects of various pin spacings to diameter and edge distance to pin diameter ratios for $[(0)_n]_s$, $[(0/90)_n]_s$, and $[(0/+45/-45)_n]_s$ glass and graphite epoxy laminates. Failure mechanisms were studied using a layer by layer application of Hoffman's[8] quadratic failure rule. The effects of pin friction were accounted for in this approach by the authors in a latter work.[9] In a similar approach, de Jong[10] calculated the stress distributions around both isotropic and orthotropic pin-loaded holes. As in the earlier work of Oplinger and Gandhi, the pin was considered to be rigid and frictionless. The effects of pin friction and loading direction were analyzed later by de Jong[11]. He concluded that pin friction had a significant effect on both the stress distribution and strength of the connector.

Garbo and Ogonowski[12] used the anisotropic two dimensional theory of elasticity in conjunction with laminate plate theory and the point stress failure hypothesis of Whitney and Nuismer[13] on a ply by ply basis in their Bolt Joint Stress Field Model (BJSFM). Stress distributions and ultimate strength of pin-loaded laminates were predicted assuming a cosinusoidal radial pressure distribution for the pin/laminate interaction. Reasonable experimental agreement was found for tension and shearout failure modes, but bearing failure predictions appeared to be conservative.

A more compact analytical solution to the problem was obtained by Zhang and Ueng[14] by first assuming displacement expressions that accommodated the displacement requirements and then calculating the appropriate stress functions by anisotropic elasticity. A rigid pin that included frictional effects was assumed while $[(+45/-45)_n]_s$ and $[(0/+45/-45)_n]_s$ laminates were modeled. Mahajerin and Sikarskie[15] modified the boundary element method (BEM) to evaluate singularities thus improving the accuracy of the methodology. They evaluated a pin-loaded laminate with a rigid, no slip, and cosinusoidal distribution of surface traction pin/plate interaction. Computational comparisons to a two dimensional linear elastic finite element approximation

of the same problem were presented.

The effects of pin elasticity, clearance, and Coulomb friction on the stresses developed in an infinite pin-loaded plate were studied by Hyer *et al*[16] in a two bodied elasticity contact problem. A complex Fourier series was used to model the unknown boundary tractions on infinite plates of varying orthotropy. Collocation was employed to arrive at a solution that satisfied all boundary conditions while an iterative technique established the proper contact angle. The results indicated that pin rigidity had negligible influence on radial and circumferential stress magnitudes and distributions, while material orthotropy had a great effect. Radial tractions along the pin boundary were significantly different from Bickley's cosinusoidal assumption for highly orthotropic plates where the principal stiffness direction is perpendicular to the pin loading direction. For moderately orthotropic plates, increasing friction reduced and shifted the peak bearing stress on the top of the pin while the sign of the circumferential stress was reversed at this location. Increases in pin clearance acted to widen the peak circumferential stress distribution and shift it towards the top of the pin. Radial stress magnitudes were increased.

The effects of washer clamp-up in composite bolted joints was investigated by Smith *et al*[17]. Through thickness clamping forces from pin washers were modeled in the hope of explaining observable increased ultimate bearing failures.

There have been numerous finite element approximations of the pin-loaded orthotropic connector. Various levels of problem modeling involving assumptions for pin/plate boundary conditions, material linearity and elasticity, failure mechanisms, and three dimensional effects may be seen in past efforts.

Waszczak and Crews[18] modeled $[(+45/-45)_n]_s$, $[(0/+45/-45)_n]_s$, $[(+45/-45/90)_n]_s$, and $[(+45/-45/0/90)_n]_s$ pin-loaded laminates with a two dimensional finite element approximation in an attempt to predict joint strength and failure mode. A cosinusoidal radial pressure distribution was used with a frictionless assumption to represent the pin/plate interaction while the Tsai-Hill[19] distortional energy failure criterion was used to predict laminate failure strength and mode. An excellent correlation of failure modes to experimentally available data was reported, but conservative strengths were

obtained.

Wong and Matthews[20] used a two dimensional finite element approximation to obtain strain distributions in single and double bolted orthotropic joints. Like the earlier work of Wasczcak and Cruse, a cosinusoidal radial pressure was used, but failure laws were not applied. A similar approach was attempted by Chang[21] where the Yamada-Sun[22] failure criterion was used in conjunction with a characteristic failure curve. Pin/plate interaction was modeled with a rigid pin and a cosinusoidal radial pressure distribution. An iterative determination of the contact angle was made based on the sign of the radial stresses. The joint strength and failure modes agreed well with those available in existing literature, leading Chang to conclude that the cosinusoidal radial stress distribution is acceptable if a proper failure criterion is employed.

Agarwal[23] used the first ply failure criterion of Grimes and Whitney[24] to determine laminate strength and the Whitney-Nuismer[25] average stress criteria to predict failure strength in a two dimensional NASTRAN finite element approximation of $[(0/90)_n]_s$, $[(+45/-45)_n]_s$, and $[(0/90/+45/-45)_n]_s$ connectors. Surprisingly, Agarwal used a uniform displacement condition at the opposite end of the coupon yet enforced a complete ninety degree contact angle about the rigid pin. Failure strength and mode compared favorably with existing experimental data with the exception of conservative failure strengths for those laminates that exhibit nonlinear stress-strain behavior. In similar approaches, Soni[26] and Pipes *et al*[27] altered Agarwal's analysis by using the Tsai-Wu[28] tensor polynomial failure criterion along with a last ply failure stress assumption and the Pipes-Wetherhold-Gillespi point stress failure criterion respectively. As in the Agarwal results, failure strengths were conservative.

The assumption of an elastic pin can be seen in the work of Crews *et al*[29] where $[(0)_n]_s$, $[(0/90)_n]_s$, $[(+45/-45)_n]_s$, and $[(0/90/+45/-45)_n]_s$ finite width connectors were modeled with a two dimensional finite element approximation. The discretized pin was connected to the coupon through short, stiff spring elements thus insuring a frictionless contact between the two. The contact angle of the connector was found through an iterative procedure where the stiffness of those springs that had tensile forces in them were negated. Radial stress peak values and distributions were seen to vary

dramatically with increasing orthotropy while maximum tensile stresses were strongly influenced by finite width and edge distances.

The effects of nonlinear material behavior after initial ply failure upon bearing failure strengths were investigated by Tsujimoto and Wilson[30]. Their two dimensional finite element analysis attempted to model bearing failure by assuming an elastic-perfectly elastic bimodular material model. A cosinusoidal pressure distribution signifying a rigid, perfectly fitted pin was used as well as the Coulomb friction assumption. Incremental failure contours for each laminae were obtained using laminate plate theory and the Hill[31] yield criterion. Comparison to linear elastic analysis with point stress failure assumptions (that use the Tsai-Hill or Tsai-Wu quadratic interaction failure models) and available experimental results indicate a more accurate prediction of joint strength and failure type.

Eriksson[32] mirrored the two body elasticity approach of Hyer and Klang when he investigated the effects of material orthotropy, pin elasticity, clearance, and friction with a two dimensional, linear elastic finite element model. Similar results to Hyer and Clang were obtained and experimental strains along the coupon bearing plane and net section were in agreement with model strains.

Through thickness effects in the pin bearing problem were investigated by Matthews *et al*[33] in their three dimensional, linear elastic finite element analysis. Effective laminate three dimensional constitutive equations were arrived at by the application of laminate theory (ie; inplane transformation of unidirectional lamina and application of three dimensional, orthotropic constitutive relationships along with a thickness weighted average). Single element, half thickness, half width symmetry was used in defining the mesh while pin-loading was accomplished by a an axial displacement boundary condition of the central nodes to the coupon. Establishment of the contact angle was done in a similar fashion in the afore mentioned work of Crews *et al* with the exception that contact forces were averaged through the thickness. Lamina and interlamina stresses were obtained by the substitution of the finite element strains into the individual lamina constitutive equations. In addition to the well known pin-loaded configuration, they also simulated pin-loading with both a finger tightened and a fully tightened clamped bolt washer assembly by imposing through

thickness displacement and pressure boundary conditions respectively on the first ring of elements in the mesh during the pin-loading of the coupon. Results for $[(0/+45/-45)_n]_s$ and $[(0/90/+45/-45)_n]_s$ laminates indicated that through thickness tensile forces were reduced from the straight pin-loaded case to the finger tightened clamped case. Significant increases in the axial compressive stress and one interlaminar shear stress were observed at the washer edge for the fully tightened bolt washer assembly.

The issue of interlaminar stress singularities at curved free edge surfaces and their possible role in delamination initiation was studied in greater detail by a host of investigators. Rybicki and Schmueser[34] used a three dimensional linear elastic finite element analysis to observe the effects of stacking sequence at curved free edge surfaces. By todays standards, a relatively course mesh was used to model a circular hole in tension. Certain adjacent plies were "smeared" or averaged creating effective properties to reduce the number of required elements.

Stacking sequence has been found to greatly affect the normal interlaminar stress in magnitude and in some cases in sign. Raju and Crews[35] used a highly refined mesh in their three dimensional linear elastic finite element analysis of the same problem in hopes of modeling the interlaminar stress singularity. Two dimensional modeling was done away from the hole while three dimensional modeling in which each lamina received a layer of elements was done near the hole. A three dimensional to two dimensional transition region was placed in between them while $[0/90]_s$ and $[90/0]_s$ laminate arrangements were looked at. Mesh refinement increased the singularities magnitude and definition. Carlsson[36] investigated the same problem, but with a laminate that had twenty eight plies. Each ply was modeled with three 20 node volume elements through the thickness in his linear elastic three dimensional finite element approximation. High interlaminar stress locations were found to agree closely with TBE enhanced X-ray photographs of a fatigue damaged specimen. Lucking *et al*[37] used the concept of substructuring to evaluate the effects of geometry on the interlaminar stresses in a $[0/90]_s$ laminate. Large values of hole radius to laminate thickness ratios tended to increase interlaminar stresses thus leading the authors to conclude that laminate strength might be reduced.

2.2 EXPERIMENTAL APPROACHES

Early experimental efforts in the mechanical fastening of composite materials were centered on the effect of geometric and material joint parameters on ultimate strength. Testing of both single and multiple joint connectors was undertaken in an empirical approach to design optimization. Later efforts focused on the application of various experimental techniques to determine actual mechanical response.

Collings[38] investigated the effects of laminate orientation, bolt clamping pressure, and laminate thickness on the ultimate strength of single and multiple joint configurations for various specimen widths and hole diameters in carbon fiber reinforced plastics. Single configuration results indicate that the inclusion of +45/-45 plies into the laminate acted to reduce the net section stress concentration by "softening" the joint. Optimum bearing strengths were obtained by a laminate that consisted of 55% - 80% of 0 plies with the remainder of the laminate comprised of +45/-45 plies to add transverse strength. Maximum tensile and shear strengths were obtained when the ratio of 0 to +45 plies were 2:1 and 1:1 respectively. Clamping pressure was found to increase bearing strength significantly up to a point. This was also found to be true in glass fiber reinforced laminates in the work of Stockdale and Matthews[39]. Although the effects of laminate thickness appeared insignificant with clamping pressure, increasing the ratio of pin diameter to specimen thickness was found to significantly reduce bearing strength. Minimum values of width and edge distance to pin diameter ratios are required for full bearing strength. Laminate orientation was found to affect these minimum values.

Quinn and Matthews[40] investigated the effects of stacking sequence on single connector bearing strength in glass epoxy quasi-isotropic laminates. Bearing strength was found to increase for those stacking sequences that had 90 plies close to the surface. They inferred that stacking sequence could alter interlaminar stresses thus affecting bearing strength. Collings and Beauchamp[41] found a direct correlation of bearing strengths with bearing stiffness in carbon fiber reinforced plastics. Johnson and Matthews[42] offered a definition of limit load for graphite reinforced plastic single connectors.

For crossply orientations, a .4% elongation of original hole diameter induced significant visible damage thus defining a design load limit that could be used to determine safety factors. The use of glass/carbon hybrid composites and their effect on bearing strength was investigated by Matthews *et al*[43]. The bearing strength of $[(0/90)_n]_s$ laminates was found to be the highest in all glass and all carbon laminate constructions while hybrid laminates with varying ratios of the materials were weaker in bearing strength. All carbon laminates had brittle failure characteristics while all glass and hybrid laminates failed in a ductile fashion.

Collings[44] attempted to use a semi-empirical approach to predict the bearing strength of single connector carbon fiber laminates of varying 0, 90, and +45/-45 ply construction. Individual layer type bearing failure was predicted by a simplified stress analysis and interaction effects based on experimental results were used to try to predict the bearing strength of multilayer type laminates. With the interaction effects expressed in terms of [0] ply longitudinal and transverse compressive strengths as well as [0] ply constrained bearing strength, comparisons of predicted results with mean values of experimental results was good.

Multiple bolt connectors were tested by Collings[45] in an attempt to describe hole interaction effects using single bolt results. Specimen dimensions, bolt spacing, and clamping pressure were selected for two hole tandem, two hole side by side, and two tandem side by side configurations so that full single bolt bearing strengths could be achieved. Interaction effects were found to be negligible between the bolts and joint strength could be predicted from single bolt test results. Pyner and Matthews[46] found that interaction effects became significant in multiple bolt connectors if specimen and bolt spacing dimensions were selected such that single bolt bearing strengths could not be achieved. They concluded that the load/bolt ratio decreases as joint geometry becomes increasingly complex.

Experimental stress techniques have been applied by some researchers to characterize joint behavior at loads other than ultimate. Full field displacement, strain, and stress distributions in single and multiple bolt connectors have been obtained. Nisida and Saito[47] determined principal stress components along the hole edge in an isotropic, single pin connector using an interferometric photoelastic technique. The relations between these stresses

and edge distance to hole diameter ratio were determined.

Orthotropic photoelastic methodologies have been applied by Prabhakaran[48] and Hyer and Liu[49 50]. Prabhakaran investigated the in-plane shear stress distribution along a shearout plane for quasi-isotropic and unidirectional orthotropic photoelastic laminates for various edge distance to pin diameter ratios. He concluded that higher shear stress levels are obtained for shorter edge specimen dimensions in quasi-isotropic connectors. Hyer and Liu took this type of analysis further by the application of a finite difference technique and plane stress equilibrium equations to separate stresses in pin-loaded $[(0/+45/-45/90)_n]_s$, $[(0)_n]_s$, $[(+45/-45)_n]_s$, and isotropic material systems. Stresses in quasi-isotropic connectors were found to behave very similarly to those in isotropic connectors with the exception of having negative hole shear stress values, slightly higher bearing stresses, and a skewed peak radial stress. Stresses in the unidirectional connectors were found to vary from those in the quasi-isotropic cases by a lower value of hole hoop stress (that rose dramatically to a maximum value) at the net section and higher net section stresses at the hole edge. Hoop stresses in the $[(+45/-45)_n]_s$ connectors were found to vary from those in the quasi-isotropic cases by having a negative value at the top of the hole that increased to a maximum value at a location roughly two thirds around the connector.

Conventional bar and space grating moire methodologies have been applied to $[(0/90)_n]_s$ and $[(+45/-45)_n]_s$ graphite connectors by Koshide[51]. Full field, front surface, loading direction displacement contours were obtained at various pin-load levels for both conventional and woven fabric laminates. Bearing and net section longitudinal strains were obtained by eye estimations of fringe centers at various locations along these sections. The nonlinear contact behavior for a clearance fit bolt was studied using a fiber optic technique by Prabhakaran and Naik[52]. The contact angle for a quasi-isotropic laminate with a one millimeter clearance was determined.

2.3 Combined Approaches

Combined experimental and analytical studies in bolted composite

joints have been limited in comparison to separate experimental or analytical studies. Some studies have tended to emphasis one approach more than the other. There have been few that give equal weighting to both approaches thus allowing for the valid comparison of experimental and analytical results. Some studies have used finite element approximations to model and predict the ultimate strength of the connector. These models were validated by ultimate strength testing of representative connectors.

Chang *et al*[53] employed a two dimensional linear elastic finite element approximation to obtain the stress distribution of various pin-loaded laminates. A cosinusoidal radial stress distribution around the pin was used with linear elastic material assumptions. Failure prediction was accomplished by assuming laminate failure as per the Yamada-Sun[54] failure criterion along a chosen characteristic failure curve whose normal radii were determined experimentally. The failure mode was determined by the angular location of the failure. Models were verified by comparisons with previous investigators experimentally determined values of ultimate strength and failure modes in graphite epoxy laminates of $[(0/90)_n]_s$, $[(+45/-45)_n]_s$, and $[(0/90/+45/-45)_n]_s$ configurations. This approach was extended to evaluate two hole tandem and two hole side by side bolted configurations[55] in $[(0/\pm45/90)_3]_s$, $[(90_2/\pm60/\pm30)_2]_s$, $[(\pm45)_6]_s$, and $[(0/90)_6]_s$ laminates with various pin diameters, edge distances, and widths. Results for quasi-isotropic laminates and $[(90_2/\pm60/\pm30)_2]_s$ laminates revealed that predicted strengths were conservative by 10-30 percent with specimen geometry having little effect. Crossply and angleply laminate results indicated predicted strengths were conservative by 10-40 % with better accuracy being obtained for smaller holes. Failure modes were predicted with much greater success. Chang *et al*[56] used this model and results to design bolted connections with more then two bolts. No experimental verification was presented.

Chang *et al*[57] modified their analysis to include nonlinear intralaminar shear stress-strain behavior in hope of reducing their conservative predictions for single bolted configurations only. Comparison to earlier experimental results indicated that inclusion of this nonlinear material behavior reduced predicted strength values for $[(0/90)_n]_s$ and $[(+45/-45)_n]_s$ laminates to a 10-25 % level from a previous 10-40 % level. Failure mode predictions in these laminates were more realistic.

In an attempt to understand the progressive nature of failure in laminated composites, Chang *et al*[58] altered their two dimensional nonlinear elastic finite element analysis to include an incremental loading and failure approach. At each load increment, incremental and total stresses and strains were found and transformed into laminae stresses and strains. Failure criterion that predicted the failure modes of matrix cracking, fiber-matrix shearing, and fiber breakage were used. A material property degradation model that altered laminae stiffnesses was employed to recalculate updated laminate stiffness. Stresses were redistributed by rebalancing the finite element equilibrium equations at the particular load level with these updated stiffnesses for that load step using a Modified Newton-Raphson iterative scheme. Joint failure was assumed when damage was present across a complete boundary of the laminate. The matrix failure criterion was the summation of the squared normalized transverse and shear stresses where normalization was to ultimate transverse tensile and shear strengths respectively. The fiber-matrix shearing and fiber breakage failure criterion were similar, but used the longitudinal stress and ultimate stress value respectively. Property degradation took the form of setting the transverse stiffness and Poisson ratio values to zero for matrix cracking within a lamina. For fiber breakage and/or fiber-matrix shearing, setting the longitudinal stiffness and Poisson ratio to zero was accompanied by a reduction in the transverse and shear moduli in accordance to a micromechanics approach for fiber bundle failure. The ultimate strength of tensile specimens with a central circular hole was predicted for various laminate orientations. Model verification was done by experimentally obtaining the ultimate strengths. Predicted results agreed to experimental ones within 20 % while failure modes were accurate.

Chang *et al*[59] extended this analysis to pin-loaded composite connectors. Compressive matrix failure was incorporated into the analysis through the Hashin Failure Criterion[60]. Comparisons to earlier pin-loaded ultimate strengths and failure modes showed that the predicted ultimate strengths were within 20 % of the experimental values and that failure modes were accurately determined.

An experimental/analytical investigation into the damage build up in glass and graphite $[(0/+-45)_3/0]_s$ laminates was conducted by Tsiang and Mandell[61]. Both tensile specimens with central circular holes and pin-loaded

specimens were incrementally loaded. Ply by ply specimen damage was found through a de-plying technique at the various load levels. A two dimensional linear elastic finite element approximation was undertaken with the application of the Tsai-Hill and Whitney-Nuismer failure criteria. First ply failure around the hole was predicted with the Tsai-Hill criterion while ultimate specimen strength was predicted by the point and average stress methods of the Whitney-Nuismer criterion. Comparisons of these predictions and the observed damage at the various load levels were done. No direct physical correlation was found suggesting that the non-frictional cosinusoidal radial pressure distribution used in the analysis was incorrect.

Oplinger[62] investigated the linear and nonlinear joint response of pin-loaded laminates by using an analytic two dimensional linear elastic boundary collocation scheme, and experimental techniques of strain gages and conventional moire methodologies. Comparison of net section strain gage readings with analytic results for $[(0)_4/(+-45)_3]_s$, and $[(+45/-45)_n]_s$, laminates as well as aluminum specimens suggested that $[(0)_4/(+-45)_3]_s$ laminate behaved linearly while $[(+45/-45)_n]_s$ specimens behaved nonlinearly like its aluminum counterpart. Comparison of strains from front surface experimental moire displacement contours and linear elastic analytic results suggested that [0/90] laminates behaved nonlinearly in shear along a prescribed locus of maximum shear strain. The experimental shearout failure mode for [0/90] laminates was found to be along this locus.

Wilkinson and Rowlands[63] used a combined experimental and numerical approach in their study of Sitka-spruce single pin-loaded connectors. Conventional moire methods and strain gages were used to obtain front surface strain values along the bearing section for specimens of varying pin to hole diameter, edge to width, and edge to end distance ratios. Comparisons were made along the bearing section to a two dimensional linear elastic finite element analysis that accounted for friction effects and pin-hole separation (i.e. contact angle determination). Model results indicated that friction was found to reduce the bearing area thus increasing peak radial stresses while radial and tangential stresses were found to be independent of edge distances. Radial stresses were found to be reduced and more uniformly distributed with decreasing end distances. Decreasing the pin to hole ratio was found to reduce contact area thus increasing maximum radial stress values. This

modeling effort was expanded to include tandem connector arrangements in boron and glass epoxy laminates.[64] Pin bypass loads were assumed.

Cloud *et al*[65] applied both conventional and interferometric moire techniques to obtain displacement contours of the orthotropic pin-loaded connectors that Mahajerin [15] had modeled earlier with a boundary element analysis. Net section strains were obtained and net section stresses were calculated using a two dimensional Hooke's stress-strain approximation. Laminate longitudinal and transverse moduli as well as Poisson's ratio were obtained from single respective direction tension tests. Comparison showed that these experimentally obtained net section stresses were approximately 25 % lower than those from the boundary element analysis.

Serabian[66] applied conventional moire techniques and a two dimensional linear elastic finite element analysis in his investigation of $[(0/90)_3,0]_s$ S2-glass pin-loaded laminates. Both u and v front surface displacement contours of the laminate were found at various load increments up to incipient failure. Experimental shear strains along a maximum locus were obtained at each load level from these displacement contours through graphical analysis. A frictionless finite element approximation of the coupon that accounted for pin/hole separation effects and an end loading arrangement predicted a similar locus of maximum shear strain. Figure 2.1 illustrates the finite element mesh of the coupon that was employed. An extensive lamina characterization was undertaken to develop an average lamina (in-plane) mechanical property data base[67]. Tangent lamina mechanical properties were used in conjunction with laminate plate theory to provide effective laminate mechanical properties in the finite element approximation. A two dimensional version of Hoffman's failure criteria [8] was applied to transformed laminate strains and ply failure zones at each load increment were obtained. Finite element displacement fields were post processed to reflect experimental optical processing conditions. Visual comparisons of these displacement fields with their experimental counterparts, as seen in Figure 2.2, indicated increasingly higher experimental shear strains near the pin-hole interface. This difference was more pronounced with increasing load levels. Numerical comparisons of these shear strains as seen in Figure 2.3 indicated similar results. Locus location of these variations in these strains corresponded well with ply failure zone location for all load increments.

The effects of intralaminar shear nonlinearity was investigated by Serabian and Oplinger[68] by comparison of these analytical results with those obtained from a similar finite element approximation that modeled shear softening through an effective secant moduli approach. An exaggerated nonlinear material shear stress shear strain law was used in search of shear softening. Comparisons of linear and nonlinear shear strains along the maximum locus as seen in Figure 2.4 indicate a definite shear softening phenomenon.

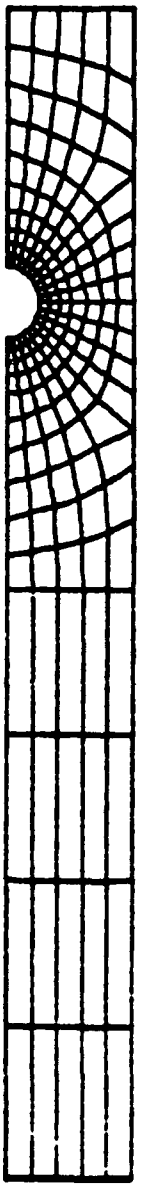

Figure 2.1 Two Dimensional Mesh of Pin-Loaded Coupon [ref. 66]

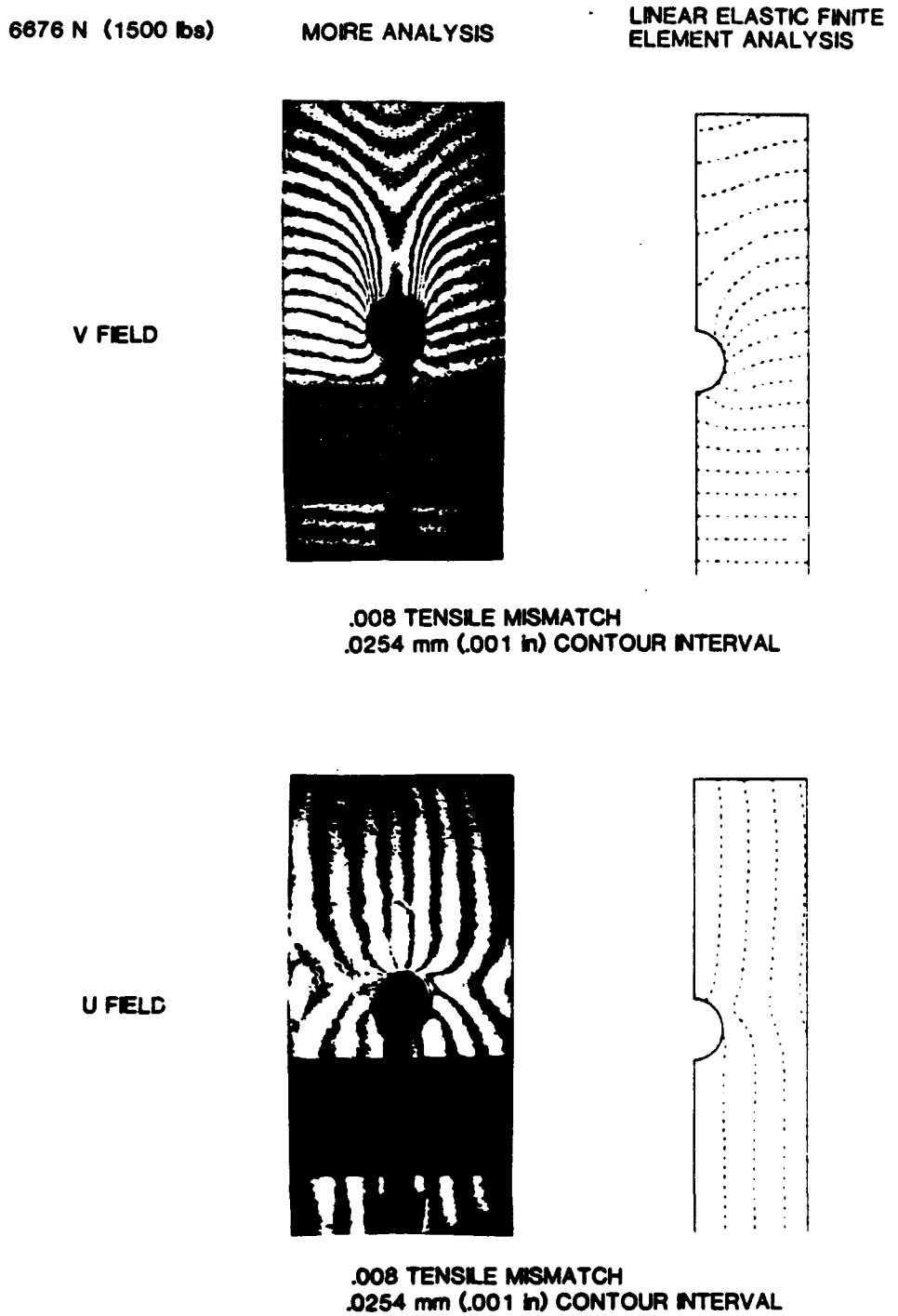

Figure 2.2 Comparisons of Experimental and 2D linear Elastic Finite Element Displacement Contours of a 0/90 Pin-loaded Laminate (1500 lbs) [ref. 66]

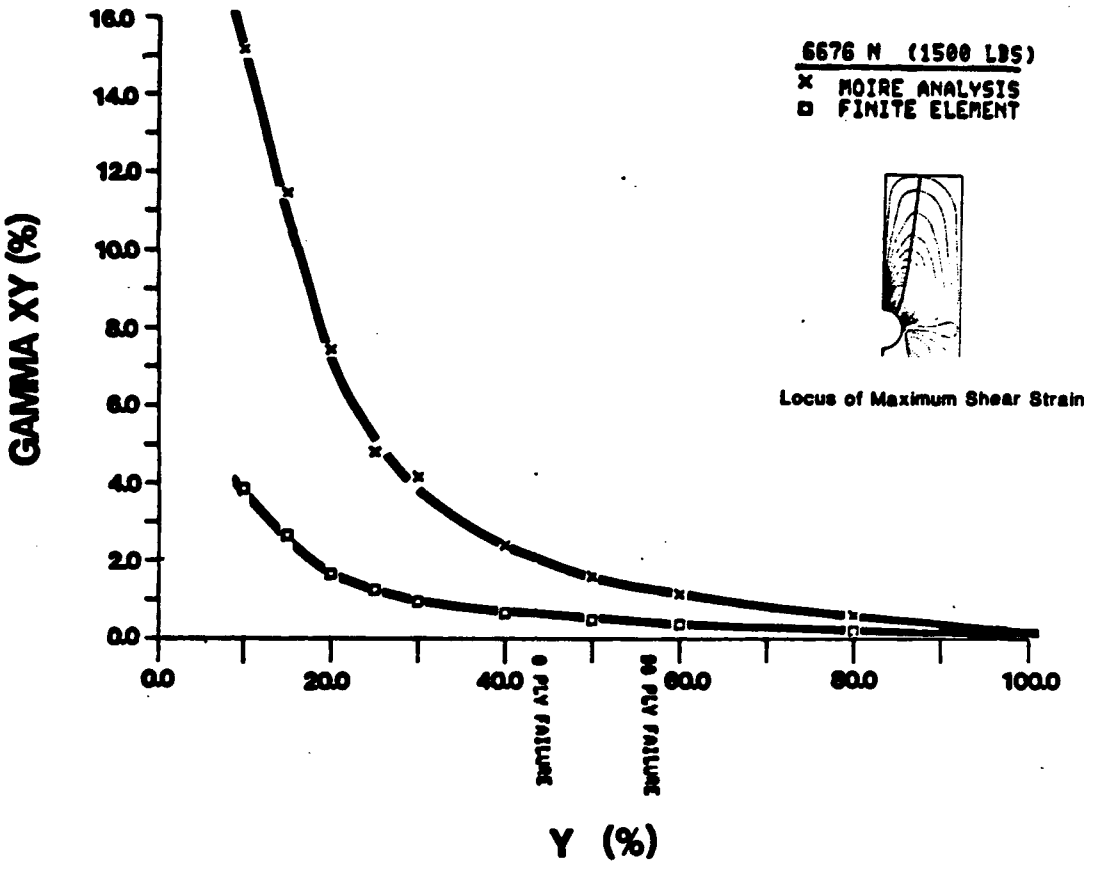

Figure 2.3 Comparisons of Experimental and Linear Elastic 2D Finite Element Shear Strains Along Locus of Maximum Shear Strain of a 0/90 Pin-Loaded Laminate (1500 lbs) [ref. 68]

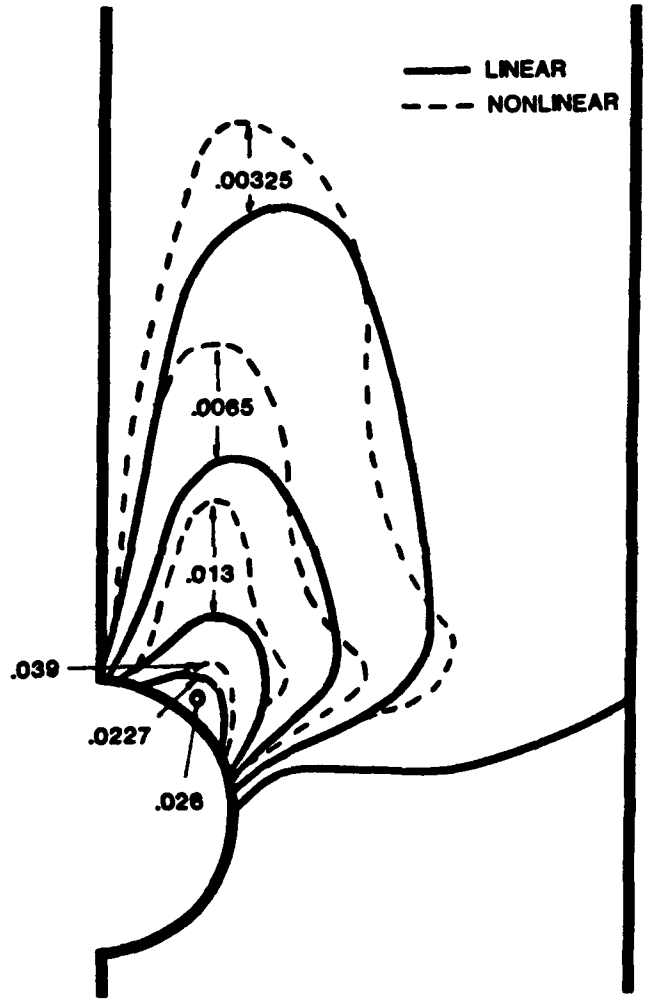

Figure 2.4 Comparisons of Linear and Exaggerated Nonlinear Elastic Shear Strains in a 0/90 Pin-loaded Laminate [ref. 68]

CHAPTER 3. UNRESOLVED CRITICAL ISSUES

3.1 THREE DIMENSIONAL EFFECTS

Three dimensional effects in bolted composite connectors have been left all but untreated by investigators. Although experimental efforts have looked at the effects of washer clamp-up on bearing strength, treatment of three dimensional effects has been limited to the modeling of unloaded holes in uniaxial tension or compression and Matthew's *et al* [33] analysis of a pin-loaded coupon. From these studies, it is apparent that high interlaminar stresses exist near the hole boundary. These through thickness stresses intuitively must play a major role in the initiation of failure. If accurate joint strength predictions are to be made, inclusion of these stresses necessitate a three dimensional approach. Variations in ultimate strength and observed damage from washer clamp-up is testament to this fact.

From the literature, it can be seen that there has been no known experimental determination of out-of-plane deformation of pin-loaded laminates. An experimental determination of this throughout the load history of the laminate could lead to an understanding of this phenomenon and point to the inadequacy of two dimensional modeling approaches.

3.2 CONSTITUTIVE EQUATION MODELING

It is apparent from past studies that laminate configuration greatly affects the mechanical response of pin-loaded laminates. Analysis based on linear elastic behavior, while sufficient for certain classes of laminates, clearly becomes inadequate for others in particular $[(0/90)_n]_s$ and $[(+45/-45)_n]_s$. Joint strength prediction for these classes of laminates from analysis based on linear elastic material behavior are extremely conservative.

Shear or tensile stress reduction, referred to as "softening" by some investigators, is not accounted for by linear elastic approaches thus leading to unreasonably high predicted stresses and lower ultimate strengths from associated failure theories. Recent two dimensional modeling efforts that include intralaminar shear nonlinearity have provided more realistic stress states thus reducing this conservatism, but not eliminating it.

Past work by the author [66] that characterized the lamina mechanical properties of his fiber/resin system showed that other secondary nonlinearities do exist beside the major intralaminar shear nonlinearity. It is not apparent to what extent these secondary nonlinearities affect laminate mechanical response. Furthermore it is apparent that the use of laminate theory with these lamina nonlinearities will not include those nonlinearities that are produced from ply interaction effects. A prime example of this is matrix cracking in crossply laminates. Occurring at low strain levels, it has been shown to reduce axial stiffness by as much as 35% for minimally constrained fiberglass laminates such as $[0/90_n]_s$[69]. The property degradation model of Chang and co-workers tries to account for this nonlinearity on a layer by layer basis by eliminating the layer's transverse modulus and Poisson's ratio when their transverse tensile and shear strengths are reached. This type of "on-off" approach, more commonly referred to as "ply discounting", does not allow for a gradual degradation of those properties and has been shown to over estimate axial stiffness loss in highly constrained laminates such as $[(0/90)_n]_s$.[70] In addition to this, since it is applied on an element level, its macroscopic effects are dependant on the refinement of the mesh used in the analysis. Clearly constitutive equation modeling should account for nonlinearities resulting from ply interaction effects and should be independent of mesh refinement. Computational efficiency is also prudent for large scale finite element implementation.

Three dimensional modeling requires the use of three dimensional constitutive equations. The use of two dimensional laminate theory along with three dimensional orthotropic constitutive equations to predict three dimensional mechanical response has been successfully used by some investigators. Inherent in this approach are the use of laminate properties such as through thickness Poisson ratios and tensile modulus as well as transverse shear moduli. For lack of experimentally determined values, these

laminate mechanical properties have been assumed. It is not apparent what effect that these assumptions have on the results of their analyses. Proper characterization of these properties or sensitivity analyses should be undertaken to clarify this.

3.3 Pin/Composite Interface Interaction

The representation of pin-loading has evolved from the simple cosinusoidal pressure distribution of Bickley [2] to a complicated complex variable collocation procedure of Hyer *et al* [16]. The effects of pin elasticity, friction, and clearance have been analytically shown in a two dimensional elasticity analysis to affect the stress distributions in pin-loaded orthotropic connectors. Most past two dimensional finite element approximations have not simultaneously included all three facets of the problem. Three dimensional element approximations have only accounted for contact angle determination. Experimental verification of pin elasticity, friction, and clearance effects cannot be found in the literature.

3.4 Composite Material Failure Mechanisms

Chang et al [55-59] have included failure mechanisms into models of pin-loaded composite connectors. Their progressive approach, that models various types of damage in conjunction with the Yamada-Sun failure criteria, has proven somewhat effective in modeling two dimensional failure aspects. Ultimate strength predictions have been made to within 20 % of experimentally obtained values while failure mode predictions have followed observable trends. Delamination damage is not treated in this two dimensional type of analysis.

Three dimensional treatment of failure mechanisms in pin-loaded connectors has not been undertaken to date. Three dimensional modeling of both unloaded and pin-loaded holes has revealed that high interlaminar stresses exist near the hole boundary. At the present time, it is not clear to what extent these stresses play in failure initiation and, in particular,

the delamination mode of failure. Experimental determination of damage within pin-loaded coupons, although limited to $[(0/+45/-45)_3/0]_s$ laminate orientations, has shown that delamination damage is present within the coupon.

3.5 Experimental/Analytical Comparative Link

There have been limited comparisons between experimental and analytical studies. Many comparisons have been made with ultimate strength and failure modes while more quantitative comparisons have been limited to strain comparisons at certain points (ie; strain gage) or along specified sections (ie; moire displacement contouring) in the coupon. While illustrating the differences between modeling and experimentation, they lack the informativeness that a two dimensional, load level dependent, comparison would yield. This type of comparison would allow the investigator to quantitatively identify the load dependency of their modeling assumptions through "zones" of difference rather then sections.

Comparisons have generally been limited to the aforementioned due to the lack of an automated full field data reduction system. Most section comparisons have been done by cumbersome graphical hand techniques that require that displacement contour fringe centers be found by eye and curve fitted to obtain strain values. Automation of this technique has been accomplished through video digitizing equipment and an automated multi section approach has been established to yield full field results[71]. However; the accuracy of this particular method has not been determined to date.

Recently Tessler *et al*[72] have applied a least squares penalty constraint finite element method to generate strain fields from moire displacement contours. This approach allows for a two dimensional smoothing of the raw video intensity data. To date, the methodology has only been applied to limited test cases to assess its accuracy. Initial results indicate that extremely accurate strain fields may be obtained. However; effects of fringe curvature and mismatch strains need to be investigated.

CHAPTER 4. RESEARCH OBJECTIVE AND APPROACH

4.1 RESEARCH OBJECTIVE

The objective of this dissertation is to quantitatively establish the effects of crossply intralaminar shear material nonlinearity on the modeling accuracy of $[(0/90)_n]_s$ and $[(+45/-45)_n]_s$ pin-loaded laminates.

4.2 RESEARCH APPROACH

The dissertation's research objective was carried out by the following combined experimental/analytical approach. The mechanical response of both $[(+45/-45)_3]_s$ and $[(0/90)_{3,0}]_s$ pin-loaded laminates were determined through three dimensional experimental displacement contouring using both conventional and projected moire methodologies.

The in-plane mechanical property data base of the fiber/resin material system was extended from past efforts [66] to include intralaminar shear stress shear strain response by the ASTM D3518 specification. Effective laminate mechanical properties were calculated using these in-plane values and classical laminate plate theory.

Based on the appreciable through thickness mechanical response of the pin-loaded laminates, a three dimensional modeling approach was taken. This approach necessitated the need for laminate through thickness Poisson ratio and transverse shear moduli values. A modified three point bend test was used to obtain values of laminate transverse shear moduli while through thickness contraction measurements on laminate tension tests were employed to obtain estimates of the Poisson ratio values.

Three dimensional constitutive equations for the $[(0/90)_n]_s$ laminate were developed from effective and actual lamina mechanical properties.

Three dimensional constitutive equations for the $[(+45/-45)_n]_s$ laminate were developed from a material axis transformation of the $[(0/90)_n]_s$ three dimensional constitutive equations. The validity of these constitutive equations and the effects of nonlinear intralaminar shear behavior were experimentally investigated through a comparison with uniaxial tension tests of both laminates. A sensitivity analysis of through thickness modulus was also done in this comparison in hope of providing insight into the selection its magnitude.

Implementation of these constitutive equations was accomplished by developing two user material subroutines (UMAT) for the finite element code ABAQUS. Both verification and performance rating of these subroutines were done on both a single and multi three dimensional element level using the ABAQUS finite element code.

Three dimensional finite element models of the pin and coupon were generated. Interaction of these two structures was modeled using INTER9 interface elements within the ABAQUS element library. Both linear elastic and nonlinear elastic three dimensional finite element approximations of both laminate configurations were generated.

Comparisons of both linear and nonlinear finite element results with graphically determined strain values from the experimental moire displacement contouring were made. Assessment of nonlinear crossply intralaminar shear behavior on modeling accuracy was determined.

A qualitative investigation into the effects of material damage on the mechanical response of the pin-loaded laminates was done by taking advantage of the translucent nature of the specimens. Backlit specimens soaked in liquid penetrant at various pin-load levels were photographed in hope of qualitatively investigating damage development.

CHAPTER 5. THREE DIMENSIONAL EXPERIMENTAL DISPLACEMENT CONTOURING

Out-of-plane displacements of the pin-loaded laminates were determined with projection shadow moire. Optical system qualification was accomplished by contouring a centrally loaded clamped circular plate. Out-of-plane contouring sensitivity of the pin-loaded laminates was limited to .001" by experimental concerns. In-plane displacement contouring of the pin-loaded laminates was obtained by geometric moire. A contouring interval of .001" was obtainable by using 500 line/inch specimen gratings and Fourier filtering techniques.

5.1 Specimen Description and Fabrication

Coupon geometry followed that of reference [66] which is shown in Figure 5.1. The 6" x 1" $[(+45/-45)_3]_s$ coupons were cut from the central section of a 3' x 3' laminated plate that was manufactured from a 3M SP250-S2 glass fiber/resin system. The prepreg tape of 2-5/8" width was cut into 3' long sections and laid up in a $[(+45/-45)_3]_s$ laminate orientation. This layup was then sandwiched between two flat aluminum plates, vacuumed bagged, and cured in an autoclave under the temperature and pressure conditions specified by 3M. A solid carbide drill was used to drill the .251" diameter pin hole in the center of the coupon 1" down from the top. The $[(0/90)_{3,}0]_s$ coupons were obtained from the similar manufacturing processes of an earlier effort [ref. 66].

5.2 Out-of Plane Displacement Contouring

5.2.1 Projection Shadow Moire

The geometric shadow moire technique was employed to determine the out-of-plane deformations of both the $[(0/90)_3,0]_s$ and $[(+45/-45)_3]_s$ pin loaded coupons.[73] In this technique, the interference of a projected grating and its shadow upon a specimen that has undergone an out-of-plane deformation produces fringes that represent a depthwise contour map.[74] This phenomenon may be seen in Figure 5.2 where an originally flat specimen with incident projected grating pitch (P_s) and projection angle (α) has been displaced out-of-plane by a distance QA. As seen from the recording camera's viewing angle (β), the original projected grating covering length TS *appears* to cover length TR upon the deformed surface. This length variation (RS) may be used to trigonometrically relate the out-of-plane displacement (w) to both the projection and viewing angles through the grating pitch. Upon doing so, we find that;

$$w = N\,P_{eff} = \frac{N\,P_s}{(\tan\alpha + \tan\beta)} \tag{5.1}$$

5.2.2 Projection and Optical Processing Experimental Arrangements

The optical arrangement in Figure 5.3 was used to form and project a moire grating on the surface of the pin-loaded coupon. A 15 mW Helium Neon laser was spatially filtered by passing it through a 40X microscope objective and 10μm pinhole. A multi element transform lens was employed to bring the frequency content of a moire glass master line grating of given pitch P into the Fourier filtering plane. Passage of the $\pm N_d$ diffraction orders from this filtering plane produced a sharpened line grating image of pitch P/2. A field lens collimated this grating image and projected it onto the coupon at a given angle (α) from its normal. Designating the distance from the moire glass master grating to the Fourier filtering plane as S and the distance from the field lens to the Fourier filtering plane as f, the projected pitch (P_s) of

the grating on the surface of the specimen is given as;

$$P_s = \frac{f\ P}{[S\ (N_d + 1)\ \cos\ \alpha\ ]} \tag{5.2}$$

For a normal camera viewing angle ($\beta = 0$), the equivalent out-of-plane contour level is given from equations 5.1 and 5.2 as;

$$P_c = \frac{f\ P}{[S\ (N_d + 1)\ \sin\ \alpha\ ]} \tag{5.3}$$

Actual photographed grating pitch (P_i) was controlled through image magnification by the recording camera. For a given camera magnification (M_c), the imaged grating pitch may be expressed as;

$$P_i = \frac{f\ P\ M_c}{[S\ (N_d + 1)\ \sin\ \alpha\ ]} \tag{5.4}$$

Superposition of the original projected specimen grating with that its image on the deformed specimen resulted in the formation of out-of-plane fringe contours. This was accomplished by either a double exposure technique or a single exposure manual superposition method. Both the loaded and no loaded grating images were photographed on a single piece of recording medium in the double exposure technique. In the manual superposition method, the loaded and no loaded grating images were photographed on separate pieces of recording medium, sandwiched together, and manually aligned. Manual superposition allowed for comparisons of the no load grating image with a series of progressively loaded grating images thus forming an out-of-plane contouring history.

Sharpening of fringe contours obtained from either the double exposure or manual superposition techniques was accomplished through Fourier filtering. The optical processing arrangement shown in Figure 5.4 was used to

accomplish this. A 6 mW Helium Neon laser was spatially filtered by passing it through a 40X microscope objective and 10μm pinhole. The expanding beam was collimated through a collimating lens and passed through the photographs of the superimposed load no load projected gratings. A transform lens transformed this information into the frequency domain. The +1 diffraction order was allowed to pass from the Fourier filtering plane and photographed by a camera. Micropositioning equipment was utilized for the proper alignment of the load no load projected grating images.

5.2.3 SYSTEM QUALIFICATION

A clamped centrally loaded circular aluminum plate of 2" radius and .121" thickness was illuminated with a projected grating ($1/P_s$) of 425 lines/inch. This specimen grating was created by the projection of the +1 and -1 diffraction orders of a 300 line/inch (1/P) glass master grating with a magnification (f/S) of 1.08 and projection angle (α) of 40°. A normal recording camera viewing angle (ie; $\beta = 0$) and camera magnification (M_c) of 1 produced a photographed grating image of 425 lines/inch and an out-of-plane contouring sensitivity of .0028". This experimental arrangement was constructed on top of a vibration isolation table.

The undeformed projected grating image was photographed through an *f*/11 recording camera aperture onto an AGFA 10E75 holographic plate. The rear surface of the plate was displaced by .032" and the deformed projected grating image was superimposed onto the undeformed by the double exposure technique. Exposure times of 6 minutes per photograph were necessary to adequately image the projected gratings. Fourier filtering of this holographic plate in the optical processing arrangement of Figure 5.4 yielded the fringe pattern shown in Figure 5.5. The contour interval times the number of observed fringes yielded an experimental out-of-plane deflection of .0308" for an experimental error of about 4 %.

5.2.4 EXPERIMENTAL TESTING

Increased out-of-plane contouring sensitivities were attempted for the pin-loaded coupon specimen by increasing both the frequency of the projected grating and its projection angle. Larger projection angles tended to increase projected grating exposure times while increases in projected grating frequencies resulted in poorer fringe quality. POLAROID type 55 film was employed to reduce exposure times along with larger recording camera apertures. Larger recording camera apertures hampered photographing the projected grating by decreasing the image depth of field. Smaller recording camera aperatures to increase image depth of field enlarged image speckle size. As can be seen in Figure 5.6, image speckle size must be kept lower than grating pitch for adequate grating imaging. For these reasons, experimentally obtainable out-of-plane contouring sensitivities were bounded by the trade off conditions that existed between projection grating frequency, recording camera *f*/stop and exposure times, fringe quality, and grating image depth-of-field.

An experimental projection arrangement that obtained modest sensitivity with excellent fringe quality, relatively short exposure times, and good depth-of-field considerations was arrived upon after balancing all experimental concerns. A 500 line/inch glass master grating was projected with a magnification of .966 and projection angle of 75° after +1 and -1 diffraction order Fourier filtering. A normal recording camera angle and magnification of 1.3125 formed an image grating of 204 lines/inch and equivalent contouring sensitivity of .001". Exposure times of 1.5 seconds were obtainable on POLAROID 55 film with a recording camera aperture opening of *f*/8.

The hydraulically actuated pin-loading arrangement used in the authors earlier work of reference [68] and shown in Figure 5.7 was positioned in the projection moire arrangement such that proper coupon illumination prevailed. A substantially larger pin support bracket was used than in the author's earlier work [66] to insure the fixed boundary condition of the pin front. Pin-load level was monitored by a hydraulic pressure transducer. Both $[(0/90)_3,0]_s$ and $[(+45/-45)_3]_s$ coupons were cleaned with acetone. A uniform thin coating of a flat white spray paint was applied with care to avoid

excessive paint buildup within the coupon hole. A white metal target area was juxtaposed next to the coupon in the same focal plane.

For each specimen, a no load projection grating photograph was taken followed by separate progressively loaded deformed projection grating photographs. Specimen loading was continued until coupon failure occurred. Manual superposition of the no load photograph with the loaded photograph in the optical processing arrangement produced an out-of-plane contouring history of each specimen type. During this process, rotational alignment of the photographs was insured by obtaining a null field of the target area since this area was void of deformations.

5.2.5 Experimental Results

Figures 5.8 and 5.9 illustrate the out-of-plane contouring results for the $[(0/90)_3,0]_s$ and $[(+45/-45)_3]_s$ pin-loaded coupons respectively. Results are presented starting at load levels were out-of-plane deformations are present and ending at the load levels just prior to failure. As can be seen, maximum out-of-plane deformation for the $[(0/90)_3,0]_s$ laminate were between .001" and .002" while being between .002" and .003" for the $[(+45/-45)_3]_s$ laminate. For the given specimen thickness, considerable through thickness strain values were present. Initial .001" deformation was observed at 1050 lbs for the $[(0/90)_3,0]_s$ laminate and at 1200 lbs for the $[(+45/-45)_3]_s$ laminate thus indicating three dimensionality at load levels well below coupon failures.

5.3 In-Plane Displacement Contouring

5.3.1 Geometric Moire

In-plane displacement contouring of the $[(0/90)_3,0]_s$ and $[(+45/-45)_3]_s$ pin-loaded coupons was done using the geometric moire technique. This full field technique has been successfully used by many experimentalists attempting to observe the effects of material anisotropy and nonlinear

behavior in composite materials [74].

As in the case of projection moire, in-plane contouring is based upon the interaction of superimposed bar and space specimen grating images. In this instance however; grating images are created by photographing a specimen grating that is adhered to the front surface of the specimen that has undergone deformation. Superposition of this deformed specimen grating image onto a glass master grating of original undeformed specimen grating pitch produces contours of in-plane displacement.

Fringe formation is governed by resulting intensity variations created by the superposition of deformed and undeformed gratings as seen in Figure 5.10 High intensity values occur when the bars of the two gratings align themselves, while low intensity values occur when the bar of one grating aligns itself with the space of the other grating. These low intensity values are located where deformed grating displacements (u), normal to undeformed grating bars, are an integral value (N_x) of undeformed grating pitch (P) [74]. High intensity values are formed at half integral values. This may be stated as;

$$u = N_x P \qquad \text{where } N_x = 0, .5, 1, 1.5, 2 \ldots. \quad (5.5)$$

In a similar fashion, use of orthogonal bar and space specimen gratings will yield intensity variations for displacements normal to those discussed above which may be expressed as;

$$v = N_y P \qquad \text{where } N_y = 0, .5, 1, 1.5, 2 \ldots. \quad (5.6)$$

In-plane strains contouring may be obtained from in-plane displacement fringe fields through differentiation. Scans and cross scans of an in-plane displacement u fringe field will yield curves of fringe order, N_x, versus specimen location, x or y, as seen in Figure 5.11. Similarly, scans and cross scans of an in-plane v fringe field will yield curves of fringe order, N_y, versus specimen location, x or y. Numerical differentiation of these curves will yield normal and shear strain components. These may be expressed as;

$$\varepsilon_x = \partial u/\partial x = P\ \partial N_x/\partial x \tag{5.7}$$

$$\varepsilon_y = \partial v/\partial y = P\ \partial N_y/\partial y \tag{5.8}$$

$$\gamma_{xy} = [(\partial u/\partial y) + (\partial v/\partial x)] = [(P\partial N_x/\partial y) + (P\partial N_y/\partial x)] \tag{5.9}$$

In some instances, the plots of fringe order vs specimen location may not be defined sufficiently due to localized regions of low fringe density. Erroneous strain values may result in the differentiation of these curves. Linear mismatch methods may be used to overcome this problem [74]. Increases in fringe density may be created by employing an initial pitch differential between master and specimen gratings. A resulting uniformly spaced fringe field representing an initial artificial strain increases fringe density. The magnitude of this fictitious strain (ε_a) is related to original grating pitch (P_1) and fringe field spacing (δa) by;

$$\varepsilon_a = P_1/\delta_a \tag{5.10}$$

When this artificial strain value is superimposed with subsequent strains due to loading, more clearly define fringe order versus specimen location plots are generated. Subtraction of the initial artificial strain value from resulting strains will yield specimen strains due to deformation only. Both compressive or tensile mismatch strain fields may be used.

5.3.2 Experimental Testing

A contact printed image of an orthogonal 500 line/inch chrome master grating on KODAK transparent stripping film was adhered to the front surface of the $[(+45/-45)_3]_s$ with a thin uniform layer of ECOBOND #45 clear adhesive and # 15 clear catalysts. The coupon was initially cleaned in acetone and covered with an even coating of flat white spray paint. Grating alignment was obtained by trimming one edge of the grating parallel with its bars and the use of a curing fixture. This curing fixture aligned both the trimmed grating and coupon edges while immobilizing them during the adhesive cure cycle. The thin flat uniform layer of adhesive was obtained by covering the grating with

a weighting rigid surface. The backing of the stripping was carefully removed from the specimen after curing of the adhesive. The photographic emulsion containing the orthogonal array of grating bar and spaces remained intact on the specimen surface. Its magnified image may be seen in Figure 5.12. Excess grating emulsion and adhesive were carefully trimmed along the coupon sides and hole with an X-ACTO knife.

The loading frame and pressure transducer were mounted on an 8" machinist's rotary stage affixed to the vibration isolation table. Specimen illumination was accomplished by concentrating a high intensity quartz-iodine lamp using a 10" single element lens. The specimen grating was photographed with a 4" x 5" back SINAR-P copy camera. Proper camera alignment (ie normal viewing) and 1:1 specimen magnification was obtained by placing an orthogonal 500 line/inch glass grating in the film plane of the camera. Adjustments to the camera and/or loading frame were made until a null field (no fringes) was observed in the back of the camera signifying its alignment. Pin shadow elimination and enhanced specimen grating imaging were obtained by rotating the loading frame -45° with the rotary table.

A series of trial exposures were made with KODAK ortho type III film using an $f/16$ camera aperture to provide adequate depth of field. Exposures were controlled by switching of the quartz-iodine lamp with a timer mechanism to avoid shutter induced camera vibrations that were found earlier to blur the specimen grating image. All shiny metallic loading frame and fixture surfaces were covered to avoid back reflections of the illumination source that were found earlier to produce specimen grating intensity variations. Correct exposure and fine focusing of the photographs was obtained by their microscopic inspection.

The $[(+45/-45)_3]_s$ coupon was pin-loaded and photographed for increasing pin-load levels. A specimen loading history was obtained from monitoring the transducer output. Deformed grating photographs were developed in accordance to film specifications.

5.3.3 Optical Processing of Experimental Results

Optical processing of the deformed grating photographs for in-plane displacement contouring was done with a Fourier optics system shown in Figure 5.13. The system effectively allowed for the projection of a photographed specimen grating onto the image of a glass master moire grating to produce fringes of constant displacement. Fourier filtering of the deformed specimen grating photograph was done for separation of orthogonal displacement components, fringe multiplication for increased contouring sensitivity, and fringe sharpening.

The light of a 15 mW Helium-Neon laser was expanded by a 40x microscope objective and filtered through a 10 μm pinhole. This expanded beam was passed through the no load specimen grating photograph and focused in the Fourier filtering plane by a transform lens. Passage of the (+1,0) and (-1,0) Fourier frequency components into a field lens and onto a 500 line/inch glass master moire grating in the image plane with a two fold magnification created a v displacement field with a contouring sensitivity of .001". Rotary and orthogonal adjustments of the specimen grating as well as magnification adjustments through field lens translation were made to properly align and magnify the projected specimen grating image with respect to the glass master grating. This effect was noted by creation of a null fringe field on the glass master grating. Translation of the field lens created the initial pitch differential between the specimen grating image and the glass master grating for a .010 inch/inch tensile mismatch v displacement field. Use of this tensile mismatch field produced increased fringe density in the net section of the coupon for more accurate ε_y strain determinations. No load specimen grating photographs were then replaced with deformed grating photographs to produce the in-plane v displacement contouring of the $[(+45/-45)_3]_s$ specimen for the various pin-load levels. This procedure was repeated with an initial -.010 compressive mismatch field to increase fringe density in the bearing section of the coupon for more accurate ε_y strain determinations. All fringe fields were photographed with a 4" x 5" back camera and POLAROID type 55 film.

5.3.4 EXPERIMENTAL RESULTS

The in-plane contour v displacement fields of the $[(+45/-45)_3]_s$ coupon for both the +.010 inch/inch and -.010 inch/inch mismatch fields are shown in Figures 5.14 through 5.18. The 300 lb pin-load level fringe field was unable to be processed due to a poor deformed specimen grating exposure. The in-plane u and v displacement fields of the $[(0/90)_3,0]_s$ coupon from the authors earlier work [66] may be seen in Figures 5.19 through 5.24.

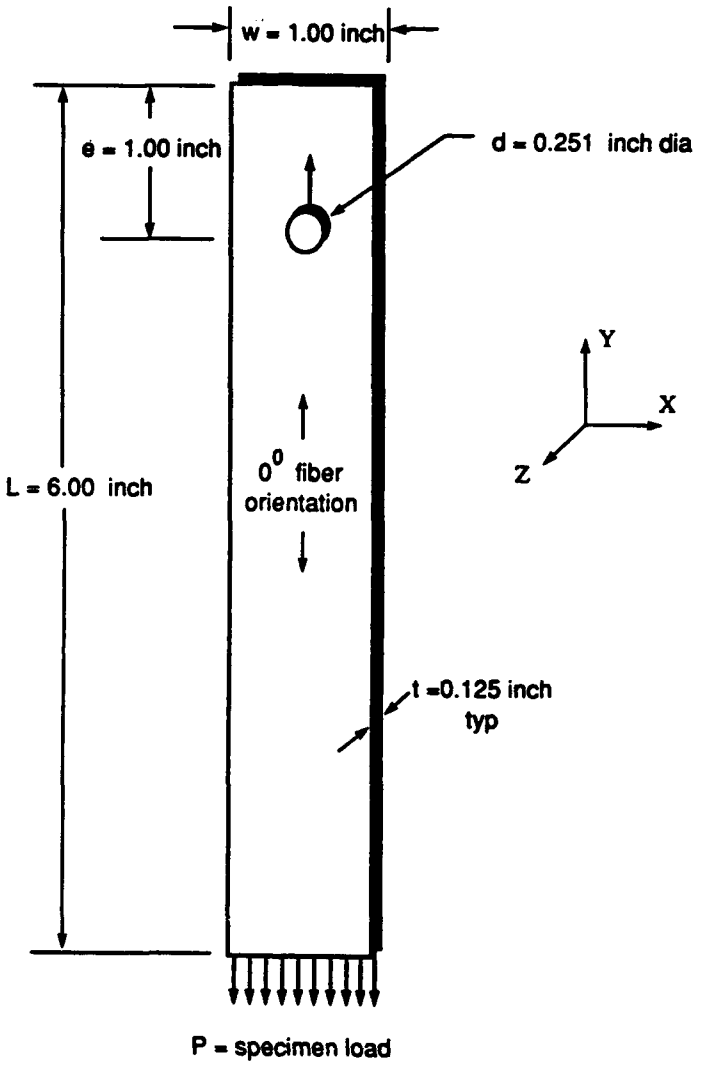

Figure 5.1 Pin-Loaded Coupon Specimen Configuration

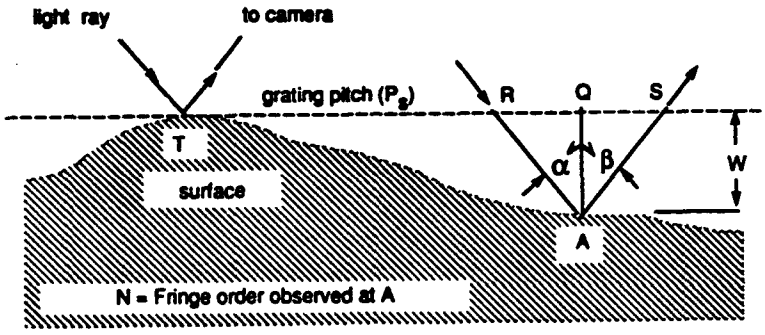

$$W = N P_{eff} = \frac{N P_s}{[\tan(\alpha) + \tan(\beta)]}$$

Figure 5.2 Projection Moire Fringe Formation Fundamentals [ref. 73]

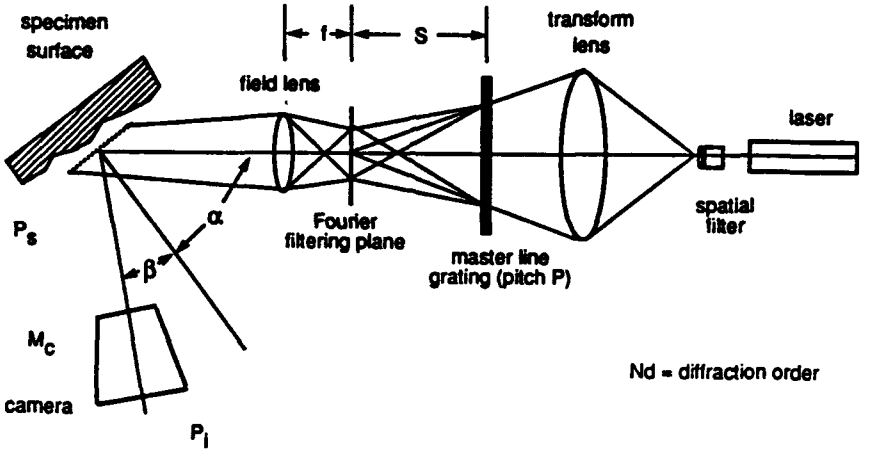

$$P_s = \frac{fP}{[S(N_d + 1)\cos(\alpha)]}$$

$$P_i = \frac{fPM_c}{[S(N_d + 1)\sin(\alpha)]} \qquad \{\text{for } \beta = 0.0\}$$

Figure 5.3 Projection Moire Optical Arrangement [ref. 73]

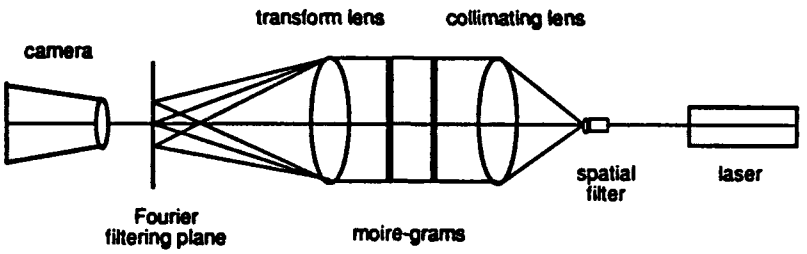

Figure 5.4 Optical Processing Arrangement [ref. 73]

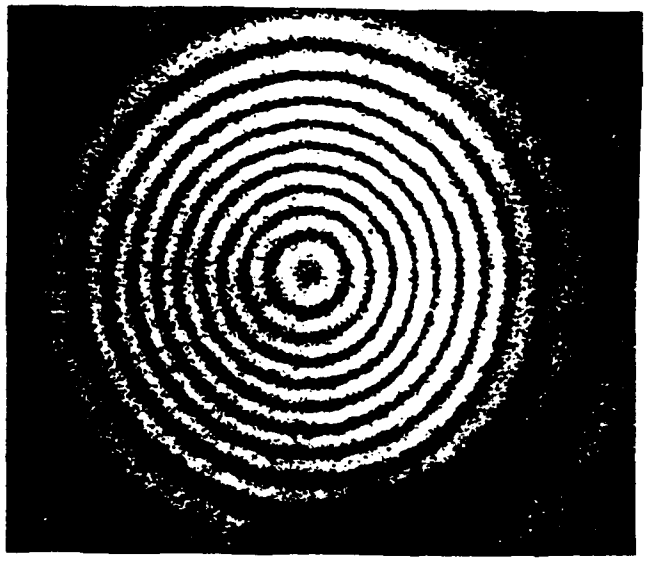

Figure 5.5 Out-of-Plane Displacement Contours of Centrally Loaded Clamped Circular Circular Plate [ref. 73]

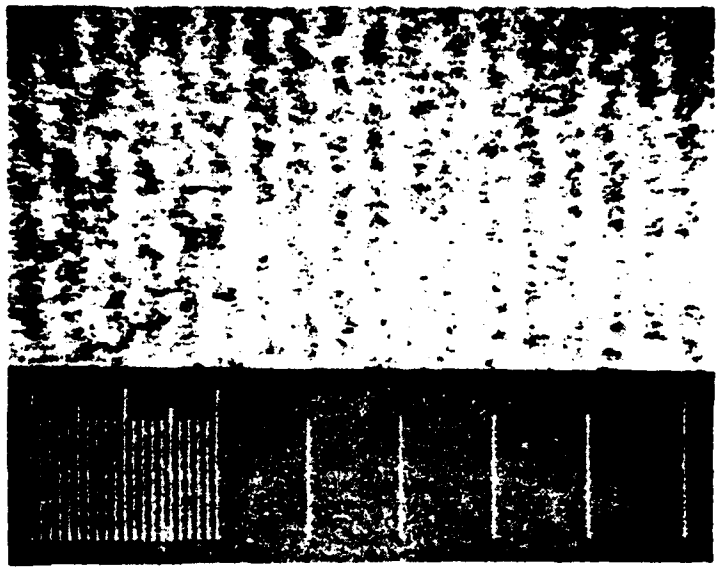

Figure 5.6 Magnified Typical Projection Moire Grating

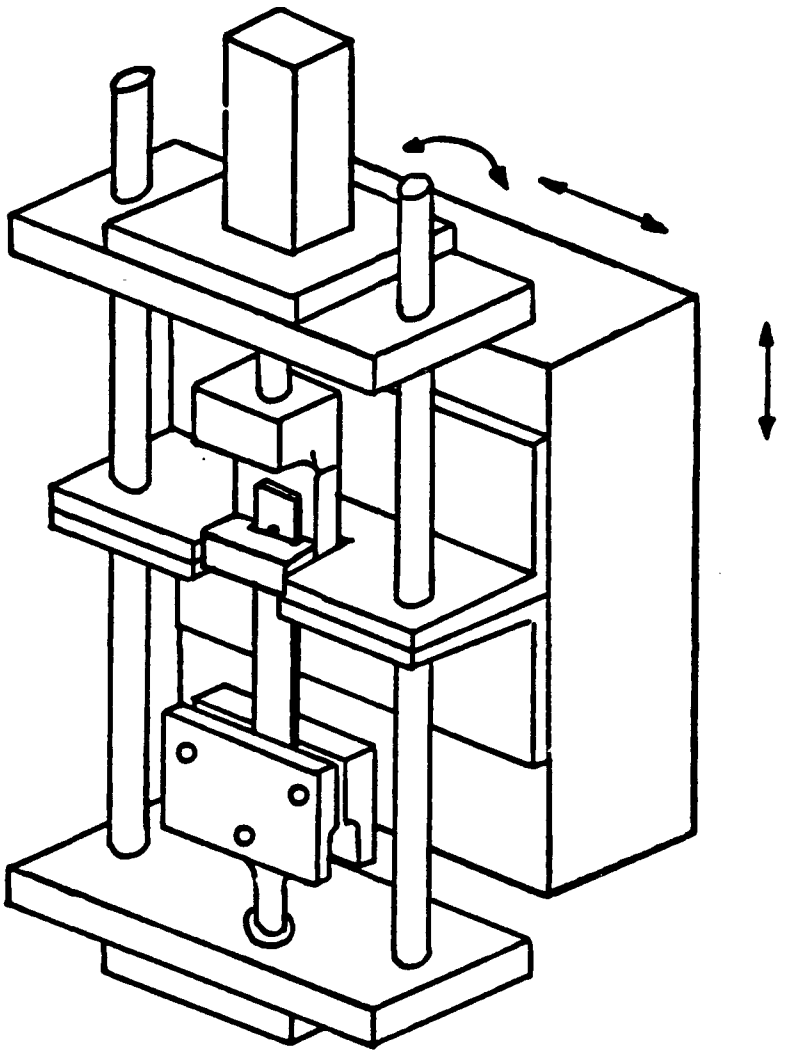

Figure 5.7 Hydraulically Actuated Loading Frame

4673 N (1050 lbs)

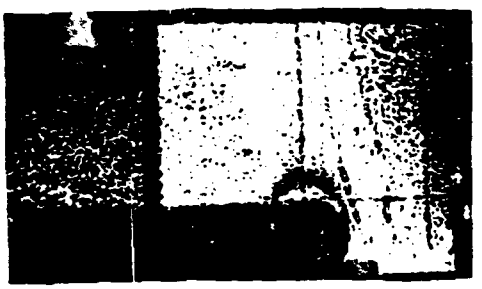

5341 N (1200 lbs)

CONTOUR INTERVAL
.0254 mm (.001 in)

6009 N (1350 lbs)

6676 N (1500 lbs)

Figure 5.8 $[(0/90)_3,0]_s$ Out-of-Plane Experimental Displacement Contours

4451 N (1000 lbs)

5341 N (1200 lbs)

CONTOUR INTERVAL
.0254 mm (.001 in)

6231 N (1400 lbs)

7121 N (1600 lbs)

Figure 5.9 $[(+45/-45)_3]_s$ Out-of-Plane Experimental Displacement Contours

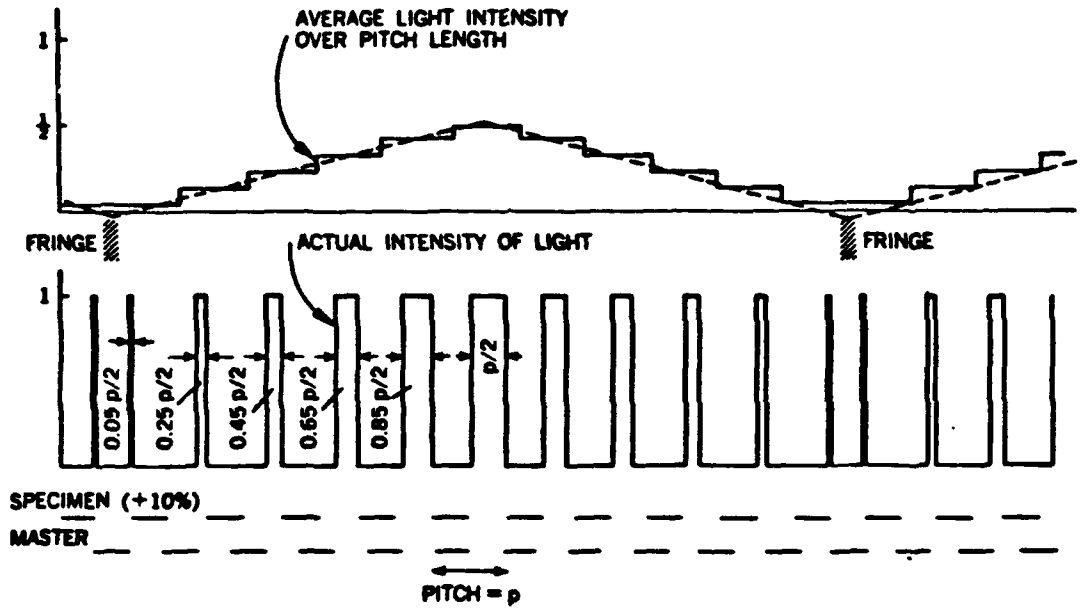

Figure 5.10 Intensity Variations Due to Moire Grating Deformation [ref. 74]

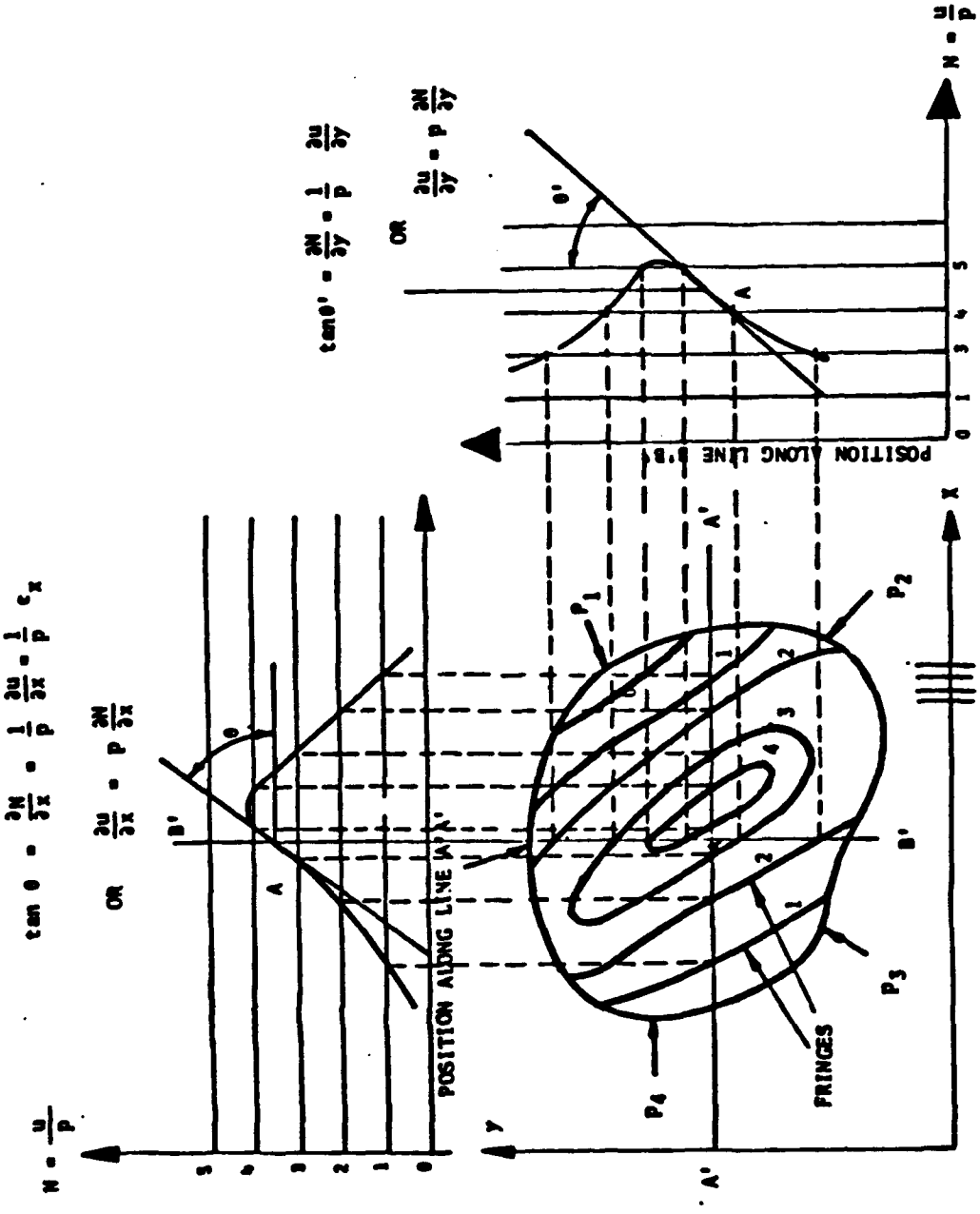

Figure 5.11 In-Plane Strain Contouring [ref. 74]

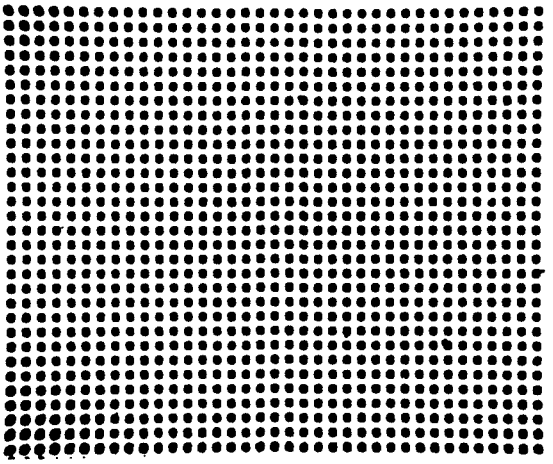

Figure 5.12 Magnified Specimen Grating

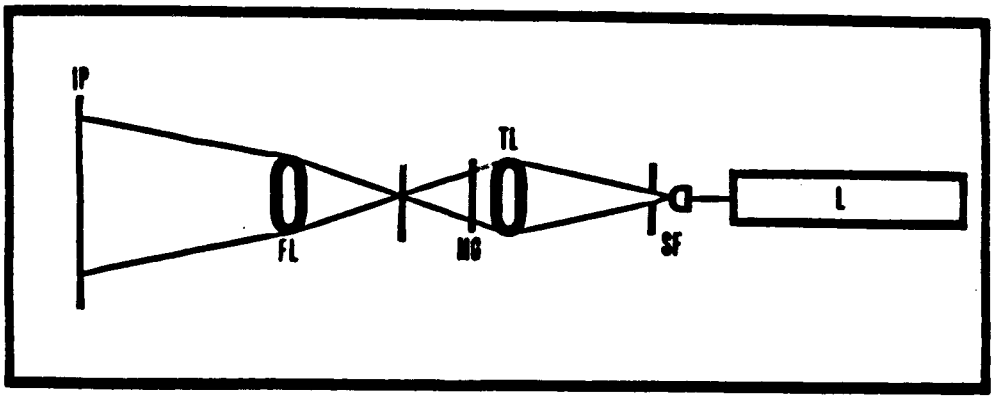

IP	image plane	TL	transform lens
FL	field lens	SP	spectrum plane
L	laser	SF	spatial filter
MG	moire grating		

Figure 5.13 Fourier Filtering Optical Arrangement

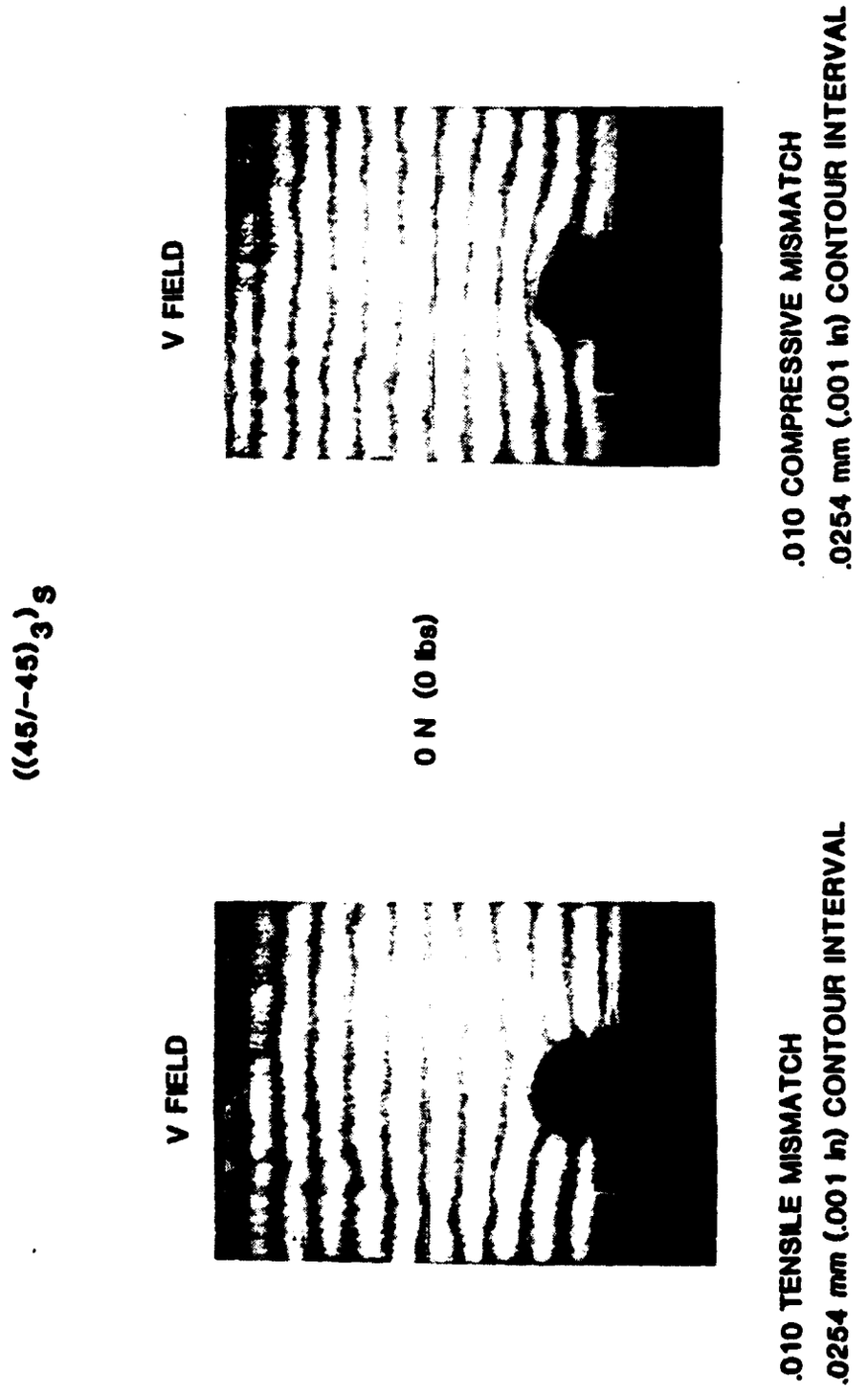

Figure 5.14 [(+45/-45)3]s Experimental In-Plane v Displacement Contours [0 lbs] [±.010 in/in mismatch]

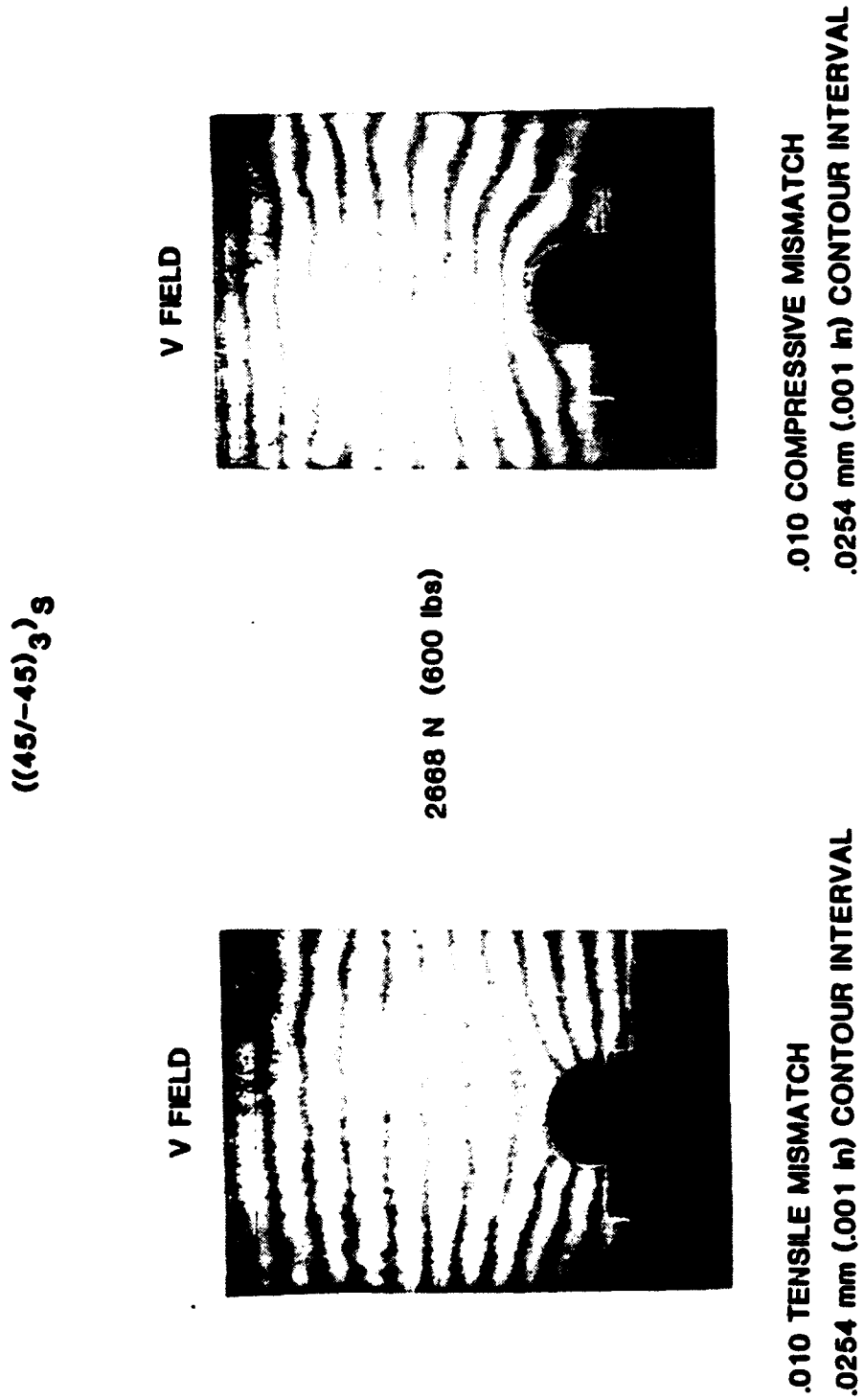

Figure 5.15 [(+45/-45)3]s Experimental In-Plane v Displacement Contours [600 lbs] [±.010 in/in mismatch]

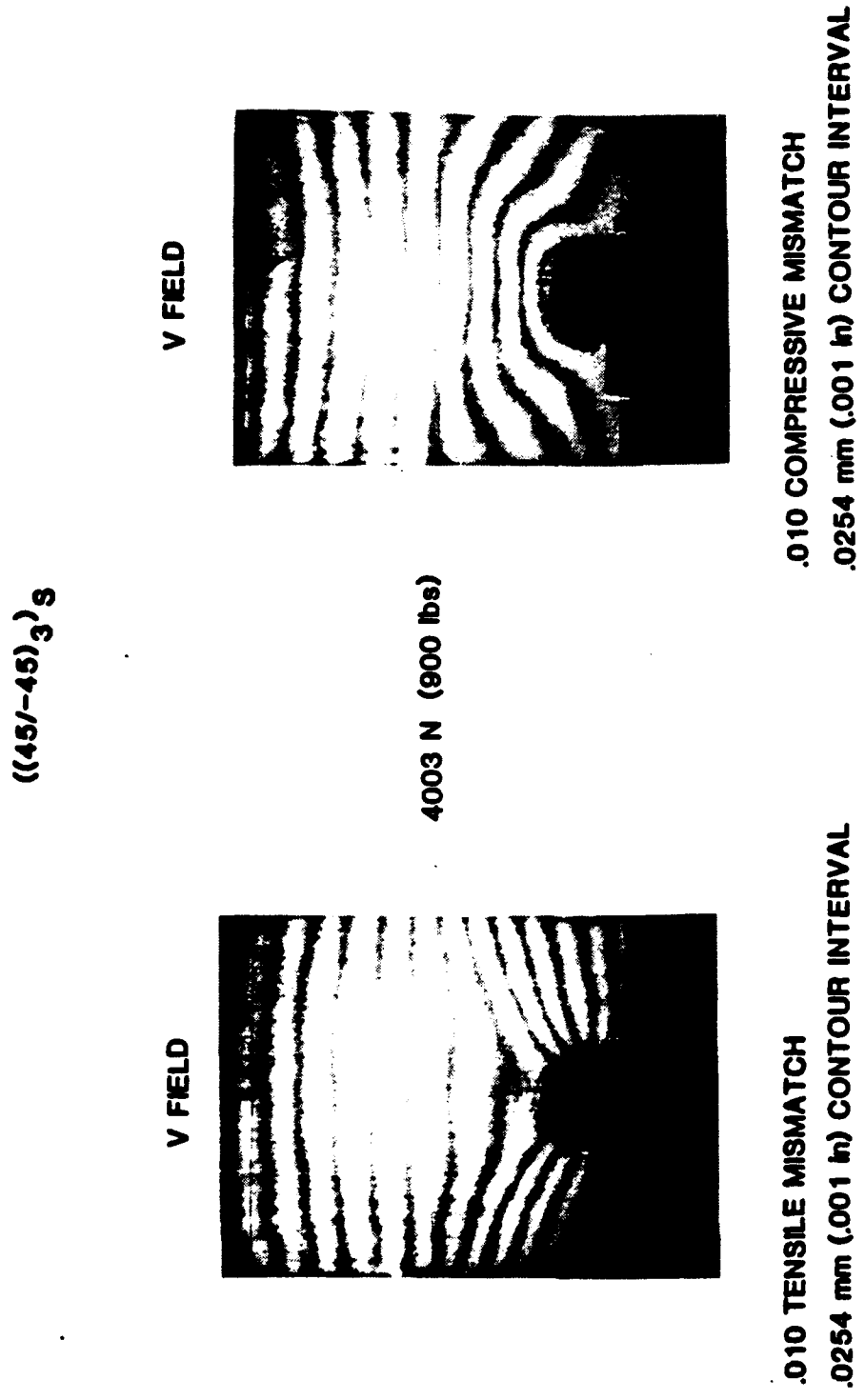

Figure 5.16 [(+45/-45)3]s Experimental In-Plane v Displacement Contours [900 lbs] [±.010 in/in mismatch]

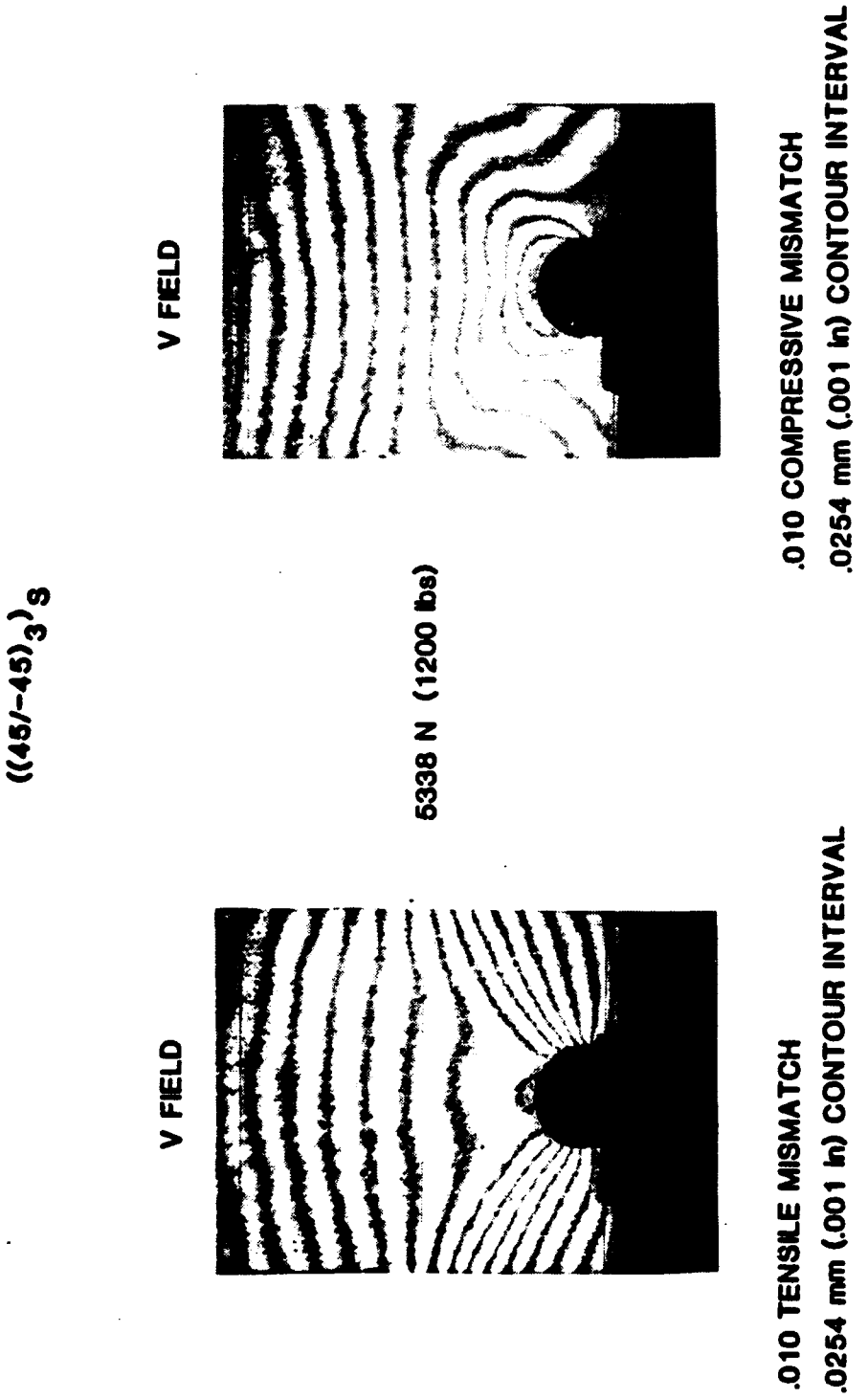

Figure 5.17 [(+45/-45)3]s Experimental In-Plane v Displacement Contours [1200 lbs] [±.010 in/in mismatch]

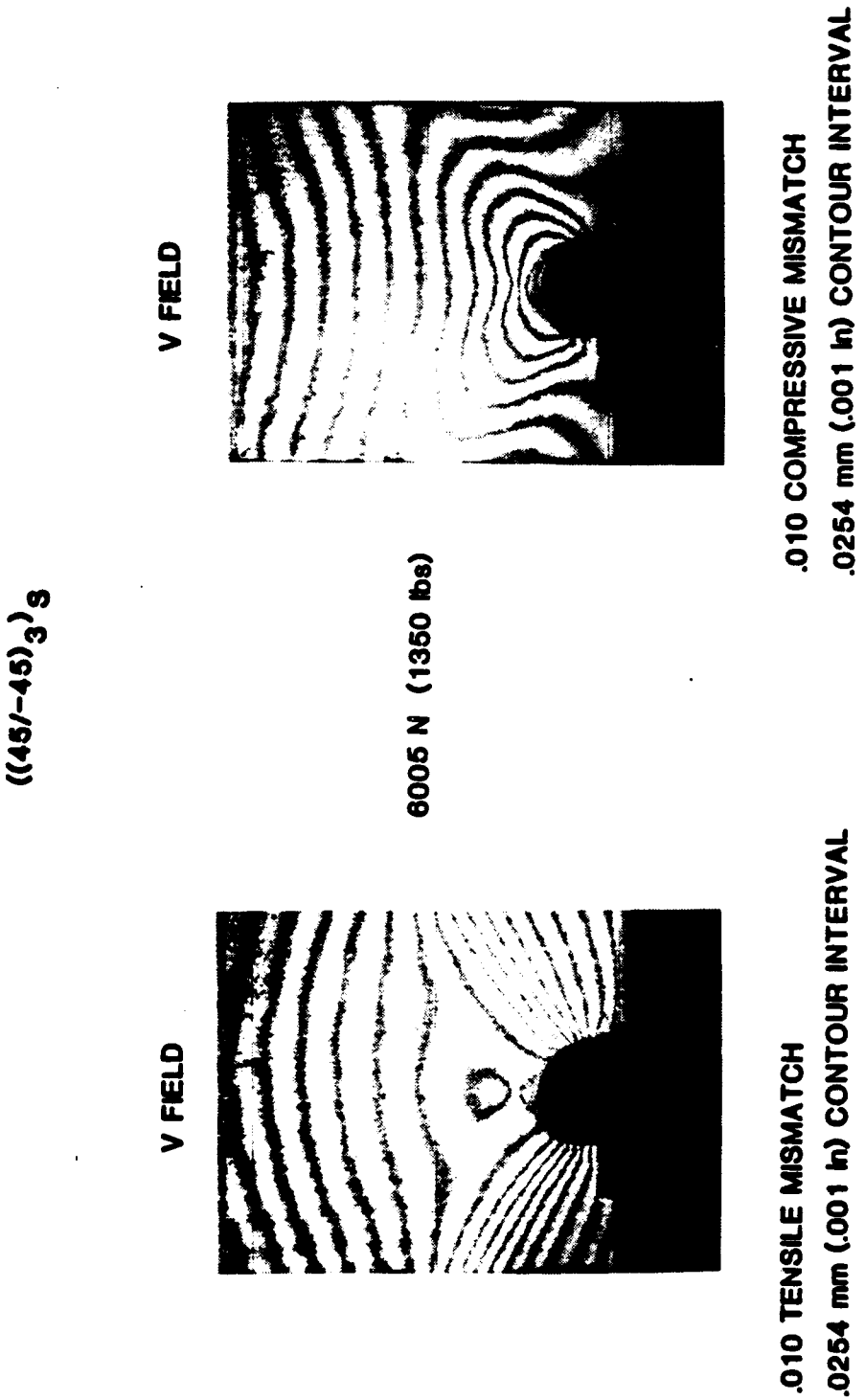

Figure 5.18 [(+45/-45)3]s Experimental In-Plane v Displacement Contours [1350 lbs] [±.010 in/in mismatch]

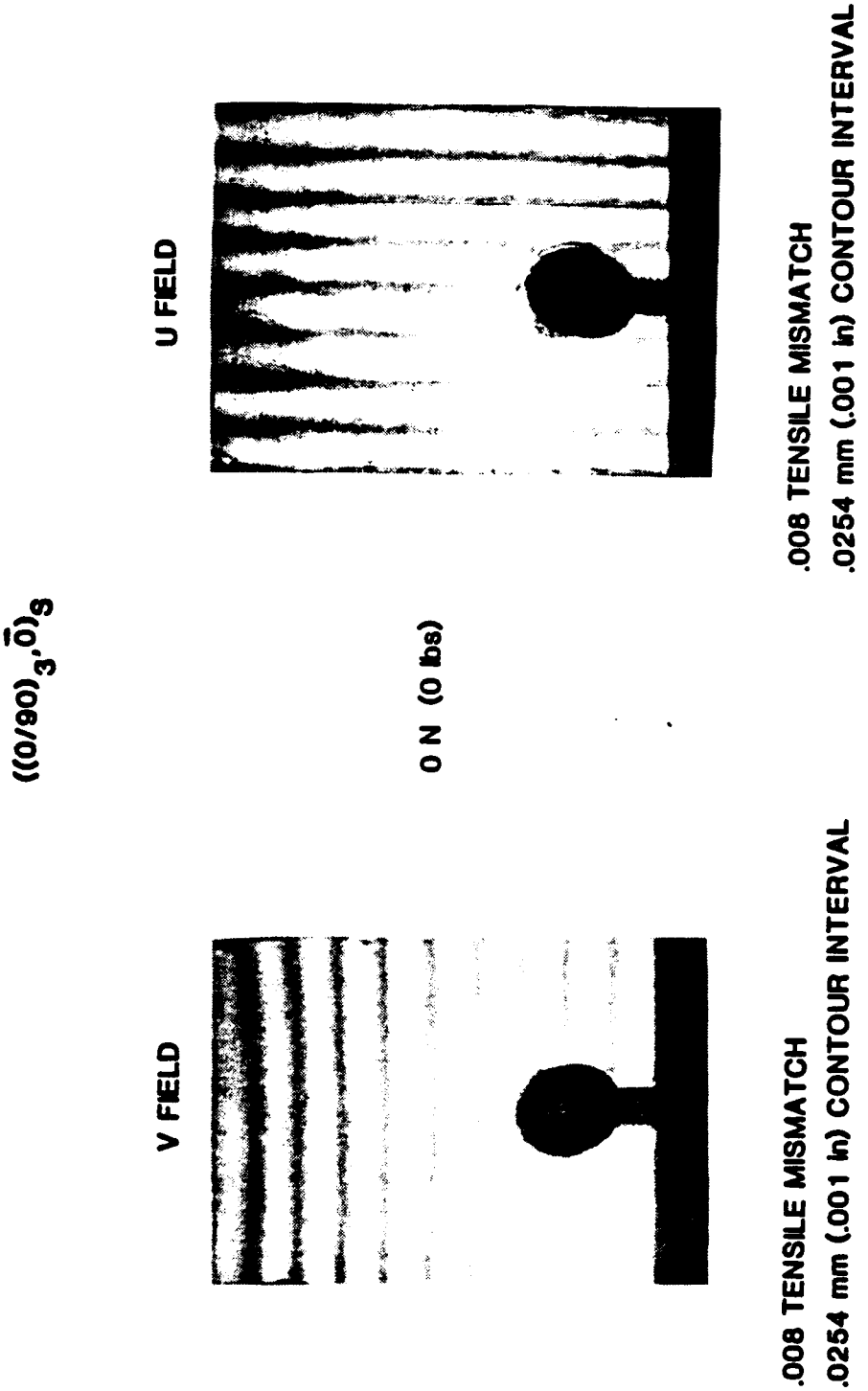

Figure 5.19 $[(0/90)_3,0]_s$ Experimental In-Plane u and v Displacement Contours [0 lbs] [+.008 in/in mismatch] [ref. 66]

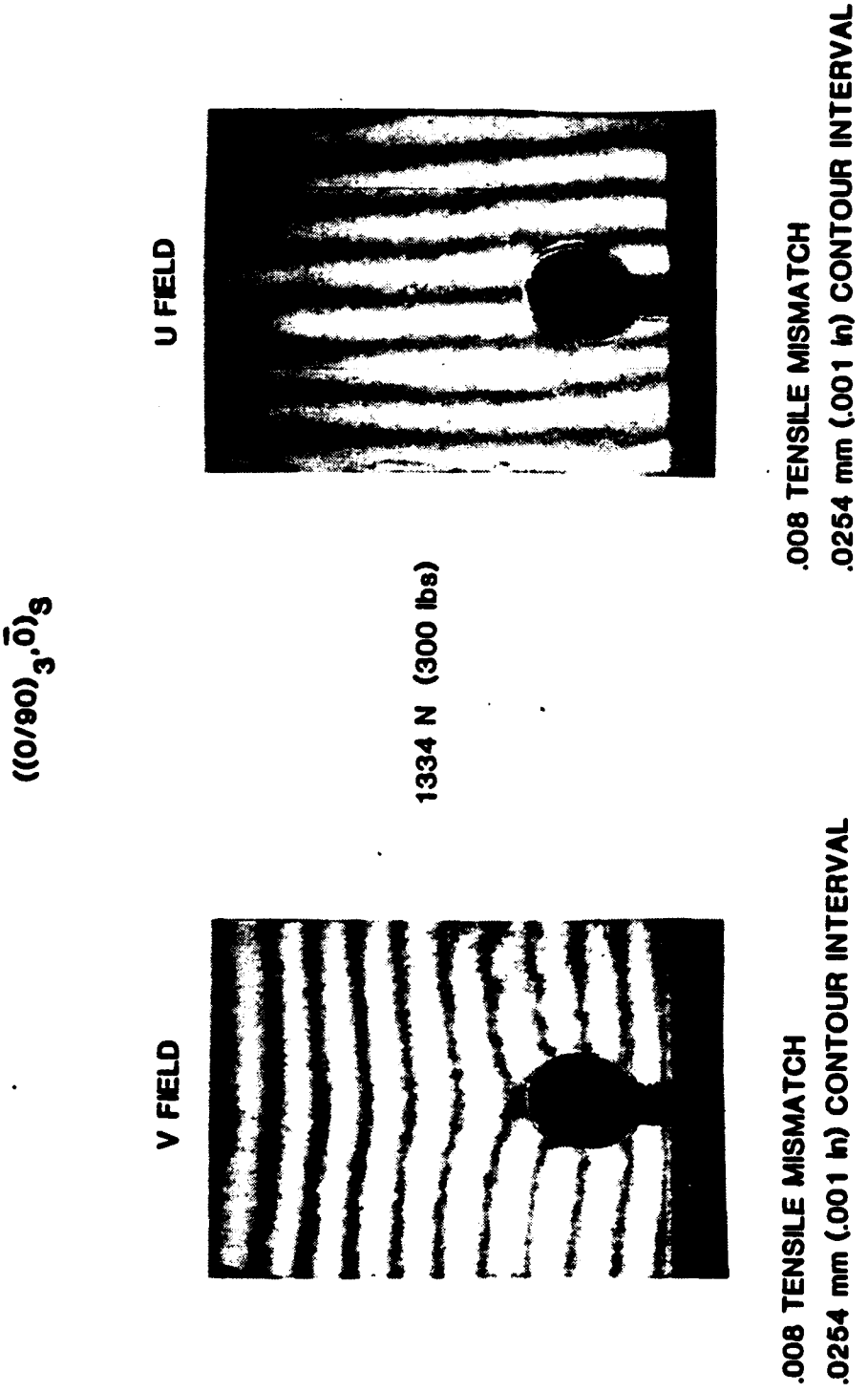

Figure 5.20 [(0/90)3,0]s Experimental In-Plane u and v Displacement Contours [300 lbs] [+.008 in/in mismatch] [ref. 66]

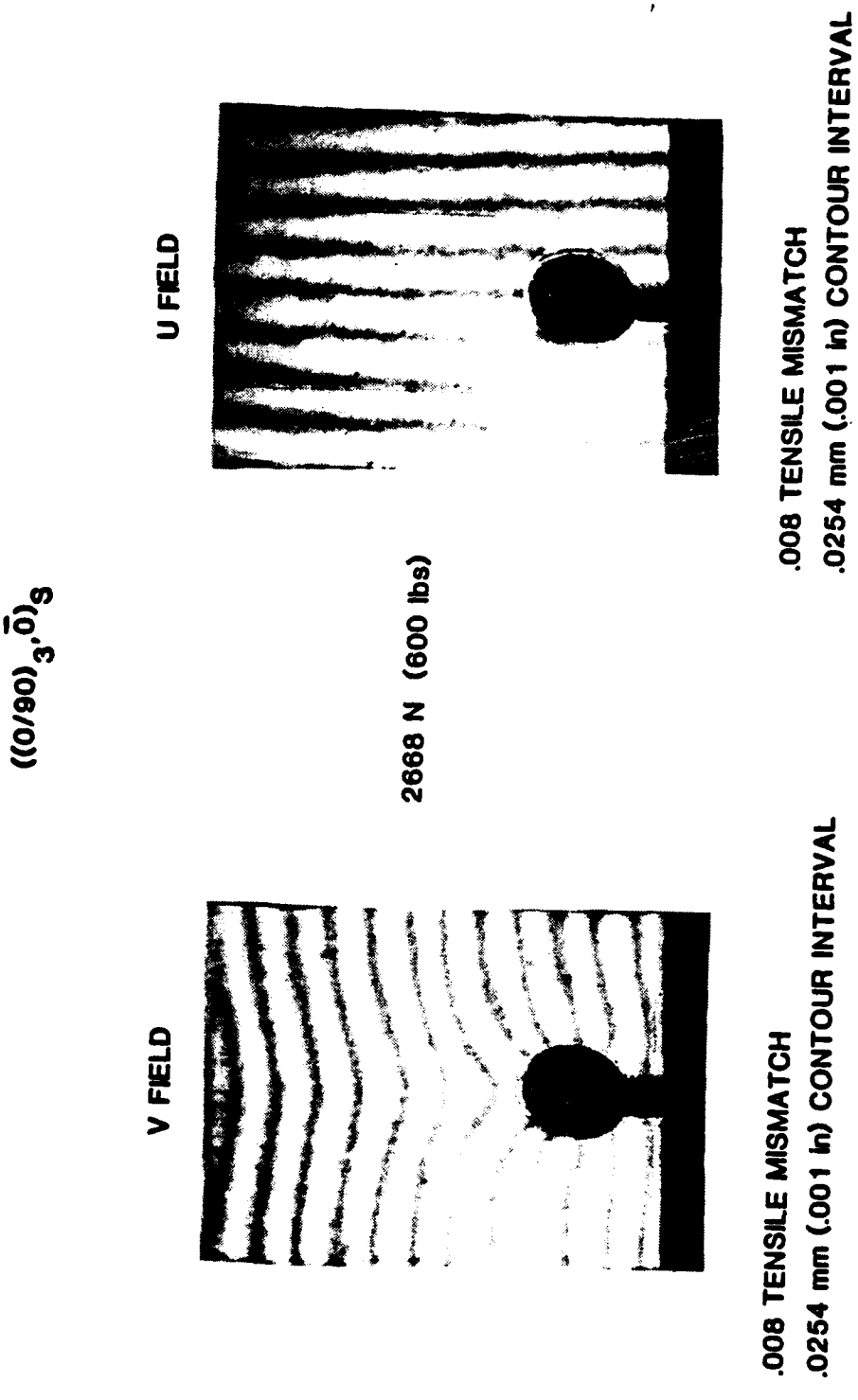

Figure 5.21 [(0/90)3,0]s Experimental In-Plane u and v Displacement Contours [600 lbs] [+.008 in/in mismatch] [ref. 66]

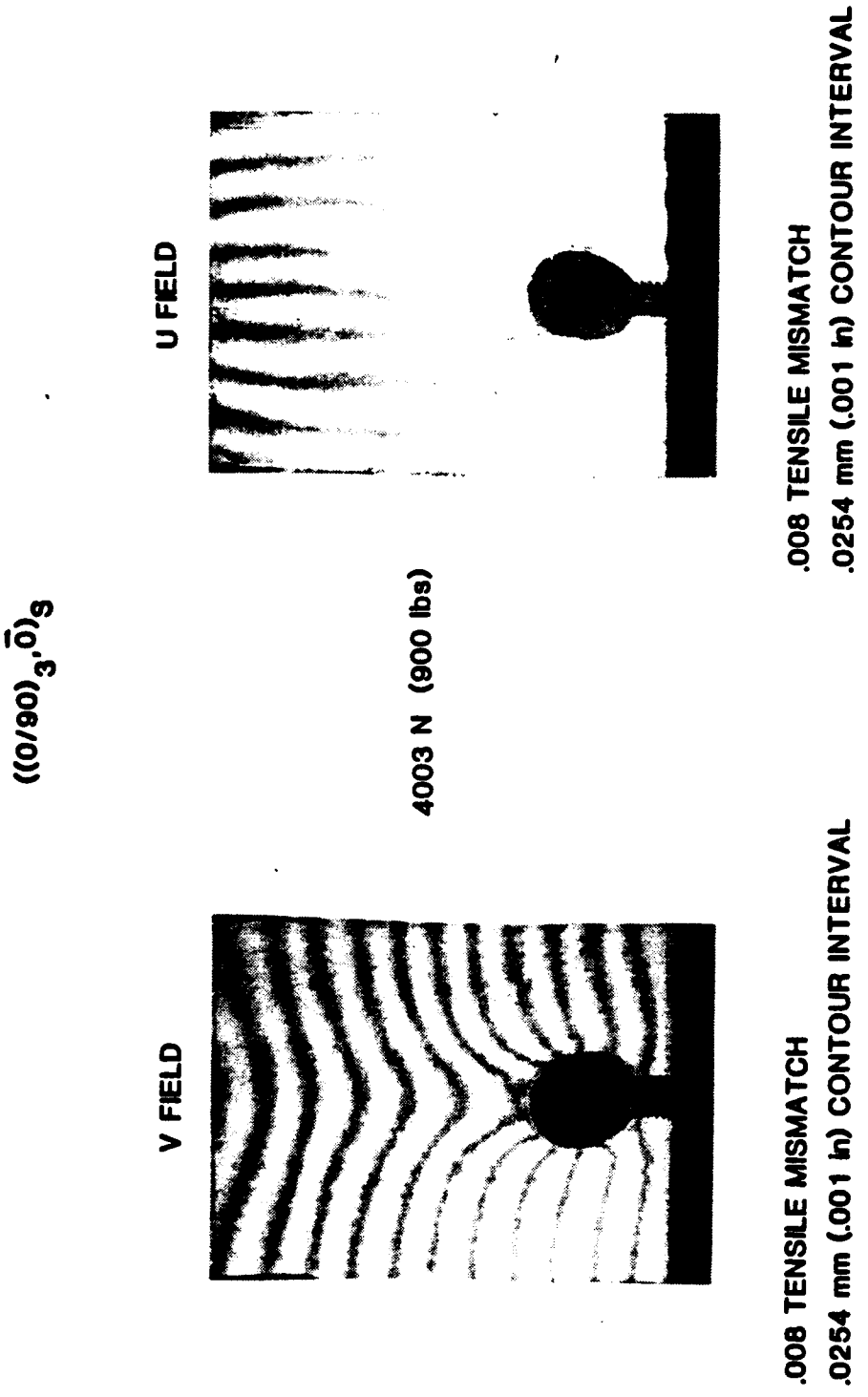

Figure 5.22 $[(0/90)_3,0]_s$ Experimental In-Plane u and v Displacement Contours [900 lbs] [+.008 in/in mismatch] [ref. 66]

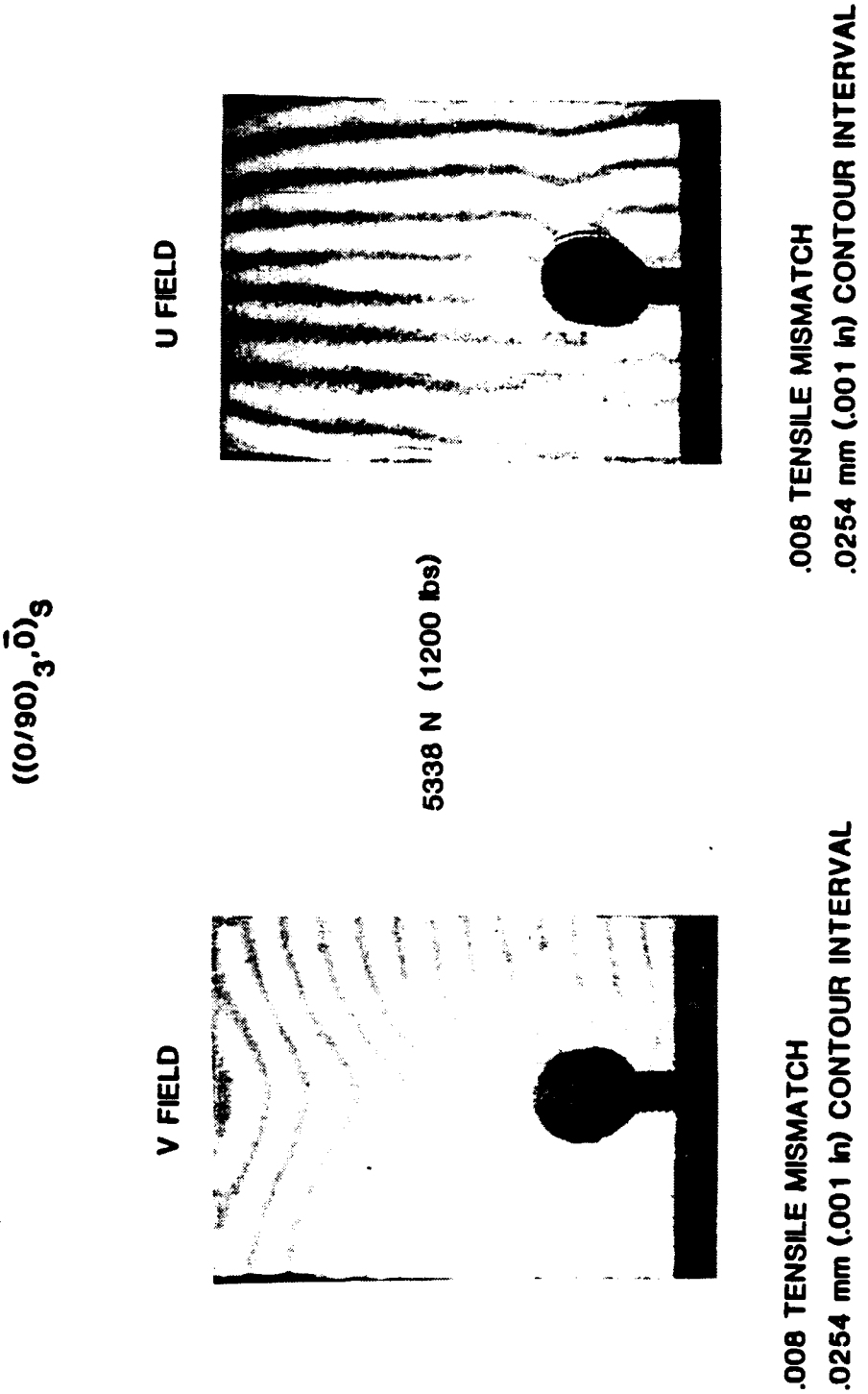

Figure 5.23 $[(0/90)_3,0]_s$ Experimental In-Plane u and v Displacement Contours [1200 lbs] [+.008 in/in mismatch] [ref 66]

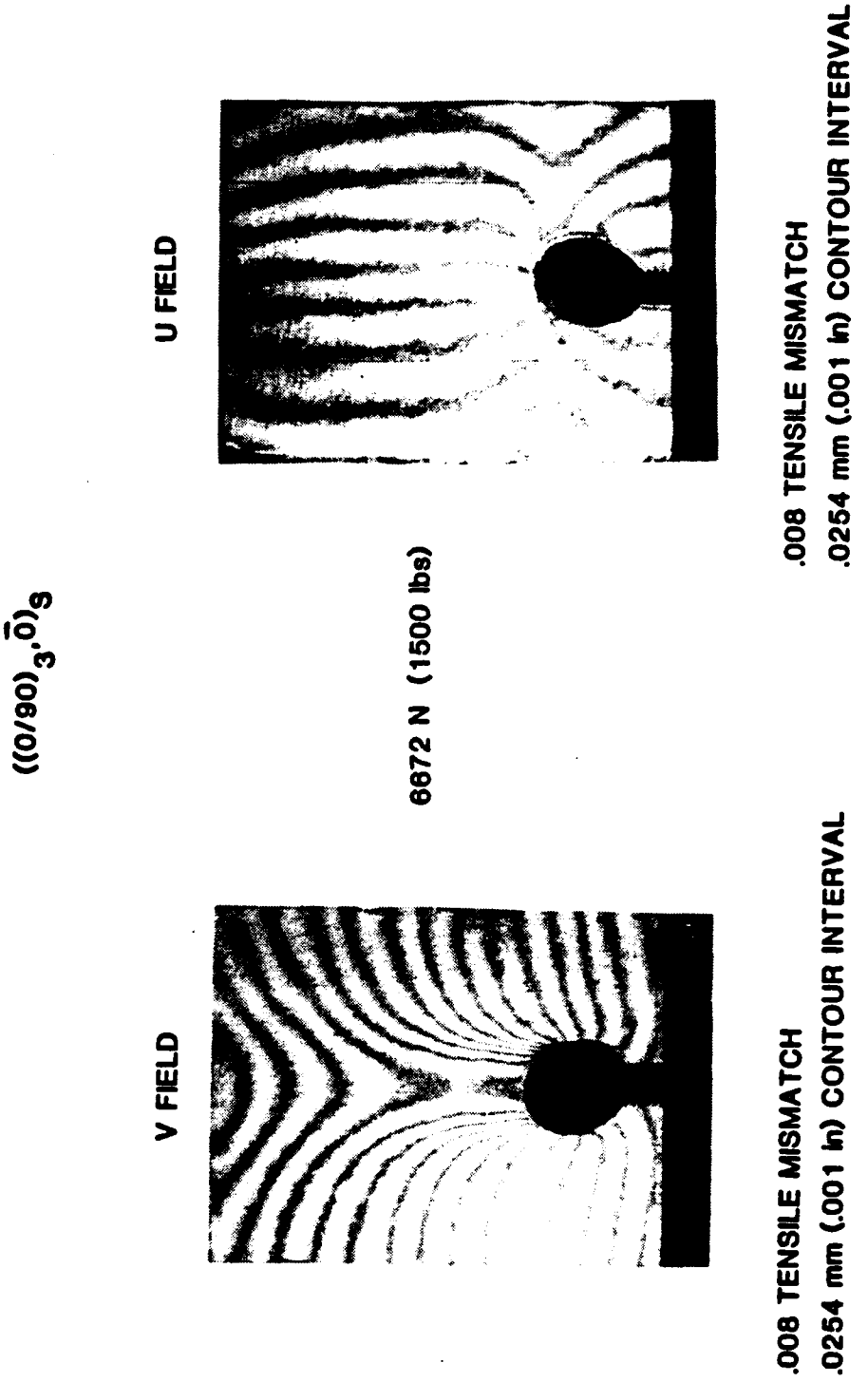

Figure 5.24 $[(0/90)_3,0]_s$ Experimental In-Plane u and v Displacement Contours [1500 lbs] [+.008 in/in mismatch] [ref. 66]

CHAPTER 6. LAMINA/LAMINATE MECHANICAL PROPERTY EVALUATION

Three dimensional constitutive equations were developed for each laminate configuration from a lamina/laminate mechanical property data base. Intralaminar shear response was characterized by the ASTM D3518-76 specification and used with previously determined [66] in-plane lamina properties (E_1, E_2, ν_{12}, and ν_{21}) to form the lamina mechanical property data base. Through thickness laminate Poisson ratio and transverse shear moduli properties were determined from tension and modified three point bend tests to form the laminate mechanical property data base. This section will first review the authors' earlier in-plane lamina property tests and results. A discussion of the intralaminar shear, transverse shear, and through thickness Poisson ratio tests and results will then be discussed.

6.1 In-Plane Lamina Mechanical Property Data Base

Both in-plane lamina moduli and Poisson ratio values of the SP250-S2 Glass fiber/resin system were successfully previously characterized by the author [66]. AMMRC SL-3 streamlined tension specimens, shown in Figure 6.1, were manufactured from eight ply SP250-S2 Glass unidirectional laminated plates. A total of six $(0)_8$ and six $(90)_8$ specimens were shaped on a pantograph by carbide router bits and instrumented with back to back BLH FAET-06A-35-S13E strain gages. These gages were wired in series and connected to the single active arm of a Wheatstone bridge to alleviate specimen bending effects. The specimens were tested in a 20K INSTRON testing machine. Longitudinal and transverse specimen strains and loads were monitored using conventional XY recorders.

The load-strain curves of the SL-3 tension specimens were digitized. Average as well as plus and minus standard deviation stress-strain curves were

found for both the longitudinal and transverse directions. The in-plane Poisson ratio values for both the longitudinal and transverse directions tension tests were also calculated. Average and plus and minus standard deviation Poisson ratio curves were also determined. Figure 6.2 illustrates the average moduli curves while Figure 6.3 illustrates the average Poisson ratio curves. Table 6.1 lists the average lamina moduli and Poisson ratios.

Table 6.1 Average Lamina Moduli and Poisson Ratios

STACKING SEQ	E_1 (psi)	E_2 (psi)	ν_{12}	ν_{21}
$[(0)]_8$	6.654E+6	1.858E+6	0.2972	0.0883

6.2 Intralaminar Shear Testing

6.2.1 ASTM D3518-76 Test Arrangement

The ASTM D3518-76 test consists of a uniaxial tension test of a $[(+45/-45)_n]_s$ specimen. Rosen[1], upon simplification of Petit's[2] approach, expressed the shear stress of a unidirectional lamina, $\mathcal{T}_{12}$, in terms of the uniaxial stress state, σ_{11}, of a $[(+45/-45)_n]_s$ laminate as;

$$\mathcal{T}_{12} = \sigma_{11}/2 \tag{6.1}$$

He further described the shear strain of the unidirectional lamina, γ_{12}, in terms of the $[(+45/-45)]_s$ longitudinal and transverse normal strains, ε_L and ε_T, as:

$$\gamma_{12} = (\varepsilon_L - \varepsilon_T) \tag{6.2}$$

The intralaminar unidirectional shear modulus, G_{12}, is defined from these quantities as;

$$G_{12} = \partial\sigma_{12}/\partial\gamma_{12} \tag{6.3}$$

The intralaminar shear modulus of the $[(0/90)_n]_s$ laminate configuration, G_{xy}, can be shown to be equal to this unidirectional shear modulus, G_{12}, within the bounds of Classical Lamination Theory [80].

A recent comparison of intralaminar shear tests by Lee and Munro[3] have shown the ASTM D3518-76 test to be quite attractive in comparison to other shear test methods. The basis for their decision lay in various criteria that include accuracy of strength and stiffness predictions and ease of specimen preparation and test procedure.

6.2.2 Specimen Description and Preparation

The geometry of the intralaminar test specimen was taken from ASTM specification D3518-76. Illustrated in Figure 6.4, the specimen was manufactured from a $[(+45/-45)_2]_s$ laminated plate that was fabricated from 3M SP-250 S2-Glass prepreg tape. Beveled tabs manufactured from specimen material were adhered to the specimens with American Cyanamid FM-1000 film adhesive. Both sides of the specimen were instrumented with BLH FAET-06A-35-S13E biaxial strain gages. A total of four test specimens were produced.

6.2.3 Test Procedures and Results

All of the D3518-76 test specimens were placed into a 20K Instron testing machine. Front and rear surface strain gages were wired into a two active arm Wheatstone bridge that was used in conjunction with a PACIFICO signal conditioning unit. Both longitudinal and transverse strains as well as load levels were digitally recorded using a KEITHLEY/IBM data acquisition system. Tension test were conducted at a rate of .02 in/min while data acquisition was done at a 4 sample/second rate.

The resulting digital data files were transferred into the Computational Mechanics local area network. Processing on an APOLLO DN3000 work station resulted in average as well as plus and minus standard deviation

curves of uniaxial longitudinal stress vs. longitudinal strain and uniaxial longitudinal stress vs. transverse strain. An average intralaminar shear stress strain curve was then determined using relations (6.1) and (6.2). This average intralaminar shear stress-strain curve was then approximated with a two part least squares curve fit. Each part was of the form;

$$\tau_{xy} = C_1 + C_2\gamma_{xy} + C_3\gamma_{xy}^2 + \ldots C_n\gamma_{xy}^{n-1} \qquad (6.4)$$

where the order of fit is taken to be equal to (n-1).

Figure 6.5 shows the average and plus and minus standard deviation stress strain curves from the ASTM D3518-76 test specimens. Figure 6.6 illustrates the average resulting intralaminar shear stress strain response and its two part least squares fit. Table 6.2 is a listing of the constants for the least squares curve fits.

Table 6.2 Least Squares Curve Fit Constants For Average ASTM 3518-76 Test Results ($x10^5$)

CURVE SECTION	CONSTANTS			
	C1	C2	C3	C4
PART A	0.0000	7.3511	244.057	3137.38
PART B	0.7312	0.4656	0.96492	

6.3 Transverse Shear Testing

6.3.1 Three Point Bend Test Arrangement

Transverse shear moduli for both laminate orientations were determined from the three point bend test approach as described by Tarnopol'skii and Kincis[4]. In this approach, composite beams of various span to depth ratios (l/T) are three point loaded as shown in Figure 6.7. Load deflection measurements are used with the deflection expression derived from technical beam theory which is given as;

$$W_{max} = W\sigma + W\tau = \left[\left(\frac{Pl^3}{48E_{xb}I}\right) + \left(\frac{\alpha Pl}{4G_{xz}F}\right)\right] \tag{6.5}$$

where

W_{max} = total beam deflection
$W\sigma$ = beam deflection due to bending
$W\tau$ = beam deflection due to shear
P = beam center load
l = beam span length
E_{xb} = beam bending modulus
I = moment of inertia
α = 1.2 (rectangular beam cross sections)
G_{xz} = transverse shear modulus
F = beam cross sectional area

By denoting a fictitious bending modulus, E_{fb}, from deflections due to bending *only* as;

$$E_{fb} = \frac{Pl^3}{48IW_{max}} \tag{6.6}$$

Tarnopol'skii and Kincis developed the following linear relationship between the three moduli;

$$\frac{1}{E_{fb}} = \left[\frac{1}{E_{xb}} + \left(\frac{1.2}{G_{xz}}\right)\left(\frac{T}{l}\right)^2\right] \tag{6.7}$$

where

T = beam thickness

The laminate transverse shear modulus, G_{xz}, is found from the resulting slope $(1.2/G_{xz})$ of a $1/E_{fb}$ verses $(T/l)^2$ plot. Since both laminate configurations are orthotropic, this transverse shear modulus is equal to the remaining transverse shear modulus, G_{yz}.

6.3.2 SPECIMEN DESCRIPTION

Both $[(0/90)_4]_s$ and $[(+45/-45)_4]_s$ 3M SP250-S2 glass specimens of nominal 0.125" thickness were used in the three point bend tests. Specimen span lengths were selected as to provide *appreciable* deflections due to shear for accuracy in experimental determination of the transverse shear moduli [78]. From equation 6.5, it can readily be seen that the ratio of shear deflection to total beam deflection may be expressed as;

$$\frac{\delta_s}{\delta_T} = \left[1 + \left(\frac{1}{\alpha}\right)\left(\frac{G_{xz}}{E_{xb}}\right)\left(\frac{1}{T}\right)^2 \right]^{-1} \tag{6.8}$$

which may graphically seen in Figure 6.8. *A priori* assumption of a moduli ratio of .1 will yield deflection ratios of approximately 43%, 16%, 8%, and 4% for respective beam spans of 0.5", 1.0", 1.5", and 2.0". A specimen width of 0.5" was selected relative to the resulting span to depth ratios in accordance to the b = .59" (0.039" ≤ T ≤ 0.39") recommendation of Tarnopol'skii [78]. A specimen of 5" span were also selected to experimentally determine an E_{xb} value for comparison to the graphically obtained one from equation 6.7.

Specimens of 2.5" and 5.0" length by 0.5" width were manufactured from the 16 ply laminated plates. Their locations within the plate were selected as to minimize specimen thickness and volume fraction variations. Table 6.3 lists exact three point bend test specimen dimensions.

Table 6.3 Three Point Bend Test Specimen Dimensions

SPEC. NO.	STACKING SEQ.	b (in)	l (in)	T (in)	l/T
1	$[(0/90)_4]_s$	0.5015	0.500	0.1090	4.587
2	$[(0/90)_4]_s$	0.4920	1.000	0.1120	8.928
2	$[(0/90)_4]_s$	0.4920	1.500	0.1120	13.393
2	$[(0/90)_4]_s$	0.4920	2.000	0.1120	17.857
3	$[(0/90)_4]_s$	0.4110	5.000	0.1170	42.735
4	$[(+45/-45)_4]_s$	0.4755	0.500	0.1175	4.255
5	$[(+45/-45)_4]_s$	0.4725	1.000	0.1145	8.734
6	$[(+45/-45)_4]_s$	0.4875	1.500	0.1185	12.658
7	$[(+45/-45)_4]_s$	0.4860	2.000	0.1155	17.316
8	$[(+45/-45)_4]_s$	0.4070	5.000	0.1170	42.735

6.3.3 Test Procedures and Results

Three point bend test fixturing consisted on two 1 in^2 aluminum bars with mating transversely drilled 0.25" diameter semicircular holes that were 0.25" spaced. Matching diameter steel pins placed into these holes acted as roller supports for the three point load configuration. Specimen deflections were monitored by a TRANS-TEK model 351-000 LVDT that was perpendicularly mounted into the center of the bottom aluminum bar by threaded connection. A lock washer was employed to eliminate spurious LVDT movement. Span distances and LVDT location were maintained by locating their machining procedures from the same end of the the aluminum bars that were initially ground flat. Alignment of the bar ends during testing insured proper location of specimen loading and center deflection measurements. A 20V power supply was used to power the LVDT while a conventional XY recorder was used to monitor load and specimen deflection.

The three point bend test arrangement was placed into a 20K INSTRON testing machine. Each laminate span length was compression loaded in the fixture a total of four times. Specimens were shifted slightly in between load cycling to allow for fresh roller indentation among trials. Effects from

specimen variation were minimized by using the same specimen for all laminate orientation test groups except for cases where lower span lengths or laminate stacking arrangement were thought to have lead to fiber and resin damage. All $[(0/90)_4]_s$ specimens were loaded to 90 lbs while all $[(+45/-45)_4]_s$ specimens were loaded to 35 lbs.

Measured load deflection ratios (K_m) were found by taking an average of the slopes of the load deflection curves at 75 lbs for the $[(0/90)_4]_s$ laminates and 20 lbs for the $[(+45/-45)_4]_s$ laminates.. Corrected load displacement ratios (K_c) were calculated by subtracting out spurious effects from loading jig compliance and specimen roller indentation (K_{spur}) as per Fischer *et al*[5] by;

$$K_c = \left[\frac{K_m}{1 - (K_m/K_{spur})}\right] \tag{6.9}$$

An average value of K_{spur} was found from averaging multiple load displacement ratios determined by loading a specimen of smallest span (0.5"). For this test case, deflections due to beam bending and shearing were minimized by placing a metal plate above and below the top and bottom roller supports (i.e. an equivelant span length of $l = 0.0$").

Load deflection ratios for the 1.5" and 2.5" $[(+45/-45)_4]_s$ specimens showed a consistent reduction from loading to loading that seemed to indicate specimen damage. For this reason, only the first load deflection ratio was used in the calculations. The measured deflections and span lengths for the 5" span specimens were corrected to account for beam rotations at the roller supports as suggested by Tarnopol'skii and Kincis [78] by the following relationships;

$$\Delta W = \left[\frac{2r}{(l^2/4W) + 1}\right] \tag{6.10}$$

$$\Delta l = \left[\frac{r}{(l/2W) + (W/l)}\right] \tag{6.11}$$

where

r = support roller radius

Figure 6.9 shows load deflection data for both the $[(0/90)_4]_s$ roller indentation/jig calibration and the 1.0" span length tests which is typical of the test data obtained.

Table 6.4 lists the measured results for all test specimens. From these results, graphical representation of equation (6.7) may be seen in Figures 6.10 and Figure 6.11.

Table 6.4 Three Point Bend Test Experimental Results

SPEC. NO	STACKING SEQ.	l (in)	Km (psi)	Kc* (psi)	1/Efb (psi)
1	$[(0/90)_4]_s$	0.500	4.982E+4	6.193E+4	3.356E-7
2	$[(0/90)_4]_s$	1.000	1.443E+4	1.530E+4	1.807E-7
2	$[(0/90)_4]_s$	1.500	4.882E+3	4.977E+3	1.646E-7
2	$[(0/90)_4]_s$	2.000	2.081E+3	2.098E+3	1.647E-7
3	$[(0/90)_4]_s$	5.000	1.113E+2		1.938E-7
4	$[(+45/-45)_4]_s$	0.500	2.598E+4	3.551E+4	6.952E-7
5	$[(+45/-45)_4]_s$	1.000	6.852E+3	7.374E+3	3.974E-7
6	$[(+45/-45)_4]_s$	1.500	2.484E+3	2.459E+3	3.767E-7
7	$[(+45/-45)_4]_s$	2.000	1.027E+3	1.038E+3	3.580E-7
8	$[(+45/-45)_4]_s$	5.000	6.317E+2		3.471E-7

* K_{spur} $[(0/90)_4]_s$ = 2.548E+5 (l = 0.50")
K_{spur} $[(+45/-45)_4]_s$ = 9.682E+4 (l = 0.50")

As can be seen from the figures, a nonlinear relationship between $1/E_{xb}$ and $(T/l)^2$ existed for both laminate arrangements. This nonlinearity seemed to imply a softening of the transverse shear modulus for shorter span lengths. However; transverse shear stress as predicted by technical beam theory is not a function of span length. Furthermore, since all measurements for the various span lengths were taken at the same load level, similar

magnitudes of transverse shear stress should have been predicted for all span lengths thus ruling out transverse shear modulus softening.

An explanation of these results is that the very specimen dimensions that were necessary to induce an *appreciable* amount of shear deflection could have in fact violated the dimensional requirements of beam theory itself. This may be readily seen in Figure 6.8 where for an assumed moduli ratio (E/G) of 10, a span to depth ratio of 10 or lower was necessary for a deflection ratio ($\delta\tau/\delta T$) of 10% or greater. This was in sharp contrast to the span to depth ratio of 30 for beam assumptions.

The specimen dimensions (that were experimentally necessary for an accurate transverse shear moduli determination) could have required that the actual beam theory be of a transitional nature somewhere in between that of a shear-bending formulation to that of a pure shear formulation. This phenomenon was thought to be highly span dependent. A mathematical representation of this formulation was found by introducing a bending participation factor (ζ) into the technical beam theory of equation (6.5) resulting in the following expression;

$$W_{max} = (W\sigma + W\tau) = \left[\zeta\left(\frac{Pl^3}{48E_{xb}I}\right) + \left(\frac{\alpha Pl}{4G_{xz}F}\right) \right] \qquad (6.12)$$

Appropriately, the fictitious flexural modulus of equation (6.6) became;

$$E_{fb} = \frac{\zeta P l^3}{48 I W_{max}} \qquad (6.13)$$

while the linear relationship of (6.6) takes the form of;

$$\frac{\zeta}{E_{xf}} = \left[\frac{\zeta}{E_{xb}} + \left(\frac{1.2}{G_{xz}}\right)\left(\frac{T}{l}\right)^2\right] \qquad (6.14)$$

Here again, a plot of ζ/E_{fb} verses $(T/l)^2$ yielded a straight line whose slope was equal to the quantity of $1.2/G_{xz}$. As before, the y intercept equaled E_{xb} since a $(T/l)^2$ of zero implies a infinitely slender beam.

6.3.4 Test Modifications and Results

An experimental determination of the bending participation factor, ζ, was undertaken using Aluminum T6061-T6 beams of 0.125", 0.250", and 0.375" thickness and 0.5" width. Three load deflection curves were obtained for each span lengths of 4.0", 3.0", 2.5", 2.0", 1.5", 1.0", and 0.5" in a similar experimental procedure as before. To avoid effects from permanent specimen deformations, separate specimens were used in each determination. Average load deflection curves were obtained and correction for roller indentation and loading jig compliance were accounted for through equation (6.9). Using the flexural modulus of the 0.125" depth and 4.0" span length (assuming total bending deflection) a transverse shear modulus for the aluminum was calculated using the following relationship;

$$G_{xz} = \frac{E_{xb}}{[2(1 + \nu)]} \tag{6.15}$$

Values of ζ were back calculated using this value and the experimentally determined E_{xb}.

A plot of the bending participation factor, ζ, versus nondimensional beam length, l/T, may be seen in Figure 6.12. Averaging of ξ values from different specimen thicknesses yielded a plot of average bending participation factor verses nondimensional beam length as shown in Figure 6.13. As can be seen, ζ falls off rather sharply for smaller l/T ratios thus verifying the transitional beam theory assumption of the previous section.

Using this average bending participations factor, prior three point bend test results of the composite materials were corrected. Results may be seen in Table 6.5 and Figures 6.10 and 6.11. Note the linearization of the curves over those determined without the bending participation factor. The

deviation from linearity of the small depth to span specimens was thought to exist due to their smaller shear to total deflection ratio. Comparisons of the graphical and experimentally determined E_{xb} values yielded differences of less then 25%.

Table 6.5 Corrected Three Point Bend Test Experimental Results

SPEC. NO	STACKING SEQ.	(l/T)	ζ	Exb (psi)	Gxz (psi)	δ_s/δ_T
1	$[(0/90)_4]_s$	4.587	0.761	6.716E+6	5.192E+5	0.480
2	$[(0/90)_4]_s$	8.928	0.970			0.196
2	$[(0/90)_4]_s$	13.393	0.986			0.098
2	$[(0/90)_4]_s$	17.857	0.991			0.057
4	$[(+45/-45)_4]_s$	4.255	0.722	2.885E+6	4.231E+5	0.361
5	$[(+45/-45)_4]_s$	8.734	0.965			0.118
6	$[(+45/-45)_4]_s$	12.658	0.984			0.060
7	$[(+45/-45)_4]_s$	17.316	0.991			0.033

6.4 Through Thickness Poisson Ratio Testing

6.4.1 Uniaxial tension Test and Displacement Clip Gage Description

Uniaxial tension tests were conducted on both $[(0/90)_4]_s$ and $[(+45/-45)_4]_s$ laminates to in an attempt to measure their through thickness Poisson ratios. Specimen dimensions were equal to those of the ASTM D3518-76 configuration. Each of the two specimens that were used for both laminate configurations were instrumented on front and rear surfaces with BLH Faet-06A-S13E strain gages. In-plane strains were monitored as a function of tensile load through a dual active arm Wheatstone bridge configuration.

Through thickness strains were monitored with a sensitive displacement clip gage that is shown in Figure 6.14. Maximum front and rear surface strains of the dual cantilever beam gage were wired in a four active arm Wheatstone bridge configuration to produce maximum voltage output. With a maximum bridge excitation that allowed for stable operating performance,

displacement sensitivity was as low as 50 μin/in.

6.4.2 Test Procedures and Results

All specimens were load cycled a total of three times up to 2000 lbs. Load, longitudinal strain, and through thickness displacements were monitored with conventional XY recorders. Figure 6.15 shows typical through thickness test data for both the $[(0/90)_4]_s$ and $[(+45/-45)_4]_s$ type specimens. After linearization of these curves at initial readings, through thickness Poisson ratio was determined by;

$$\nu_{23} = -(\omega/T_i)/\varepsilon_2 \qquad (6.16)$$

where

ω = through thickness contraction
T_i = initial specimen thickness
ε_2 = longitudinal tensile strain

Table 6.6 lists specimen dimensions and test results for each specimen.

Table 6.6 Through Thickness Poisson Ratio Specimen Description and Test Results

SPEC NO.	STACKING SEQ	b (in)	T (in)	ν_{23}
1	$[(0/90)_4]_s$	1.0025	0.1180	0.4264
2	$[(0/90)_4]_s$	1.0030	0.1120	0.4104
3	$[(+45/-45)_4]_s$	0.9530	0.9800	0.3475
4	$[(+45/-45)_4]_s$	0.9880	0.0900	0.4178

As indicated in Figure 6.15, maximum through thickness specimen contractions were approximately 200 μin/in for both laminates. With a displacement sensitivity of 50 μin/in, the displacement clip gage appeared to be too course of a measurement technique for accurate laminate through

thickness Poisson ratio determinations. The experimental values obtained were thus used as best estimates.

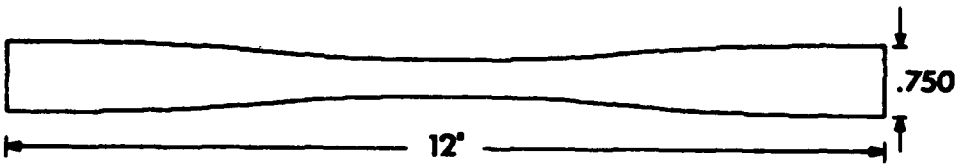

1ST QUADRANT ENLARGED

ON Y-AXIS BY 4X

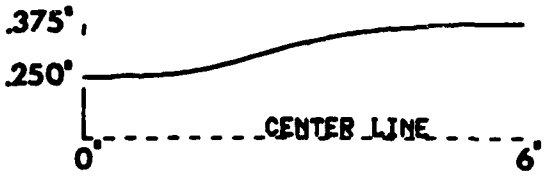

Figure 6.1 AMMRC SL-3 Streamline Tensile Specimen

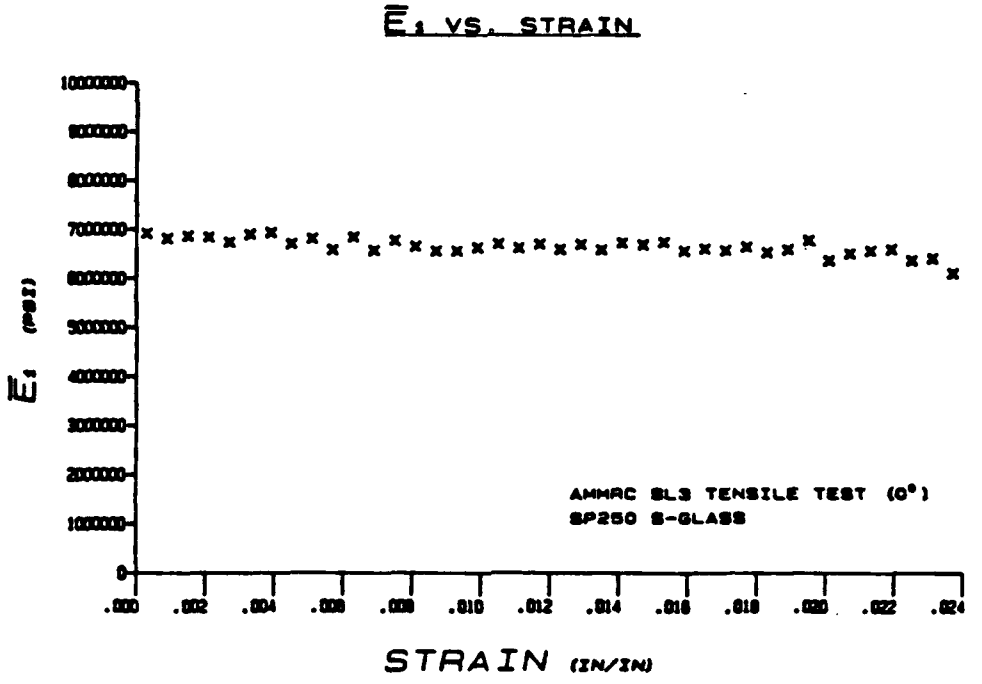

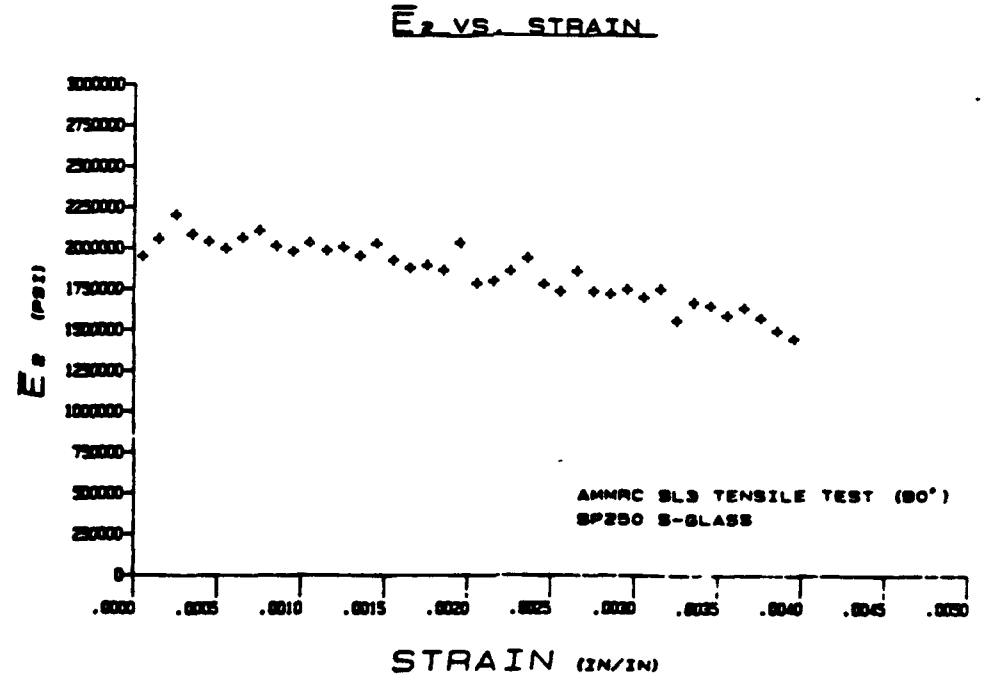

Figure 6.2 Average SP250 S-Glass Lamina Moduli [ref. 66]

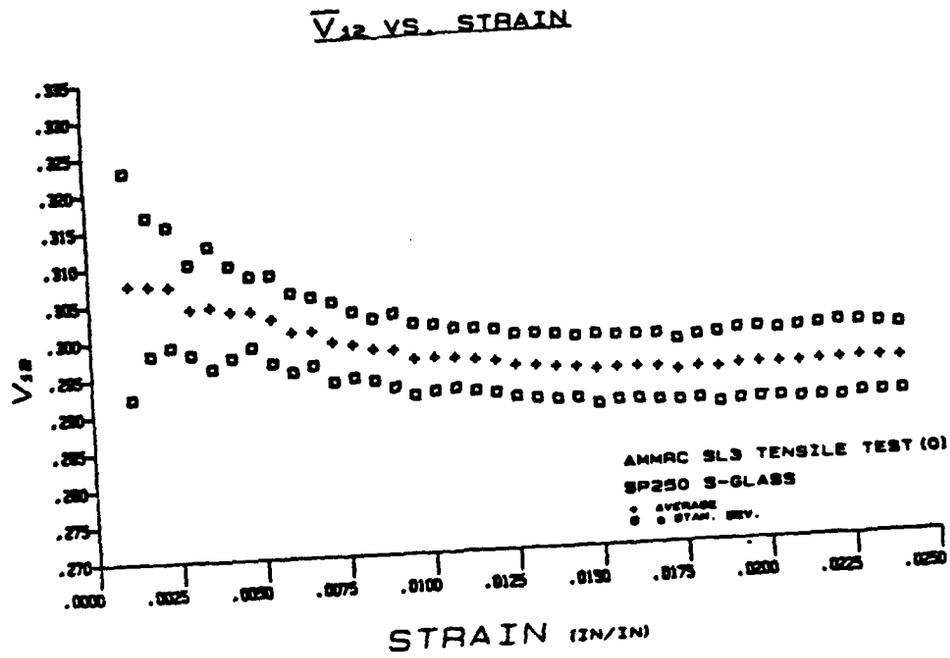

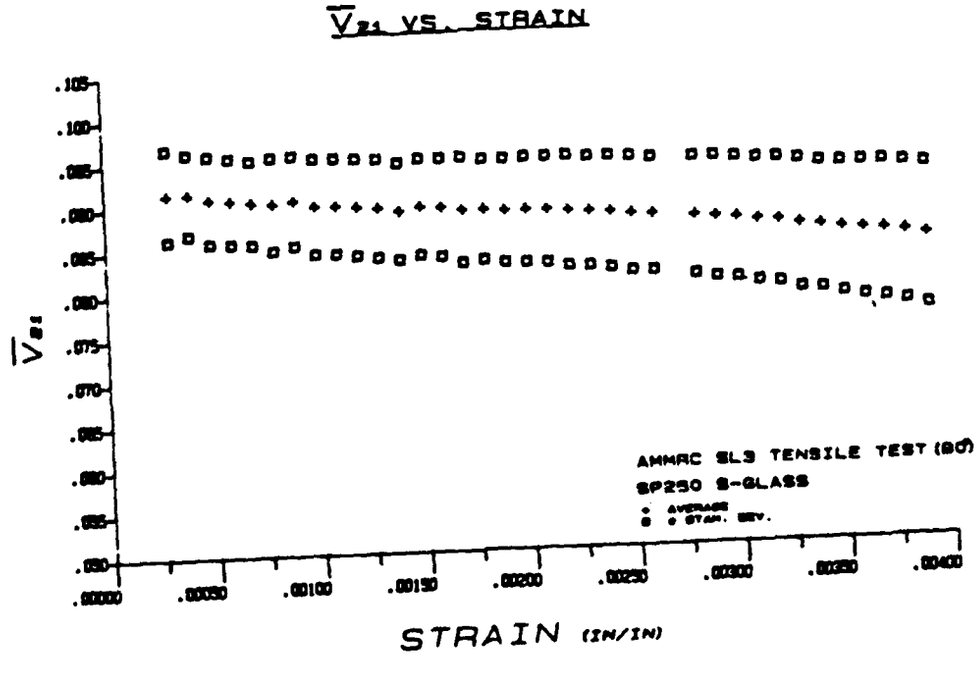

Figure 6.3 Average SP250 S-Glass Lamina Poisson Ratios [ref. 66]

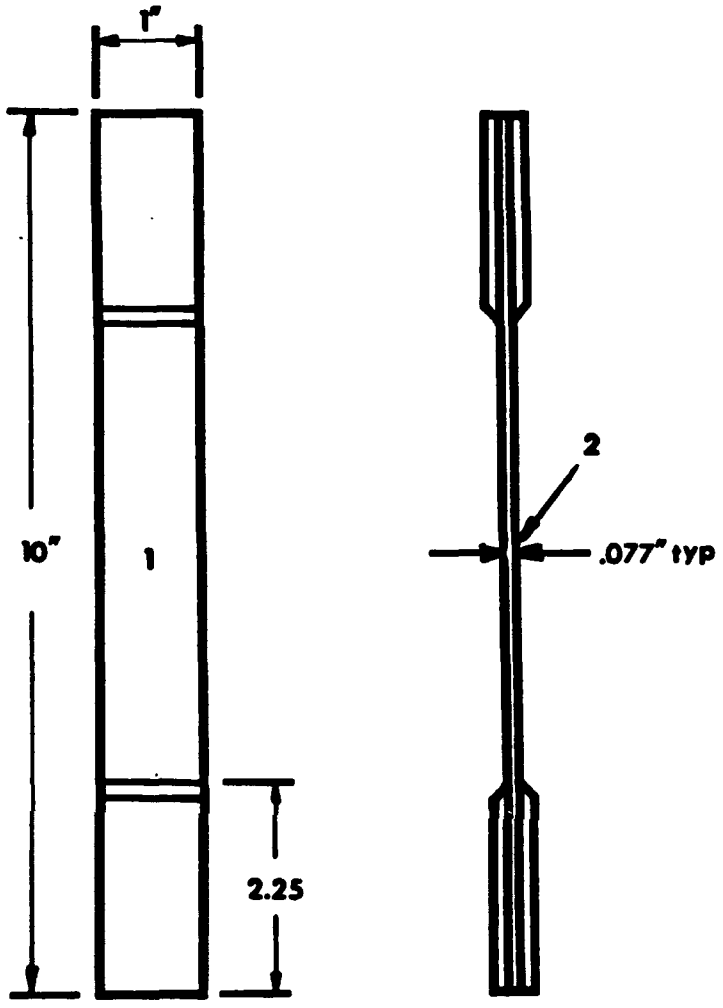

STRAIN GAGES

type	identification
biaxial	BLH Faet-06A-35-S13E

$$\tau_{12} = \bar{\sigma}_x/2$$

$$\gamma_{12} = (\epsilon_x^\circ + \epsilon_y^\circ)$$

Figure 6.4 ASTM D3518-76 Intralaminar Shear Test Specimen Configuration

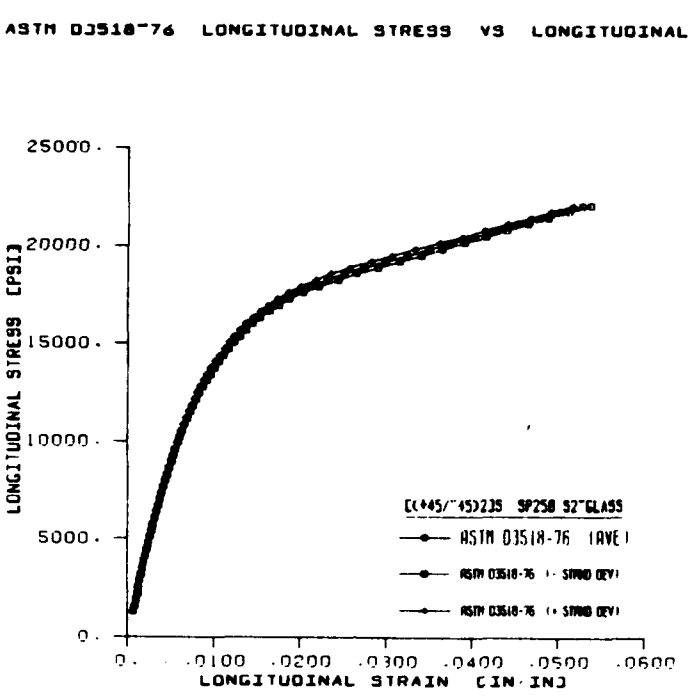

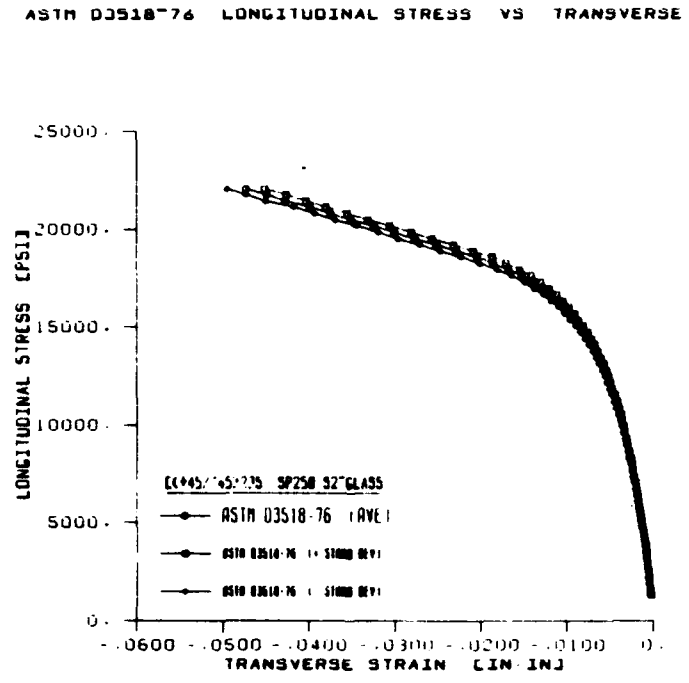

Figure 6.5 ASTM D3518-76 Intralaminar Shear Test Results

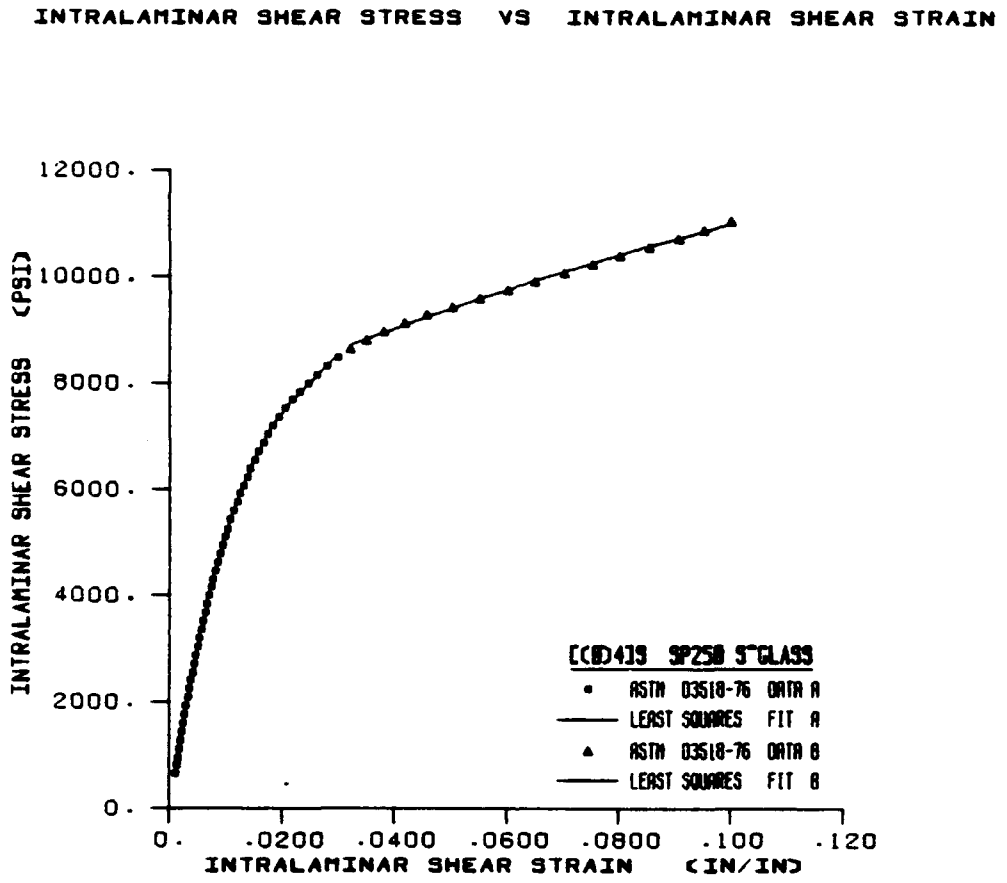

Figure 6.6 Two Part Least Squares Fit of ASTM D3518-76 Shear Test Results

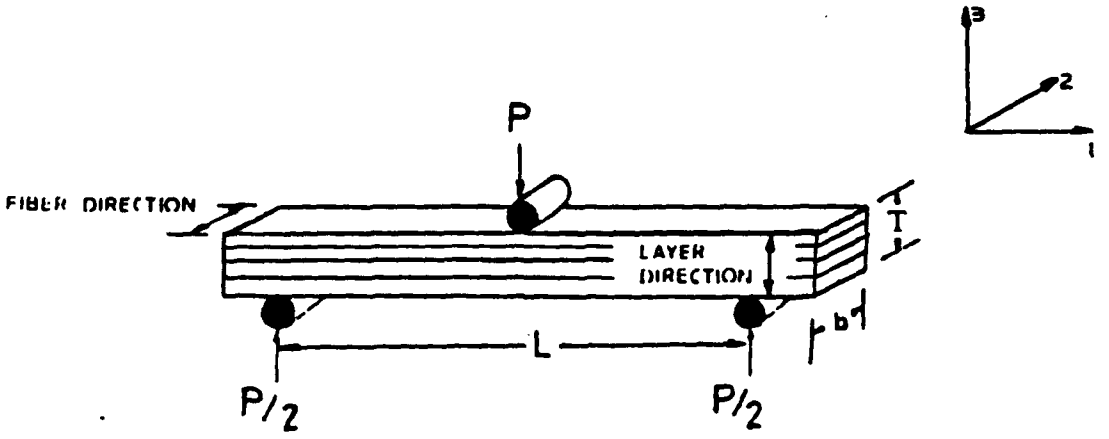

$$W_{max} = W_{\sigma} + W_{\tau} = \left[\left(\frac{P l^3}{48 E_{xb} I}\right) + \left(\frac{\alpha P l}{4 G_{xz} F}\right)\right]$$

$$\frac{1}{E_{fb}} = \left[\frac{1}{E_{xb}} + \left(\frac{1.2}{G_{xz}}\right)\left(\frac{T}{l}\right)^2\right] \qquad E_{fb} = \frac{P l^3}{48 I W_{max}}$$

Figure 6.7 Three Point Bend Test Arrangement For Transverse Shear Modulus Determination [ref. 79]

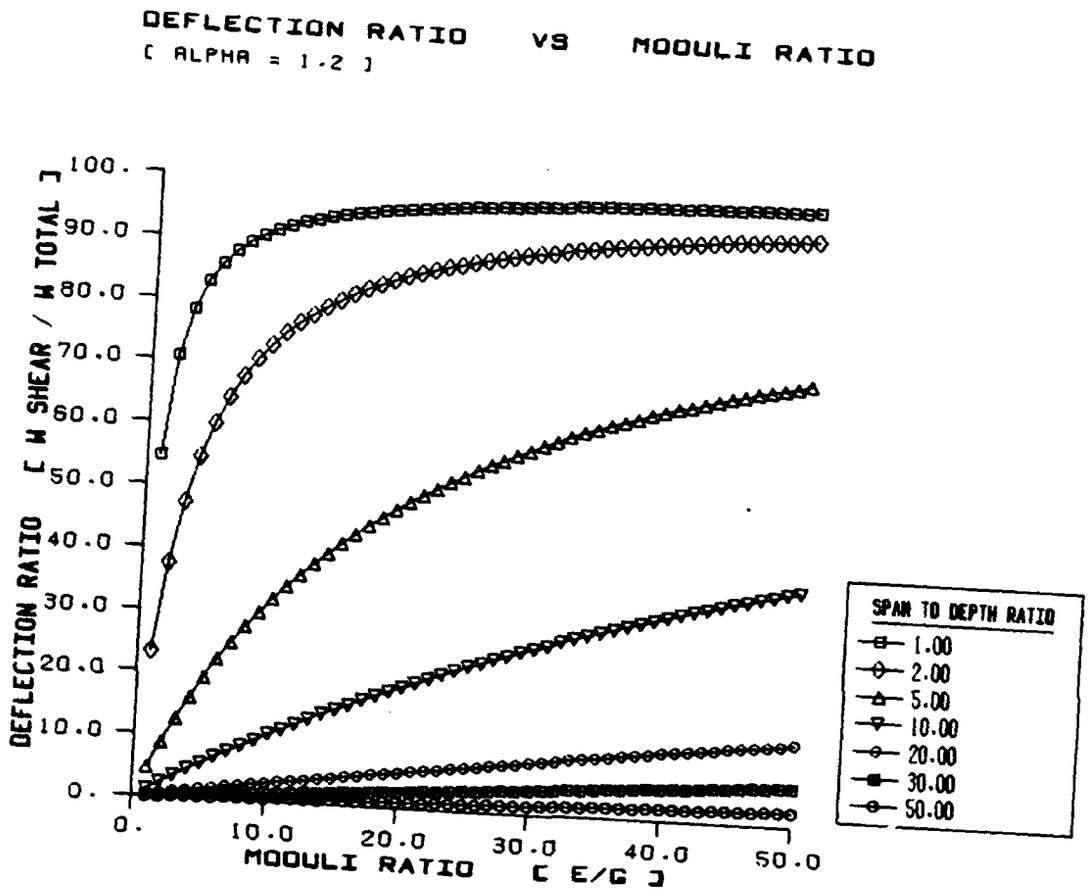

Figure 6.8 Shear to Total Deflection Ratio vs. Moduli Ratio as a Function of Span to Depth Ratio for Three Point Bend Test Arrangement

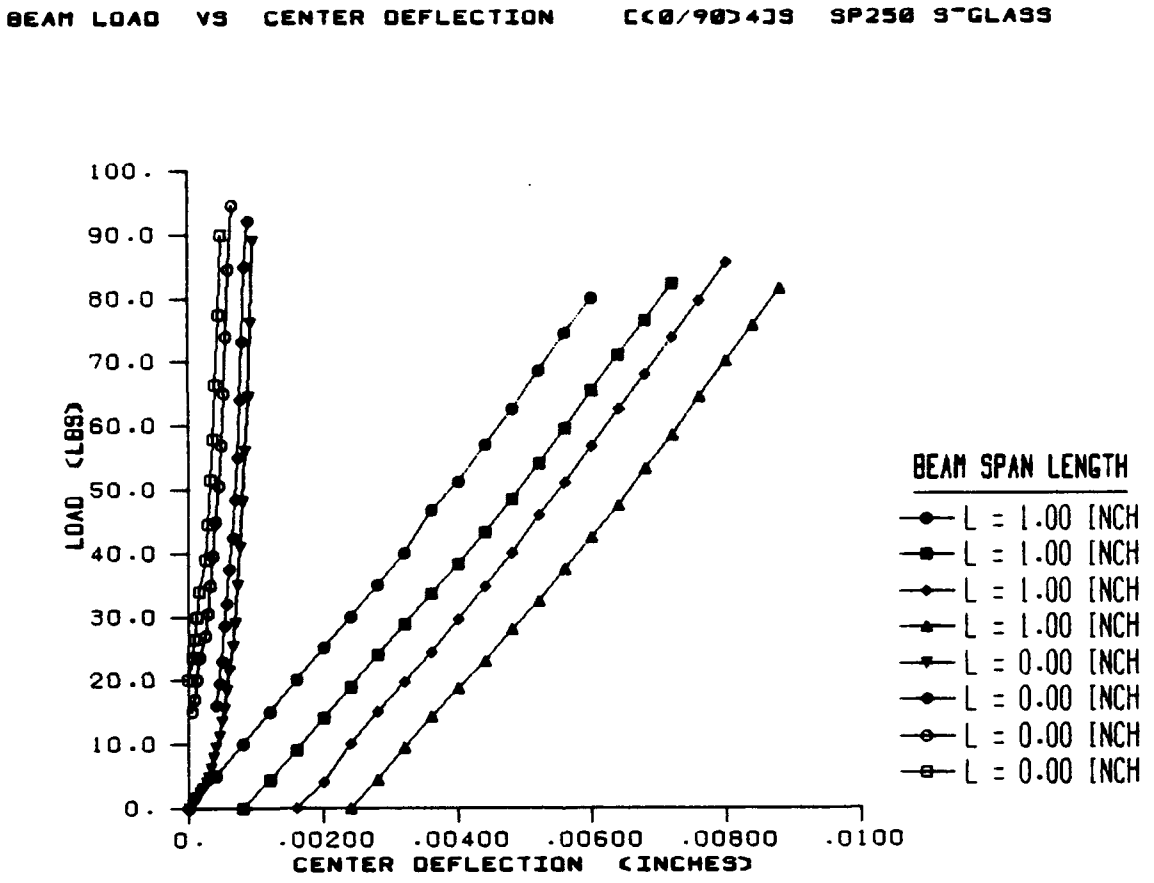

Figure 6.9 Typical Load Deflection Three Point Bend Test Data

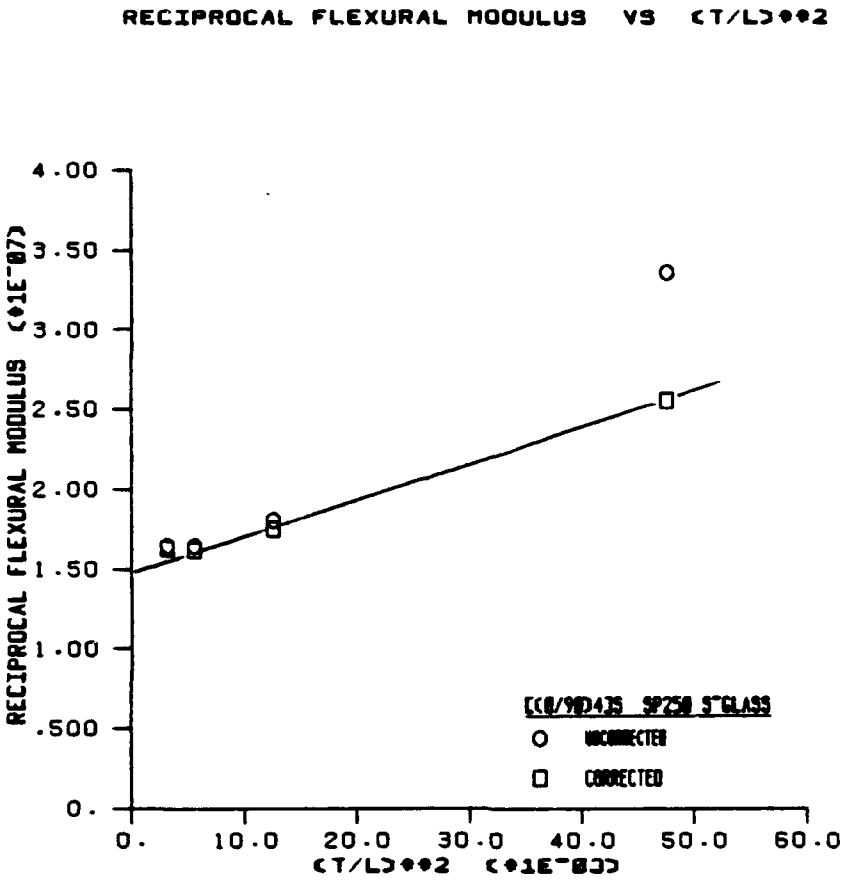

Figure 6.10 $[(0/90)_4]_s$ Reciprocal Flexural Modulus vs. Depth to Span Length Ratio Squared

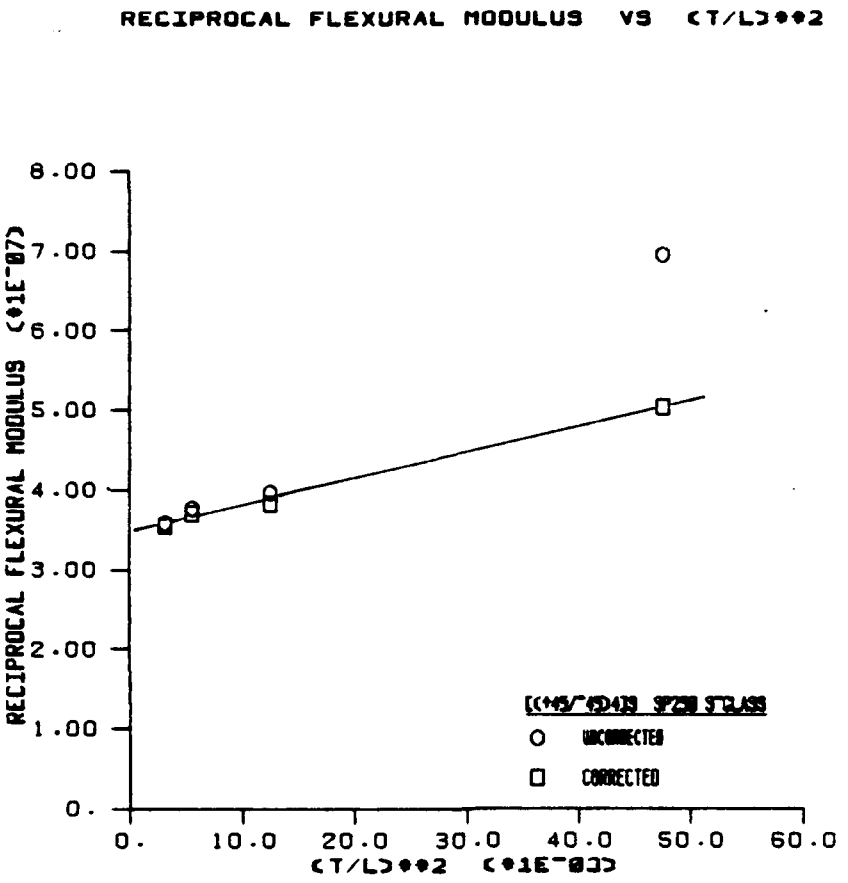

Figure 6.11 $[(+45/-45)_4]_s$ Reciprocal Flexural Modulus vs. Depth to Span Length Ratio Squared

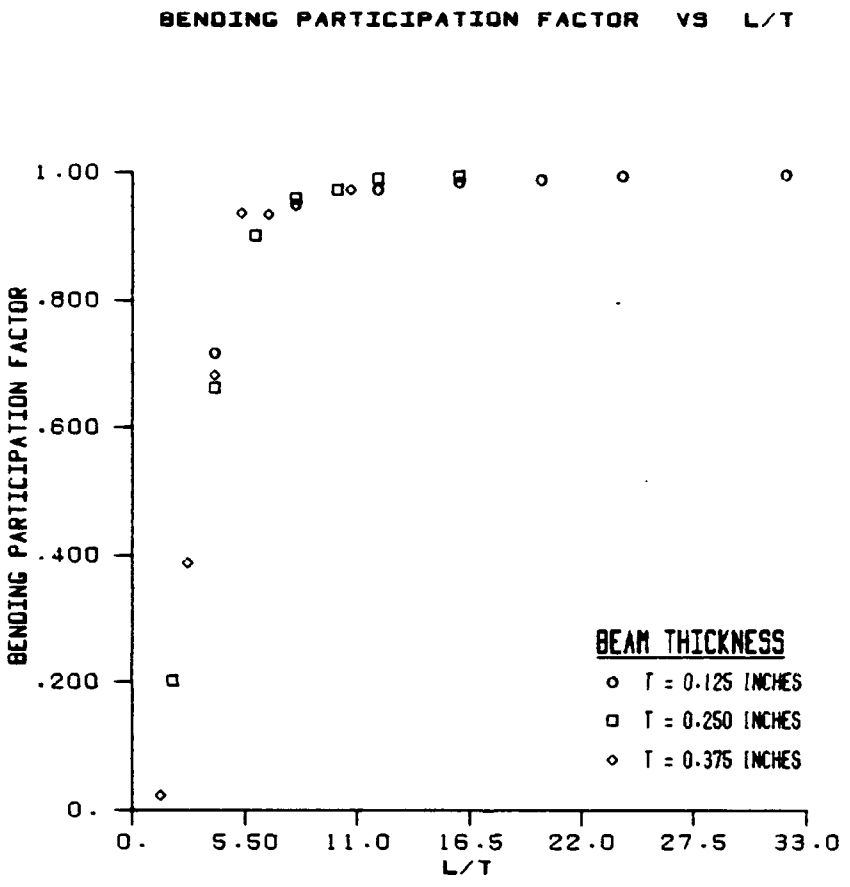

Figure 6.12 Bending Participation Factor vs. Nondimensional Beam Length

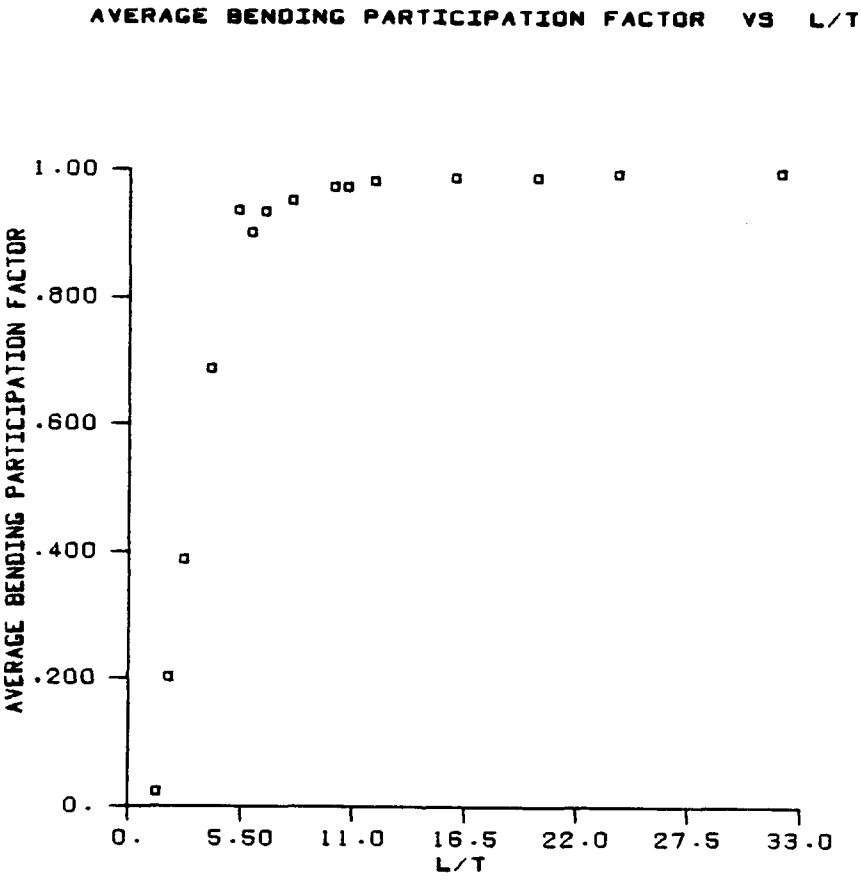

Figure 6.13 Average Bending Participation Factor vs. Nondimensional Beam Length

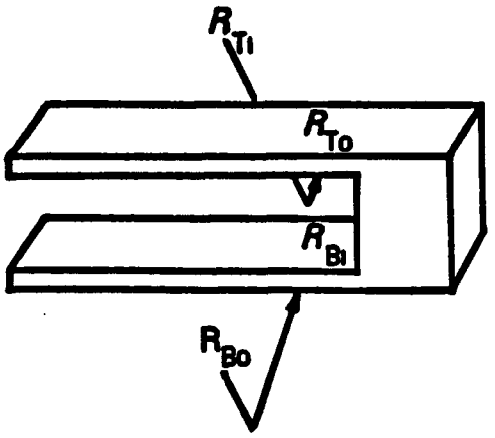

DISPLACEMENT CLIP GAGE

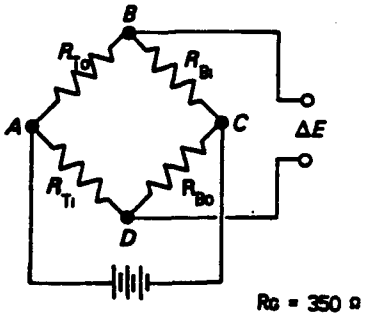

WHEATSTONE BRIDGE

Figure 6.14 Through Thickness Displacement Clip Gage Configuration

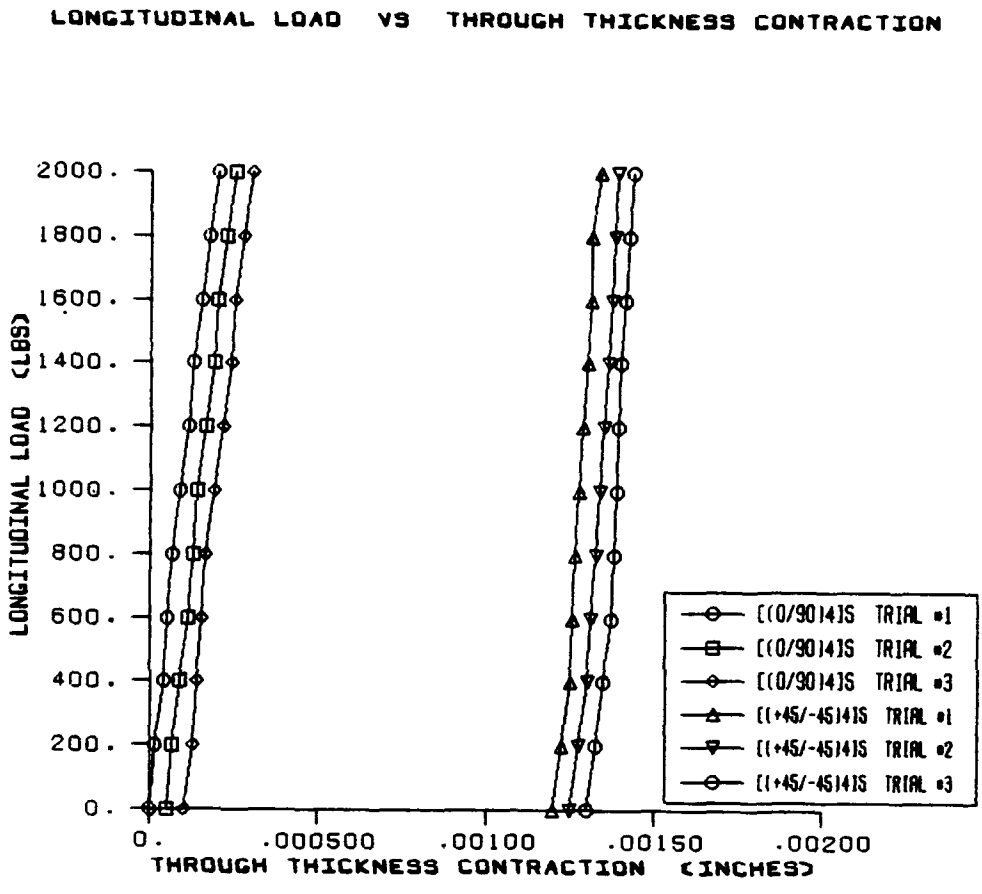

Figure 6.15 Longitudinal Load vs Through Thickness Contraction for $[(0/90)_4]_s$ and $[(+45/-45)_4]_s$ laminate Configurations

CHAPTER 7. THREE DIMENSIONAL CONSTITUTIVE EQUATION MODELING

The three dimensional constitutive equations for the $[(0/90)_3,0]_s$ laminate were derived by using effective two dimensional laminate mechanical properties from the lamina/laminate mechanical property data base. Three dimensional orthotropic stress strain laws were then used in conjunction with these effective mechanical properties. Intralaminar shear nonlinearity was accounted for by using the results from the ASTM D33518-76 test results.

The $[(+45/-45)_3]_s$ laminate constitutive equations were generated by appropriate material axes transformations of $[(0/90)_3]_s$ three dimensional constitutive equations. The laminate's constitutive equation constants were expressed as a function of trigonometric expressions and $[(0/90)_3]_s$ constitutive equation constants.

The constitutive equation were verified by uniaxial laminate tension tests. The experimental stress and strain states of the laminates were compared to those predicted by constitutive equations. The effect of nonlinear crossply intralaminar shear behavior upon $[(+45/-45)_4]_s$ modeling accuracy was determined. Sensitivity analyses of $[(0/90)_4]_s$ E_3 and ν_{23} through thickness properties and $[(0/90)_4]_s$ E_2 and ν_{21} in-plane properties were conducted to assess their effects on uniaxial stress state prediction.

7.1 Effective Two Dimensional Laminate Mechanical Properties

Effective laminate mechanical properties for $[(0/90)_3,0]_s$, $[(0/90)_3]_s$, and $[(+45/-45)_3]_s$ stacking sequences were found from the average lamina mechanical properties of Table 6.1 using the two dimensional orthotropic constitutive equations of classical laminate plate theory[6].

For plane stress conditions, the stress-strain relations of a lamina of arbitrary orientation within a laminated plate as shown in Figure 7.1 were

expressed as,

$$\begin{pmatrix} \sigma_x \\ \sigma_y \\ \tau_{xy} \end{pmatrix} = \begin{bmatrix} \overline{Q}_{11} & \overline{Q}_{12} & \overline{Q}_{16} \\ \overline{Q}_{12} & \overline{Q}_{22} & \overline{Q}_{26} \\ \overline{Q}_{16} & \overline{Q}_{26} & \overline{Q}_{66} \end{bmatrix} \begin{pmatrix} \varepsilon_x \\ \varepsilon_y \\ \gamma_{xy} \end{pmatrix} \tag{7.1}$$

where the transformed reduced stiffness matrix,

$$[\overline{Q}] = [T]^{-1}[Q]\,[T]^{-T} \tag{7.2}$$

and whose stiffness matrix terms as a function of lamina properties,

$$Q_{11} = \frac{E_{11}}{[1 - (\nu_{12})(\nu_{21})]} \qquad Q_{12} = \frac{(\nu_{12})(E_{22})}{[1 - (\nu_{12})(\nu_{21})]}$$
$$Q_{22} = \frac{E_{22}}{[1 - (\nu_{12})(\nu_{21})]} \qquad G_{66} = G_{12} \tag{7.3}$$

whose lamina transformation matrix was,

$$[T] = \begin{pmatrix} \cos^2\alpha & \sin^2\alpha & 2\sin\alpha\cos\alpha \\ \sin^2\alpha & \cos^2\alpha & -2\sin\alpha\cos\alpha \\ -\sin\alpha\cos\alpha & \sin\alpha\cos\alpha & \cos^2\alpha - \sin^2\alpha \end{pmatrix} \tag{7.4}$$

Effective in-plane mechanical properties of the laminates were found from their extensional stiffness constants by;

$$E_x' = \frac{[(A_{11})(A_{22}) - A_{12}^2]}{[(A_{22})(h_o)]} \qquad G_{xy}' = \frac{A_{66}}{h_o}$$

$$E_y' = \frac{[(A_{12})(A_{22}) - A_{12}^2]}{[(A_{11})(h_o)]} \qquad \nu_{xy}' = \frac{A_{12}}{A_{22}} \tag{7.5}$$

which were defined in terms of the reduced stiffness matrix as;

$$A_{ij} = \sum_{k=1}^{N} (\bar{Q}_{ij})_k \, (Z_k - Z_{k-1}) \tag{7.6}$$

Table 7.1 contains the effective laminate mechanical properties resulting from these calculations.

Table 7.1 Effective In-plane Laminate Mechanical Properties

STACKING SEQ.	E'x (psi)	E'y (psi)	ν'xy	G'xy (psi)
$[(0/90)_3,\bar{0}]_s$	4.104E+6	4.476E+6	0.1356	8.170E+5
$[(0/90)_3]_s$	4.290E+6	4.290E+6	0.1297	8.170E+5
$[(+45/-45)_3]_s$	2.386E+6	2.386E+6	0.5385	1.884E+6

7.2 Three Dimensional Orthotropic Constitutive Equations

7.2.1 $[(0/90)_3,\bar{0}]_s$ Laminate Configuration

Three dimensional constitutive equations for the $[(0/90)_3,0]_s$ laminate were found by using the effective in-plane laminate mechanical properties as calculated from classical laminate plate theory and 3D orthotropic stress-strain relations that were given as;

$$\begin{pmatrix} \sigma_x \\ \sigma_y \\ \sigma_z \\ \tau_{xy} \\ \tau_{xz} \\ \tau_{yz} \end{pmatrix} = \begin{bmatrix} C_{11} & C_{12} & C_{13} & 0 & 0 & 0 \\ C_{12} & C_{22} & C_{23} & 0 & 0 & 0 \\ C_{13} & C_{23} & C_{33} & 0 & 0 & 0 \\ 0 & 0 & 0 & C_{44} & 0 & 0 \\ 0 & 0 & 0 & 0 & C_{55} & 0 \\ 0 & 0 & 0 & 0 & 0 & C_{66} \end{bmatrix} \begin{pmatrix} \varepsilon_x \\ \varepsilon_y \\ \varepsilon_z \\ \gamma_{yz} \\ \gamma_{zx} \\ \gamma_{xy} \end{pmatrix} \qquad (7.7)$$

where;

$$C_{11} = \frac{[1 - (\nu_{23})(\nu_{32})]}{[(E_2)(E_3)(\Delta)]} \qquad C_{12} = \frac{[\nu_{21} + (\nu_{31})(\nu_{23})]}{[(E_2)(E_3)(\Delta)]}$$

$$C_{22} = \frac{[1 - (\nu_{13})(\nu_{31})]}{[(E_1)(E_3)(\Delta)]} \qquad C_{13} = \frac{[\nu_{31} + (\nu_{21})(\nu_{32})]}{[(E_2)(E_3)(\Delta)]}$$

$$C_{33} = \frac{[1 - (\nu_{12})(\nu_{21})]}{[(E_1)(E_2)(\Delta)]} \qquad C_{23} = \frac{[\nu_{32} + (\nu_{12})(\nu_{31})]}{[(E_1)(E_3)(\Delta)]}$$

$$C_{44} = G_{23} \qquad C_{55} = G_{31} \qquad C_{66} = G_{12}$$

and;

$$\Delta = \frac{[1 - (\nu_{12})(\nu_{21}) - (\nu_{23})(\nu_{32}) - (\nu_{31})(\nu_{13}) - 2(\nu_{21})(\nu_{32})(\nu_{13})]}{[(E_1)(E_2)(E_3)]}$$

An average through thickness Poisson ratio value ν_{23} from the apropriate test results in Table 6.6 was used. The transverse through thickness Poisson ratio, ν_{13}, was *assumed* equal to ν_{23} for the transversely orthotropic $[(0/90)_3,0]_s$ laminates. Remaining Poisson ratios were found from the reciprocity relationship;

$$\frac{\nu_{ij}}{E_i} = \frac{\nu_{ji}}{E_j} \tag{7.8}$$

A through thickness modulus value (E_3) equal to the transverse modulus of the unidirectional lamina was assumed. Nonlinear intralaminar shear behavior was introduced by using a least squares curve fit representation as given in equation (6.4) and constants listing in Table 6.4. Table 7.2 lists the 3D constitutive equation constants for the $[(0/90)_3,\bar{0}]_s$ and $[(0/90)_3]_s$ laminate arrangements.

7.2.2 $[(+45/-45)_3]_s$ Laminate Configuration

Three dimensional constitutive equations for the $[(+45/-45)_3]_s$ laminate were found by using the 3D orthotropic $[(0/90)_3]_s$ stress-strain relations and appropriate transformation theory. This approach, as previously suggested in a two dimensional sense by Serabian and Oplinger[68], allows for the nonlinear stress-strain description of a $[(+45/-45)_3]_s$ laminate in terms of $[(0/90)_3]_s$ nonlinear intralaminar shear stress-strain behavior. The transformation has the form;

$$[C]^* = [T^*]^T [C] [T^*] \tag{7.9}$$

where

$$[T^*] = \begin{pmatrix} \cos^2\alpha & \sin^2\alpha & 0 & \sin\alpha\cos\alpha & 0 & 0 \\ \sin^2\alpha & \cos^2\alpha & 0 & -\sin\alpha\cos\alpha & 0 & 0 \\ 0 & 0 & 1 & 0 & 0 & 0 \\ 0 & 0 & 0 & 0 & \cos\alpha & -\sin\alpha \\ 0 & 0 & 0 & 0 & \sin\alpha & \cos\alpha \\ -2\sin\alpha\cos\alpha & 2\sin\alpha\cos\alpha & 0 & \cos^2\alpha - \sin^2\alpha & 0 & 0 \end{pmatrix}$$

where $[C]^*$ = $[(+45/-45)_3]_s$ constitutive matrix

$[C]$ = $[(0/90)_3]_s$ constitutive matrix

For $\alpha = 45^0$, expression (7.9) may be reduced to;

$$[C]^* = \begin{pmatrix} (C_A + C_{66}) & (C_A - C_{66}) & C_B & 0 & 0 & 0 \\ (C_A - C_{66}) & (C_A + C_{66}) & C_B & 0 & 0 & 0 \\ C_B & C_B & C_{33} & 0 & 0 & 0 \\ 0 & 0 & 0 & C_{44} & 0 & 0 \\ 0 & 0 & 0 & 0 & C_{55} & 0 \\ 0 & 0 & 0 & 0 & 0 & C_c \end{pmatrix} \quad (7.10)$$

where

$$C_A = .5(C_{11} + C_{12})$$
$$C_B = .5(C_{13} + C_{23})$$
$$C_C = .5(C_{11} - C_{12})$$

In this instance, C_{66} was evaluated from an effective intralaminar shear strain that was obtained by using;

$$\gamma_{xy'} = (\varepsilon_y - \varepsilon_x) \quad (7.11)$$

Table 7.2 lists these 3D constitutive equation constants for the $[(0/90)_3,0]_s$, $[(0/90)_3]_s$, and $[(+45/-45)_3]_s$ laminate configurations. These values were determined with an intralaminar shear modulus evaluated from the condition that;

$$\gamma_{xy} = \gamma'_{xy} = 0.0 \quad (7.12)$$

Table 7.2 Initial 3D constituitive Equation Constants (psi x10^6)*

STACKING SEQ	C_{11}	C_{12}	C_{13}	C_{22}	C_{23}	C_{33}	C_{44}	C_{55}	C_{66}
$[(0/90)_3,\bar{0}]_s$	4.71	1.22	1.10	5.10	1.09	2.25	0.52	0.52	0.82
$[(0/90)_3]_s$	4.88	1.09	1.08	4.88	1.08	2.25	0.52	0.52	0.82
STACKING SEQ	C^*_{11}	C^*_{12}	C^*_{13}	C^*_{22}	C^*_{23}	C^*_{33}	C^*_{44}	C^*_{55}	C^*_{66}
$[(+45/-45)_3]_s$	3.72	2.24	1.08	3.72	1.08	2.25	0.42	0.42	1.90

E_3 = 1.858E+6
$C_{66} = G_{xy}$ (@ γ_{xy} = 0.0)

7.2.3 EXPERIMENTAL CORROBORATION

An attempt to experimentally verify the constitutive equation modeling approach was made through uniaxial laminate tension testing. The experimental uniaxial laminate stress states were compared to those predicted by the constitutive equations and experimental uniaxial laminate strains. Although only uniaxial in nature, the comparison offered some insight into the accuracy of the constitutive equations. This type of corroborative effort could be expanded to include biaxial testing for a more informative comparison.

A laminate experimental data base was constructed by tensile testing $[(0/90)_4]_s$ laminates and reusing the ASTM D3518-76 $[(+45/-45)_2]_s$ tensile data. A total of four 1/2 SL-3 $[(0/90)_4]_s$ streamline tensile specimens were instrumented with back to back BLH FAET-06A-35-S13-E electrical resistance strain gages. The strain gages were connected to a dual active arm Wheatstone bridge configuration of a KEITHLEY/IBM data acquisition system. The specimens were placed in a 10K INSTRON servo hydraulic testing machine and loaded at a rate of .01 in/min. Full scale values of 2500 lbs, 3%, and 0.2% were used for the load, longitudinal, and transverse scales to provide ample load and strain resolutions. The digital load-strain data was then transferred to an APOLLO DN-3000 work station where it was converted to stress-strain data files. All files (including the ASTM D3518-76 results)

were then sorted, linearly interpolated, and averaged among specimens to produce average stress-strain curves. Strain standard deviations were also computed for each specimen set.

Figures 7.2 and 7.3 illustrate the longitudinal (ε_y) and transverse (ε_x) stress-strain response of the $[(0/90)_4]_s$ specimens. The longitudinal and transverse stress-strain ASTM D3518-76 response was previously illustrated in Figure 6.5. Note that the $[(+45/-45)_2]_s$ response is based on the average of four specimens. Only one $[(0/90)_4]_s$ specimen reached a longitudinal 3% strain value while total response is *projected* to a 4% longitudinal strain level.

For both laminate arrangements, these experimental strains were used with the constitutive equations (7.7) and (7.10) to predict the experimental tensile stress state. Comparisons were done at each stress interval up to the maximum 4% longitudinal strain limit. The predicted stress states were then compared to the actual uniaxial stress condition. Normalized percent error functions with respect to the actual uniaxial stress were formed.

Figure 7.4 shows this normalized uniaxial stress state comparison for the $[(0/90)_4]_s$ laminate. Figures 7.5 and 7.6 illustrates a similar comparison for the $[(+45/-45)_2]_s$ specimens with linear and nonlinear intralaminar shear stress-strain behavior respectively. Maximum normalized errors of approximately 400 % and 30 % were observed for the $[(+45/-45)_2]_s$ laminate with linear and nonlinear intralaminar shear stress-strain response respectively. This observation underscored the importance of this constitutive modeling assumption particularly at higher uniaxial strain levels. Similarly, the $[(0/90)_4]_s$ laminate comparison yielded a maximum normalized error of 35 %.

It was not apparent what effect the $[(0/90)_4]_s$ E_3 and ν_{23} through thickness properties had on the resulting normalized errors. Remembering that a marginal measuring sensitivity was used to determine ν_{23} and noting that E_3 may have a lower bound of that of pure SP250 resin (0.40xE+6), a sensitivity analysis to determine these effects was undertaken.

7.3 Through Thickness Laminate Mechanical Property Sensitivity Analysis

Effects of the $[(0/90)_4]_s$ through thickness mechanical properties were investigated by introducing variations of their values in the uniaxial

stress state comparisons. For both laminate arrangements, E_3 was varied from values of pure resin to that for a transverse lamina (ie $0.40xE+6 \leq E_3 \leq 1.858xE+6$) (with ν_{23} equal to the experimentally determined value). Similarly, a separate ± 50 % variation in ν_{23} (with an E_3 of 1.858xE6) was introduced into the constitutive equations.

Figures 7.7 and 7.8 illustrate the normalized $[(0/90)_4]_s$ uniaxial stress state errors resulting from the E_3 and ν_{23} variations. Figures 7.9 and 7.10 show the normalized $[(+45/-45)_4]_s$ uniaxial stress state errors resulting from the E_3 and ν_{23} variations. Graphically, these variations are seen traversing across each normalized stress component. As can be seen, both variations had minimal affect on the $[(0/90)_4]_s$ laminate results, but greatly affected the $[(+45/-45)_4]_s$ results. In both cases, the lower bound of the through thickness modulus yields lower σ_z error values. Note also that these lower values occured with this the experimentally determined value of ν_{23}. With these through thickness values and the inclusion of intralaminar shear nonlinearity , maximum normalized $[(+45/-45)_2]_s$ uniaxial constitutive equation modeling error was reduced to approximately 20% while the maximum $[(0/90)_4]_s$ error remained at 35 %.

7.4 In-Plane Laminate Mechanical Property Sensitivity Analysis

The experimental uniaxial stress strain response of the $[(0/90)_4]_s$ laminate shown in Figures 7.2 and 7.3 indicated nonlinearities in both the in-plane Poisson ratio, ν_{21}, and tensile modulus, E_2. In order to assess the effects of these nonlinearities on the remaining normalized uniaxial stress state errors, experimental ν_{21} and E_2 nonlinearities were introduced into the constitutive equations. A five point "rolling average" of these values was computed *as a function of* longitudinal tensile strain to promote smooth descriptions.

Figure 7.11 shows the effect of in-plane Poisson ratio ν_{21} while Figure 7.12 shows the effect on in-plane modulus E_2 for the $[(0/90)_4]_s$ laminate. As can be seen, the ν_{21} nonlinearity acted to nullify the transverse normalized error while the E_2 nonlinearity acted to greatly reduce the normal normalized stress error.

Figure 7.13 illustrates the effects of both in-plane properties upon the $[(+45/-45)_2]_s$ laminate. In this case, both the $[(0/90)_4]_s$ E_1 and E_2 moduli were equated and nonlinearized due to the equality of the transformed tensile loading existing within the laminate. As can be seen, the effects were minimal in regards to the normalized stress error. However; a 20 % reduction of these moduli values nullified the remaining normalized stress errors of the $[(+45/-45)_4]_s$ laminate as can be seen in Figure 7.14. Reduced moduli values might have resulted from seperate autoclaving runs that were used to manufacture the laminated specimens.

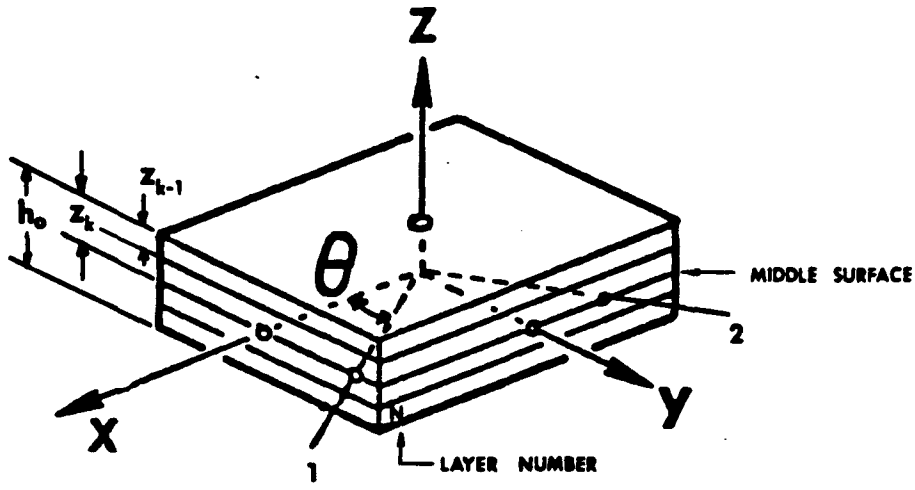

Figure 7.1 Composite Laminated Plate

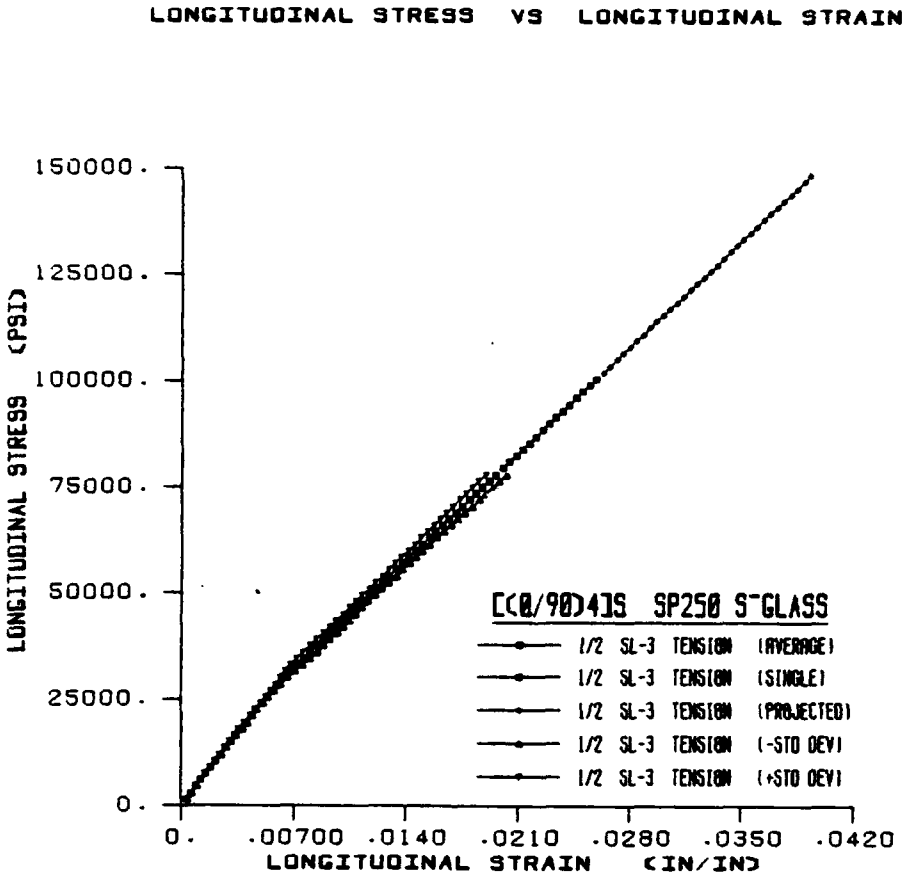

Figure 7.2 Average $[(0/90)_4]_s$ Longitudinal Stress-Strain Response

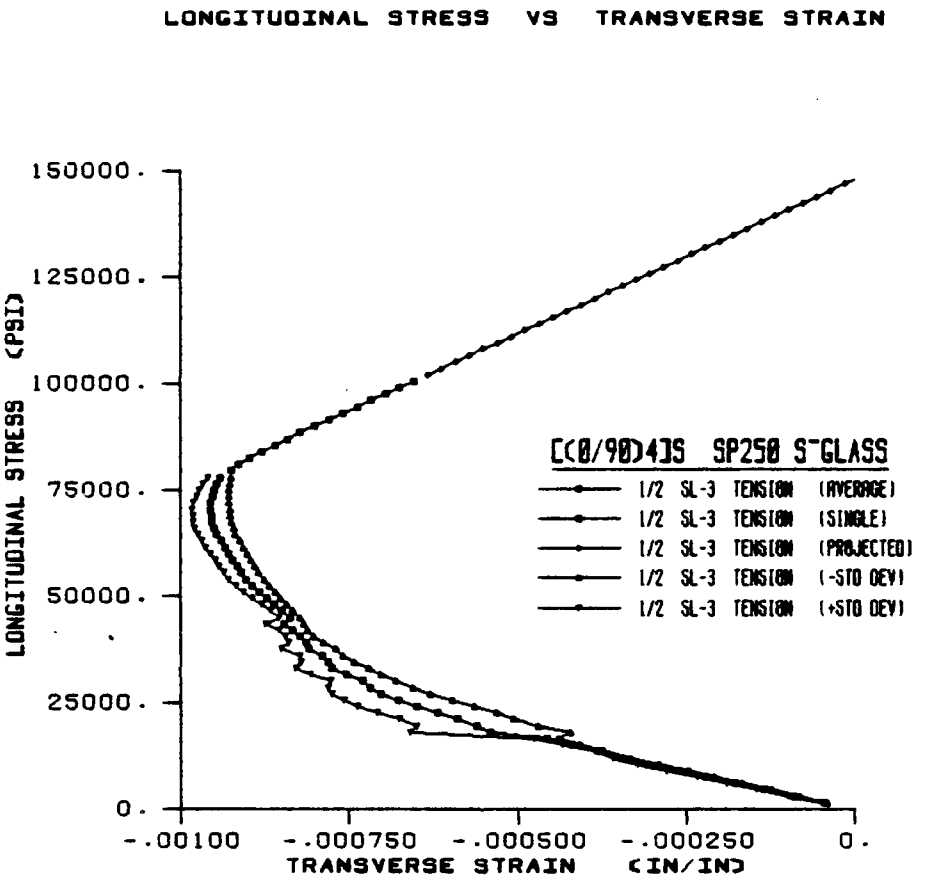

Figure 7.3 Average $[(0/90)_4]_s$ Transverse Stress-Strain Response

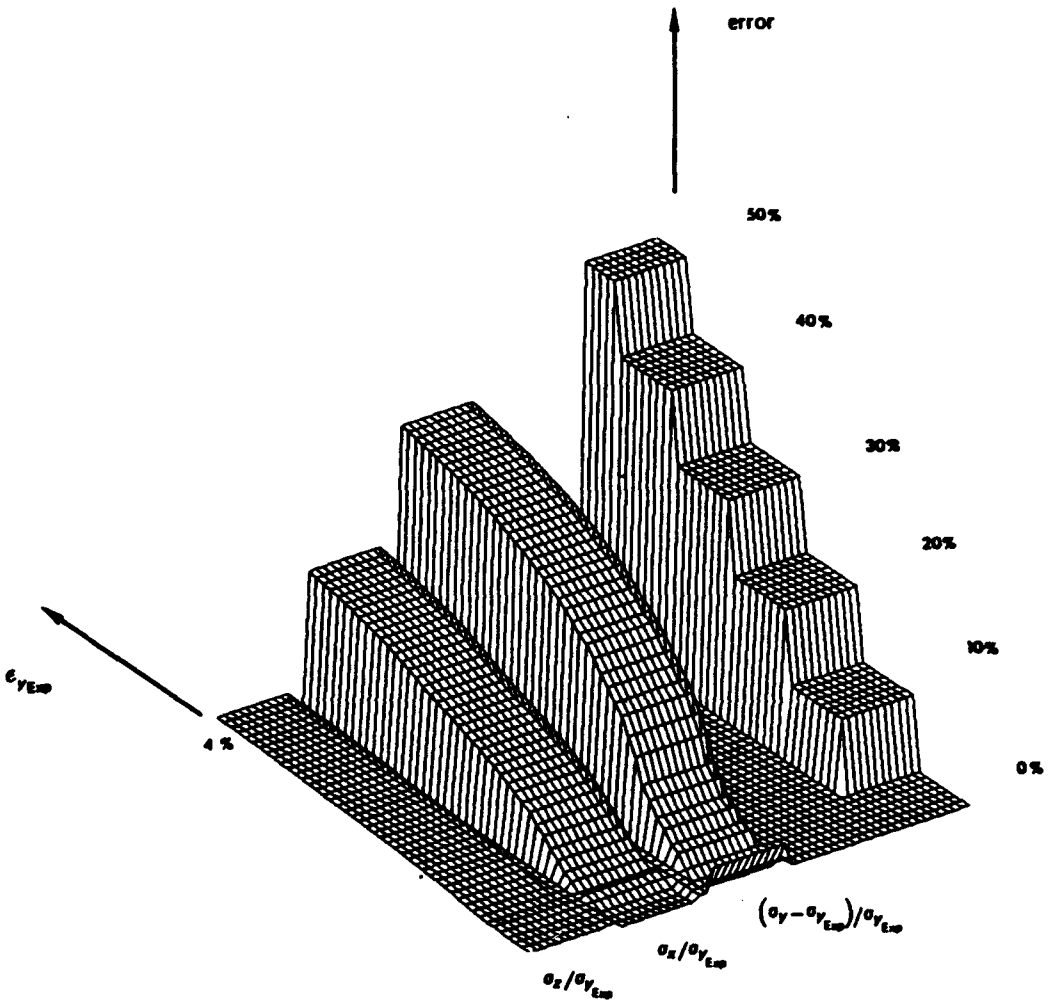

Figure 7.4 Normalized $[(0/90)_4]_s$ Uniaxial Stress State Error

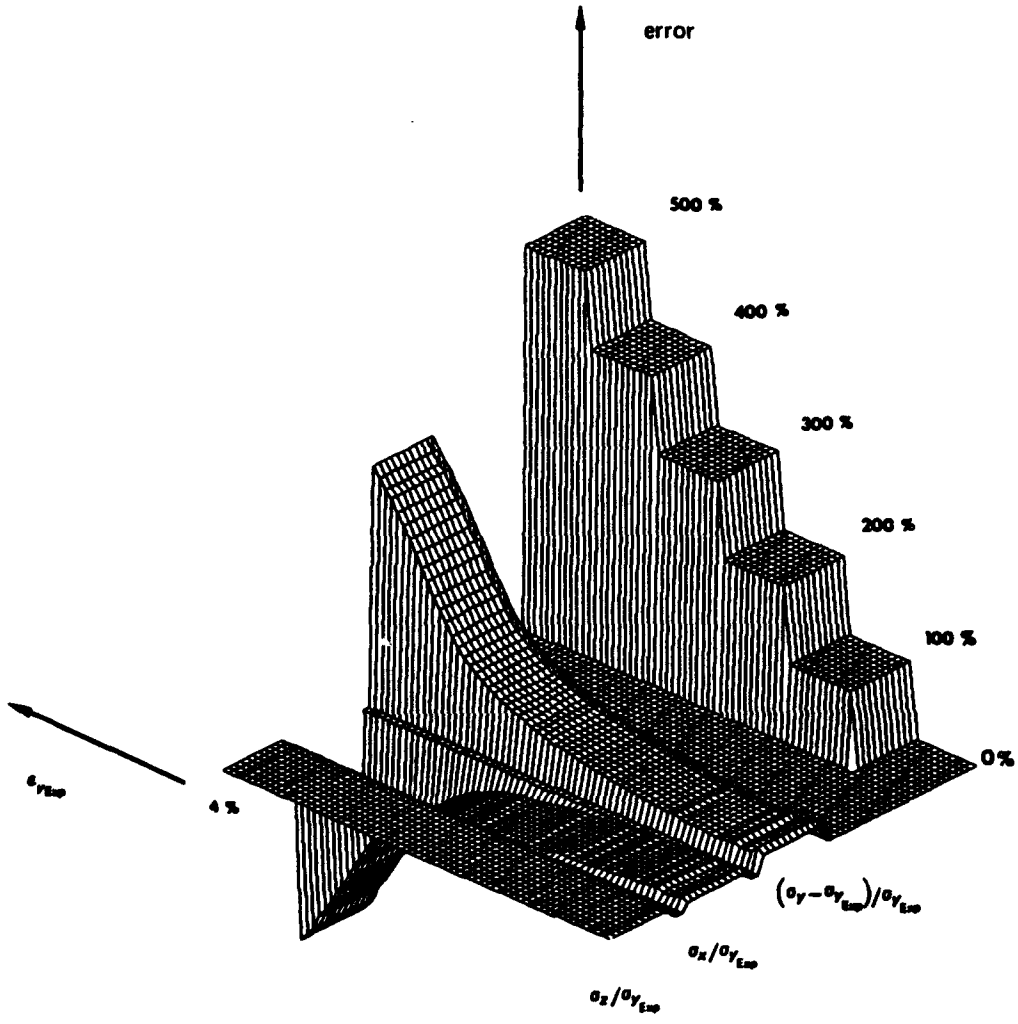

Figure 7.5 Normalized $[(+45/-45)_2]_s$ Uniaxial Stress State Error With Linear Intralaminar Shear Behavior

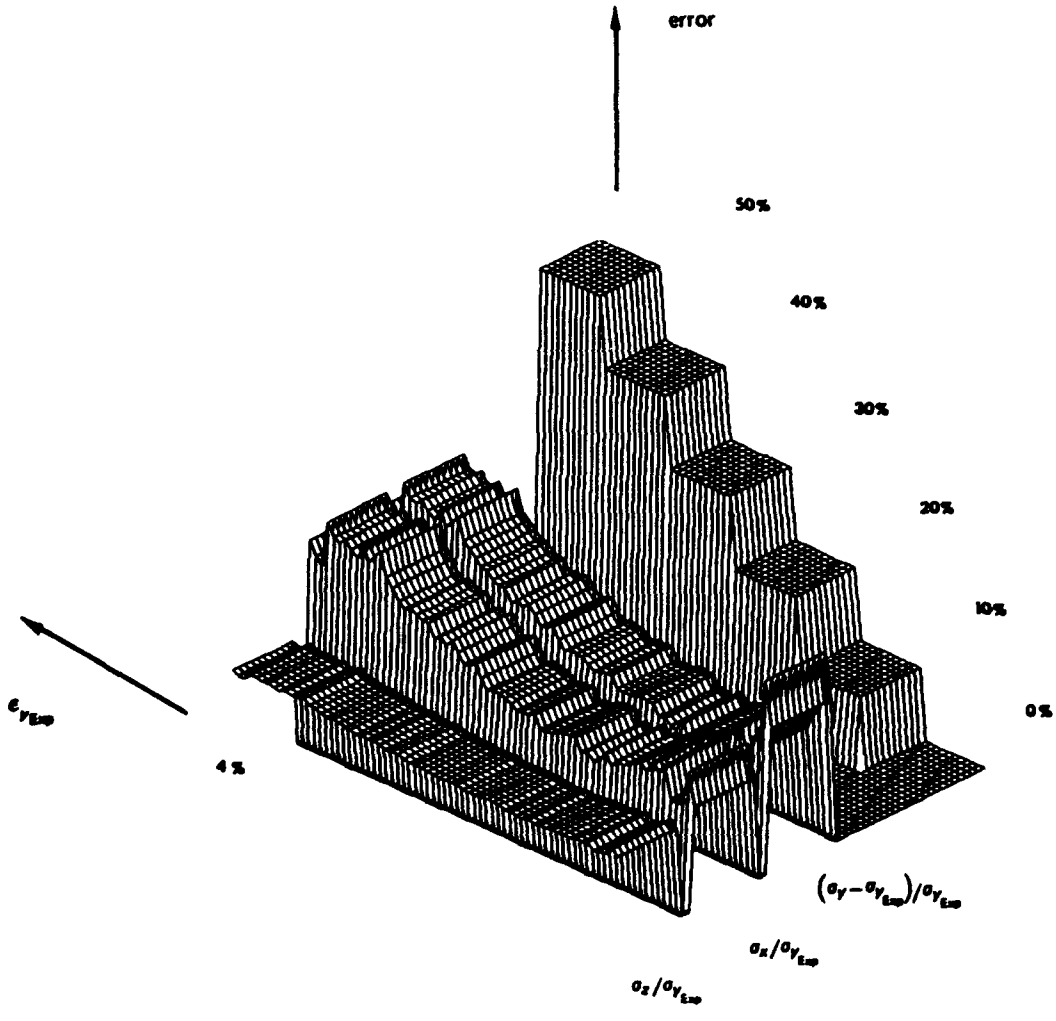

Figure 7.6 Normalized $[(+45/-45)_2]_s$ Uniaxial Stress State Error With Nonlinear Intralaminar Shear Behavior

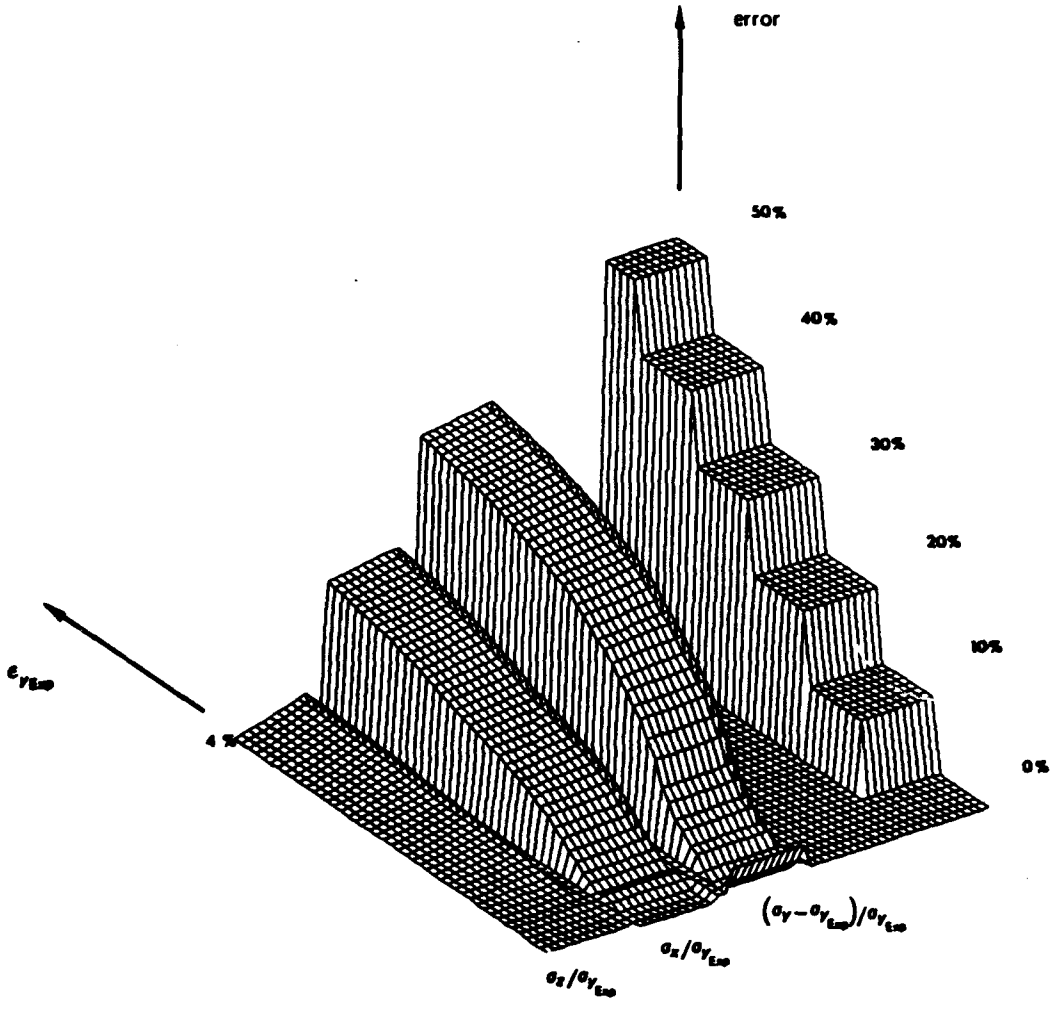

Figure 7.7 Normalized $[(0/90)_4]_s$ Uniaxial Stress State Error
[(0.40xE6 ≤ E3 ≤ 1.858xE) ($\nu_{23} = \nu_{23\ exp}$)]

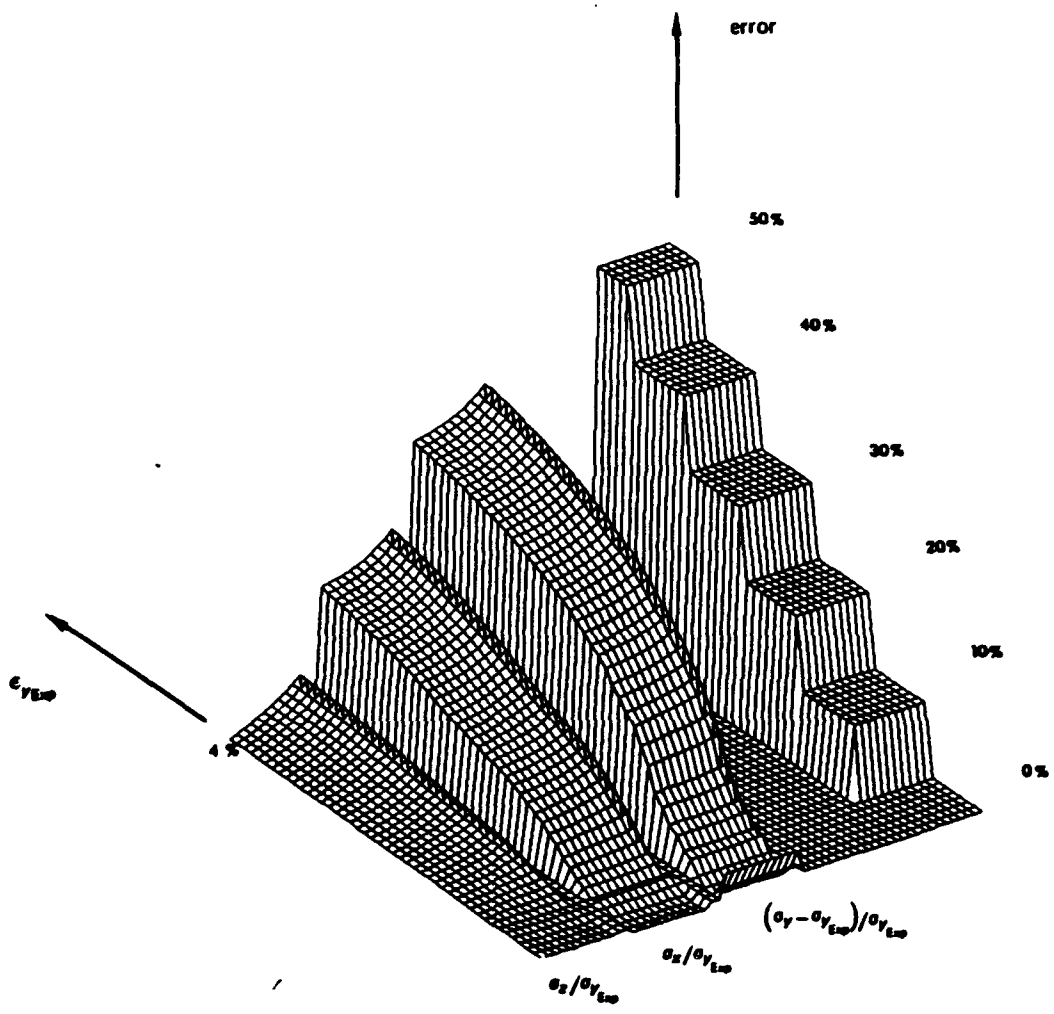

Figure 7.8 Normalized $[(0/90)_4]_s$ Uniaxial Stress State Error
[$(0.20919 \leq \nu_{23} \leq 0.6276)$ $(E_3 = 1.858xE6)$]

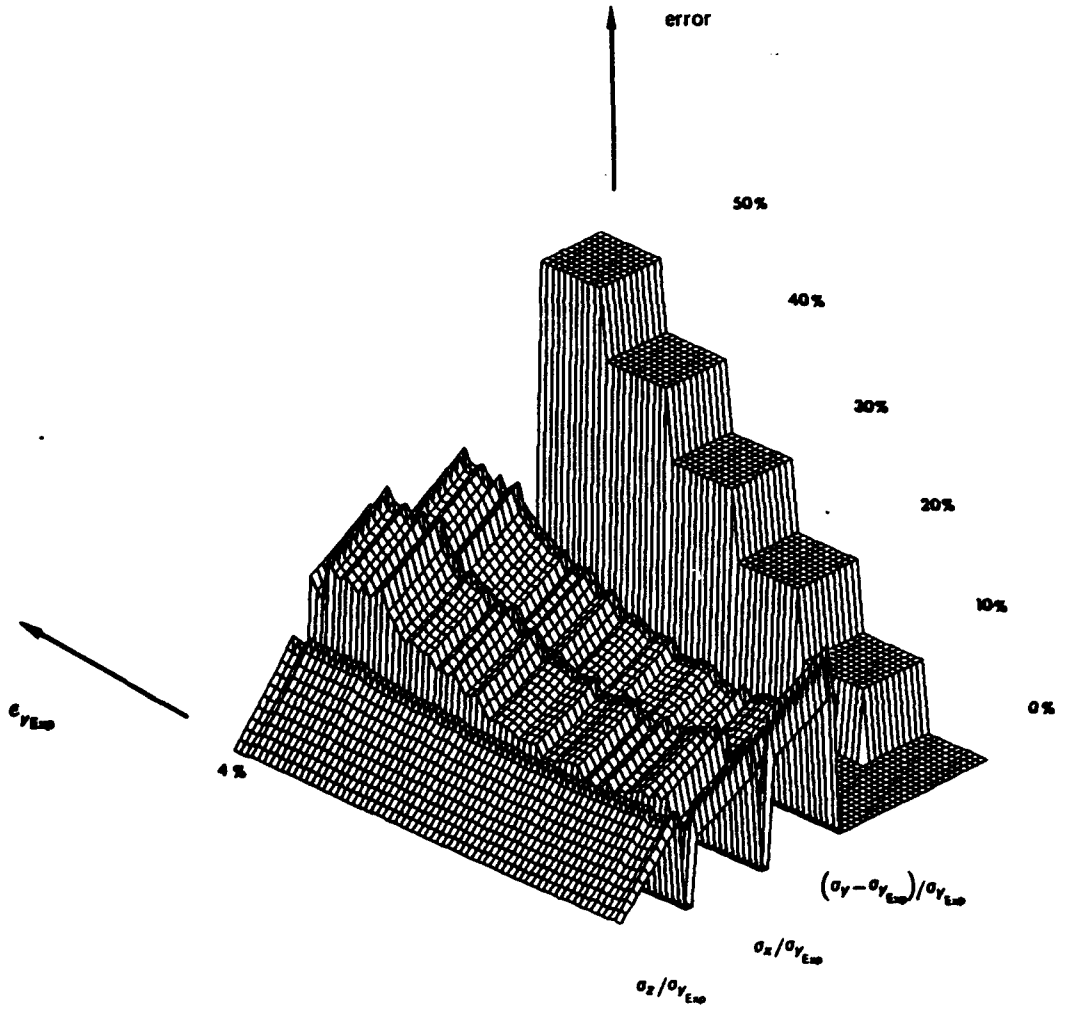

Figure 7.9 Normalized $[(+45/-45)_4]_s$ Uniaxial Stress State Error With Nonlinear Intralaminar Shear Behavior
[(0.40xE6 ≤ E3 ≤ 1.858xE6) (ν_{23} = $\nu_{23\ exp}$)]

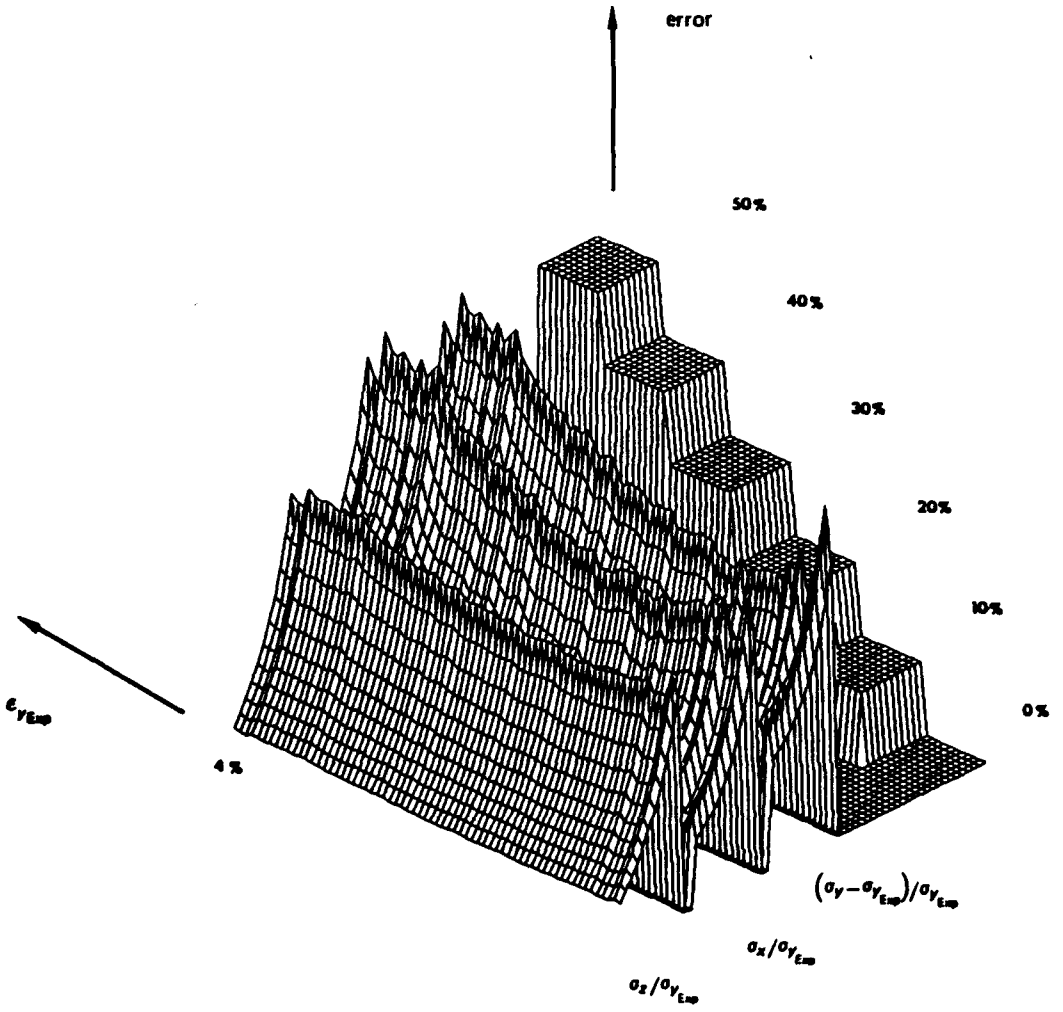

Figure 7.10 Normalized $[(+45/-45)_4]_s$ Uniaxial Stress State Error With Nonlinear Intralaminar Shear Behavior
[$(0.20919 \leq \nu_{23} \leq 0.6276)$ $(E_3 = 1.858 \times E6)$]

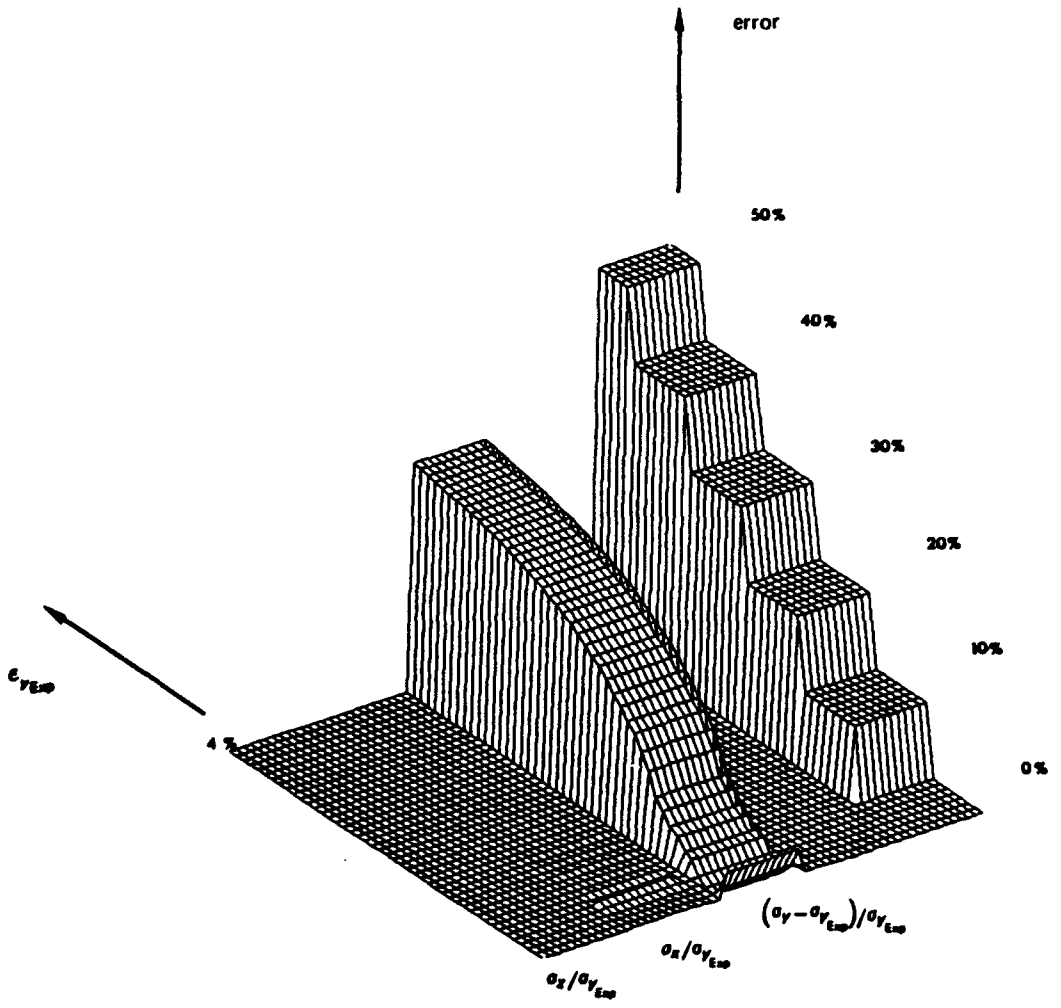

Figure 7.11 Normalized $[(0/90)_4]_s$ Uniaxial Stress State Error
$[(E_3 = 0.40xE6)(\nu_{23} = \nu_{23\ exp})(\nu_{21} = \nu_{21\ uniaxial})]$

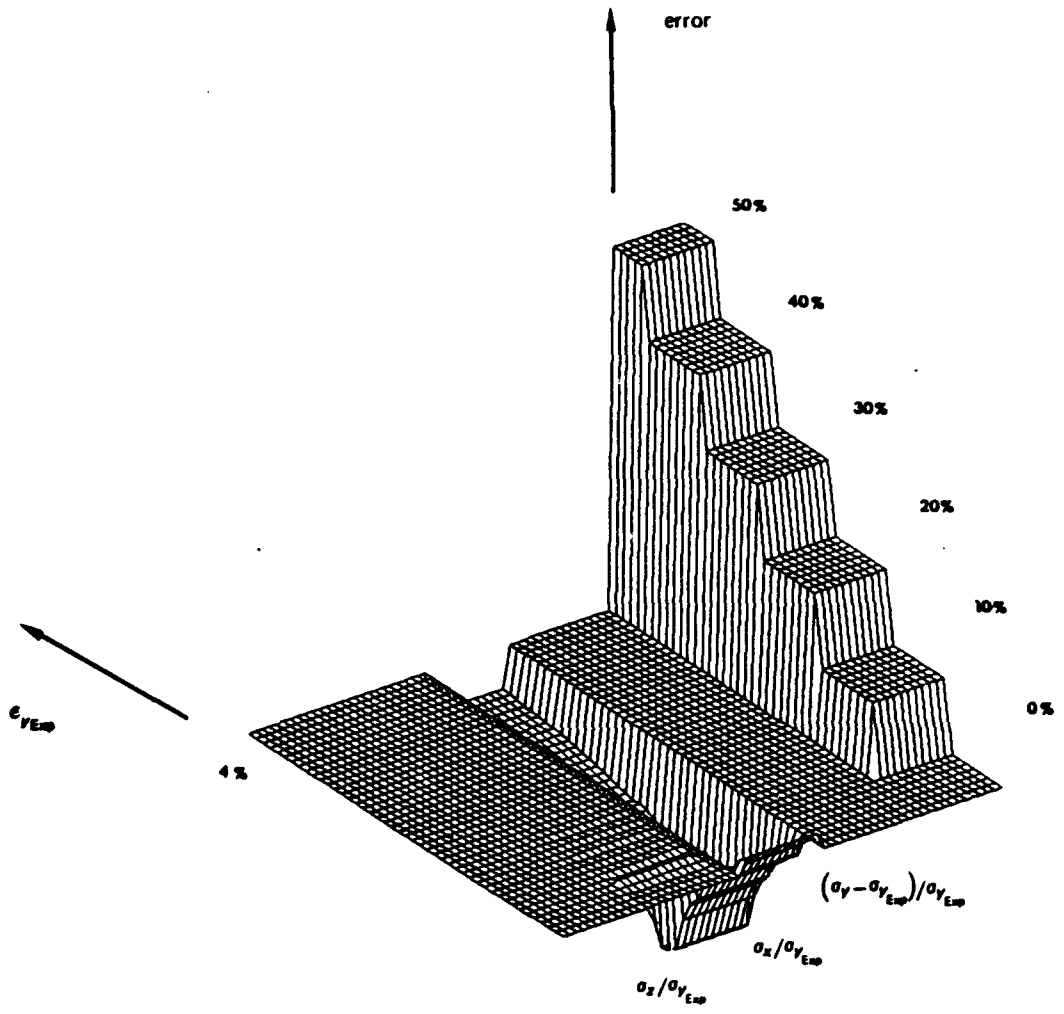

Figure 7.12 Normalized [(0/90)4]s Uniaxial Stress State Error
[(E_3 = 0.40xE6) (E_2 = E_2 exp)]
[(ν_{23} = ν_{23} exp) (ν_{21} = ν_{21} uniaxial)]

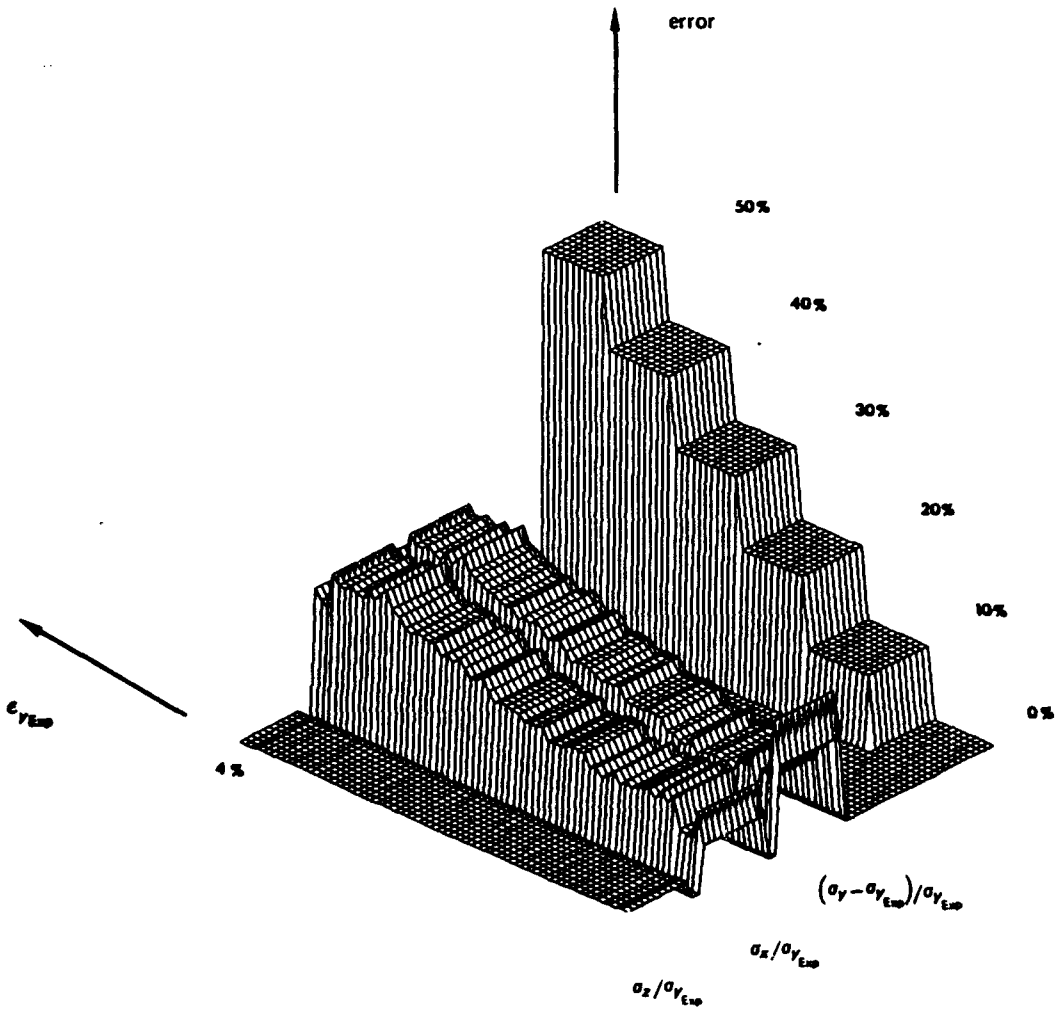

Figure 7.13 Normalized $[(+45/-45)_4]_s$ Uniaxial Stress State Error With Nonlinear Intralaminar Shear Behavior
[(E_3 = 0.40xE6) (E_1 = E_2 = $E_{2\ exp}$)]
[(ν_{23} = $\nu_{23\ exp}$) (ν_{21} = $\nu_{21\ uniaxial}$)]

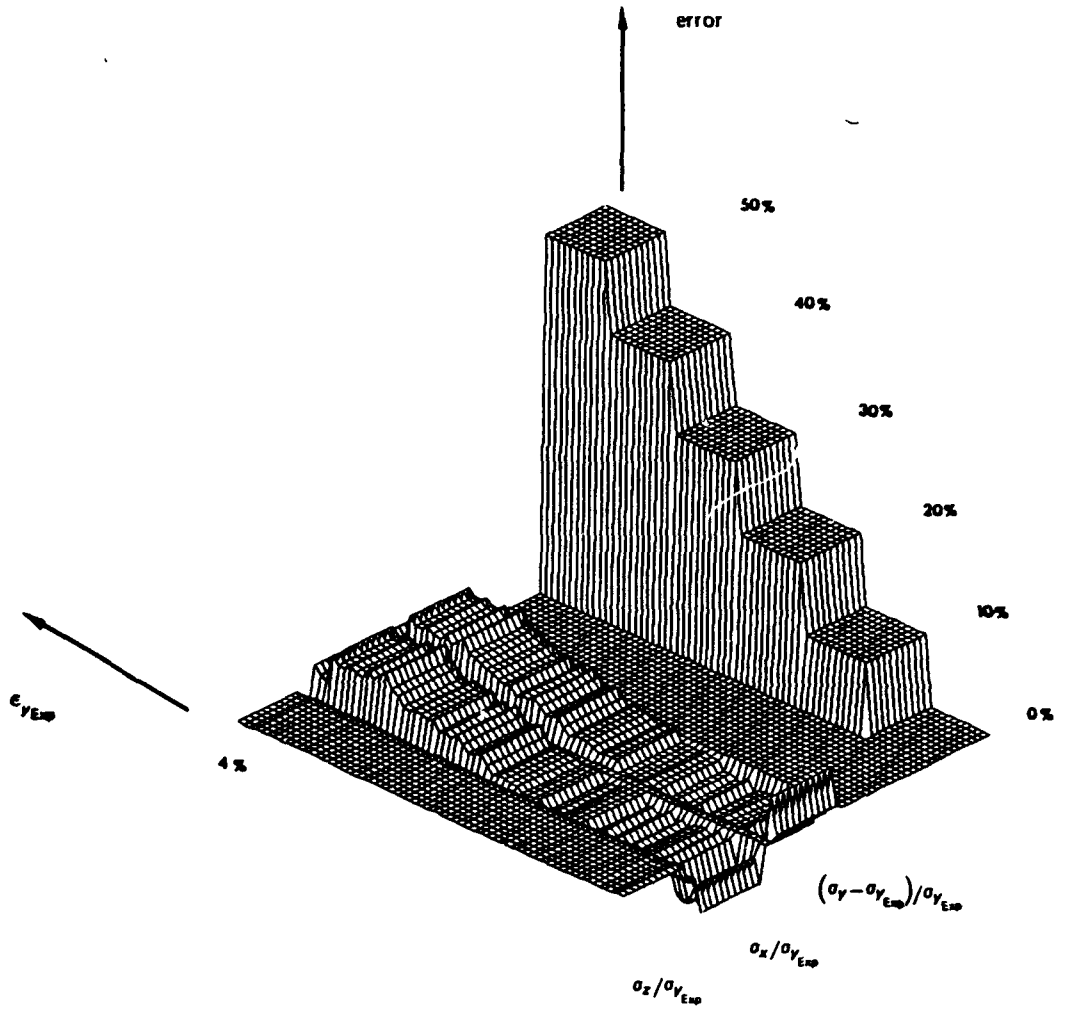

Figure 7.14 Normalized $[(+45/-45)_4]_s$ Uniaxial Stress State Error With Nonlinear Intralaminar Shear Behavior
[(E_3 = 0.40xE6) (E_1 = E_2 = 0.8$E_{2\ exp}$)]
[(ν_{23} = $\nu_{23\ exp}$) (ν_{21} = $\nu_{21\ uniaxial}$)]

CHAPTER 8. CONSTITUTIVE EQUATION IMPLEMENTATION

Results of the through thickness mechanical property sensitivity analysis were used to select the constitutive equation constants for both laminate configurations. Implementation of constituitive equations in the finite element code ABAQUS was done by developing user material subroutines. Single and multiple element verification of these subroutines was undertaken. Performance of the $[(+45/-45)_3]_s$ laminate subroutine was investigated.

8.1 FINAL CONSTITUTIVE EQUATION CONSTANTS

Selection of the final constitutive equation constants were based on the outcome of the laminate through thickness property sensitivity analysis. In-plane laminate property variations, while being informative of their effects on uniaxial stress state prediction, were not included in this work due to the complexity of their implementation into the finite element computations.

From chapter seven, the constitutive equation modeling approach was experimentally shown to be sensitive to E_3 and ν_{23} for the $[(+45/-45)_2]_s$ laminate but not for the $[(0/90)_4]_s$. It was shown that use of the experimental $[(0/90)_4]_s$ ν_{23} value obtained from displacement clip gage testing *precludes* the use of a lower E_3 value for $[(+45/-45)_4]_s$ uniaxial stress state error reduction. While the experimental value of ν_{23} was questionable due to measurement methodology, its value is in strong agreement with the 0.413 value predicted by Herakovich[7] for $[(0/90)]_s$ graphite epoxy laminates. For this reason, the experimentally obtained $[(0/90)_4]_s$ ν_{23} value was used in conjunction with an E_3 of pure SP250 resin.

Table 8.1 shows the final value of the laminate constitutive equation constants resulting from the E_3 and ν_{23} values and equations (7.7) and (7.10).

Table 8.1 Final 3D Laminate Constitutive Equation Constants (psi x 10E+6)

STACKING SEQ	C_{11}	C_{12}	C_{13}	C_{22}	C_{23}	C_{33}	C_{44}	C_{55}	C_{66}
$[(0/90)_3,\bar{0}]_s$	4.28	0.78	0.20	4.66	0.20	0.42	0.52	0.52	0.82
$[(0/90)_3]_s$	4.46	0.66	0.20	4.46	0.20	0.42	0.52	0.52	0.82
STACKING SEQ.	C^*_{11}	C^*_{12}	C^*_{13}	C^*_{22}	C^*_{23}	C^*_{33}	C^*_{44}	C^*_{55}	C^*_{66}
$[(+45/-45)_3]_s$	3.67	2.12	0.37	3.67	0.37	0.45	0.42	0.42	1.90

E_3 = 4.00E+5

8.2 ABAQUS User MAterial Subroutine Description

The constitutive equations for both laminates were implemented in the ABAQUS finite element code through the use of User Material Subroutines (UMAT). The subroutines are based on the iterative Newton-Raphson formulation that is shown in Figure 8.1. For nonlinear elastic material behavior, the solution technique required the calculation of updated stresses ($Q_{e,i-1}$) and tangent moduli stiffnesses (k^1) from updated strains (q_i). These values were returned to the finite element code where equilibrium residuals (Q_i) were calculated and applied to the system of equations in the next iteration. Iteration continued until the resulting equilibrium residuals fell below a specified tolerance (ie. $Q_i \leq Q_{tol}$).

The ABAQUS UMAT subroutines were written to 1) update current strains, 2) calculate updated stresses based on updated strains and the present value constitutive matrix, and 3) form the Jacobian of the present value constitutive matrix. These three functions were performed for both laminate arrangements by using laminate constitutive equations (7.7) & (7.10), the final laminate constitutive equation constants of Table 8.1, and the nonlinear intralaminar shear stress strain least squares curve fit of equation (6.4) and curve fit constants of Table 6.2.

As can be seen in the $[(0/90)_3]_s$ laminate constitutive equation

(7.7), the nonlinear intralaminar shear stress response was uncoupled from all other laminate stress components. Thus, updated linear elastic stresses were found directly from the normal and transverse shear constitutive constants while the updated nonlinear elastic intralaminar shear stress was found directly from its least squares curve fit representation and intralaminar shear strain. In direct contrast to this, the material axes transformation of the $[(+45/-45)_3]_s$ laminate embedded the nonlinear intralaminar shear response into normal laminate stress components. In this instance, updated $[(+45/-45)_3]_s$ stresses were found by using an appropriate secant intralaminar shear stress modulus whose intralaminar shear strain was obtained from the transformation of in-plane $[(+45/-45)_3]_s$ strains as given by equation (7.11).

Calculation of the constitutive matrix Jacobian for both laminates was accomplished through differentiation of the intralaminar shear stress-strain least squares curve fit to obtain $\partial\tau_{xy}/\partial\gamma_{xy}$ or C_{66}. The uncoupled nature of the $[(0/90)_3]_s$ laminate normal and shear stresses produced a material nonlinearity that could be solved by a "classical" Newton-Raphson solution routine. However; from constitutive equation (7.10), we find that the $[(+45/-45)_3]_s$ laminates normal stress constitutive constants had a lower bound given by C_A, C_B, and C_C. By comparison of these values with the laminate's actual uniaxial tensile behavior from the ASTM D3518-76 tests, it was apparent that the $[(+45/-45)_3]_s$ laminate's material nonlinearity might not be solved by a classical Newton-Raphson solution routine. A check of subroutine accuracy and performance was thus warrented.

8.3 Subroutine Single Element Verification

Verification of both UMAT subroutines was accomplished by single element testing. A single C3D20 three dimensional ABAQUS element was bounded with appropriate displacement and pressure boundary conditions to produce a uniaxial tension stress state for the $[(+45/-45)_3]_s$ laminate UMAT and a pure intralaminar shear stress state for the $[(0/90)_3]_s$ laminate UMAT. ABAQUS finite element runs were made for each test case shown in Figure 8.2 in which full loading (20,000 psi uniaxial tension and 10 % shear strain) was accomplished in nine equal steps. A developer's suggested convergence

tolerance equal to 1.0E-03 of the absolute maximum reaction force of each load step was employed. Figures 8.3 and 8.4 illustrate a comparison of these finite element results with the experimentally obtained stress-strain response of the appropriate laminates. As can readily be seen, agreement was quite good thus ensuring the proper functionality of both UMAT subroutines.

8.4 Subroutine Single Element Performance Investigation

The performance of the $[(+45/-45)_3]_s$ UMAT subroutine was investigated due the constrained nature of its constitutive equations and departure from a true Newton-Raphson solution approach. The single element model was run for varying convergence tolerances ranging from 1.0E-03 to 1.0E-01 of the absolute maximum reaction forces. Figure 8.5 illustrates the stress strain results of these finite element runs while Table 8.2 shows the resulting cycles to convergence.

Table 8.2 Cycles to Convergence for $[(+45/-45)_3]_s$ UMAT Subroutine

SIGMA Y	CUMULATIVE CYCLES TO CONVERGENCE					
	PTOL	5*PTOL	10*PTOL	20*PTOL	50*PTOL	100*PTOL
2000	9	7	6	5	4	3
4000	8	6	5	4	3	2
6000	9	6	5	4	3	2
8000	9	6	5	4	3	2
10000	11	7	6	4	3	2
12000	13	8	6	5	3	2
14000	18	11	8	6	3	2
16000	29	17	12	8	4	2
18000	63	33	20	12	5	2
20000	85	51	37	20	8	2

As can be seen from Table 8.2, the number of cycles to convergence increased with increasing load level for a given convergence tolerance. Reduction of the convergence tolerance generally resulted in a decrease in cycles to convergence for all load levels with a stronger reduction at higher

load levels. Figure 8.5 illustrates the resulting stress strain response as a function of convergence tolerance. As can be seen, the error in the stress strain state increased with increasing convergence tolerance and load level.

8.5 Subroutine Multiple Element Verification

The effects of element orientation on UMAT subroutine calculations were investigated by performing a patch test. The single element test cases shown in Figure 8.2 were subdivided into two 37 element (C3D20 ABAQUS) layers whose total thickness was .0625". This total thickness is similar to the thickness that was used for the pin-loaded coupon finite element model. The same displacement and pressure boundary conditions of the single element test cases were placed upon the multi element mesh shown in Figure 8.6. A convergence tolerance of 1.0E-03 of the absolute maximum reaction forces was employed while total loading was broken down into nine load steps as before. Large displacement theory was used as in the previous single element cases.

Figure 8.7 shows the variation of these calculated and experimental inplane shear and uniaxial stress states for the highest load cases for both the $[(0/90)_3]_s$ and $[(+45/-45)_3]_s$ multi element test cases respectively. As can be seen, variations from experimental results are less than .3% throughout the entire model thus indicating an element orientation independence and proper UMAT subroutine results.

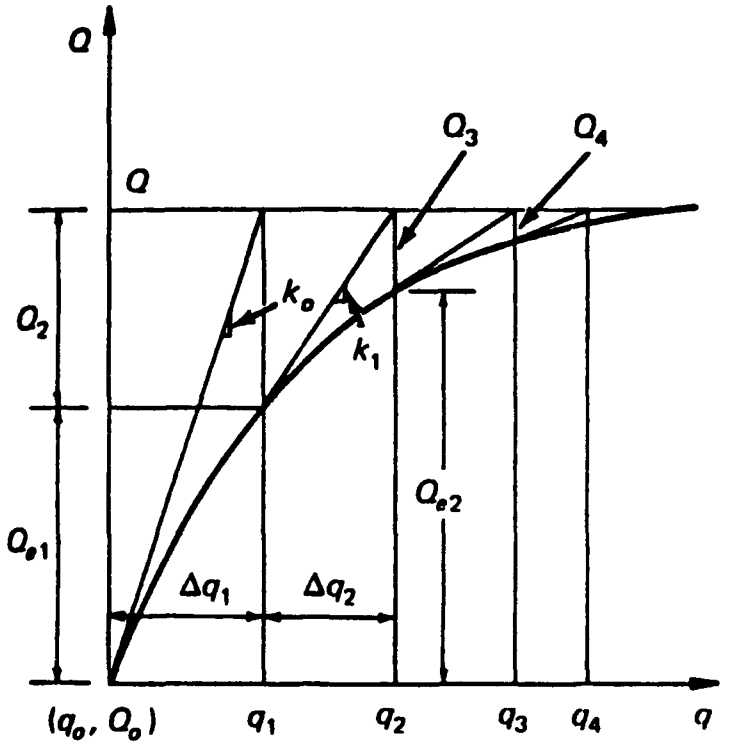

$$\{Q_i\} = \{Q\} - \{Q_{e,i-1}\}$$

$$[k^{(i)}]\{\Delta q_i\} = \{Q_i\}$$

$$\{q_i\} = \{q_o\} + \sum_{j=1}^{i} \{\Delta q_j\}$$

$$[k^{(i)}] = [k_{i-1}]$$

Figure 8.1 Newton Raphson Nonlinear Solution Technique

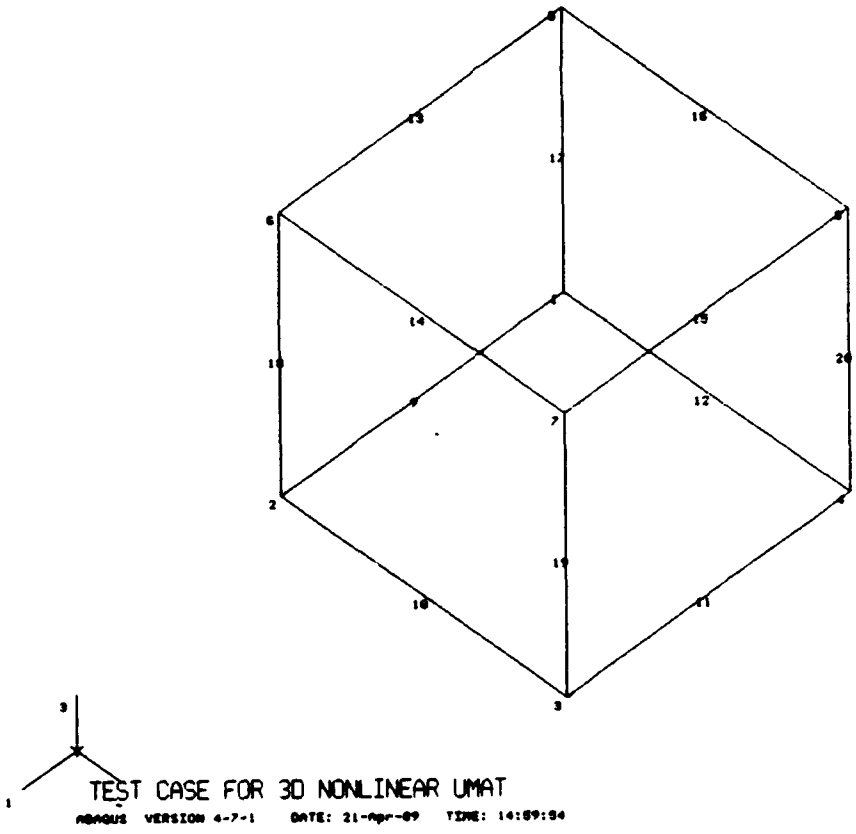

Figure 8.2 Single Element UMAT Subroutine Test Cases

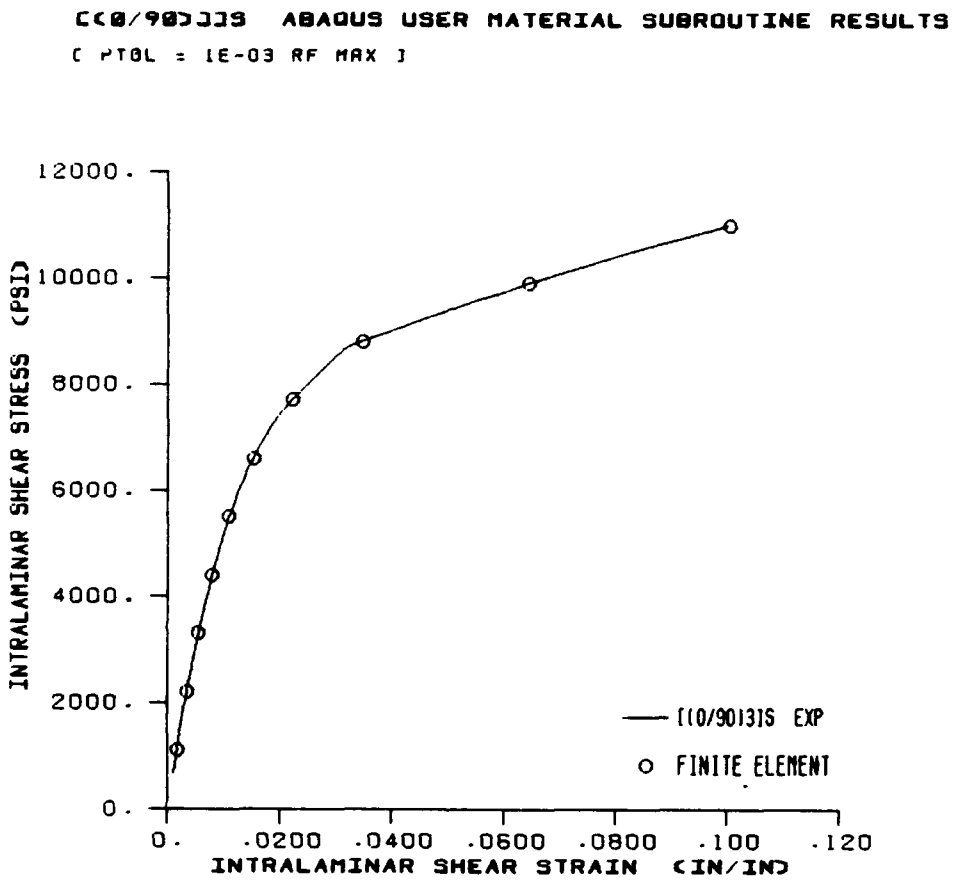

Figure 8.3 $[(0/90)_3]_s$ ABAQUS UMAT Subroutine Test Results

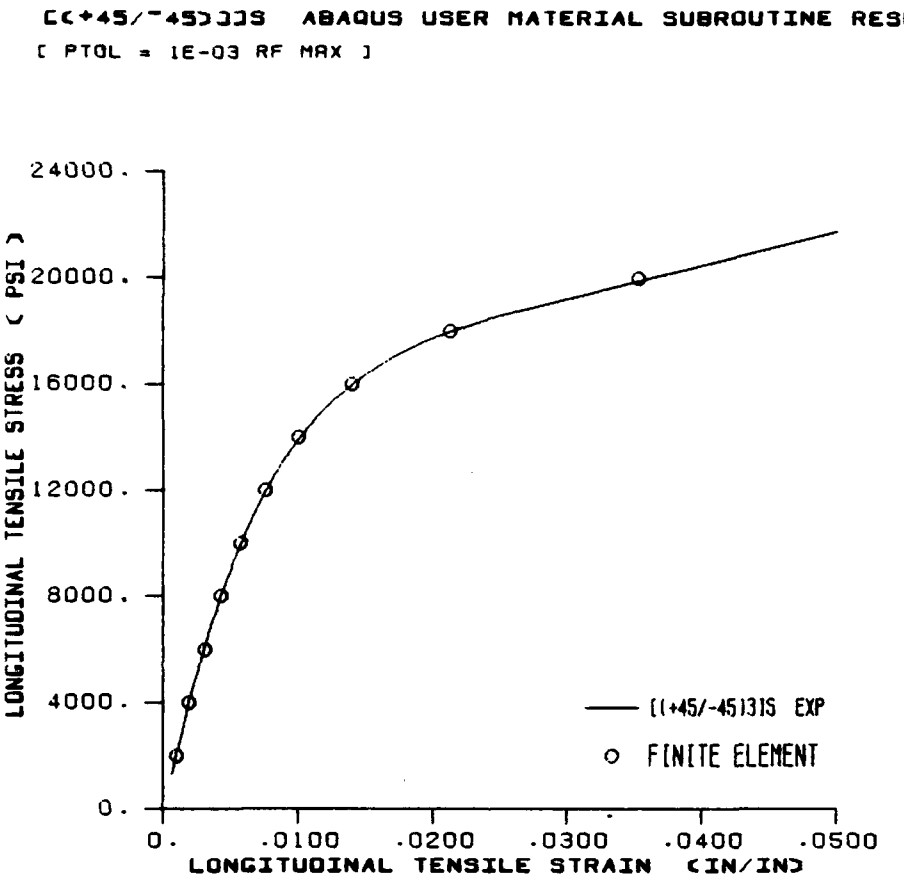

Figure 8.4 $[(+45/-45)_3]_s$ ABAQUS UMAT Subroutine Test Results

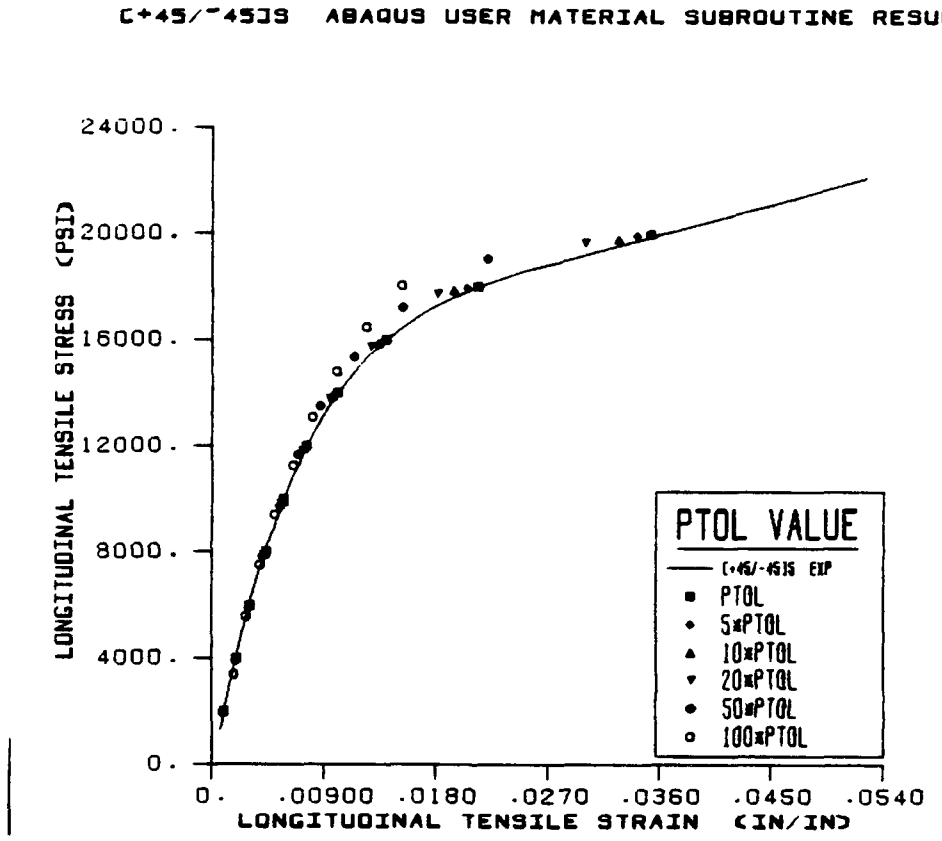

Figure 8.5 $[(+45/-45)_3]_s$ ABAQUS UMAT Subroutine Test Results as a Function of Convergence Tolerance

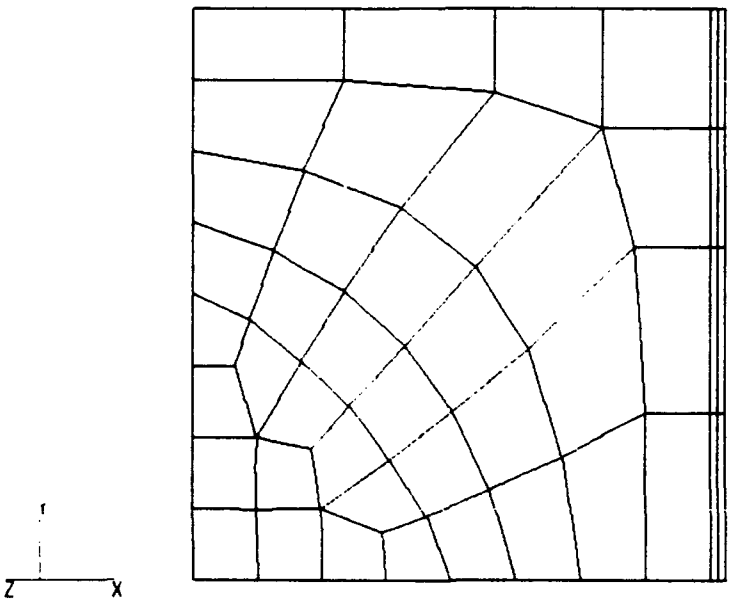

Figure 8.6 Multi Element UMAT Subroutine Test Case Mesh

Figure 8.7 Nonlinear Stress States for Full Load Multi Element UMAT Subroutine Test Cases

CHAPTER 9. FINITE ELEMENT MODELING

A three dimensional finite element modeling approach was taken due to the experimentally observed three dimensional behavior of the pin loaded coupons. Pin elasticity and pin/plate interactions were included within the model by a finite element representation of the pin and the use of gap contact elements between the two structures. Frictionless contact was assumed. Both linear elastic and nonlinear elastic finite element computations were made with the ABAQUS finite element code using the UMAT subroutines described in section seven.

Post processing of the finite element results was done to obtain net, bearing, and pin boundary sectional stresses (normalized to the maximum pin bearing stress) through the thickness of the coupon at the various load levels of the moire analysis. Total coupon front surface in-plane stresses and strains as well as out-of-plane displacements for the various load levels were obtained using the finite element post processing software PATRAN. Through thickness coupon stresses for the highest load case were also obtained. UNIX scripts were employed to automate all post processing activities.

9.1 Model Description

Four isoparametric element types from the ABAQUS element library were used in the finite element representation of the pin/coupon structure. Twenty noded C3D20 solid continuum brick elements were used to model the majority of the coupon and pin. Twenty-two noded C3D27 variable node solid continuum brick elements were employed for the inner and outer elements of the coupon and pin respectively. Fifteen noded C3D15 wedge elements were used for the inner most portion of the pin. Eighteen noded INTER9 gap interface elements were used to model the pin/coupon interaction. Figure 9.1 illustrates the

physical representation of all four of these elements.

Conventional continuum element formulations and theories govern all continuum element behavior while the Lagrange multiplier theory was used with the INTER9 elements to enforce contact between the pin and the coupon.[1] Contact between the pin and coupon occurs at a zero separation distance between respective nodes of the INTER9 elements. Tangential displacements of these nodes were permitted upon contact.

The three dimensional finite element mesh of the coupon was constructed using the two dimensional mesh of earlier efforts [68] that is shown in Figure 2.3-1. A Fortran program entitled MG3DV was written to project this mesh in the thickness direction. Program execution transformed the nodal listing and eight noded quad nodal connectivity listings of this mesh into the nodal listing and twenty noded brick connectivity listings of a two element, half thickness three dimensional representation of the coupon. Additional centroidal and midface nodes were added to the inner most ring of these coupon elements to form the necessary C3D27 variable noded elements that were connected to the INTER9 gap elements.

The three dimensional representation of the pin was constructed using the preprocessing module of PATRAN. Its diameter measures 0.124" thus leaving a 0.001" clearance between itself and the coupon. In a similar procedure as with the coupon, the outer most layer of pin elements (but first two in the axial z location) were edited to form the matching C3D27 variable noded elements for INTER9 gap elements. This pin was substructured using the superelement approach within ABAQUS to reduce computation time. Active pin degrees of freedom (those associated pin nodes that were common to the pin and gap interface elements) were retained while all others were condensed by a Guyan statical condensation technique [82]. However; this substructure was not used in finite element computations due to an associated error in the ABAQUS version being used.

Figures 9.2 and 9.3 illustrates the three dimensional discretization of the pin/coupon structure (less the C3D15 wedge elements that were not accepted in the ABAPAT translation of the model for PATRAN display). A total of 312 coupon elements, 216 pin elements, and 36 gap interface elements comprised this 564 element model.

The quarter symmetry model was bounded by constraining all nodes

along the Y axis from movements in the x direction, all nodes along the Z = 0 plane from movement in the z direction, and the pin tip (bottom side) from movement in the y direction. The constitutive equation constants of Table 8.1 were used for the material constants for the coupon while material properties of steel were used for the pin.

9.2 Finite Element Computations

The finite element computations were done with the ABAQUS finite element code. A series of six steps were used for the complete loading history of the model. The first step consisted of a 0.001" y direction rigid body translation of the coupon to place it in contact with the pin. The remaining five steps consisted of 300 lb incremental loadings of the coupon through appropriate σ_y boundary condition at its far end. A direct incrementation approach was employed with a single increment being used for the coupon rigid body translation. Load steps two and three used ten increments apiece while all remaining load steps used sixteen increments. Convergence tolerances were selected as to approach the developer's suggested 1.0E-03 of the maximum coupon reaction force.

ABAQUS restart results files were written at the midpoint and end of each step (ie 150 lb loading increments). Maximum coupon reaction forces were obtained from the restart files to insure the fulfillment of convergence requirements prior to continuation of latter modeling steps. Linear elastic approximations were made for both laminate orientations with the constitutive equation constants of Table 8.1 while nonlinear elastic approximations were made with the appropriate UMAT subroutine described in section seven. Large displacement theory was employed for the nonlinear elastic approximations.

9.3 Post Processing of Finite Element Results

Finite element results were obtained at each load level from the post processing of each restart results file. A UNIX script entitled POSTPR as well as several other fortran programs were written to accomplish this.

Figure 9.4 illustrates a flow chart of the script. As can be seen, three separate ABAQUS post processing runs (POSTNBP, POSTPBI, and POSTPIN) were done to create the necessary *.FIL files that contained nodal stresses, strains, and displacements. Net, bearing, and far field coupon data was generated in POSTNBP while pin boundary radial stress nodal data was generated in POSTPBI. Top surface pin nodal displacement data was produced from POSTPIN.

The nodal data contained in each *.FIL file was then sorted and averaged at the nodes for the various sections (ie bearing, net, far field, and pin top) by a series of fortran programs. Actual and pin bearing stresses (normalized to maximum pin bearing load S) along with strain values and displacements were obtained through the thickness of the coupon and placed into the proper format for the xy plotting routine of PATRAN PPLOT by programs NBPSECT, PBSECTC, PBSECTI, and PINSECTP.

Total coupon stress, strains, and displacements were nodal averaged and placed in proper format for PATRAN post processing software through a fortran translator program entitled STABAPAT. The translator was written to operate on the *.FIL files (generated from the ABAQUS post processing runs) to create smaller PATRAN nodal data files in liu of larger files obtained from the commercially available ABAPAT translator.

Display of coupon stresses and strains were done using the aforementioned PATRAN nodal data files and the post processing package PATRAN. PATRAN session files were written to display these results throughout the load history of each laminated coupon for both the linear and nonlinear elastic finite element analysis. Execution of PATRAN and these session files were in turn controlled by various UNIX scripts for file manipulation and hardcopy printing within the Computational Mechanics local area network.

9.4 Finite Element Results

Results obtained from post processing of finite element restart results files are presented in the following section. A presentation format to illustrate the effects of nonlinear material behavior and through thickness variations upon pertinent coupon stresses throughout the loading history was selected.

Figures 9.5 through 9.16 illustrate net, bearing, and pin boundary normalized sectional stresses for all major load levels of the $[(0/90)_3,0]_s$ linear and nonlinear elastic analyses. Both mid and front surface coupon locations (ie. Z = 0.0000" and Z = 0.0625") are shown. Figures 9.17 through 9.28 illustrate similar results for the $[(+45/-45)_3]_s$ analysis.

Intralaminar shear stresses and strains are depicted in Figures 9.29 through 9.38 for all major load levels of the $[(0/90)_3,0]_s$ linear and nonlinear elastic analysis. Normal Y stresses and strains are shown in Figures 9.39 through 9.48 for all major load levels of the $[(+45/-45)_3]_s$ linear and nonlinear elastic analysis. Out-of plane displacements of the nonlinear analysis of both laminate orientation are presented for all major load levels in Figures 9.49 through 9.53. Through thickness stresses on the front surface of each coupon element layer are shown in Figures 9.54 and 9.55 for both laminate orientations of the linear and nonlinear elastic analysis.

The $[(0/90)_3,0]_s$ nonlinear intralaminar shear modulus is shown as a function of load level in Figures 9.56 through 9.60. Pertinent $[(+45/-45)_3]_s$ nonlinear normal constitutive constants are shown as a function of load level in Figures 9.61 through 9.65.

Top surface pin displacements as a function of load level are shown for both the linear and nonlinear elastic analysis of both laminate orientations in Figures 9.66 through 9.69.

Tables A.1 through A.4 of the appendix list the historical computational aspects of the linear and nonlinear $[(0/90)_3,0]_s$ and $[(+45/-45)_3]_s$ analysis.

9.5 Modeling Observations

9.5.1 $[(0/90)_3,\bar{0}]_s$ Laminate Configuration

Both pin bearing load normalized net and bearing $[(0/90)_3,0]_s$ sectional stresses were slightly higher for the nonlinear elastic analysis than for the linear elastic analysis. This variation was more predominant at higher pin load levels. Both linear and nonlinear elastic pin bearing load normalized $[(0/90)_3,0]_s$ radial stresses (as determined from the gap interface

elements) departed from the often assumed $4\pi\cos\theta$ distribution. This was in part due to the formation of the contact angle which was created by the initial 0.001" clearance between the pin and the coupon. The contact angle had an initial angle of 55° and was seen to grow with progressive loading as the $[(0/90)_3,0]_s$ coupon was wrapped around the pin. A maximum contact angle of 74° was seen to form at the highest load level. This partial contact resulted from a net section Poisson contraction affect. The nonlinear elastic intralaminar shear material assumption caused a significant redistribution of the $[(0/90)_3,0]_s$ radial stresses. These stresses were reduced at an angular location that coincides with the location of maximum coupon intralaminar shear stress and were increased elsewhere within the contact region. This redistribution effect was increasingly seen with progressive loading. A reduction in contact angle was also seen for the nonlinear material assumptions at the Z = 0.0000" nodal plane yet not at the Z = 0.0625 " nodal plane. An increase in the $[(0/90)_3,0]_s$ circumferential stress (as determined from the inner most ring of coupon elements) was observed from the nonlinear elastic material assumption.

The simply supported pin condition was found to cause a small through thickness variation in almost all sectional stresses for both the linear and nonlinear elastic $[(0/90)_3,0]_s$ analysis. Front surface linear and nonlinear elastic coupon net and bearing sectional stresses appeared to be slightly larger than their midsurface counterparts due to the nature of the pin deflection and resulting load transfer. Linear elastic coupon radial stresses also followed this trend while nonlinear elastic $[(0/90)_3,0]_s$ radial stresses were found to be slightly higher and slightly lower in front of and behind the angular location of maximum intralaminar shear stress respectively. Both linear and nonlinear elastic $[(0/90)_3,0]_s$ coupon front surface circumferential stresses appeared to be slightly higher and lower in front of and behind the angular location of maximum intralaminar shear stress respectively than their midsurface counterparts.

The effects of the nonlinear elastic material behavior were quite evident when viewing the $[(0/90)_3,0]_s$ coupon intralaminar shear stress / shear strain results. Progressively higher intralaminar shear strains were observed along the locus of maximum intralaminar shear strain within the coupon for the nonlinear elastic analysis in comparison to the linear elastic analysis. This

variation increased with increasing pin load level with a more than a two fold increase at the highest pin load level. In a similar fashion, progressively higher linear elastic intralaminar shear stresses were observed along the locus than their nonlinear elastic counterparts. This variation also increased with pin load level with almost a three fold increase at the highest pin load level. Review of the intralaminar shear modulus along this locus and throughout the coupon revealed significant reductions (50%) at even the lowest of pin load levels. More than a ten fold intralaminar shear modulus reduction was observed at the highest of pin load levels. These results are not surprising given the observed highly nonlinear intralaminar shear stress strain behavior.

Through thickness stresses appear to be negligible in comparison to in plane stress magnitudes for the $[(0/90)_3,0]_s$ laminate. The highest of these values appeared closer to the midsurface of the coupon. The nonlinear elastic intralaminar shear stress-strain assumption acted to increase through thickness stresses slightly.

Out-of-plane deformations for the nonlinear elastic analysis appeared to be considerably lower than those obtained from the projection moire study. These variations indicated the presence of a severe through thickness matrix material nonlinearity or failure. However; the deformations appeared to agree in a qualitative sense in their similar shapes. The effects of the crossply laminate orientation was seen in the oblong shape of the front surface deformation patterns.

9.5.2 $[(+45/-45)_3]_s$ Laminate Configuration

Pin bearing load normalized $[(+45/-45)_3]_s$ net section stresses showed a reduction for the nonlinear elastic material analysis in comparison to the linear elastic analysis. However; maximum net section stresses in the vicinity of the pin appeared to be unchanged. This yielding phenomenon becomes increasingly apparent with higher pin load levels. Normalized bearing stresses appeared to be lowered significantly for the nonlinear elastic analysis in comparison to the linear elastic analysis. An outward shift along the bearing section of this maximum value was observed. As with the net

section stresses, these effects became increasingly apparent with higher pin load levels.

Both the linear and nonlinear elastic normalized $[(+45/-45)_3]_s$ radial stresses departed from the often assumed $4\pi\cos\theta$ radial pressure distribution. As with the $[(0/90)_3,0]_s$ laminate, contact angles less than 90° were obtained.. These contact angles grew with progressive pin load level as the coupon wrapped itself around the pin until a maximum of 80° was observed. The nonlinear elastic material behavior redistributed the radial stress by significantly lowering its value near the pin bearing section and increasing it for the remainder of the contact angle. Somewhat higher contact angles were observed with nonlinear elastic material assumptions as compared to linear elastic assumptions. An increase in circumferential coupon stresses (as calculated from the inner most ring of coupon elements) was noticed for the nonlinear elastic material assumptions in comparison with the linear elastic analysis. All of these effects increased with increasing pin load level.

Both linear and nonlinear elastic net, bearing, and circumferential $[(+45/-45)_3]_s$ normalized sectional stresses appeared to be unaltered by the simply supported boundary condition of the pin. However; front surface radial stresses appeared to be slightly higher than their midsurface counterparts. The redistribution of these radial stresses for nonlinear elastic material assumptions was shown to be greater for front surface coupon location than for the midsurface.

Progressively higher nonlinear elastic ε_y coupon strain values were seen in and around the net and bearing regions of the $[(+45/-45)_3]_s$ laminate than for the linear elastic analysis. The largest variations between the two analyses were observed closest to the pin. This ductile behavior, although almost unnoticeable at lower pin load levels, becomes more apparent at higher pin load levels. As much as a two and three fold increase in bearing and net section ε_y strains were respectively observed. Corresponding σ_y stresses appeared to follow suit with linear elastic stresses being higher than those of the nonlinear elastic analysis. However; appreciably smaller increases in bearing section σ_y stresses were observed than net section stresses for the linear elastic analysis in comparison to the nonlinear elastic analysis. Review of the C_{11} and C_{22} angleply constitutive equation constants throughout

the coupon revealed significant reductions in the bearing section and along the fiber directions in the net section even at the lowest pin load level. These zones of "softened" material behavior grew with increasing pin load level yet were bounded by the constitutive equations of equation 7.10 and the values in Table 8.1.

As in the case of the $[(0/90)_{3},0]_{s}$ laminate, through thickness $[(+45/-45)_{3}]_{s}$ stresses appear to be negligible in comparison to in plane stress magnitudes. The highest of these values appeared closer to the midsurface of the coupon. The nonlinear elastic material assumptions acted to increase through thickness stresses slightly.

As in the case of the $[(0/90)_{3},0]_{s}$ laminate, out-of-plane deformations for the nonlinear elastic analysis appeared to be considerable lower then those obtained from the projection moire study. These variations indicated the presence of a severe through thickness matrix material nonlinearity or failure. However; the deformations appeared to agree in a qualitative sense in their similar shapes. The effects of the angleply laminate orientation was seen in the "butterfly" shape of the front surface deformation patterns.

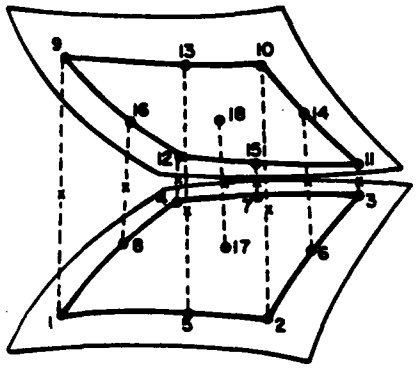

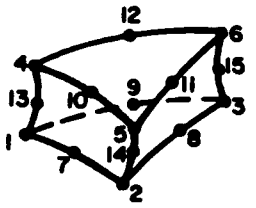

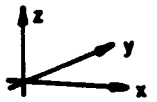

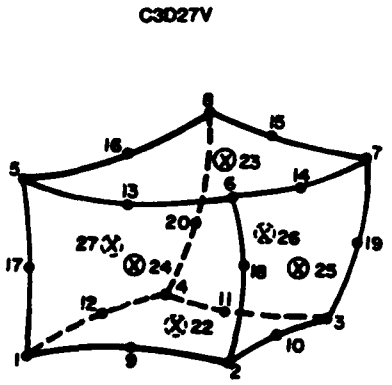

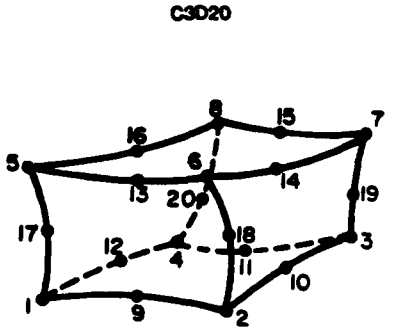

Figure 9.1 Physical ABAQUS Element Representations Employed in Pin/Coupon Finite Element Modeling Efforts

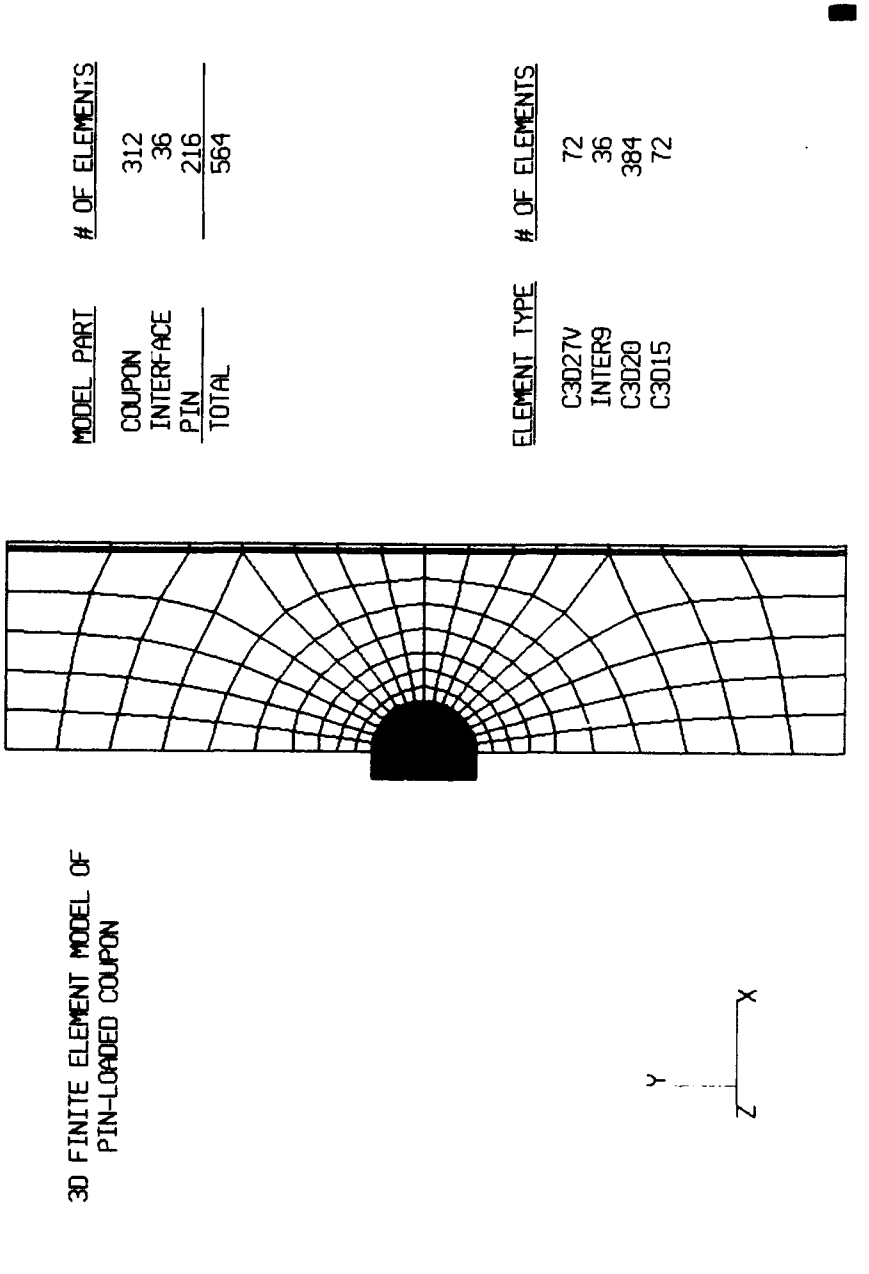

Figure 9.2 Three Dimensional Finite Element Discretization of Pin/Coupon Structure

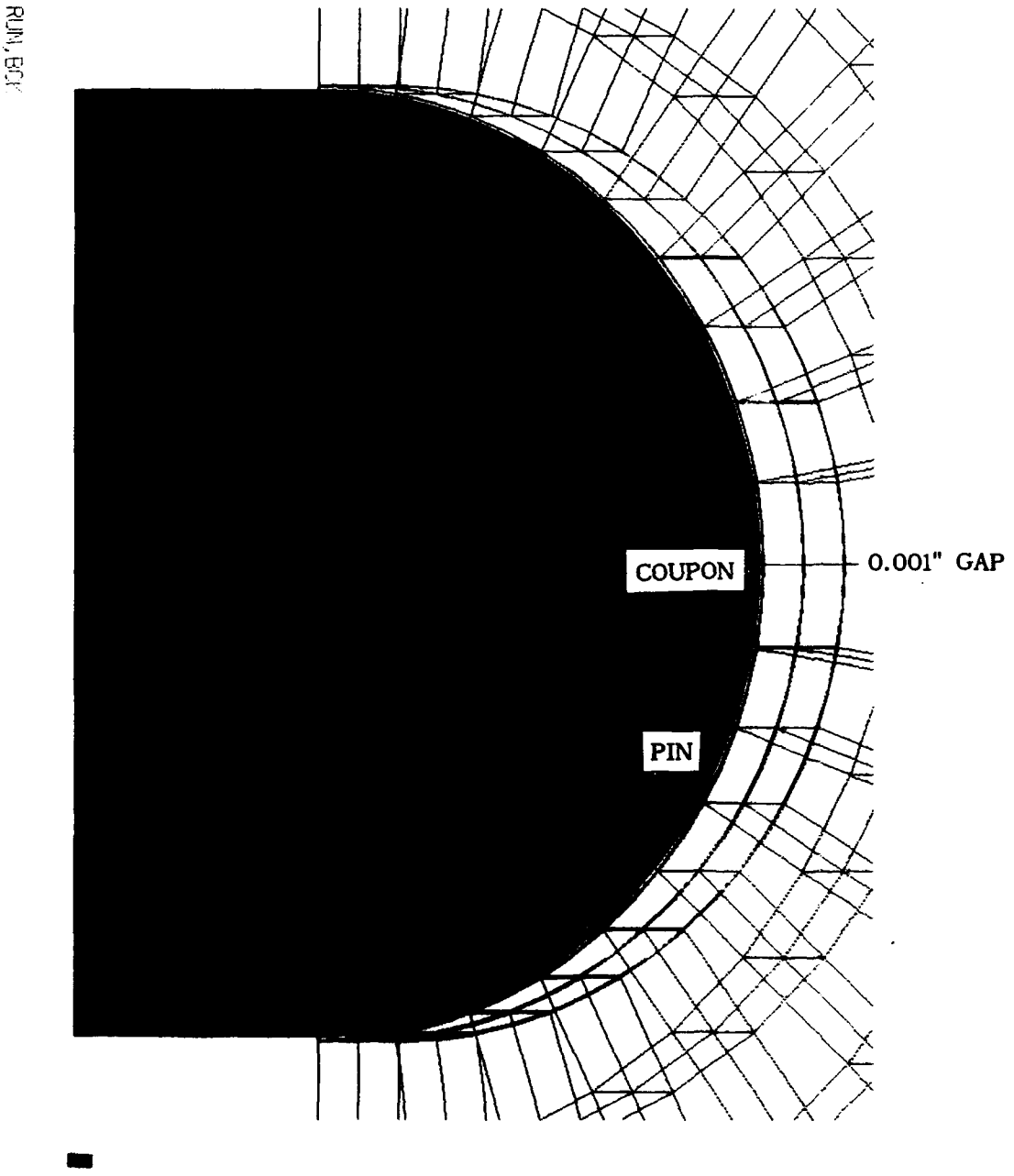

Figure 9.3 Finite Element Descretization of Pin/Coupon Interface

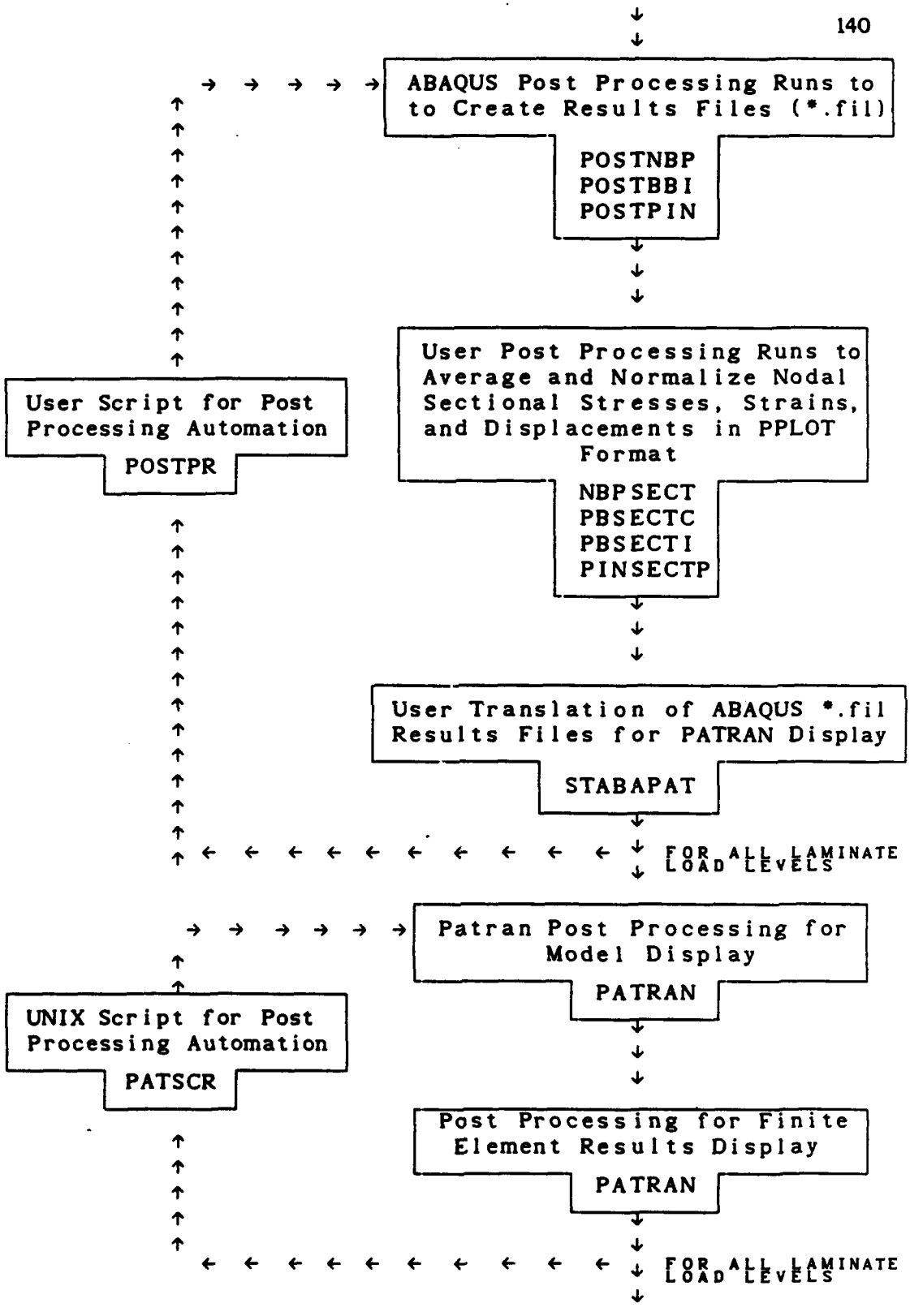

Figure 9.4 Finite Element Post Processing Flow Chart

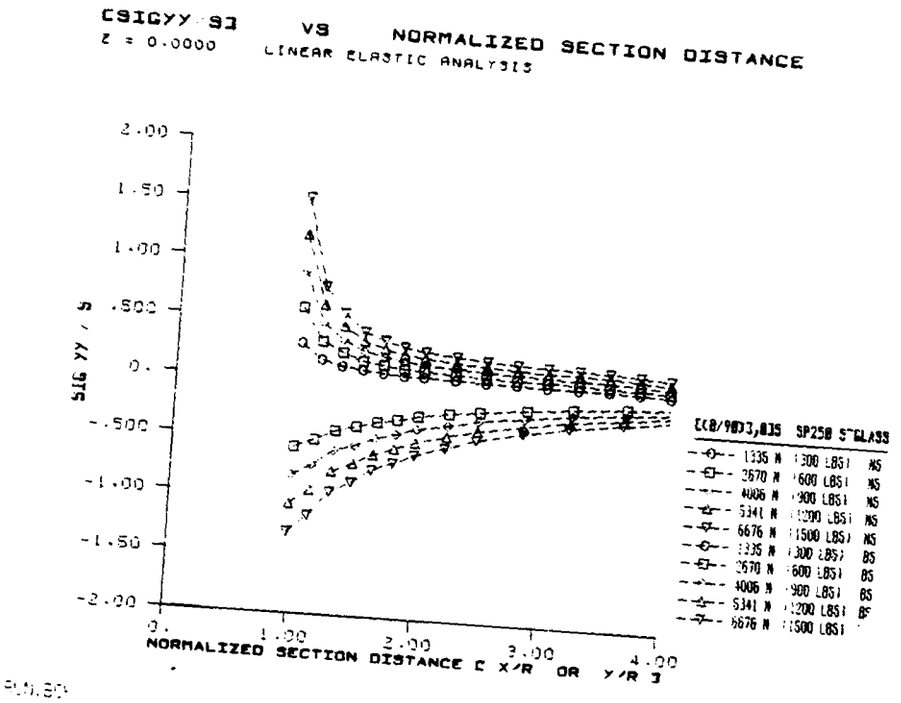

Figure 9.5 $[(0/90)_3,0]_s$ Normalized Bearing and Net Section Linear Elastic σ_y vs. Normalized Section Distance as a Function of Load Level [Z = 0.0000]

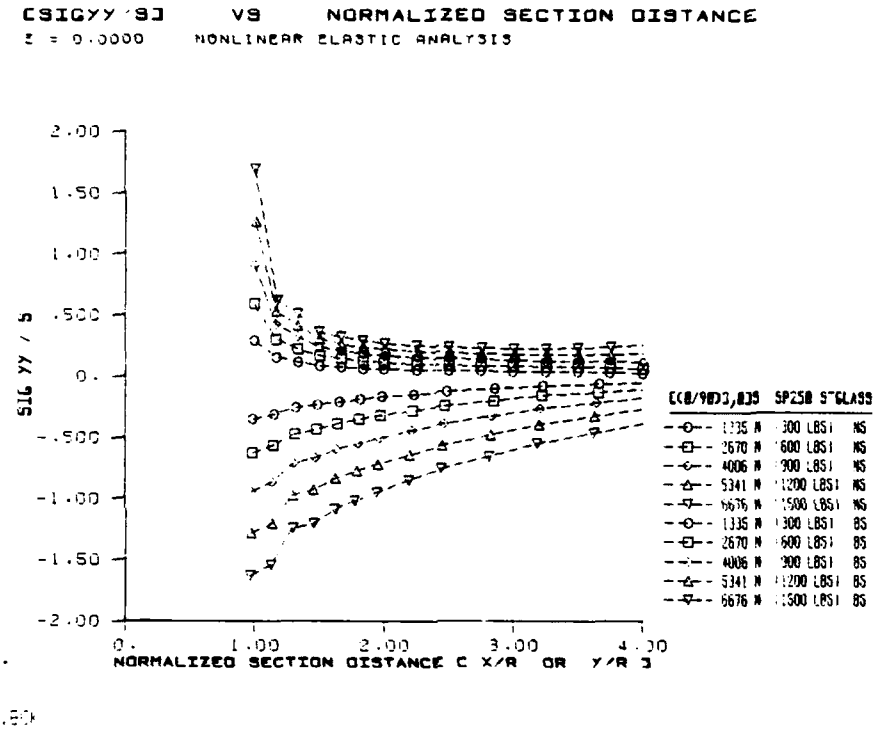

Figure 9.6 $[(0/90)_3,0]_S$ Normalized Bearing and Net Section Nonlinear Elastic σ_y vs. Normalized Section Distance as a Function of Load Level [Z = 0.0000]

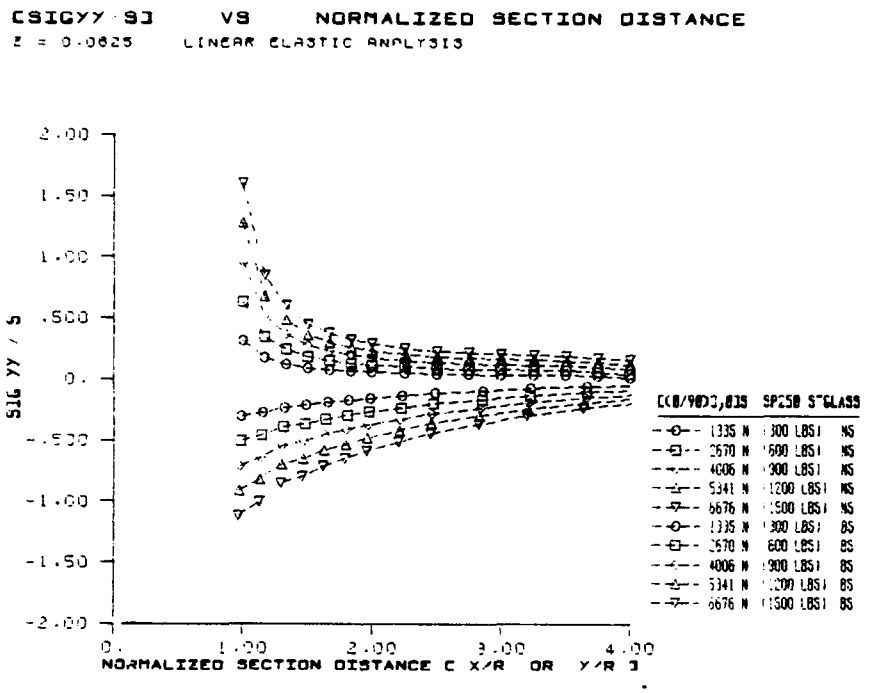

Figure 9.7 $[(0/90)_3,0]_s$ Normalized Bearing and Net Section Linear Elastic σ_y vs. Normalized Section Distance as a Function Load of Level [Z = 0.0625]

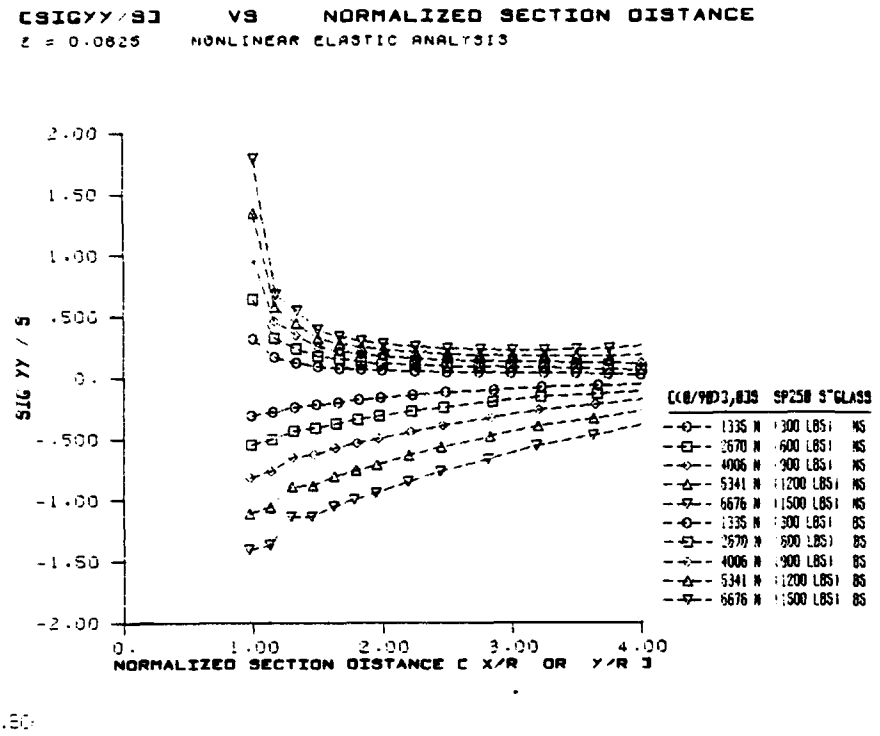

Figure 9.8 $[(0/90)_3,0]_s$ Normalized Bearing and Net Section Nonlinear Elastic σ_y vs. Normalized Section Distance as a Function of Load Level [Z = 0.0625]

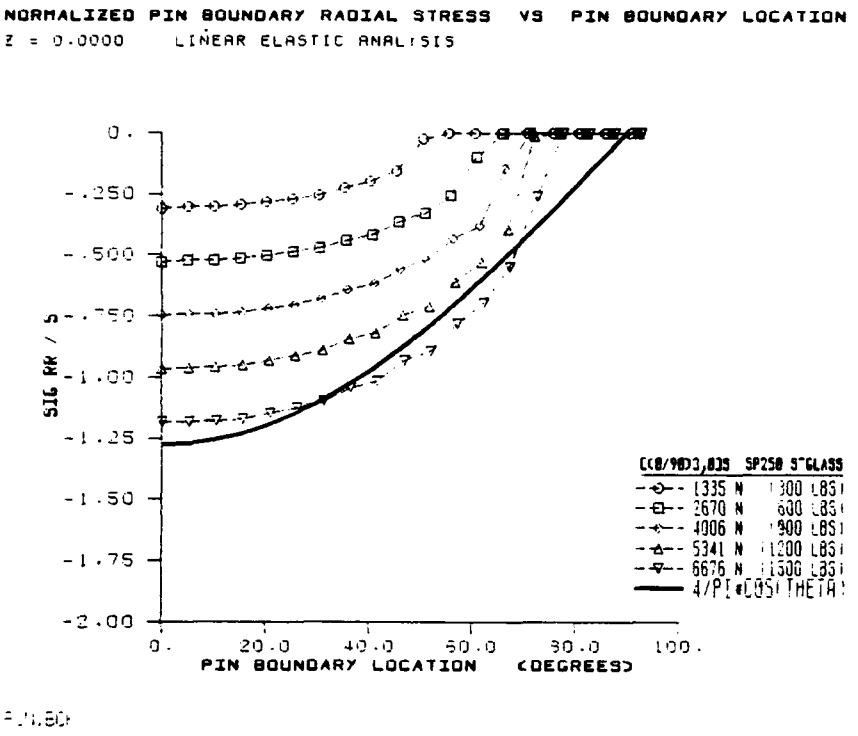

Figure 9.9 $[(0/90)_3,0]_S$ Normalized Pin Boundary Linear Elastic σ_r vs. Pin Boundary Location as a Function of Load Level [Z = 0.0000]

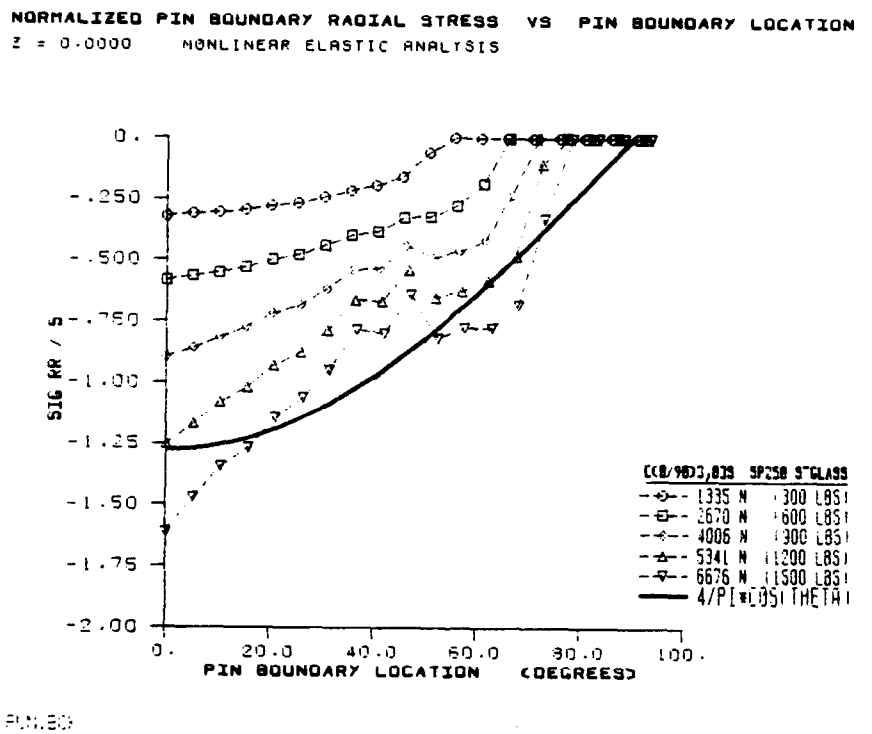

Figure 9.10 $[(0/90)_{3},0]_{S}$ Normalized Pin Boundary Nonlinear Elastic σ_r vs. Pin Boundary Location as a Function of Load Level [Z = 0.0000]

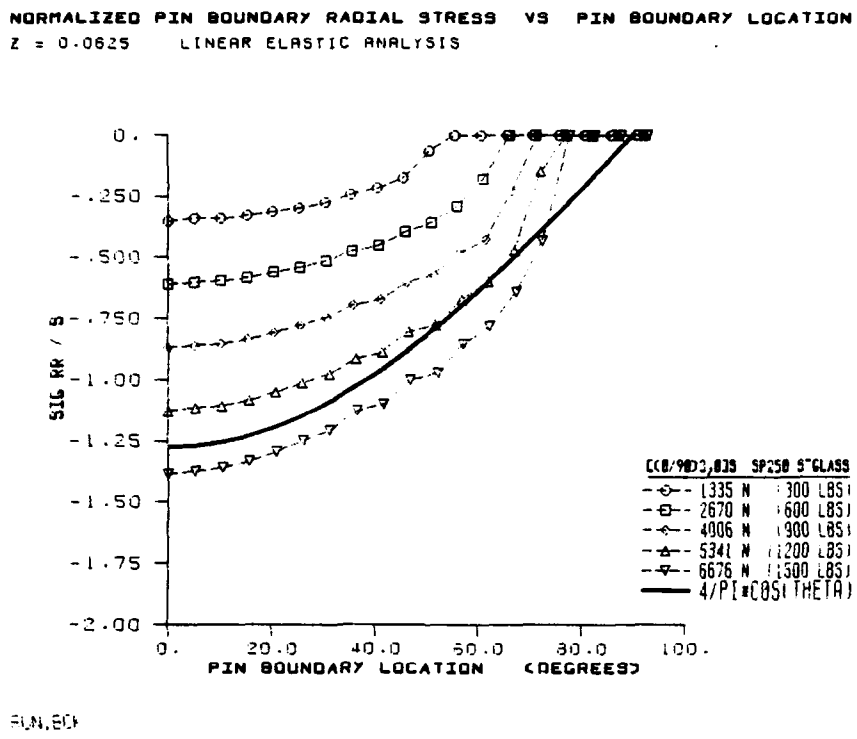

Figure 9.11 $[(0/90)_3,0]_s$ Normalized Pin Boundary Linear Elastic σ_r vs. Pin Boundary Location as a Function of Load Level [Z = 0.0625]

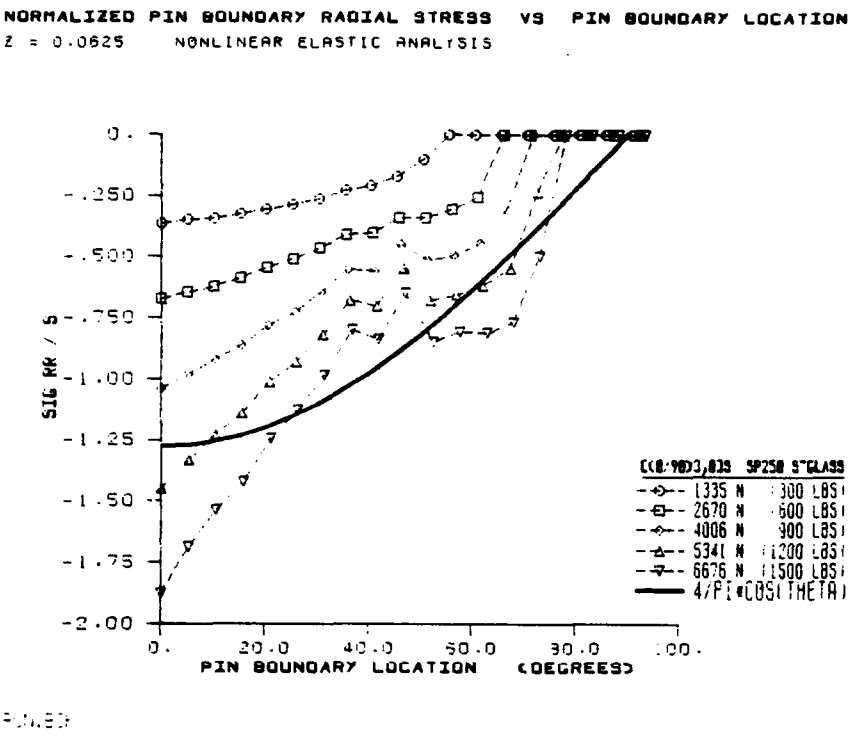

Figure 9.12 $[(0/90)_3,0]_s$ Normalized Pin Boundary Nonlinear Elastic σ_r vs. Pin Boundary Location as a Function of Load Level [Z = 0.0625]

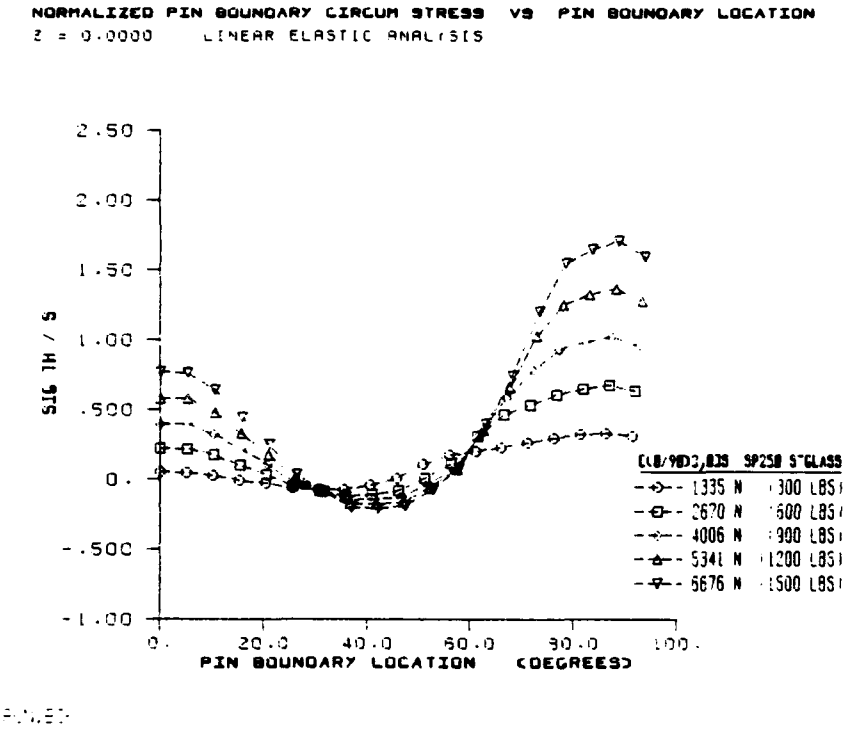

Figure 9.13 $[(0/90)_3,0]_s$ Normalized Pin Boundary Linear Elastic Circumferential Stress vs. Pin Boundary Location as a Function of Load Level [Z = 0.0000]

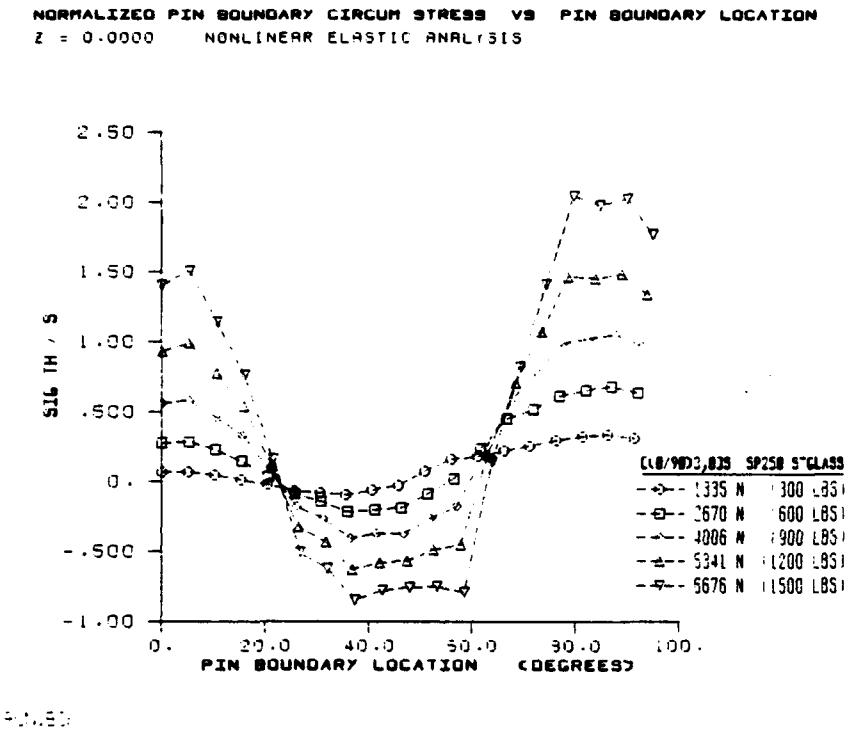

Figure 9.14 $[(0/90)_{3},0]_s$ Normalized Pin Boundary Nonlinear Elastic Circumferential Stress vs. Pin Boundary Location as a a Function of Load Level [Z = 0.0000]

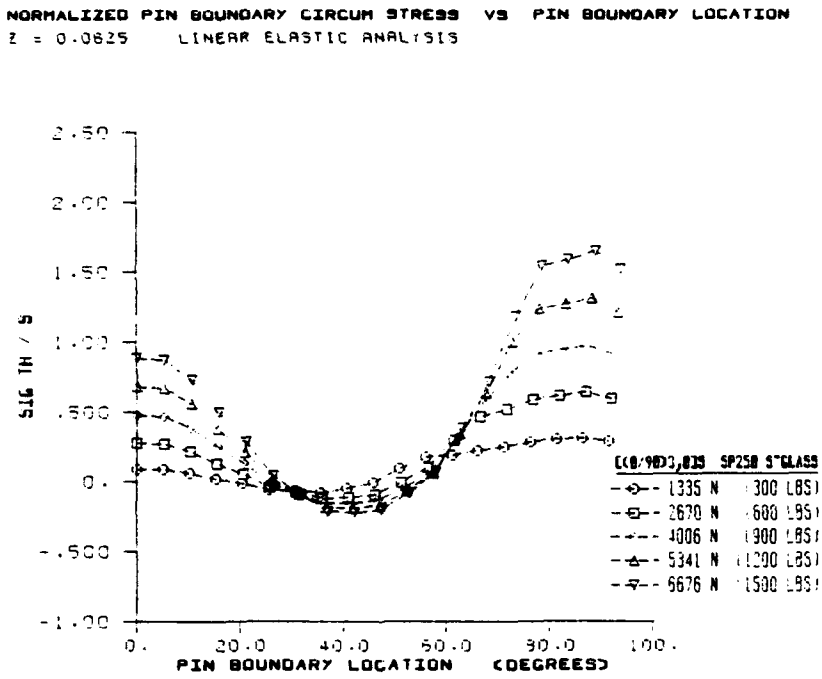

Figure 9.15 $[(0/90)_3,0]_s$ Normalized Pin Boundary Linear Elastic Circumferential Stress vs. Pin Boundary Location as a Function of Load Level [Z = 0.0625]

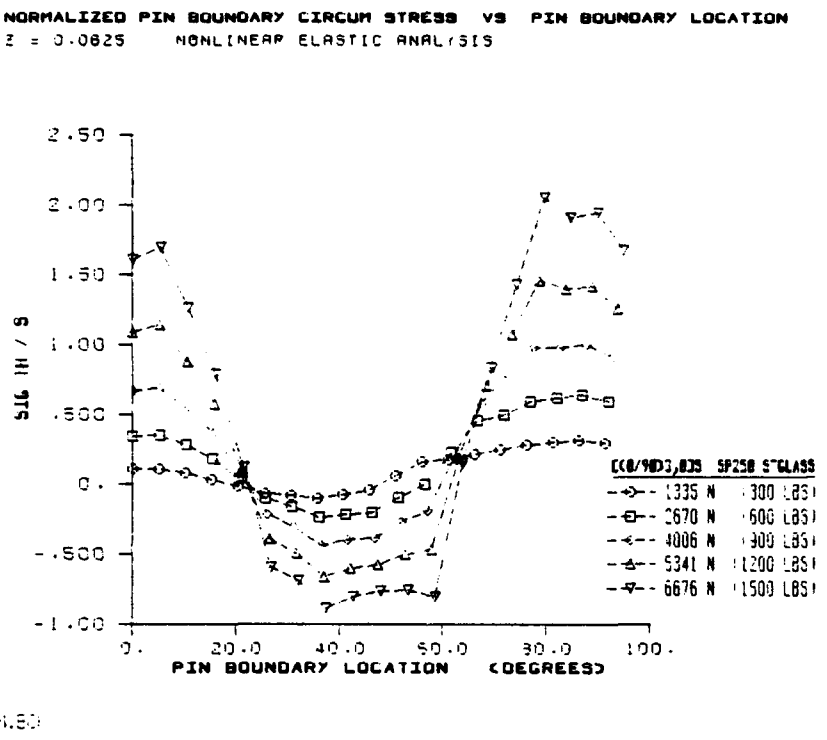

Figure 9.16 $[(0/90)_3,0]_s$ Normalized Pin Boundary Nonlinear Elastic Circumferential Stress vs. Pin Boundary Location as a Function of Load Level [Z = 0.0625]

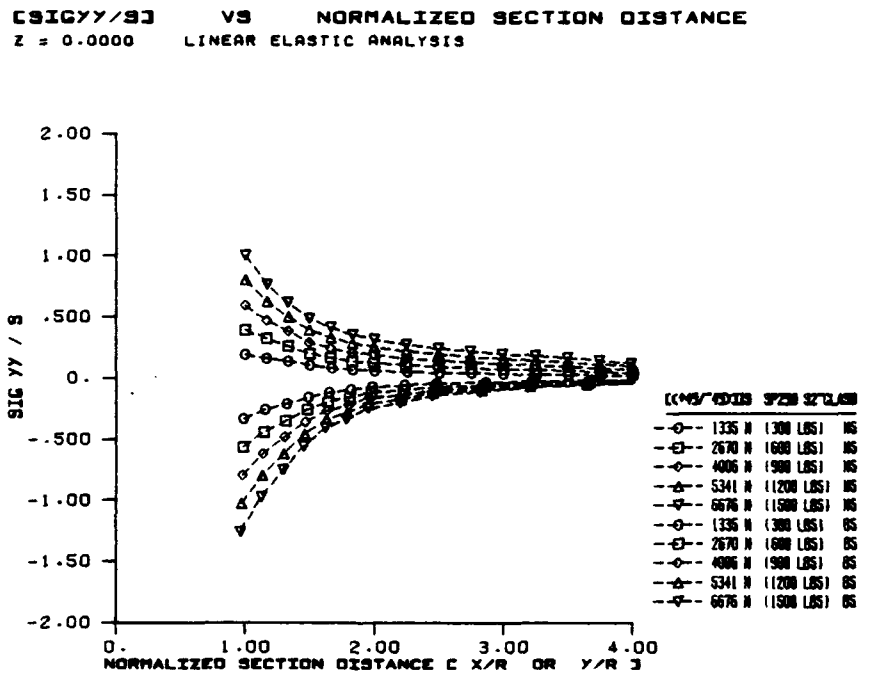

Figure 9.17 [(+45/-45)3]s Normalized Bearing and Net Section Linear Elastic σ_y vs. Normalized Section Distance as a Function of Load Level [Z = 0.0000]

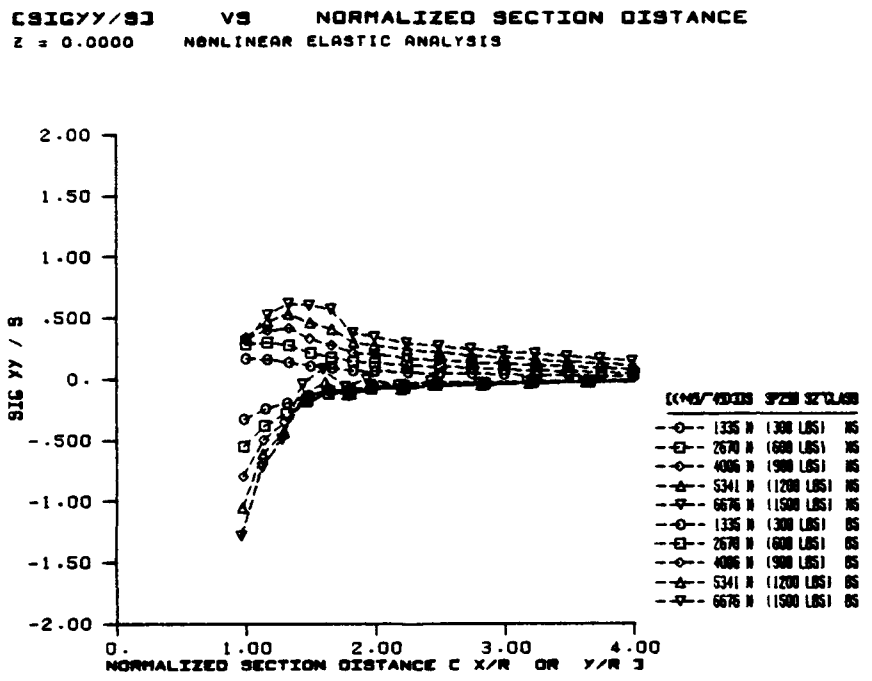

Figure 9.18 $[(+45/-45)_3]_s$ Normalized Bearing and Net Section Nonlinear Elastic σ_y vs. Normalized Section Distance as a Function of Load Level [Z = 0.0000]

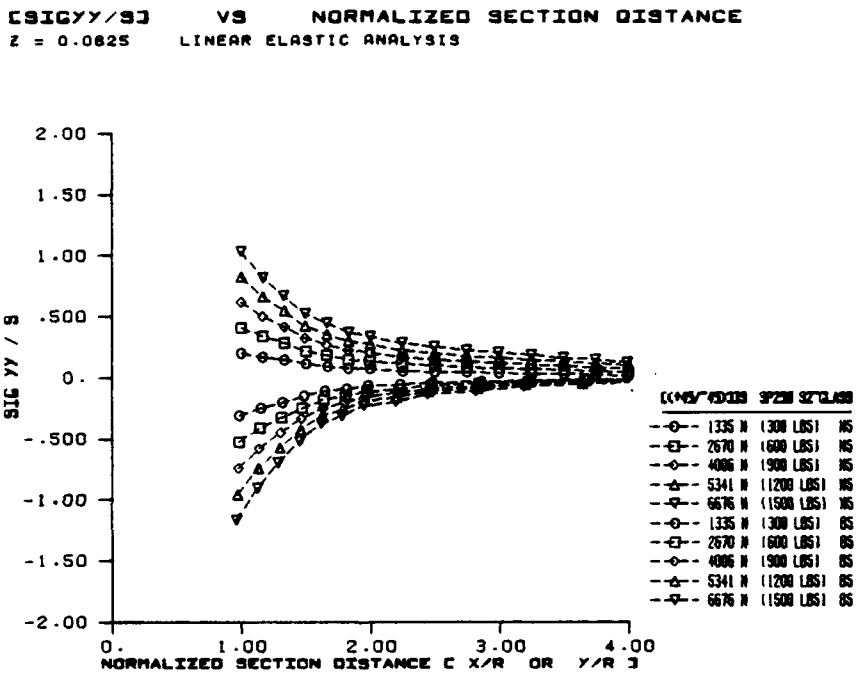

Figure 9.19 $[(+45/-45)_3]_s$ Normalized Bearing and Net Section Linear Elastic σ_y vs. Normalized Section Distance as a Function of Load Level [Z = 0.0625]

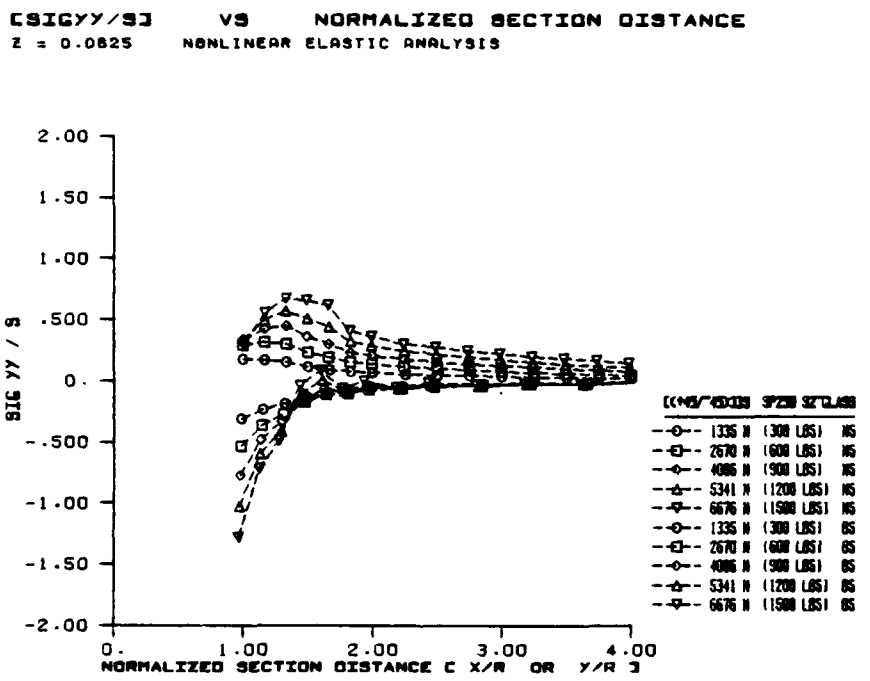

Figure 9.20 $[(+45/-45)_3]_s$ Normalized Bearing and Net Section Nonlinear Elastic σ_y vs. Normalized Section Distance as a Function of Load Level [Z = 0.0625]

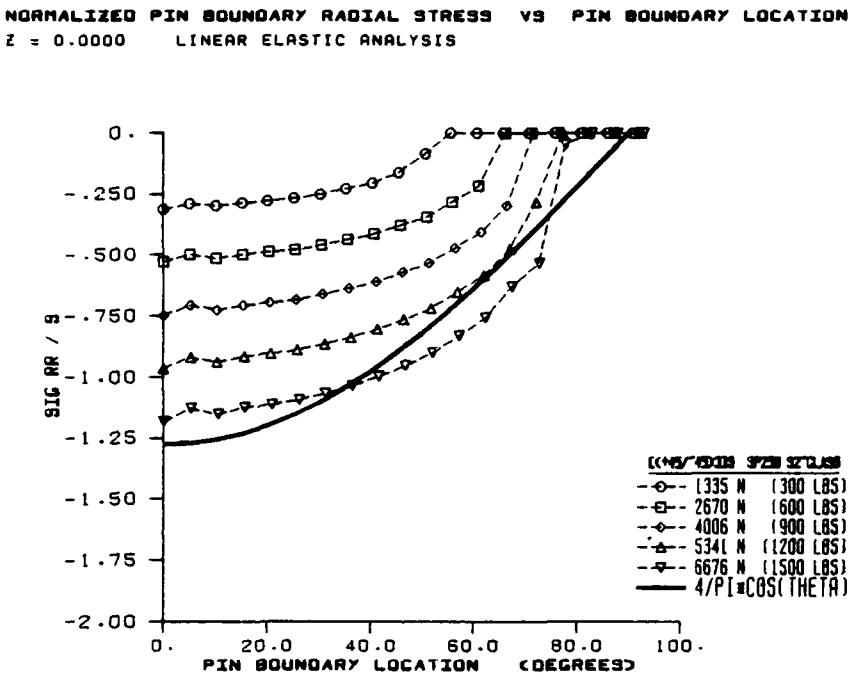

Figure 9.21 $[(+45/-45)_3]_s$ Normalized Pin Boundary Linear Elastic σ_r vs. Pin Boundary Location as a Function of Load Level [Z = 0.0000]

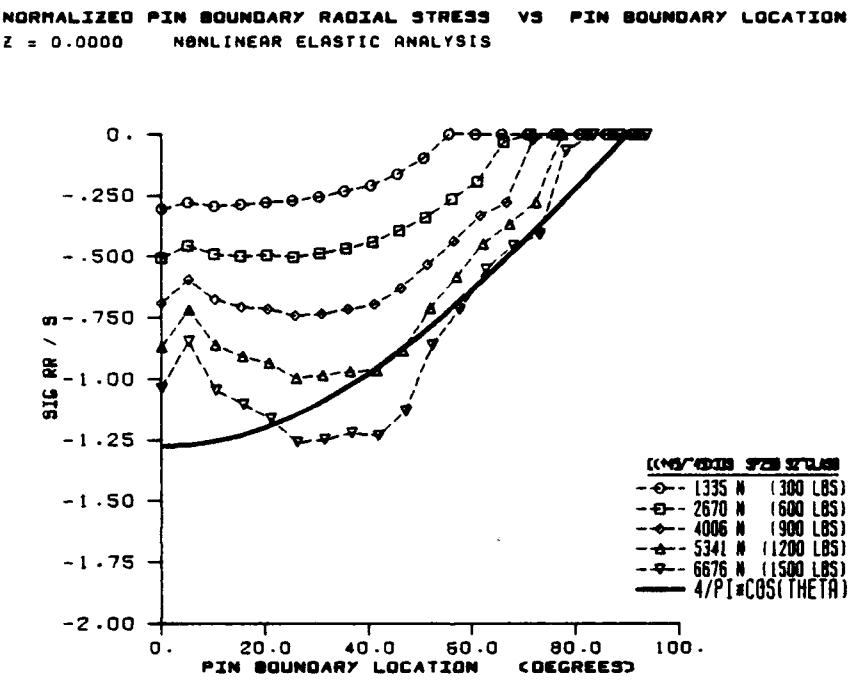

Figure 9.22 $[(+45/-45)_3]_s$ Normalized Pin Boundary Nonlinear Elastic σ_r vs. Pin Boundary Location as a Function of Load Level [Z = 0.0000]

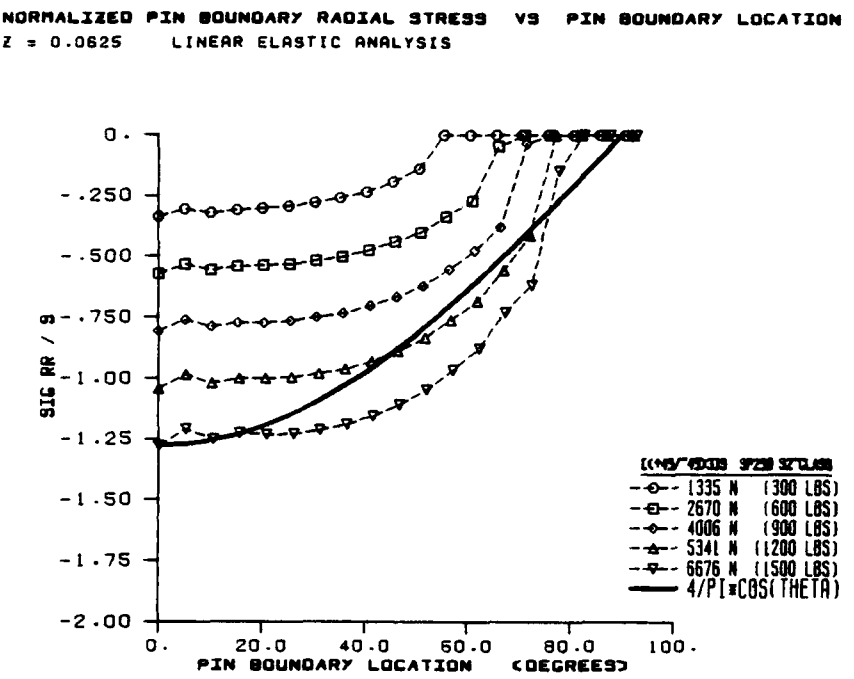

Figure 9.23 $[(+45/-45)_3]_s$ Normalized Pin Boundary Linear Elastic σ_r vs. Pin Boundary Location as a Function of Load Level [Z = 0.0625]

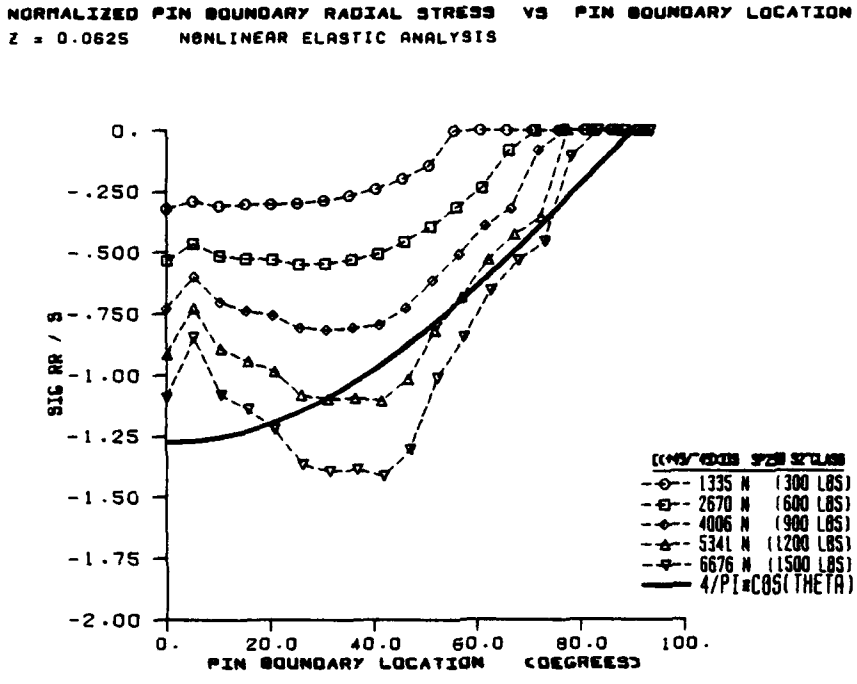

Figure 9.24 $[(+45/-45)_3]_s$ Normalized Pin Boundary Nonlinear Elastic σ_r vs. Pin Boundary Location as a Function of Load Level [Z = 0.0625]

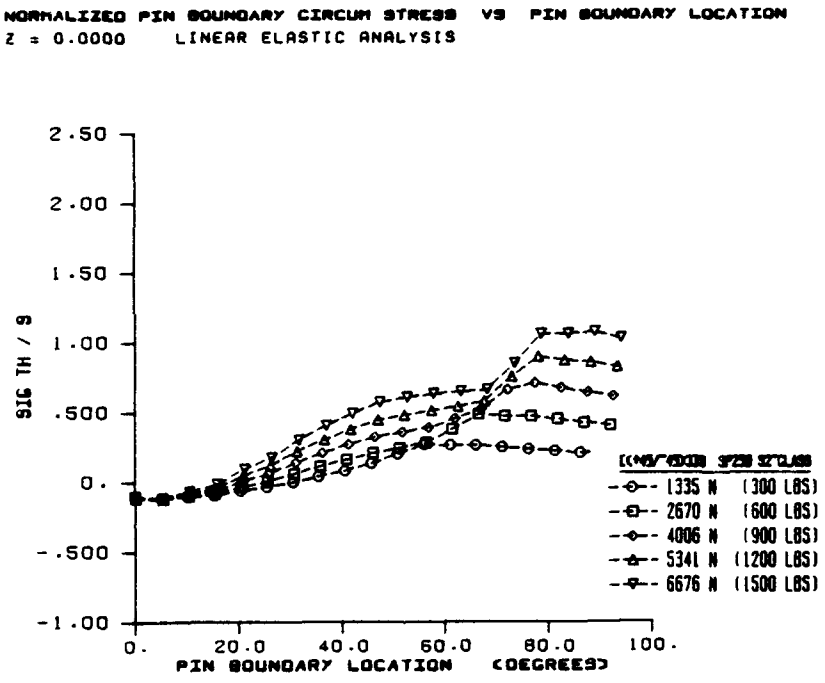

Figure 9.25 $[(+45/-45)_3]_s$ Normalized Pin Boundary Linear Elastic Circumferential Stress vs. Pin Boundary Location as a Function of Load Level [Z = 0.0000]

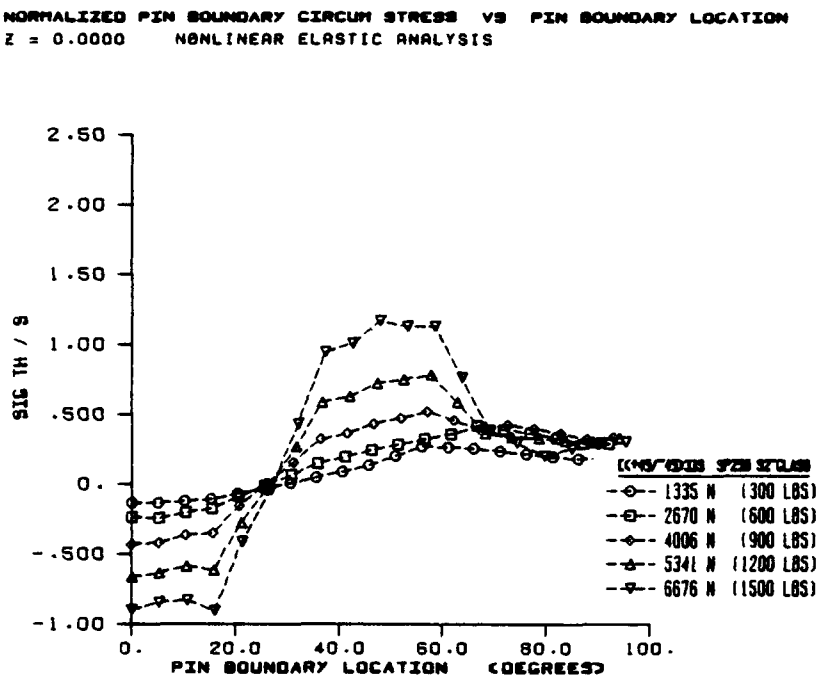

Figure 9.26 $[(+45/-45)_3]_s$ Normalized Pin Boundary Nonlinear Elastic Circumferential Stress vs. Pin Boundary Location as a Function of Load Level [Z = 0.0000]

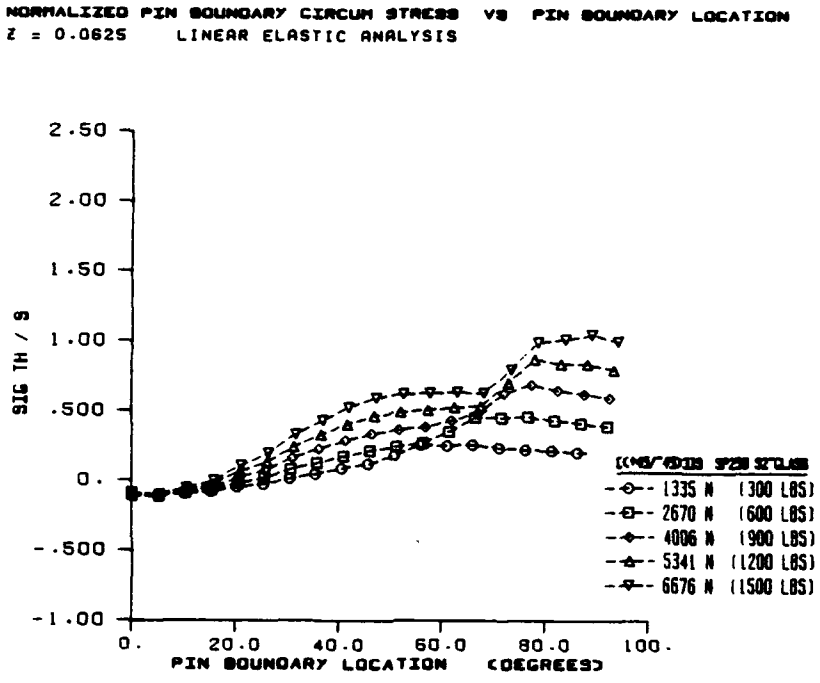

Figure 9.27 $[(+45/-45)_3]_s$ Normalized Pin Boundary Linear Elastic Circumferential Stress vs. Pin Boundary Location as a Function of Load Level [Z = 0.0625]

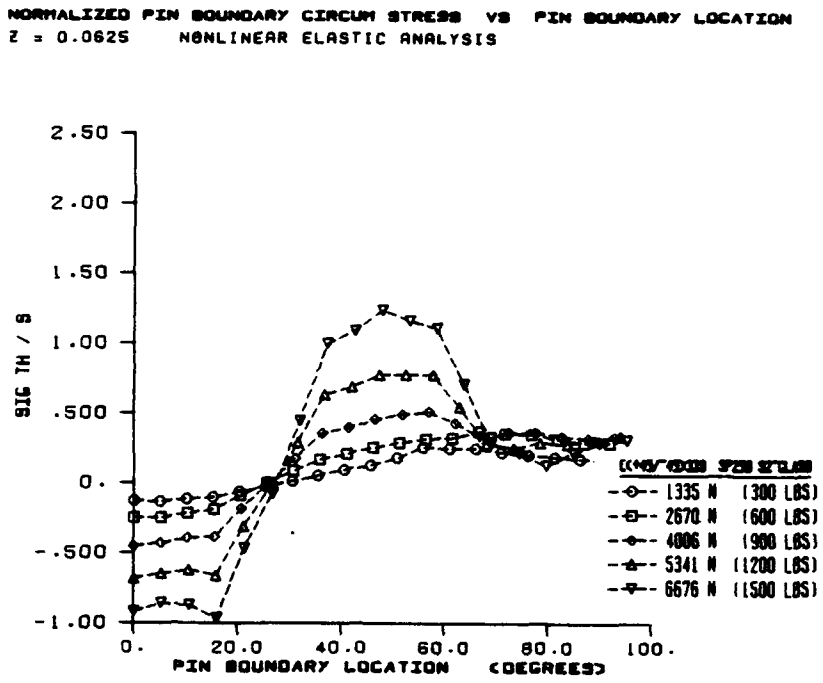

Figure 9.28 $[(+45/-45)_3]_s$ Normalized Pin Boundary Nonlinear Elastic Circumferential Stress vs. Pin Boundary Location as a Function of Load Level [Z = 0.0625]

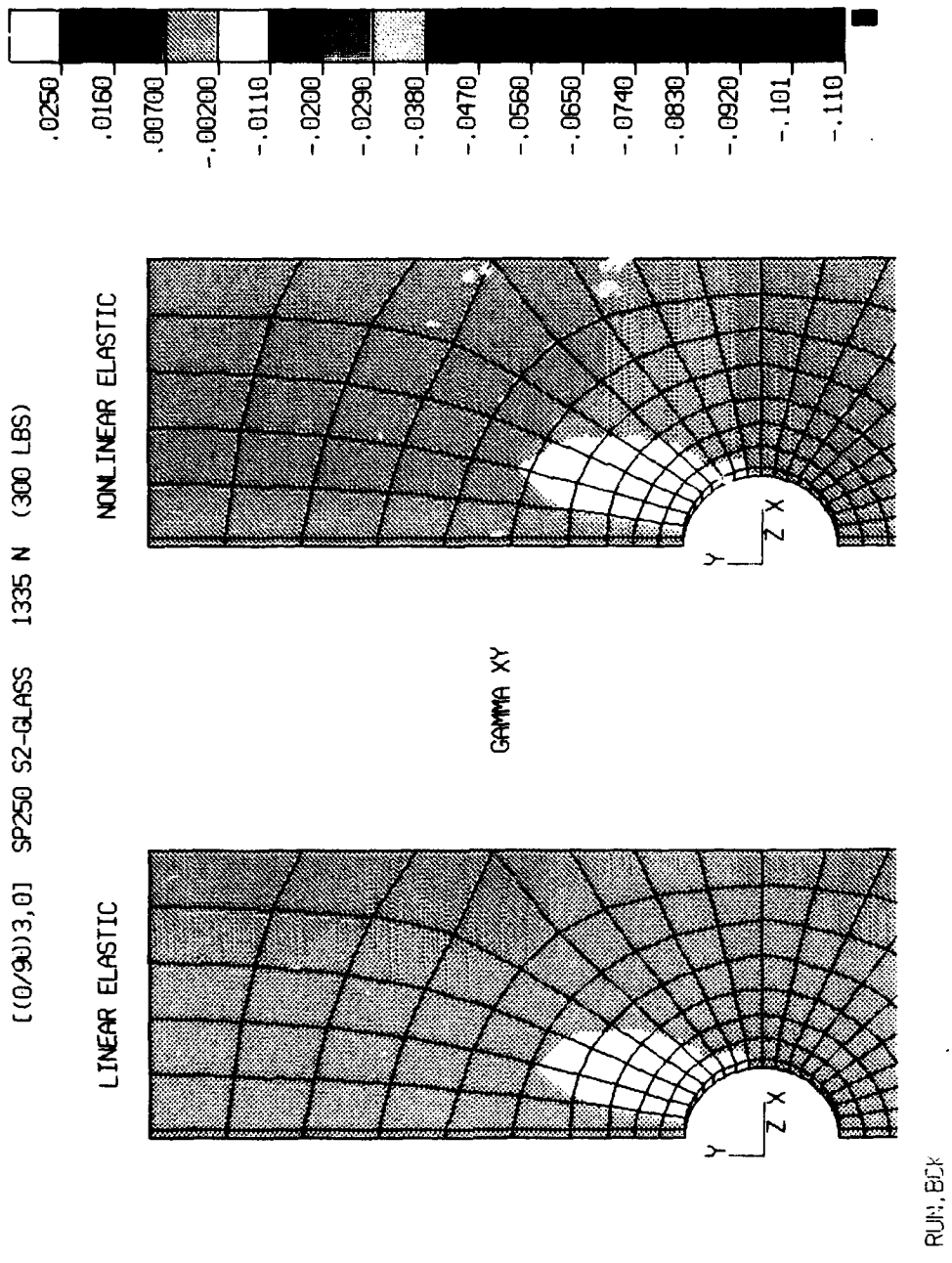

Figure 9.29 $[(0/90)_{3},0]_{s}$ Front Surface Coupon Linear and Nonlinear γ_{xy} [300 lbs load level]

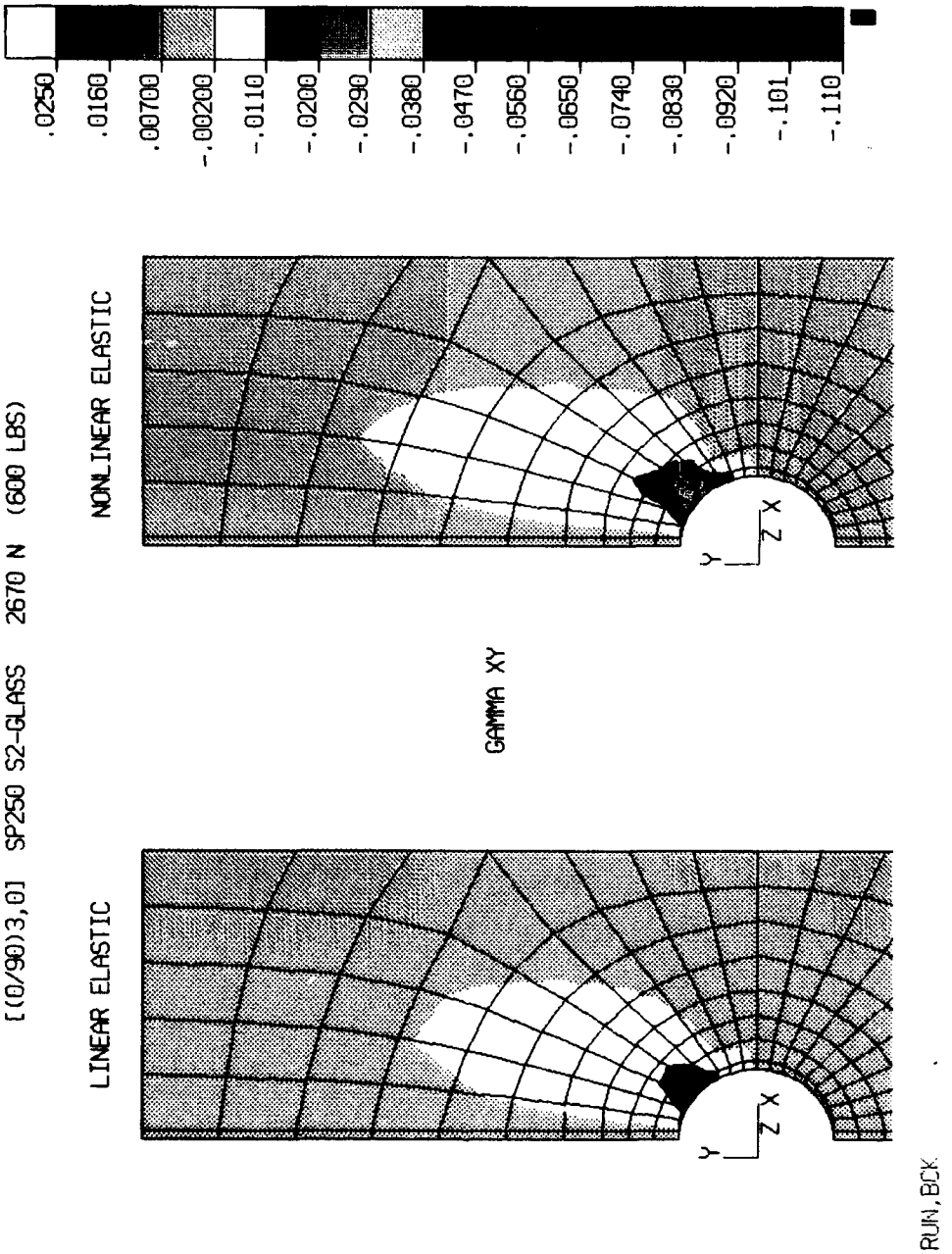

Figure 9.30 $[(0/90)_3,0]_s$ Front Surface Coupon Linear and Nonlinear γ_{xy} [600 lbs load level]

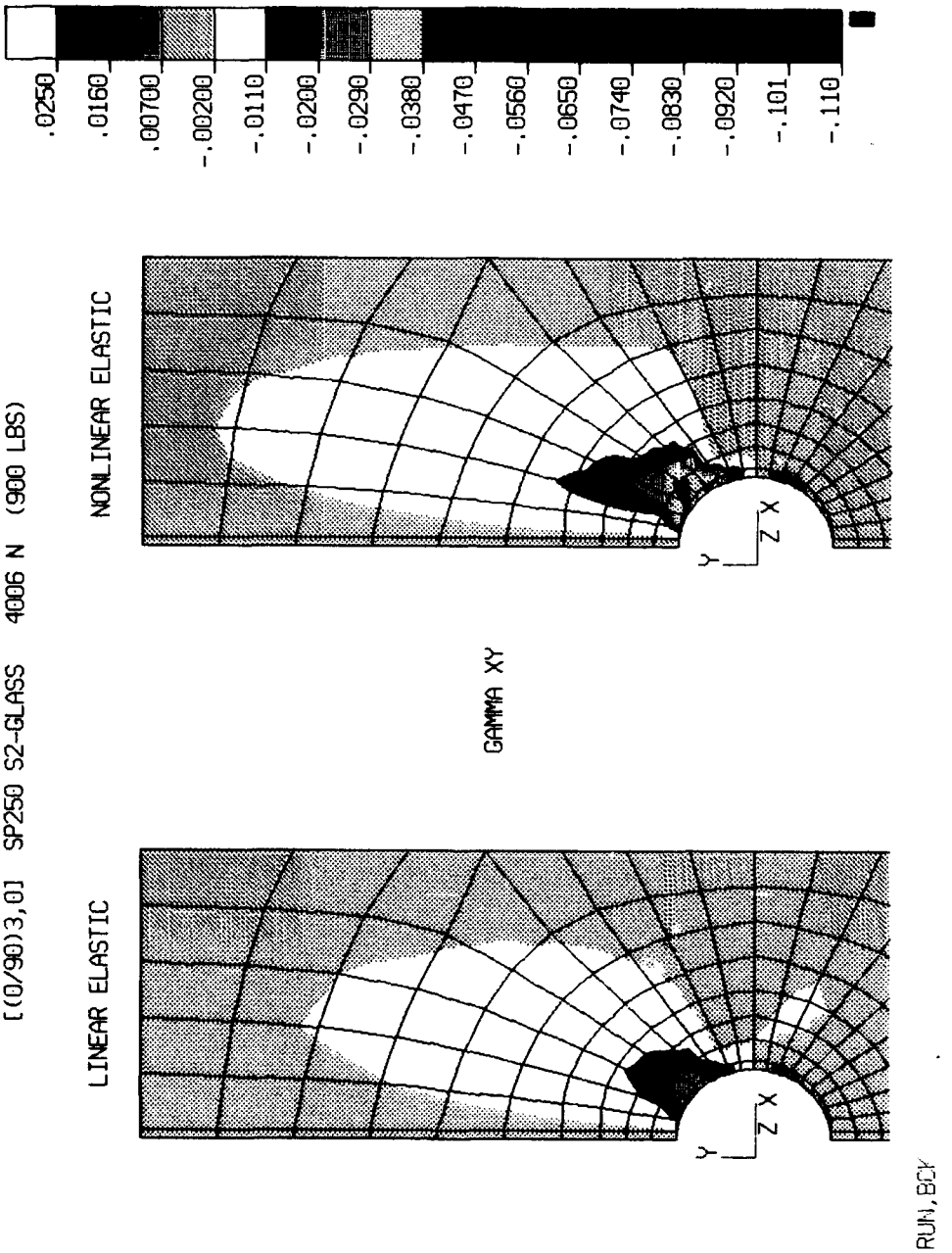

Figure 9.31 $[(0/90)_{3},0]_{s}$ Front Surface Coupon Linear and Nonlinear γ_{xy} [900 lbs load level]

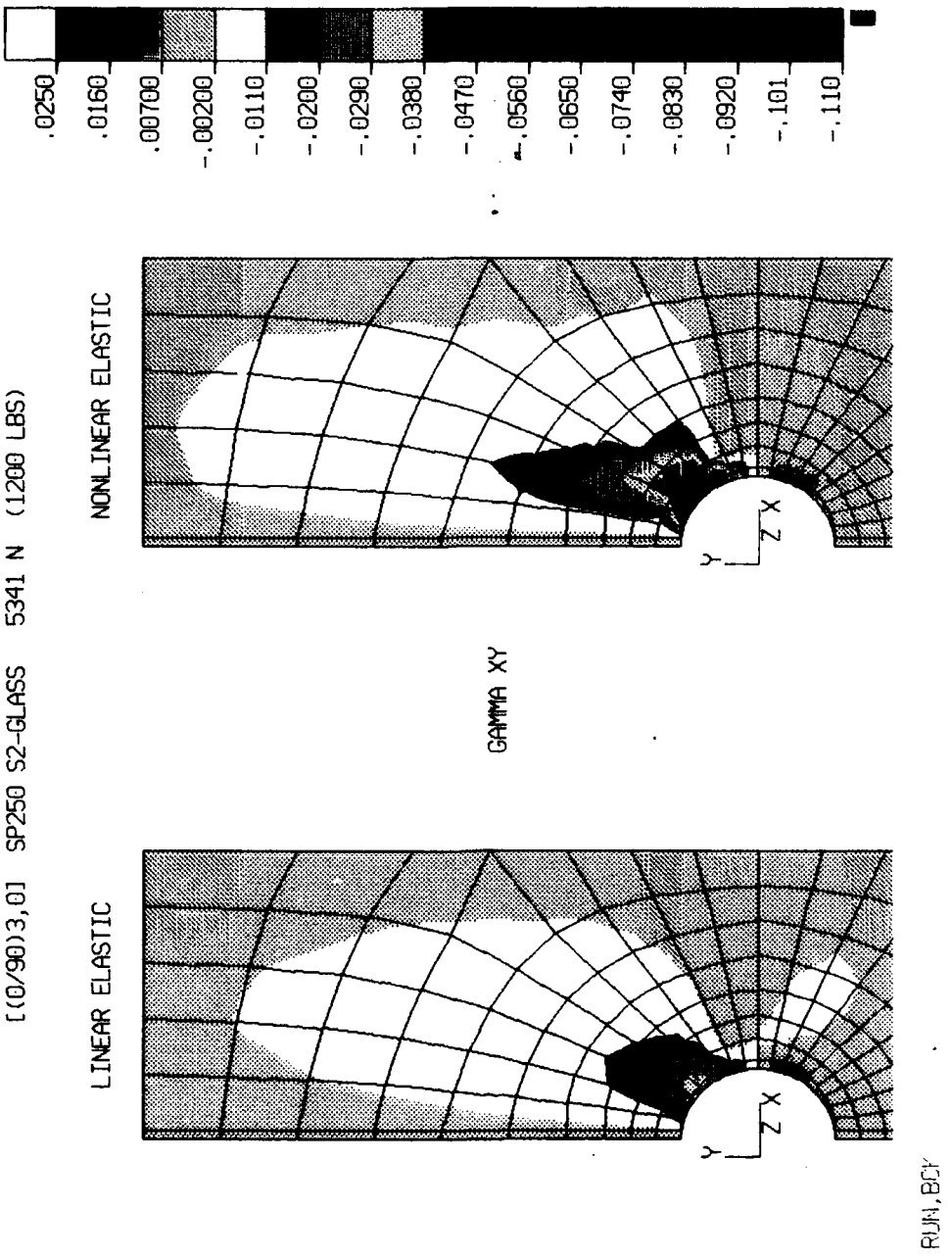

Figure 9.32 $[(0/90)_3,0]_s$ Front Surface Coupon Linear and Nonlinear γ_{xy} [1200 lbs load level]

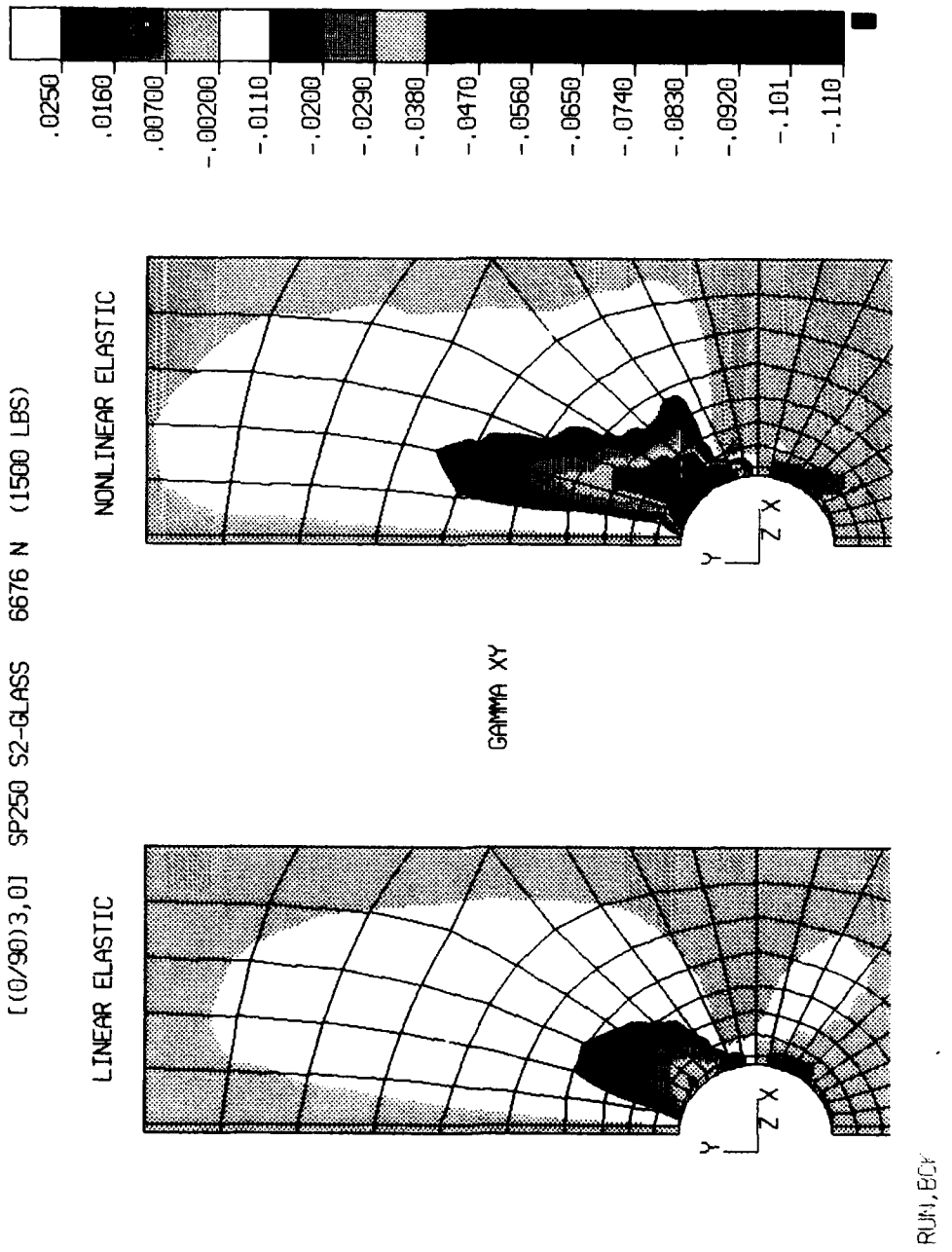

Figure 9.33 $[(0/90)_{3},0]_{s}$ Front Surface Coupon Linear and Nonlinear γ_{xy} [1500 lbs load level]

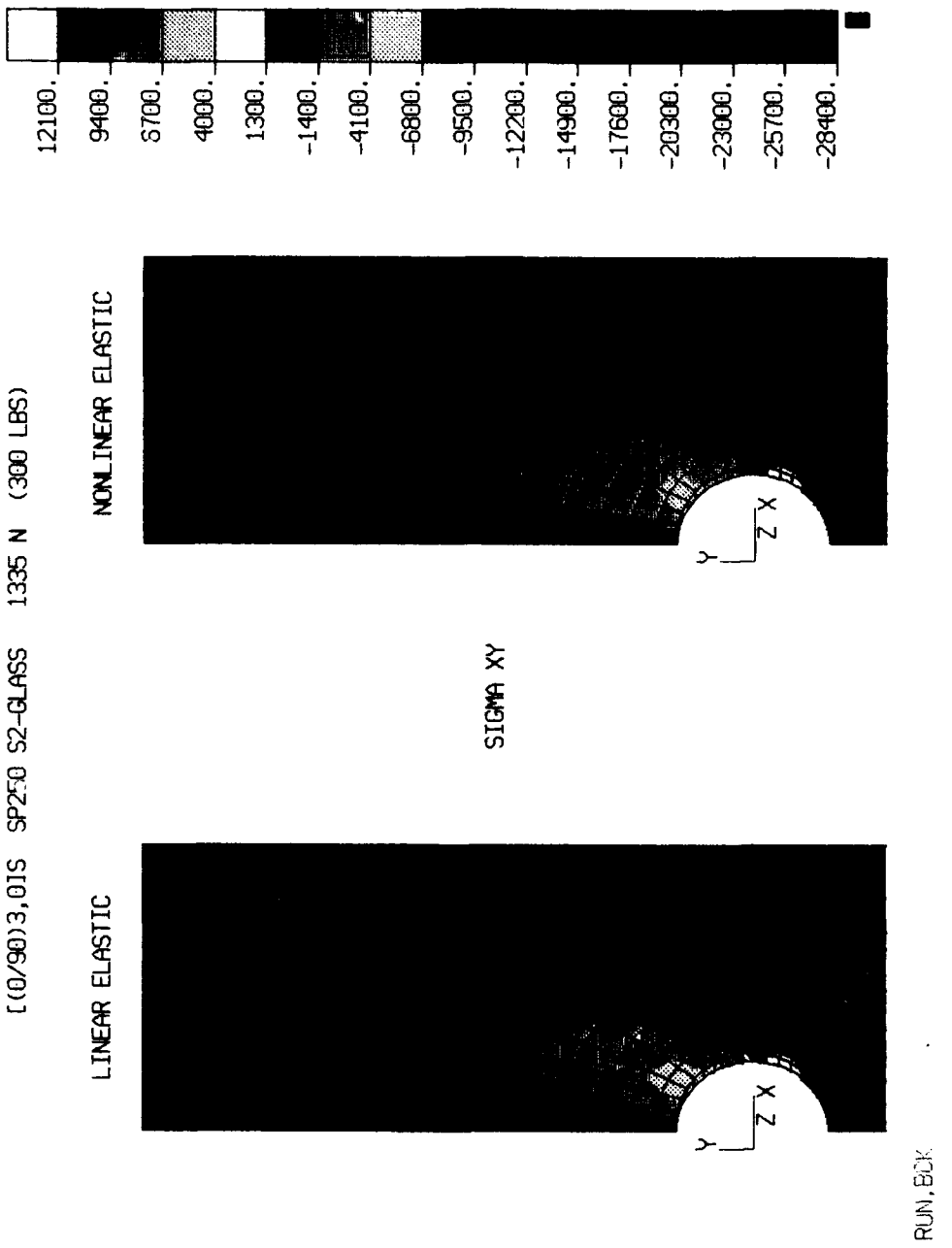

Figure 9.34 $[(0/90)_3,0]_s$ Front Surface Coupon Linear and Nonlinear τ_{xy} [300 lbs load level]

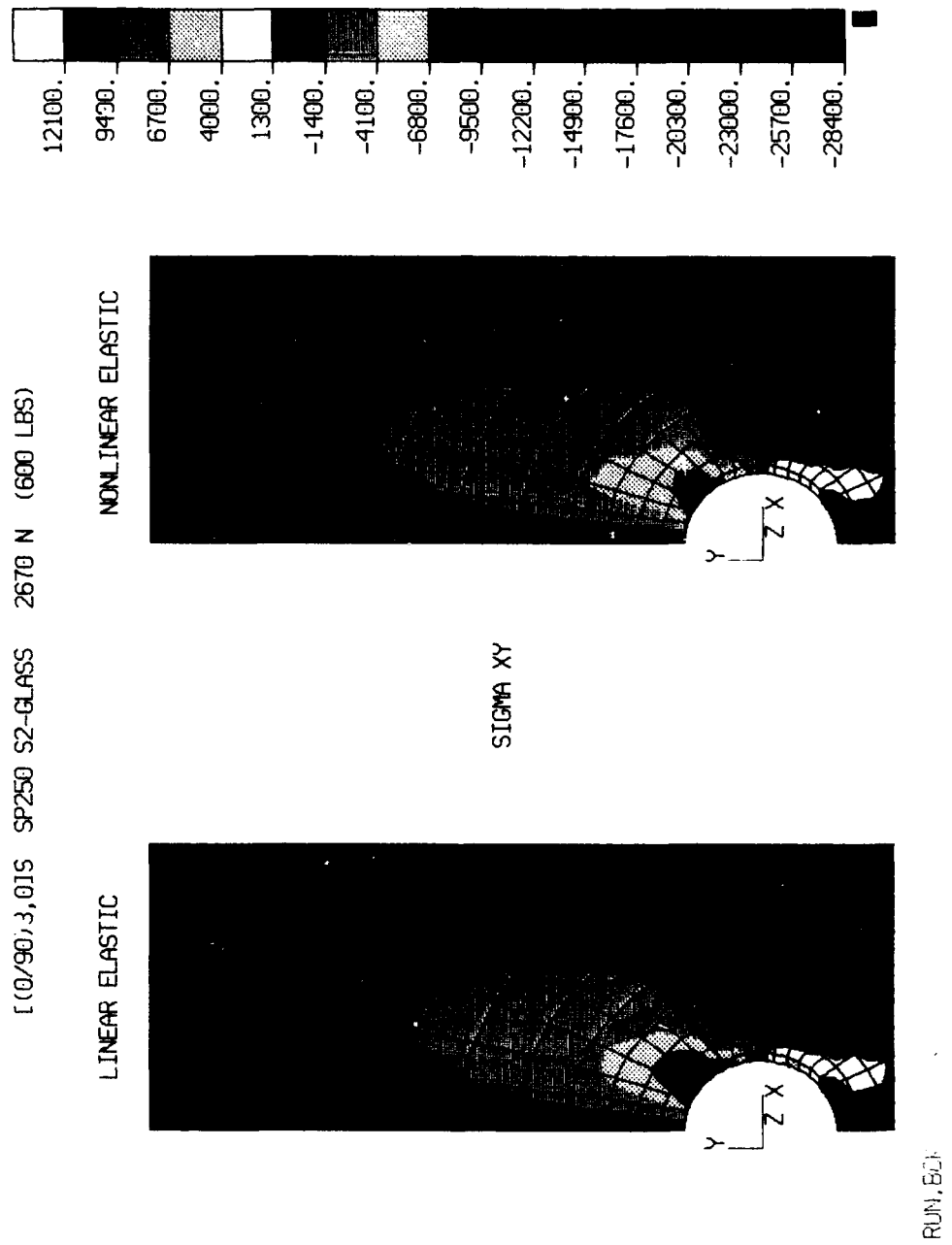

Figure 9.35 $[(0/90)_{3,0}]_s$ Front Surface Coupon Linear and Nonlinear τ_{xy} [600 lbs load level]

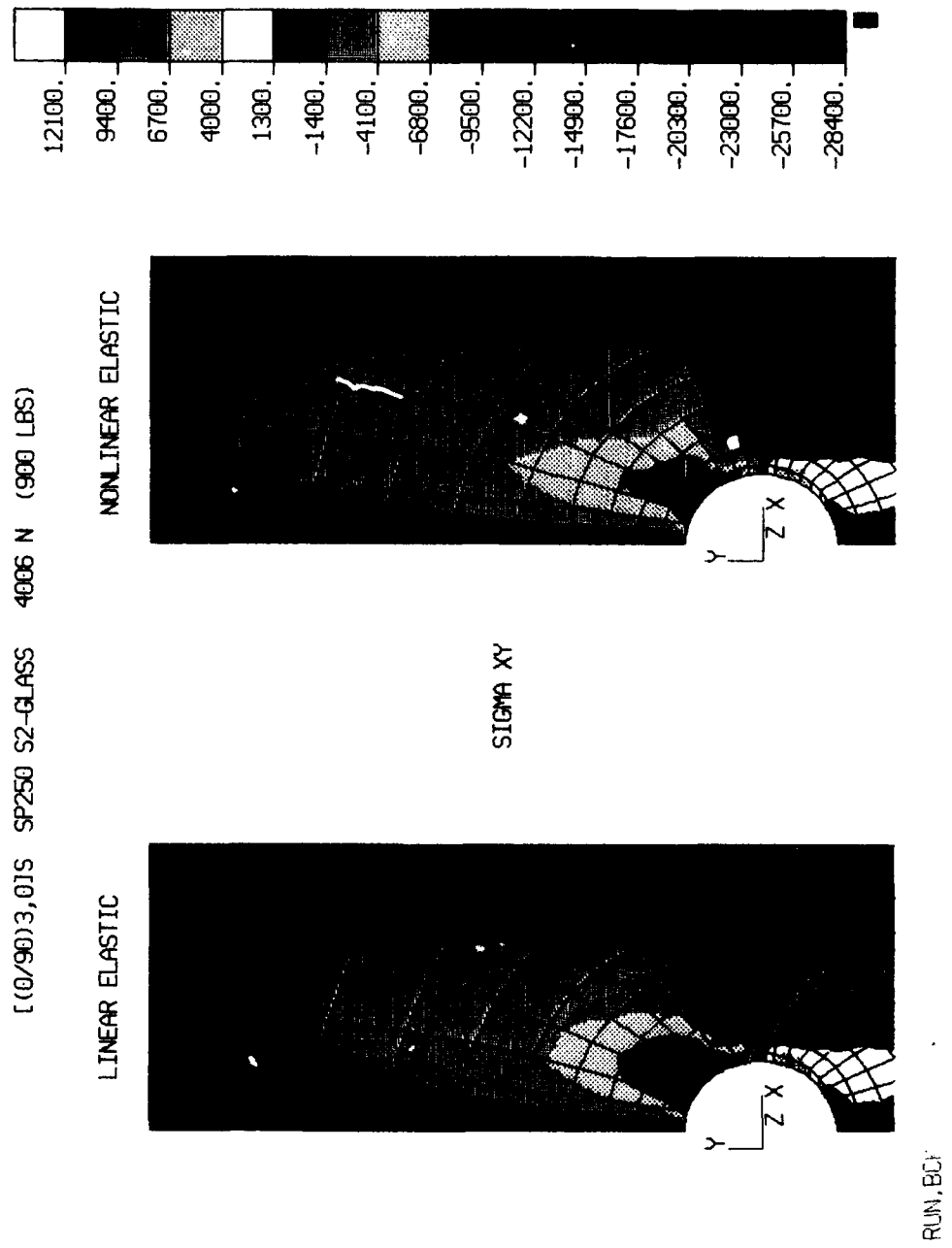

Figure 9.36 $[(0/90)_{3},0]_{s}$ Front Surface Coupon Linear and Nonlinear τ_{xy} [900 lbs load level]

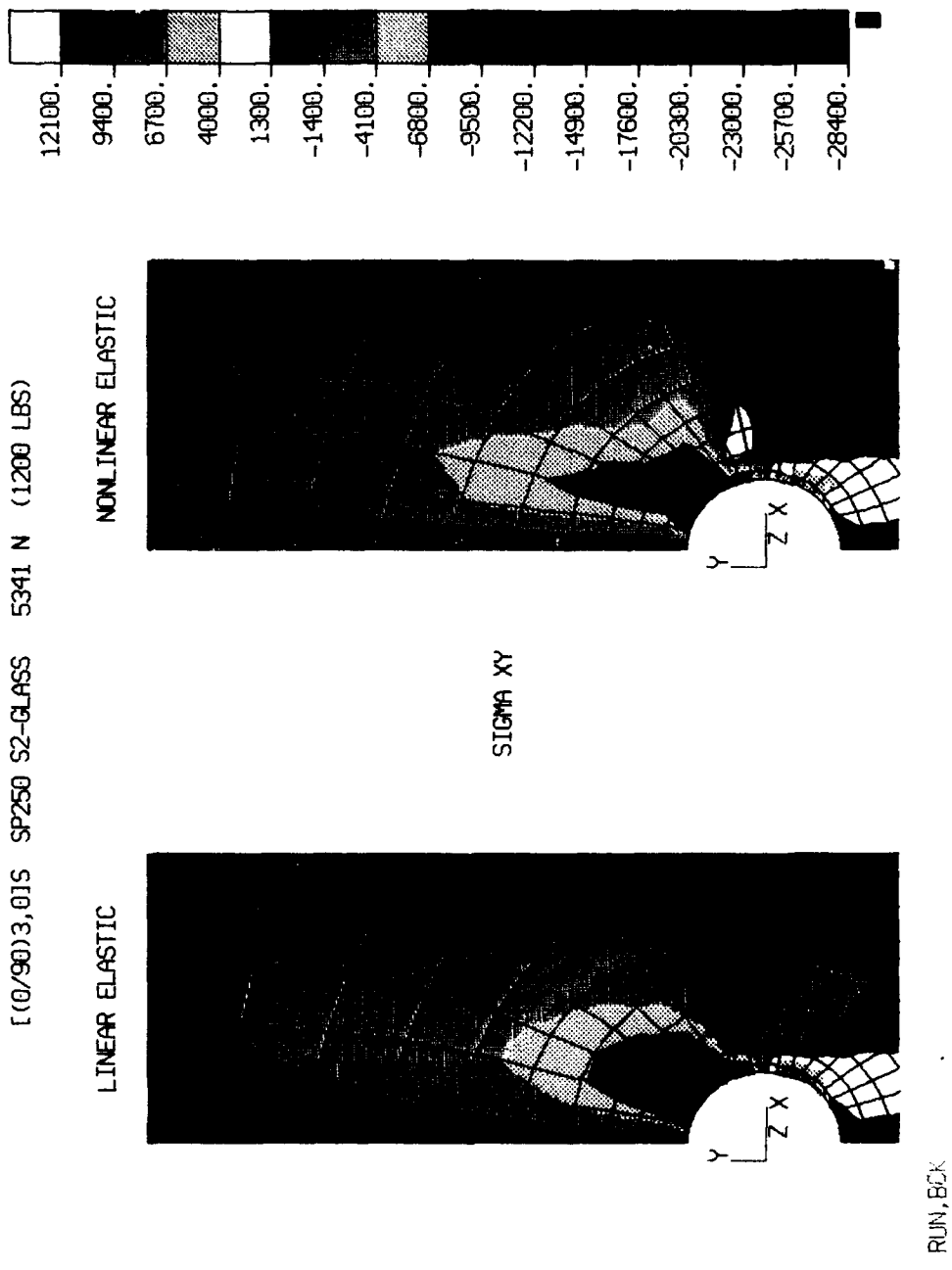

Figure 9.37 $[(0/90)_{3},0]_{s}$ Front Surface Coupon Linear and Nonlinear τ_{xy} [1200 lbs load level]

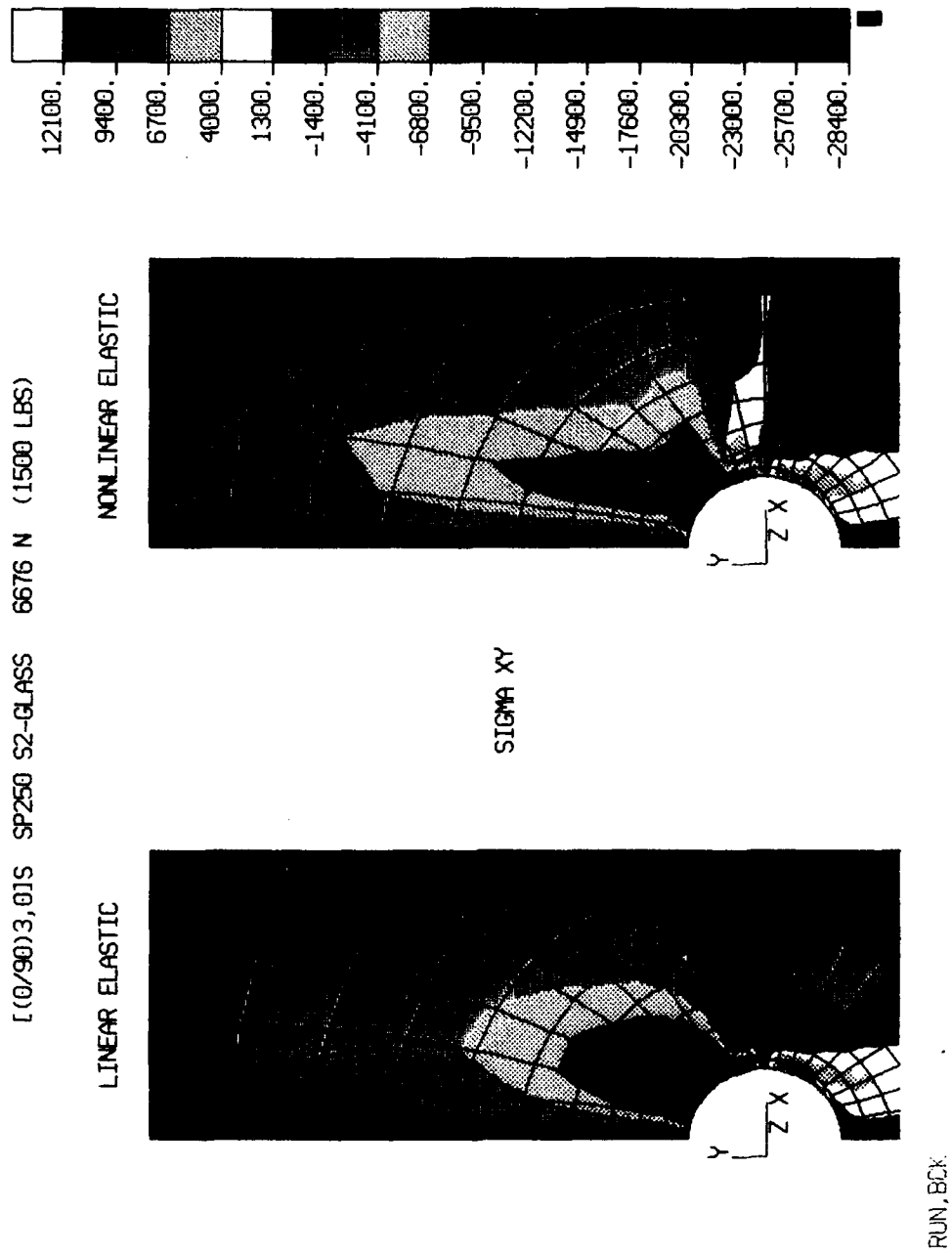

Figure 9.38 $[(0/90)_{3},0]_{s}$ Front Surface Coupon Linear and Nonlinear τ_{xy} [1500 lbs load level]

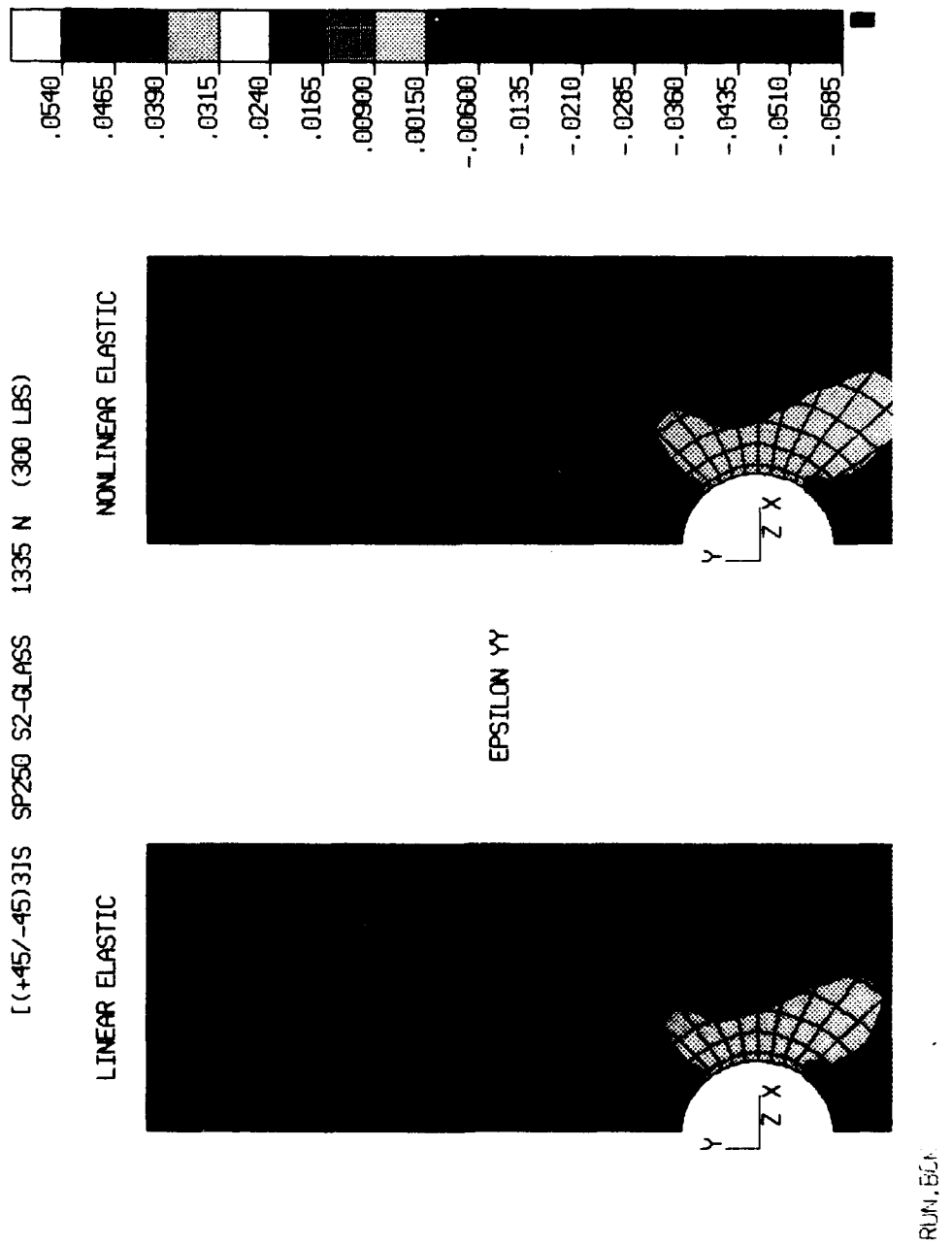

Figure 9.39 $[(+45/-45)_3]_s$ Front Surface Coupon Linear and Nonlinear ε_{yy} [300 lbs load level]

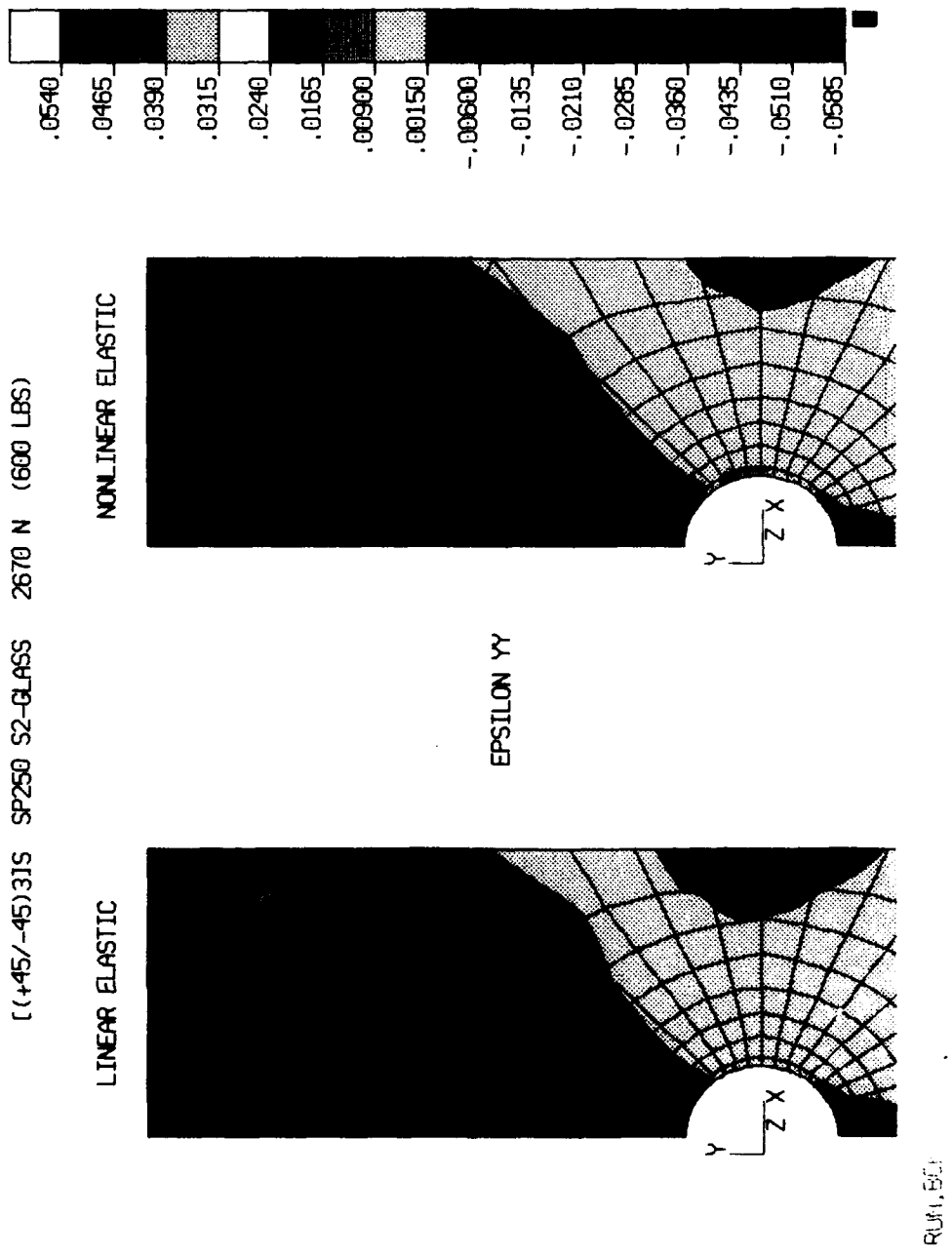

Figure 9.40 [(+45/−45)3]s Front Surface Coupon Linear and Nonlinear ε_{yy} [600 lbs load level]

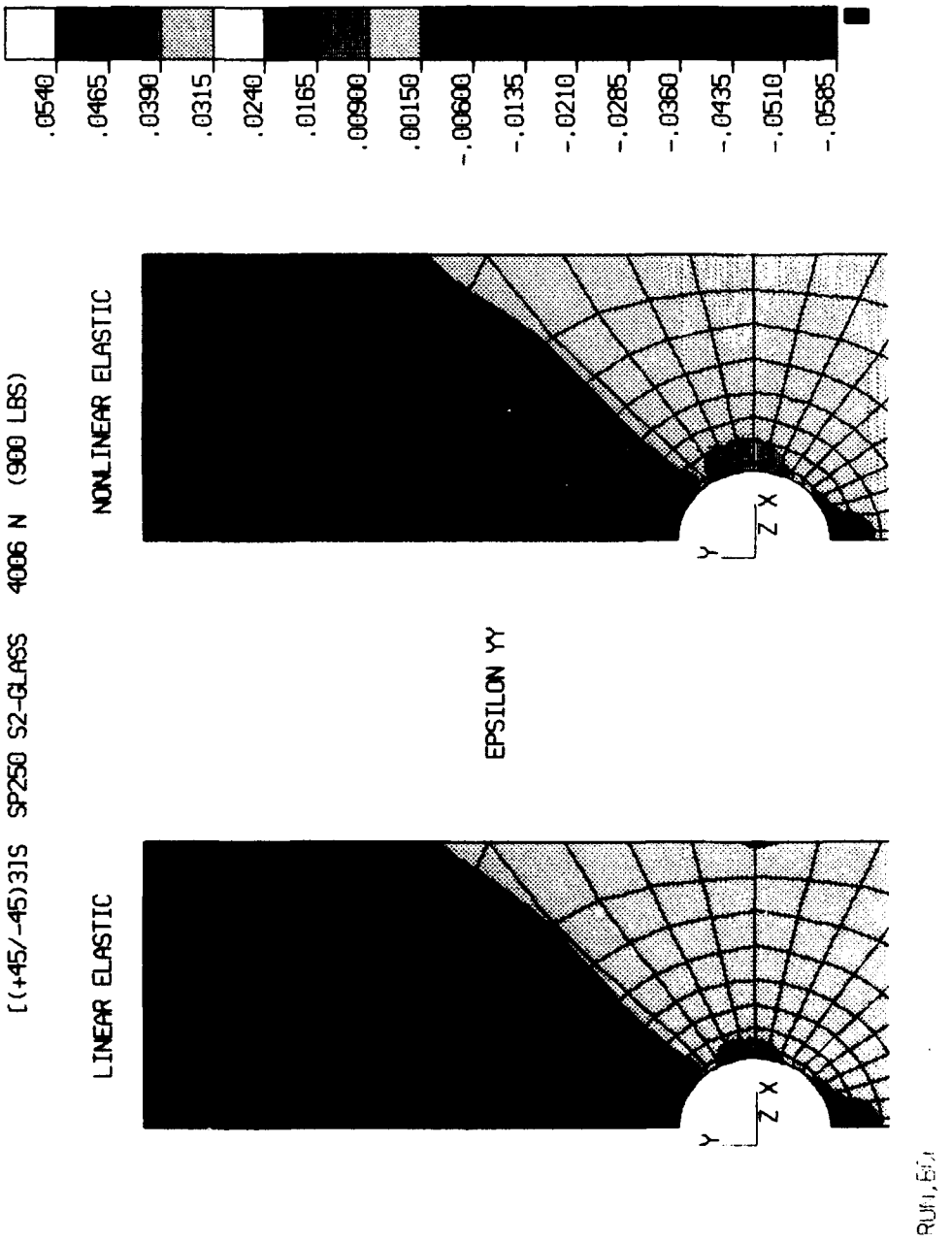

Figure 9.41 **[(+45/−45)3]s Front Surface Coupon Linear and Nonlinear ε_{yy} [900 lbs load level]**

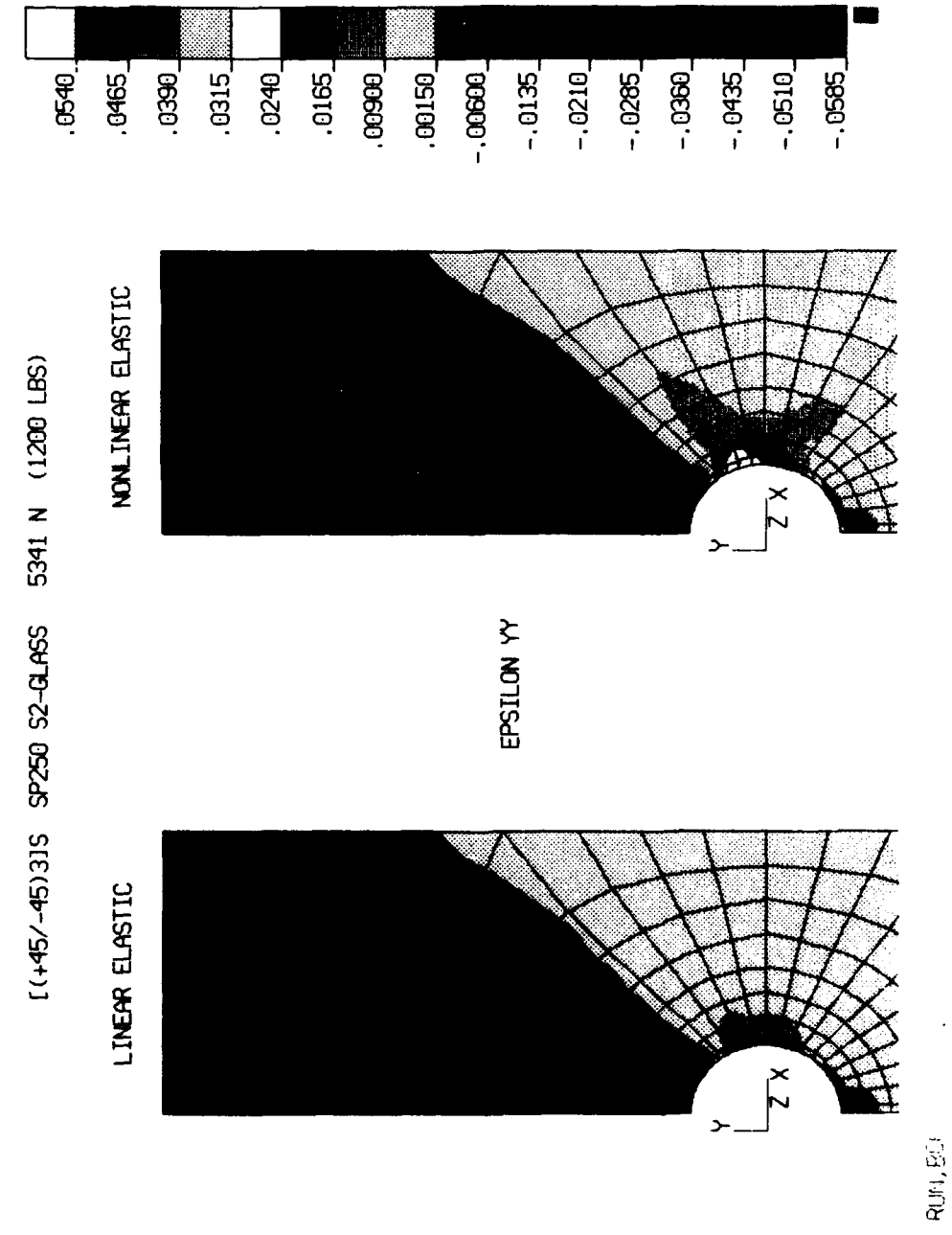

Figure 9.42 **[(+45/−45)3]s Front Surface Coupon Linear and Nonlinear εyy [1200 lbs load level]**

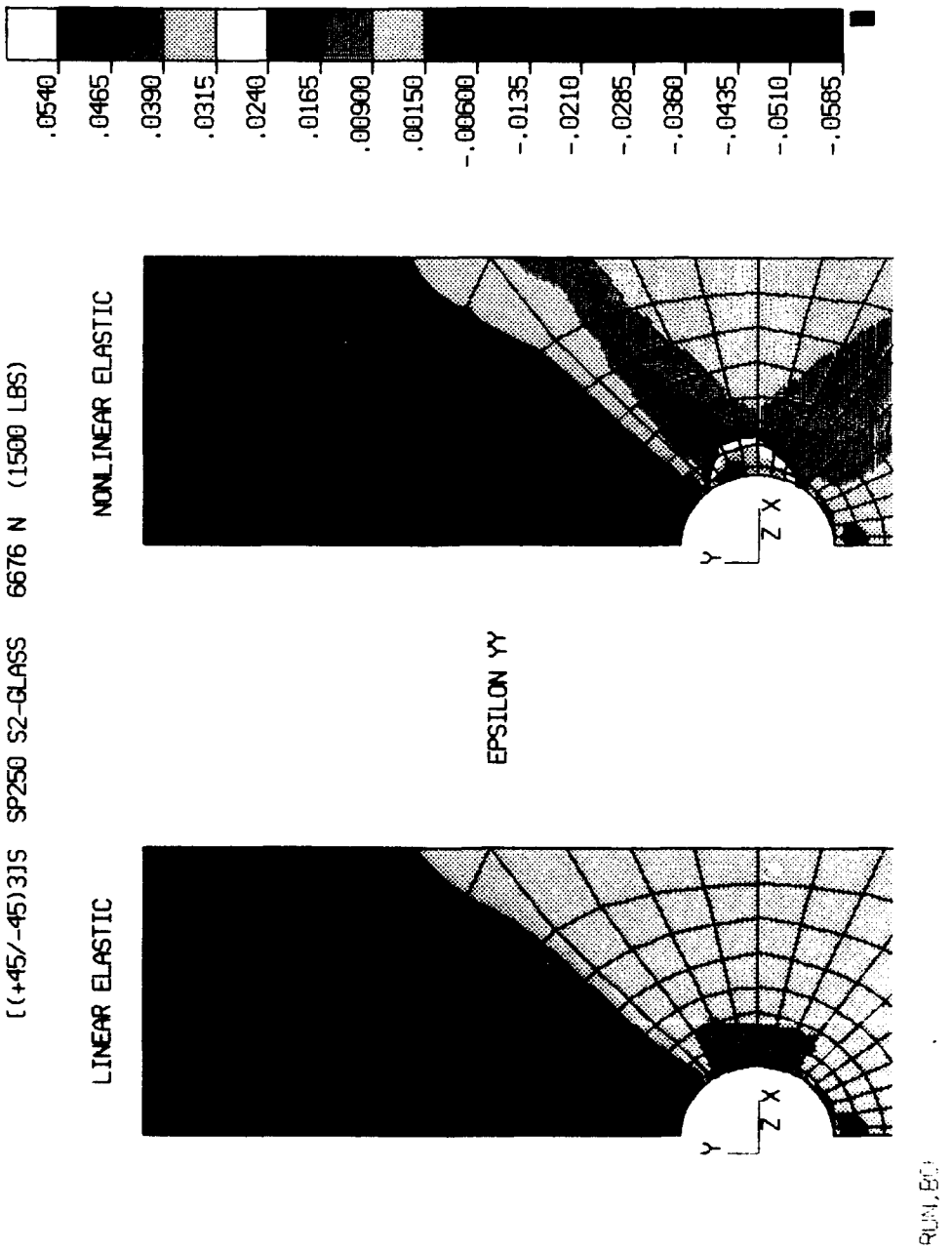

Figure 9.43 **[(+45/−45)3]s Front Surface Coupon Linear and Nonlinear ε_{yy} [1500 lbs load level]**

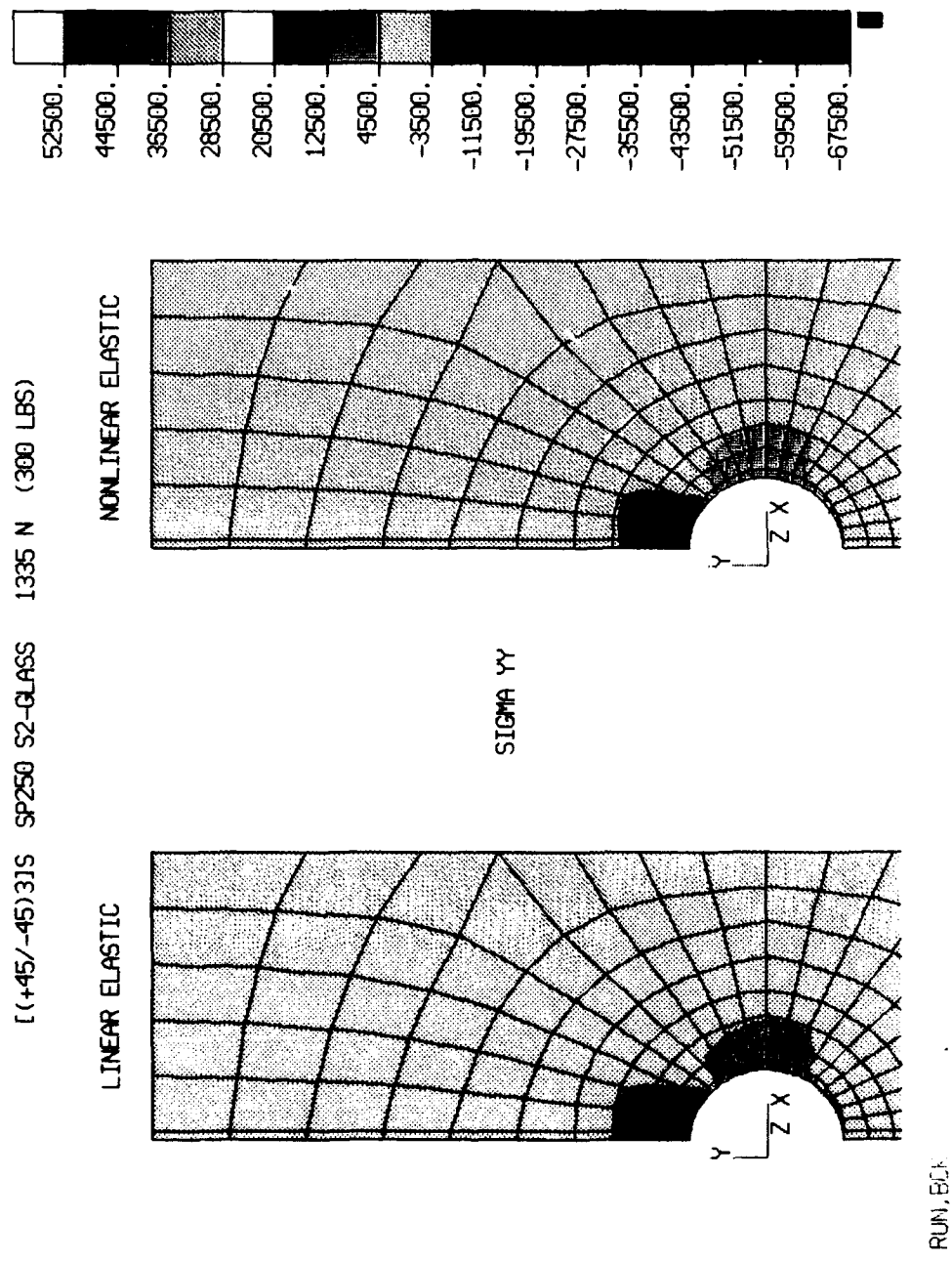

Figure 9.44 $[(+45/-45)_3]_s$ Front Surface Coupon Linear and Nonlinear σ_{yy} [300 lbs load level]

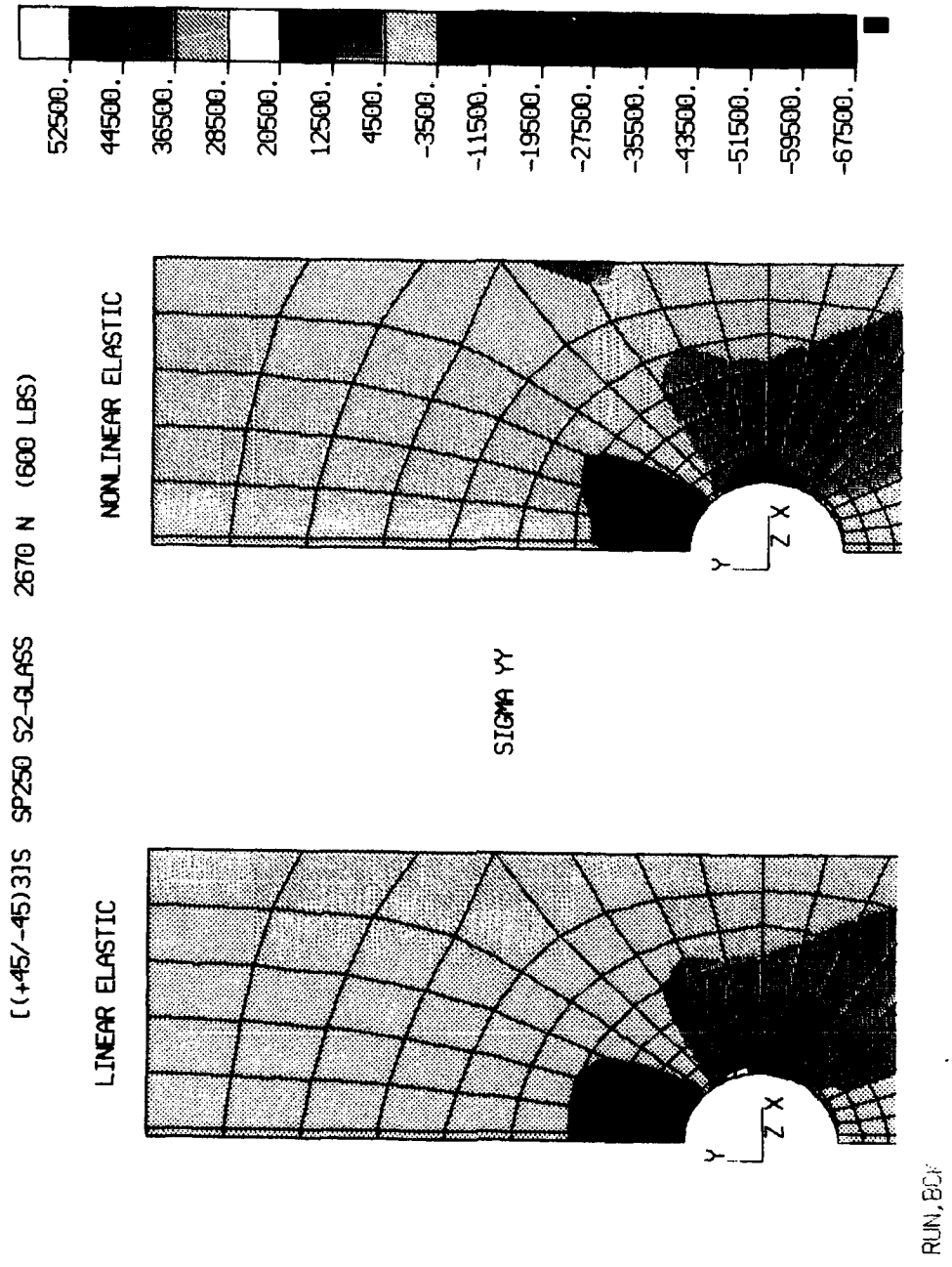

Figure 9.45 $[(+45/-45)_3]_s$ Front Surface Coupon Linear and Nonlinear σ_{yy} [600 lbs load level]

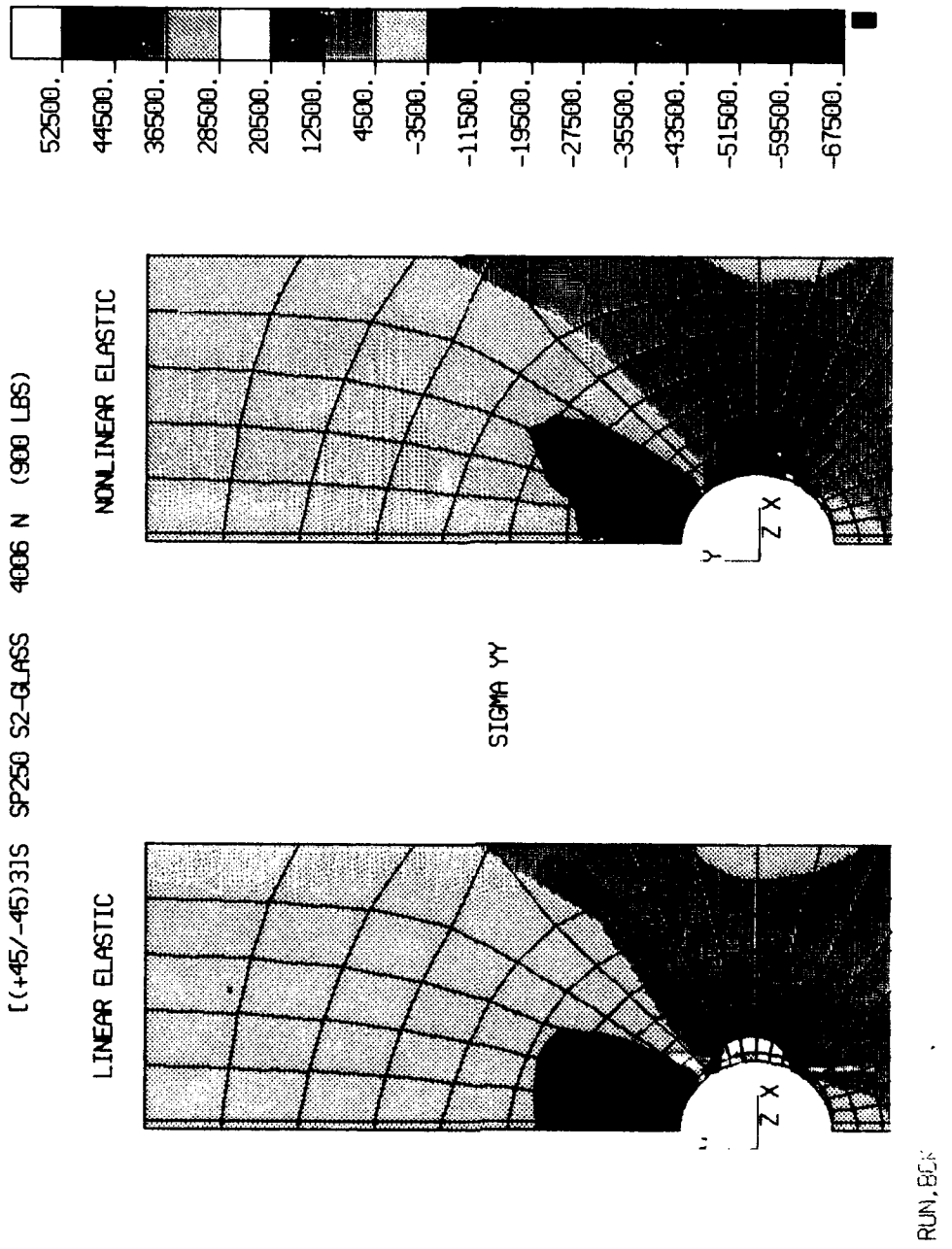

Figure 9.46 $[(+45/-45)_3]_s$ Front Surface Coupon Linear and Nonlinear σ_{yy} [900 lbs load level]

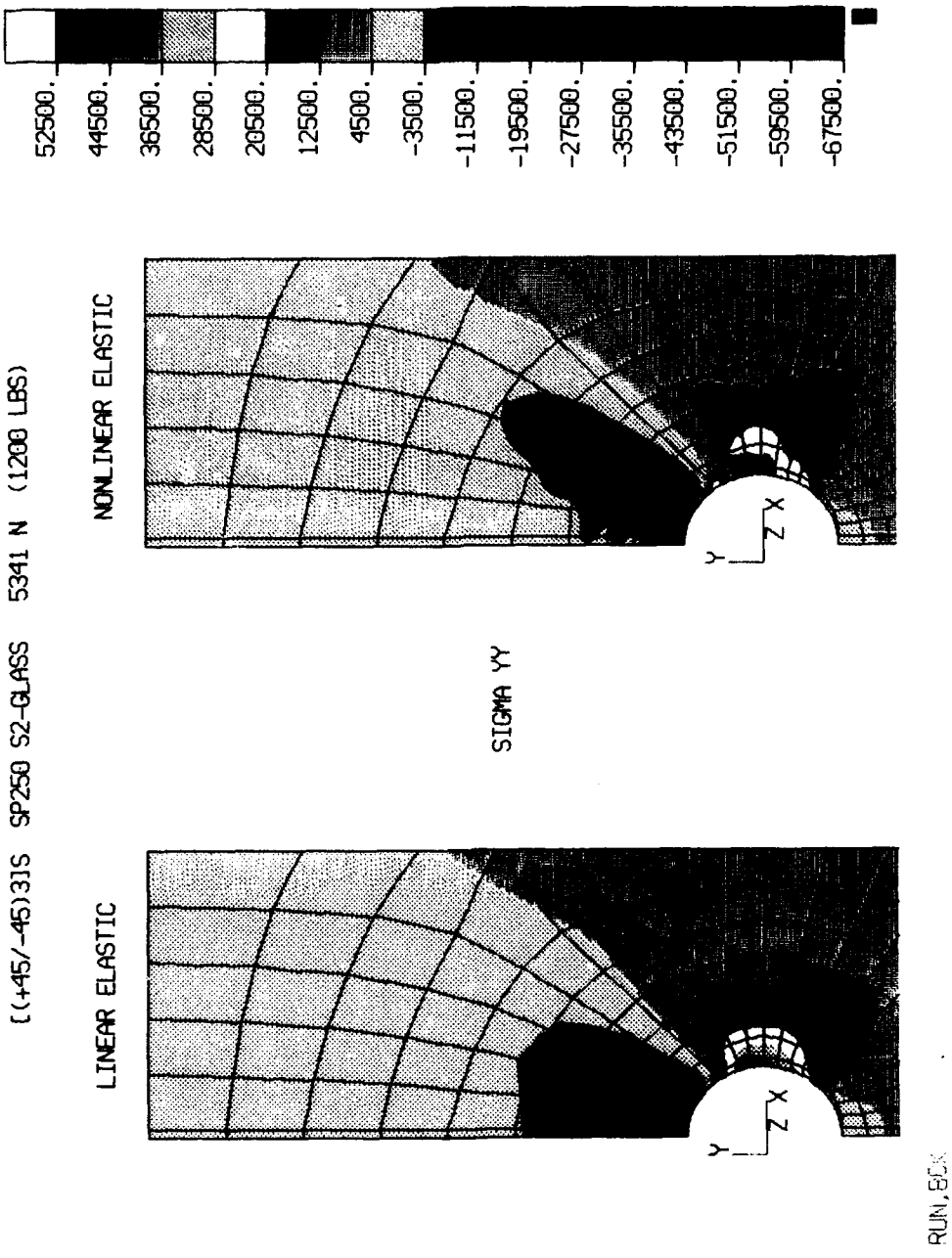

Figure 9.47 **[(+45/-45)3]s Front Surface Coupon Linear and Nonlinear σ_{yy} [1200 lbs load level]**

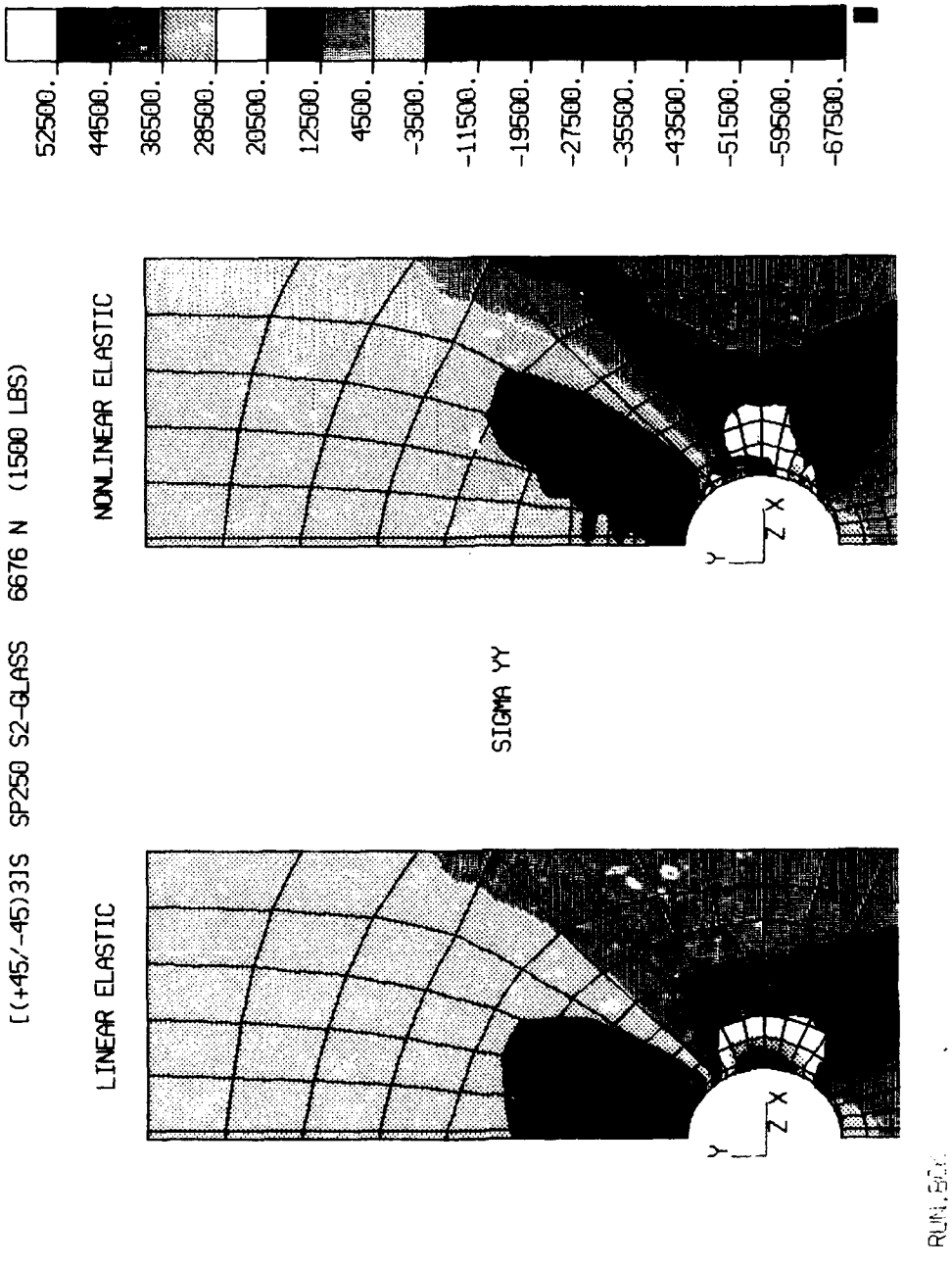

Figure 9.48 [(+45/-45)3]s Front Surface Coupon Linear and Nonlinear σ_{yy} [1500 lbs load level]

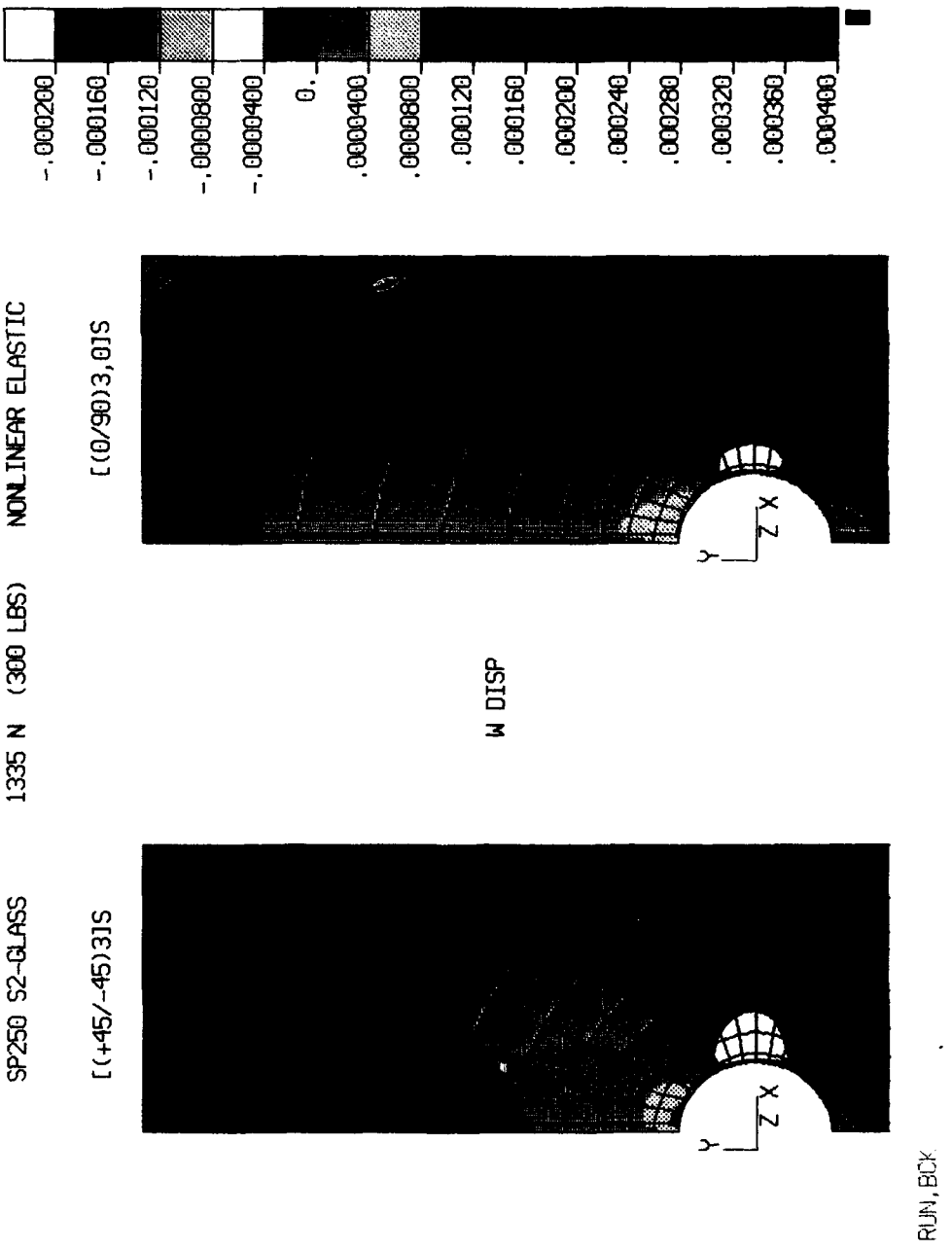

Figure 9.49 $[(0/90)_3,0]_s$ and $[(+45/-45)_3]_s$ Out-of Plane Front Surface Nonlinear Elastic Coupon Displacement [300 lbs load level]

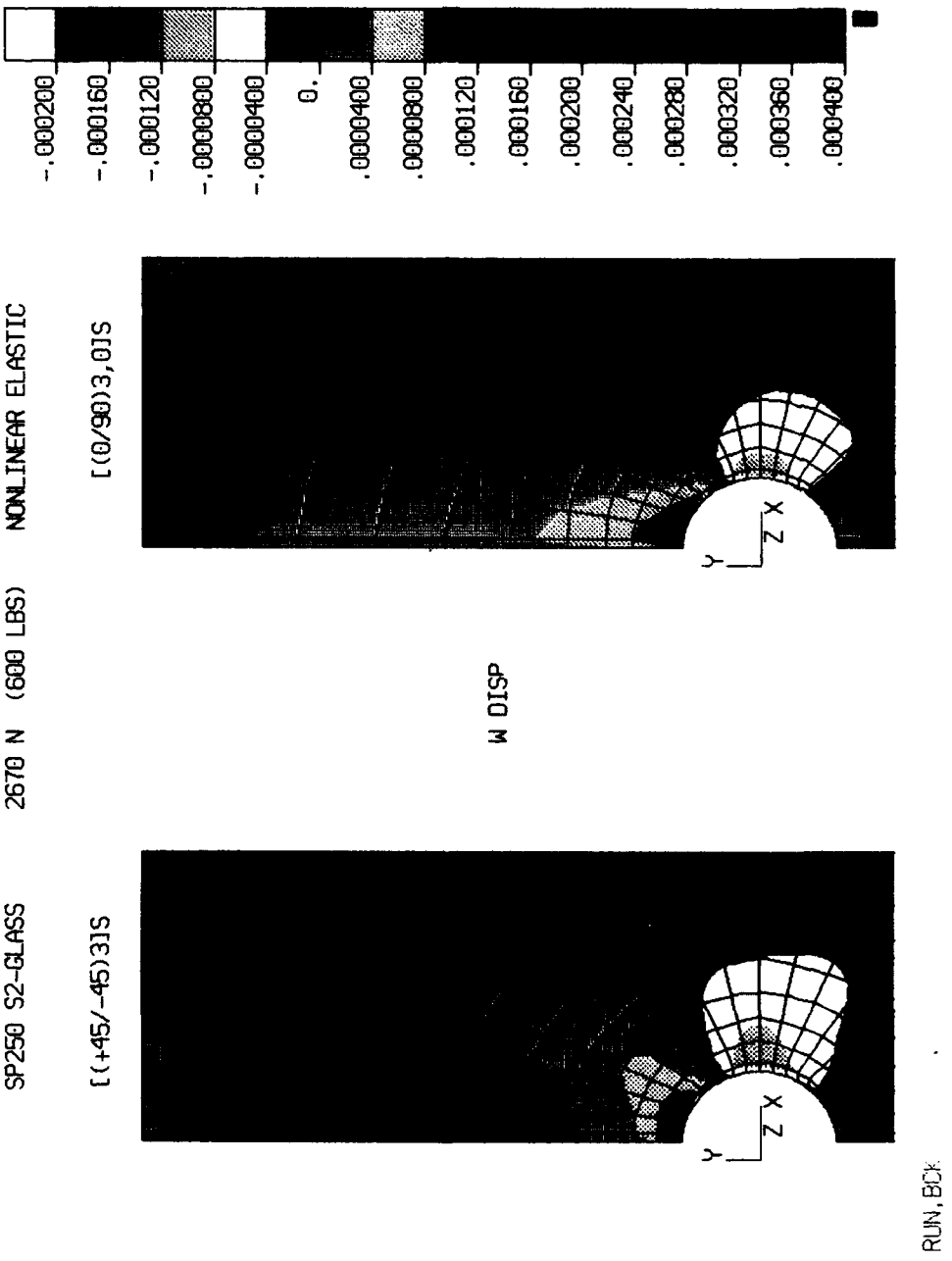

Figure 9.50 $[(0/90)_3,0]_s$ and $[(+45/-45)_3]_s$ Out-of Plane Front Surface Nonlinear Elastic Coupon Displacement [600 lbs load level]

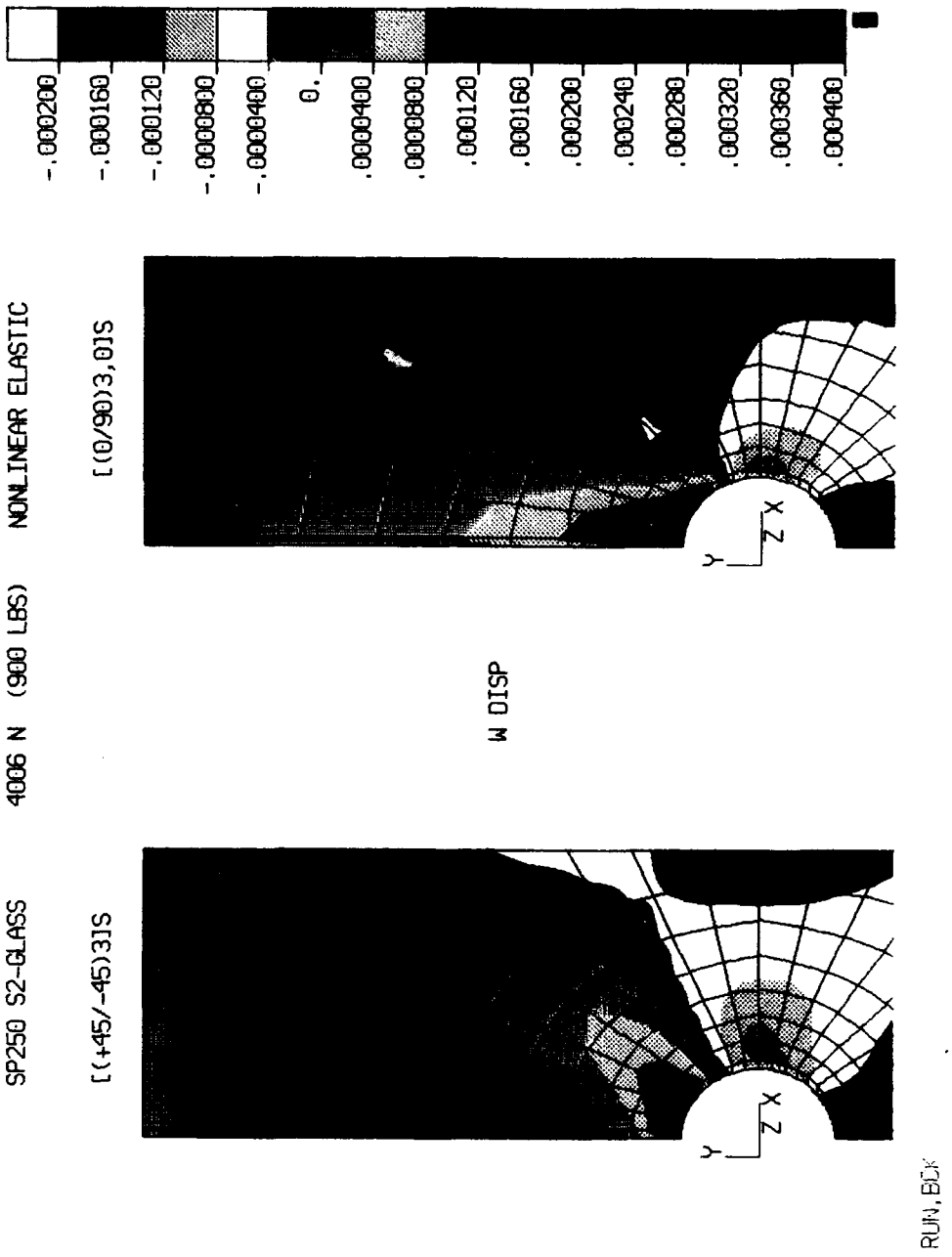

Figure 9.51 $[(0/90)_3,0]_s$ and $[(+45/-45)_3]_s$ Out-of Plane Front Surface Nonlinear Elastic Coupon Displacement [900 lbs load level]

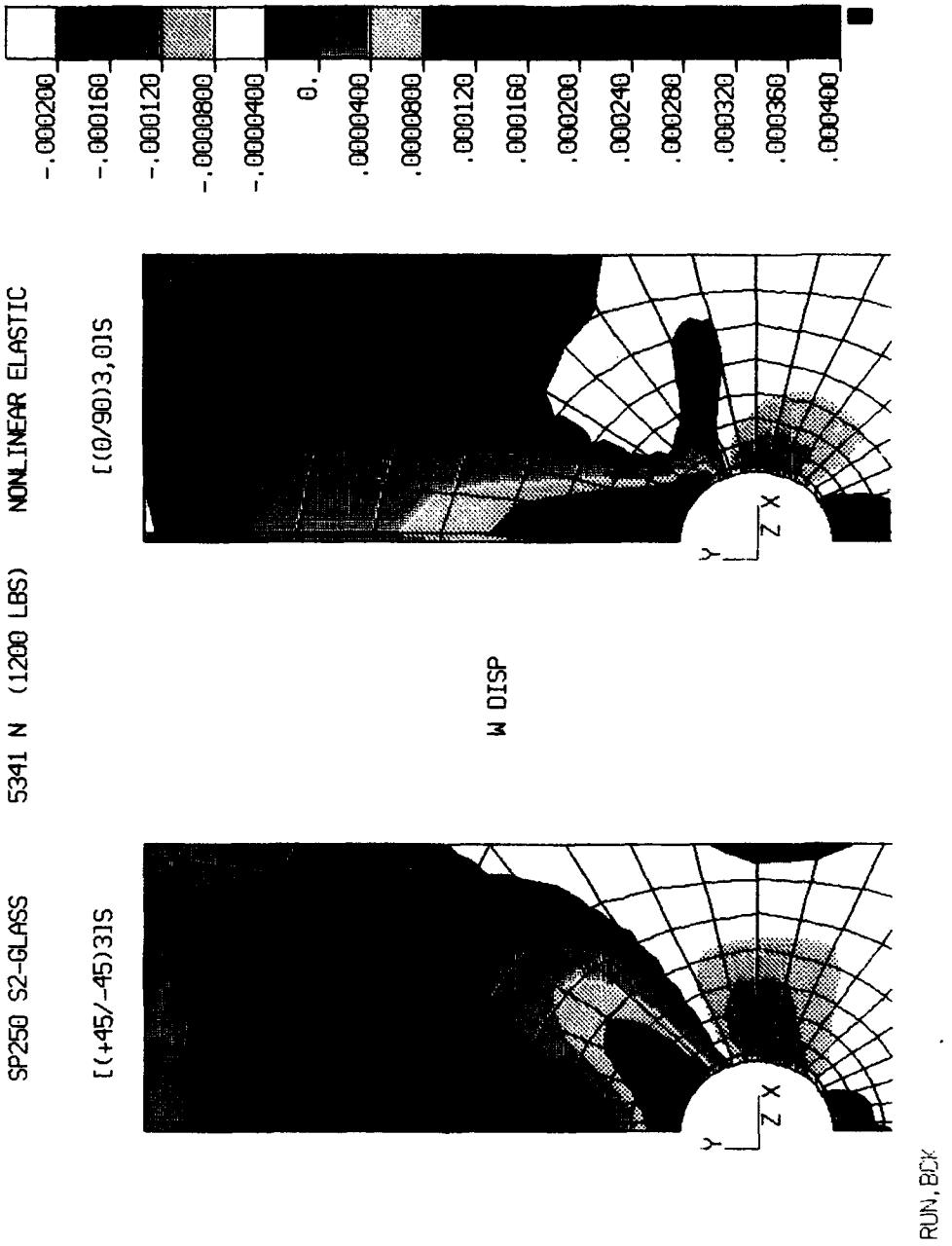

Figure 9.52 $[(0/90)_3,0]_s$ and $[(+45/-45)_3]s$ Out-of Plane Front Surface Nonlinear Elastic Coupon Displacement [1200 lbs load level]

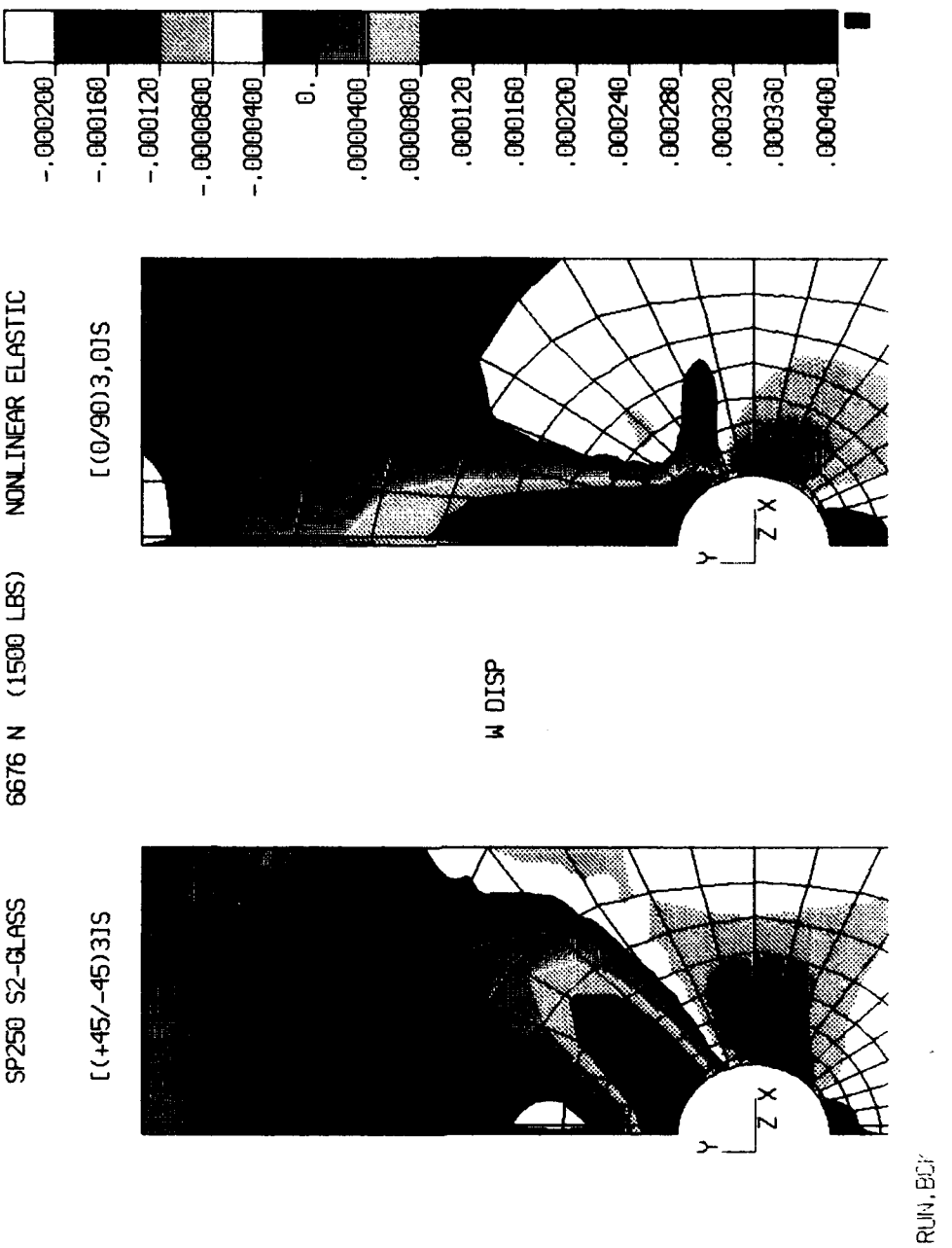

Figure 9.53 $[(0/90)_3,0]_s$ and $[(+45/-45)_3]s$ Out-of Plane Front Surface Nonlinear Elastic Coupon Displacement [1500 lbs load level]

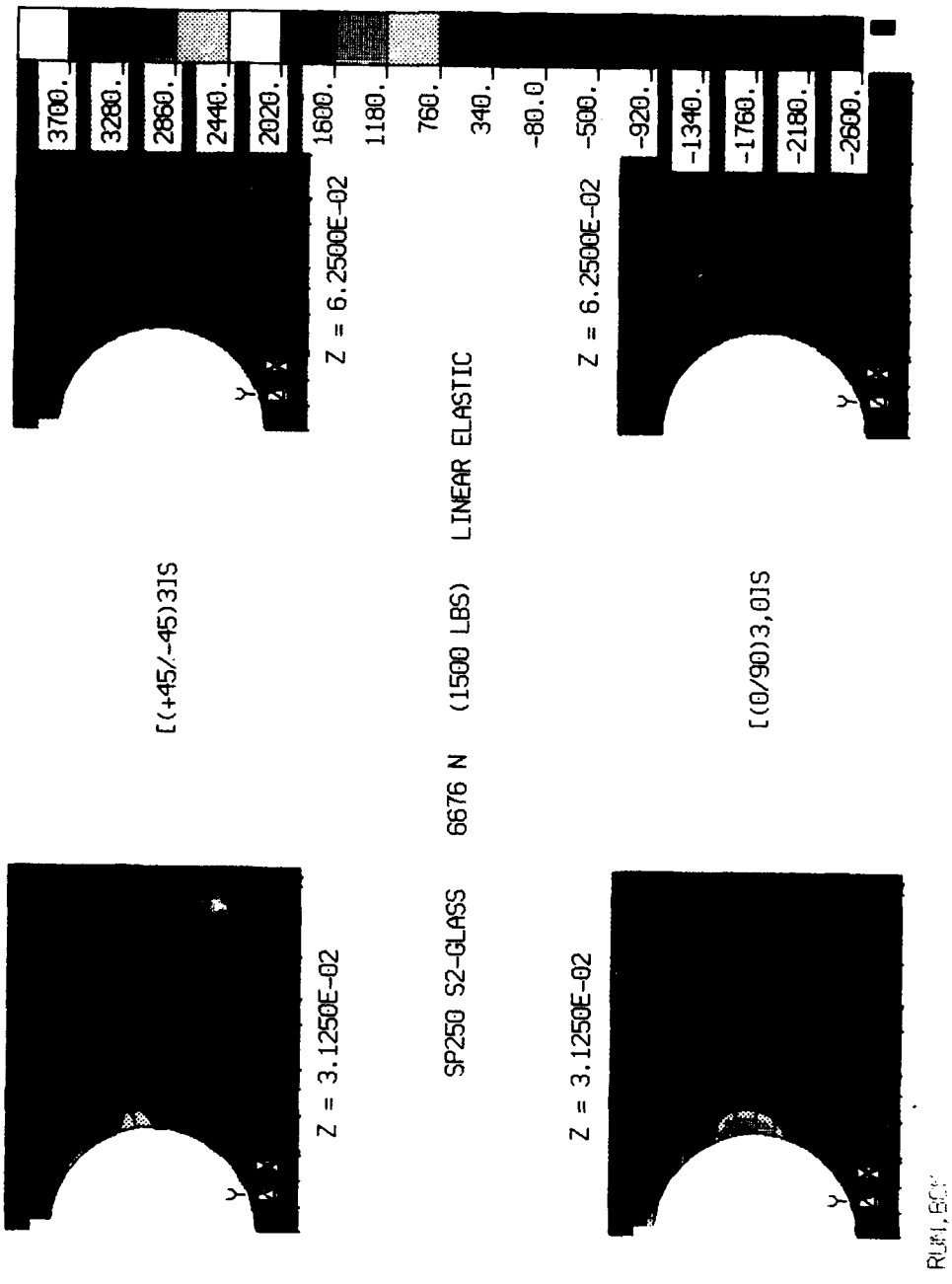

Figure 9.54 $[(0/90)_3,0]_s$ and $[(+45/-45)_3]_s$ Linear Elastic Coupon σ_z Stresses [1500 lbs load level]

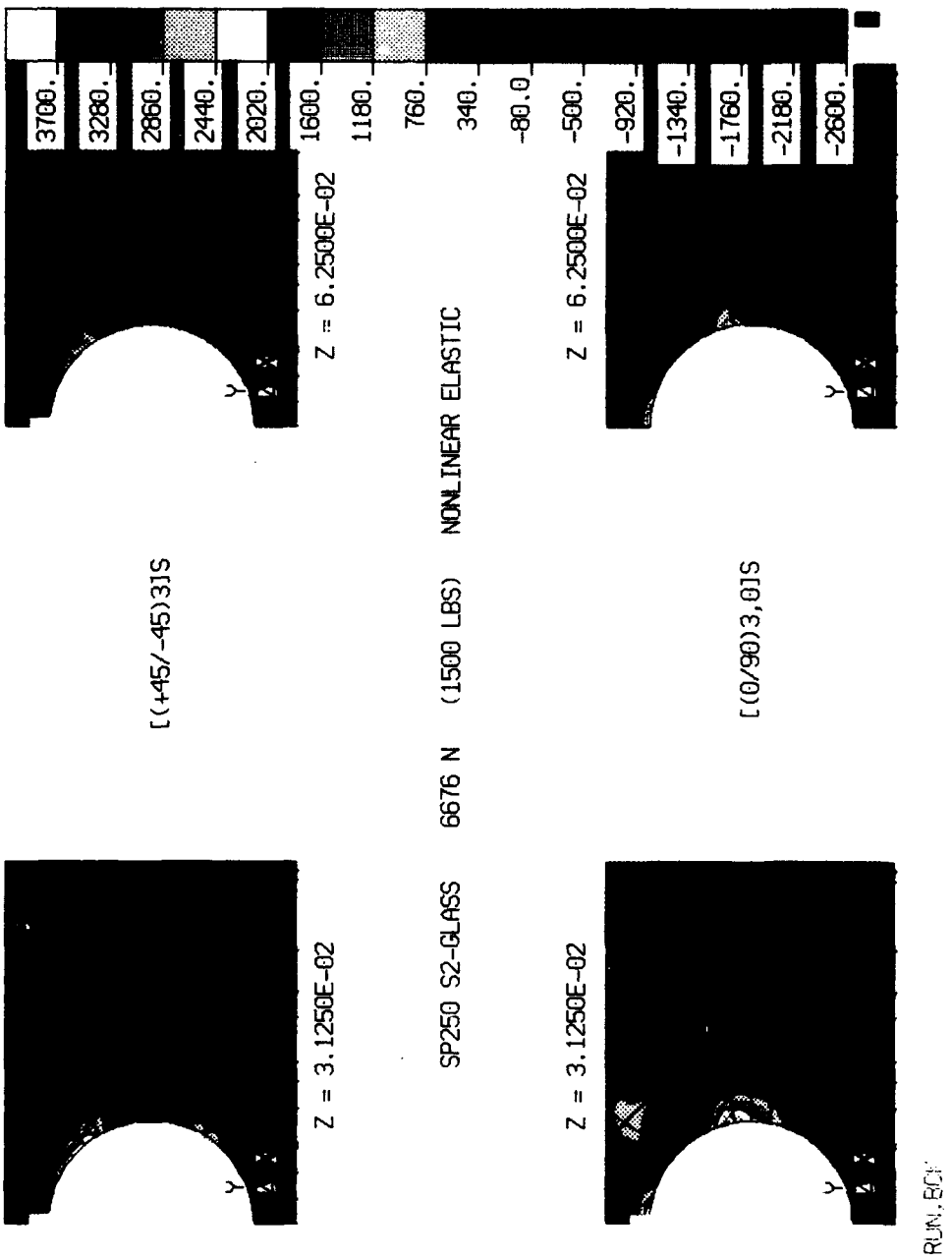

Figure 9.55 $[(0/90)_3,0]_s$ and $[(+45/-45)_3]_s$ Nonlinear Elastic Coupon σ_z Stresses [1500 lbs load level]

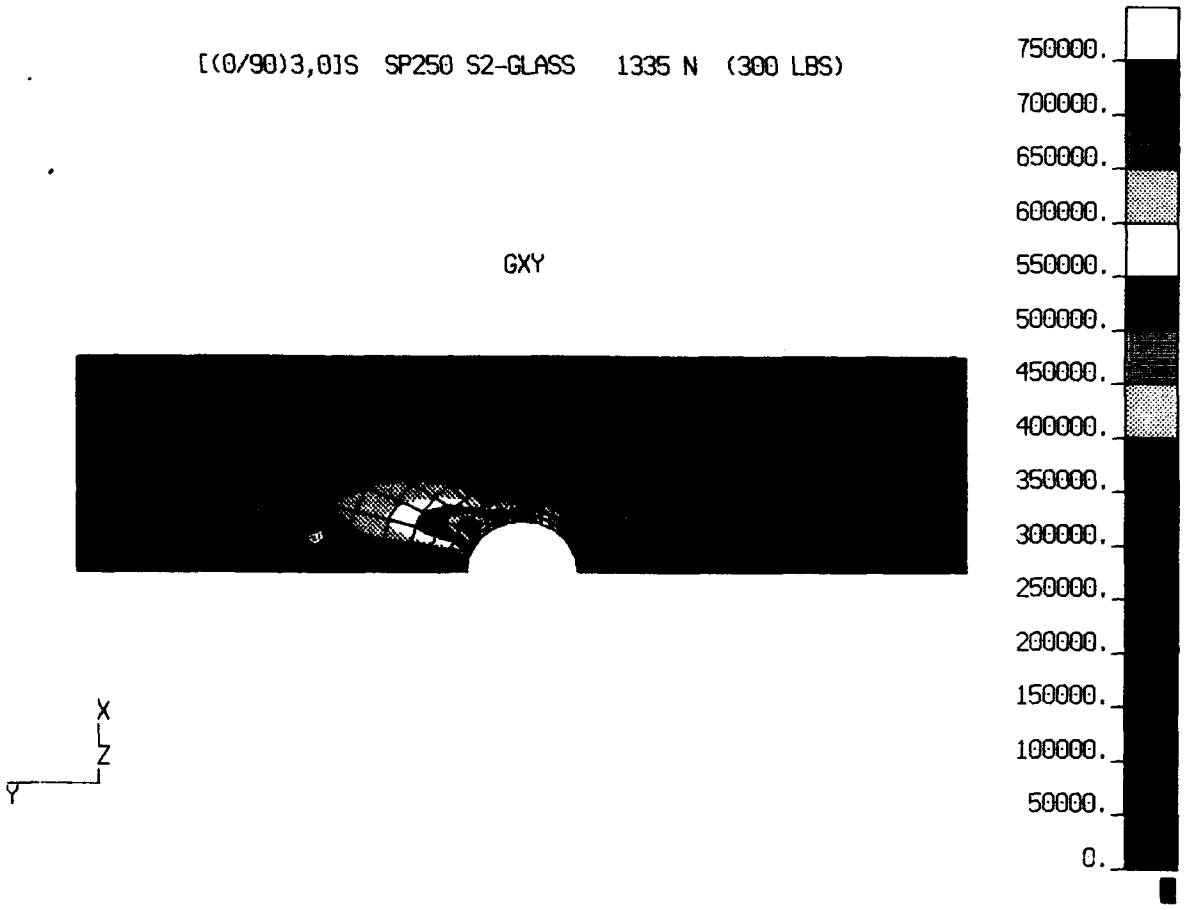

Figure 9.56 $[(0/90)_3,0]_s$ Nonlinear Elastic Coupon G_{xy} [300 lbs load level]

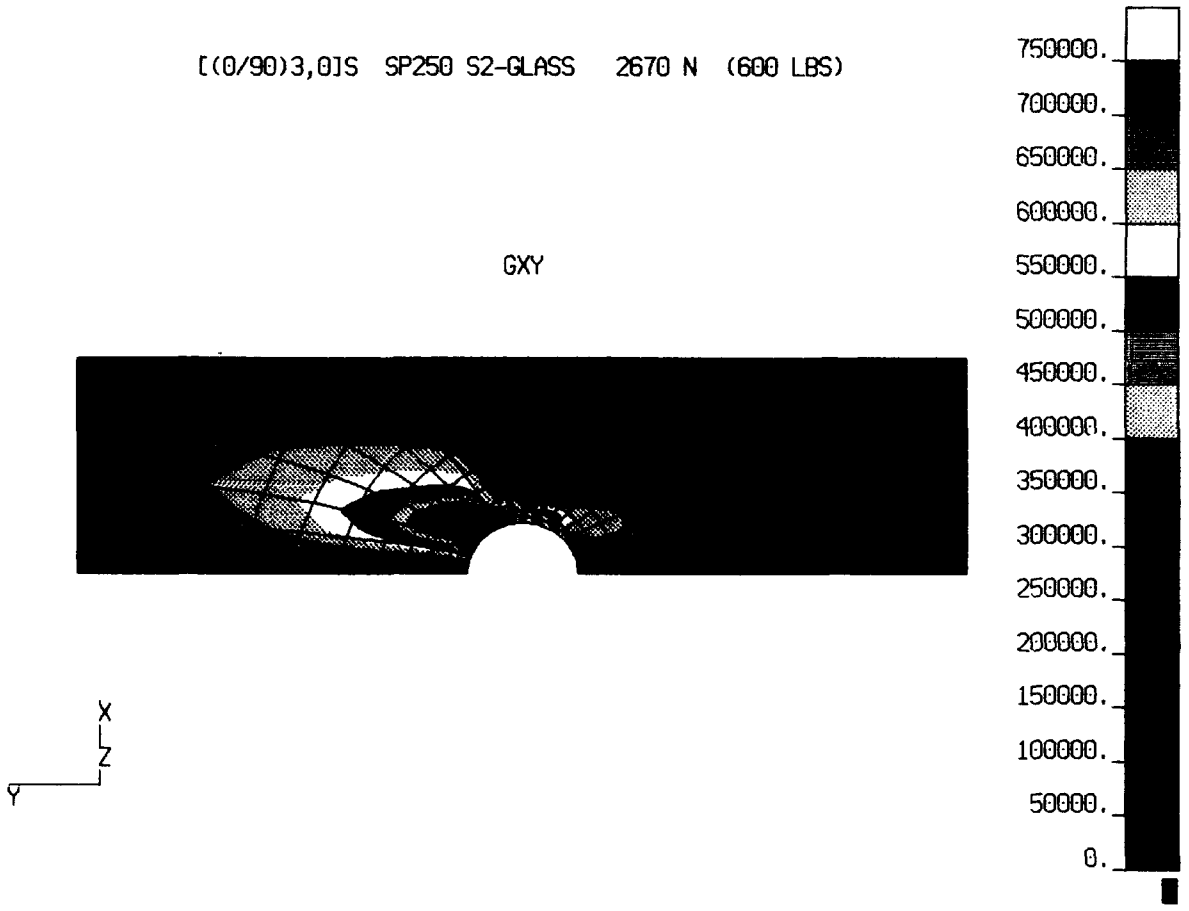

Figure 9.57 $[(0/90)_3,0]_s$ Nonlinear Elastic Coupon G_{xy} [600 lbs load level]

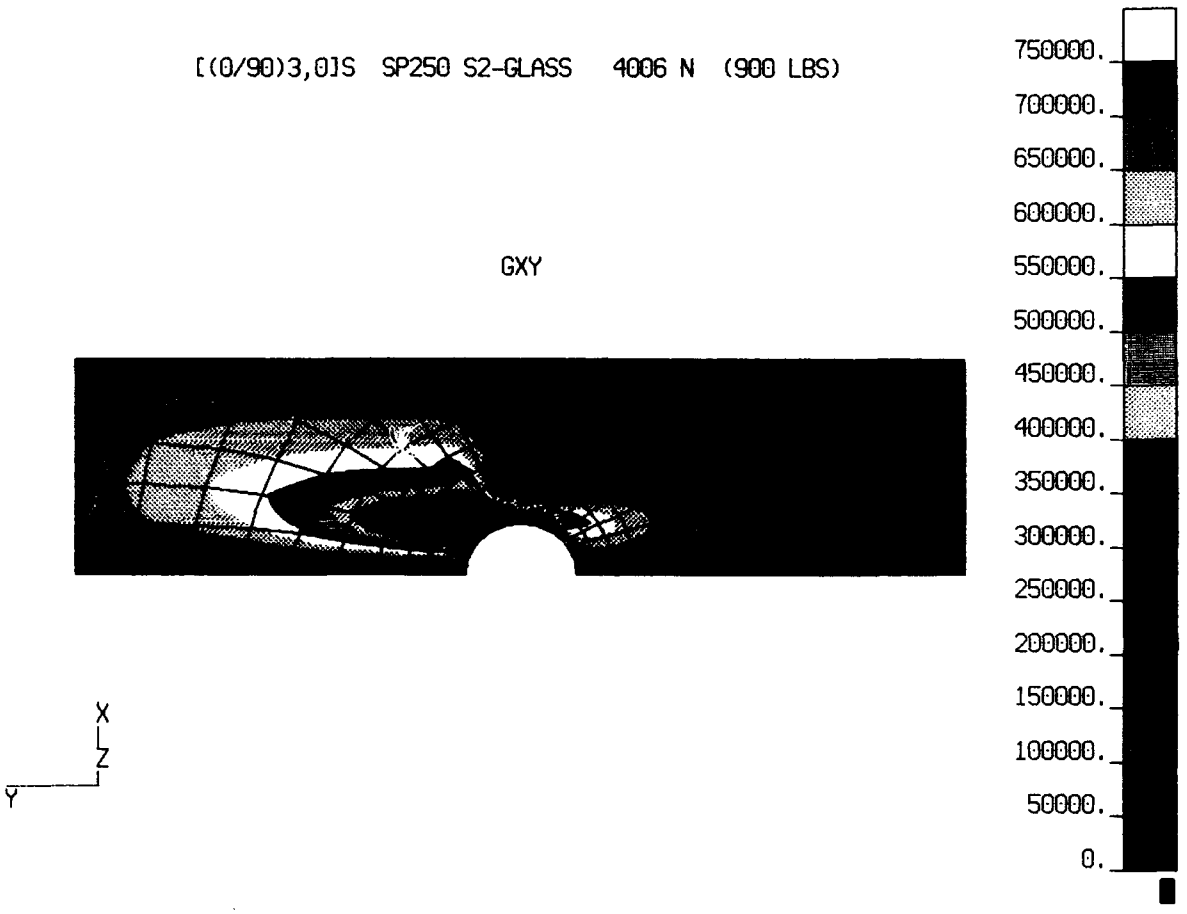

Figure 9.58 $[(0/90)_3,0]_s$ **Nonlinear Elastic Coupon** G_{xy} **[900 lbs load level]**

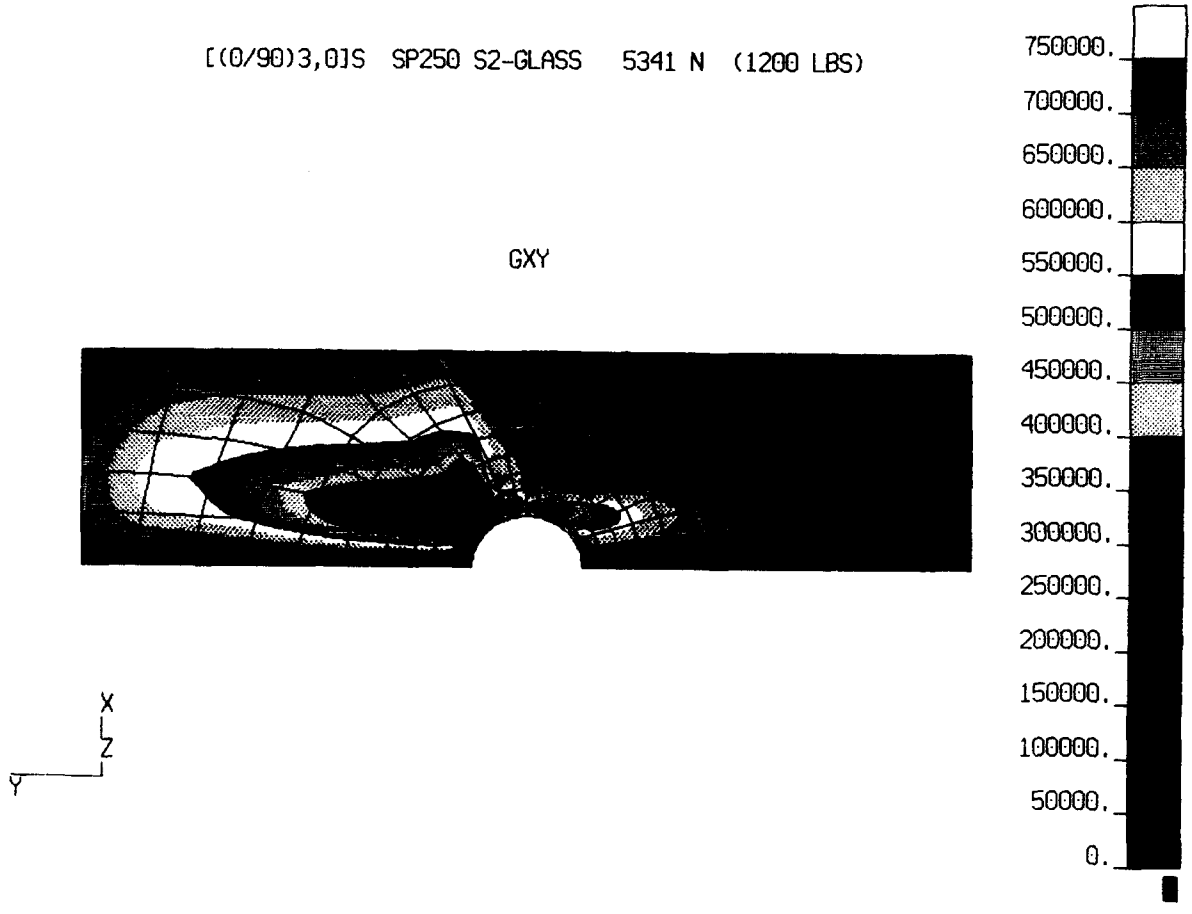

Figure 9.59 $[(0/90)_{3,0}]_s$ Nonlinear Elastic Coupon G_{xy} [1200 lbs load level]

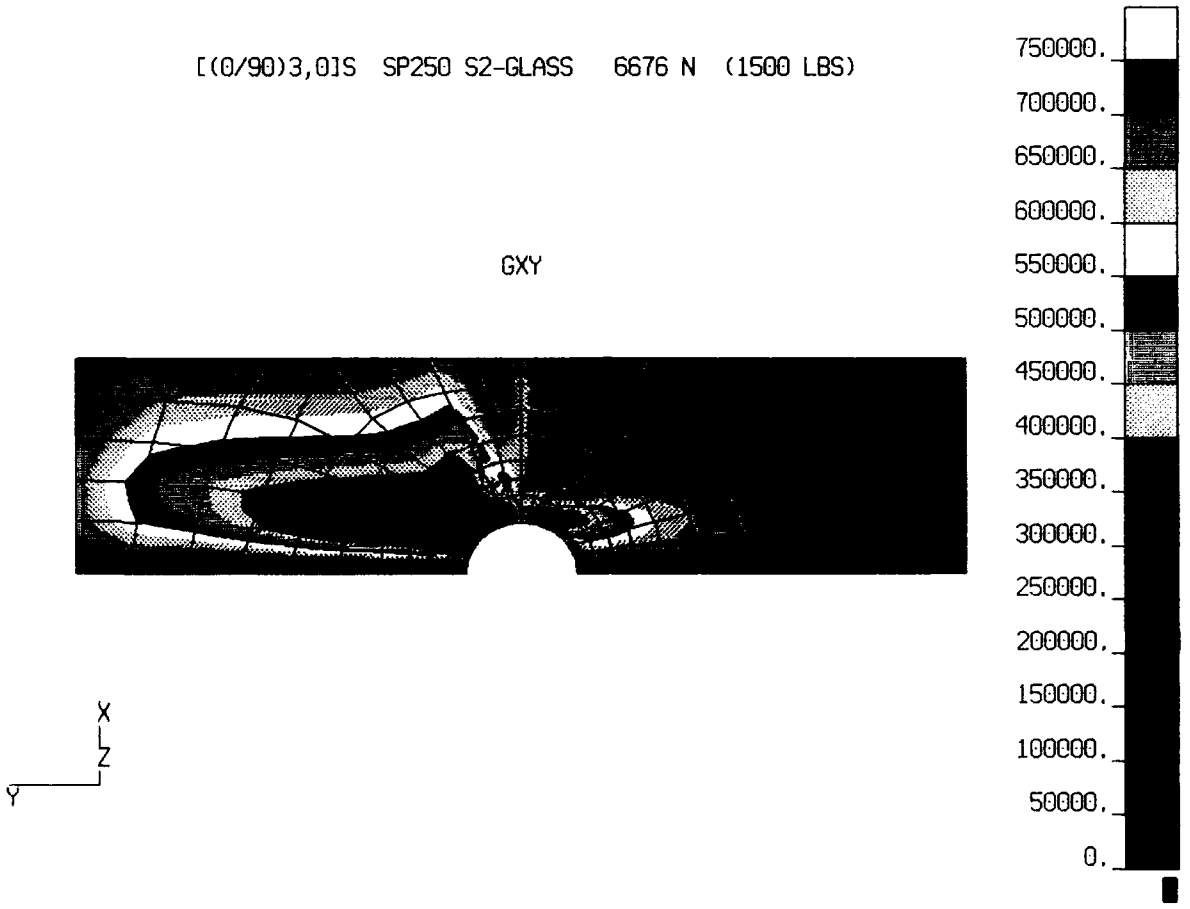

Figure 9.60 $[(0/90)_3,0]_s$ Nonlinear Elastic Coupon G_{xy} [1500 lbs load level]

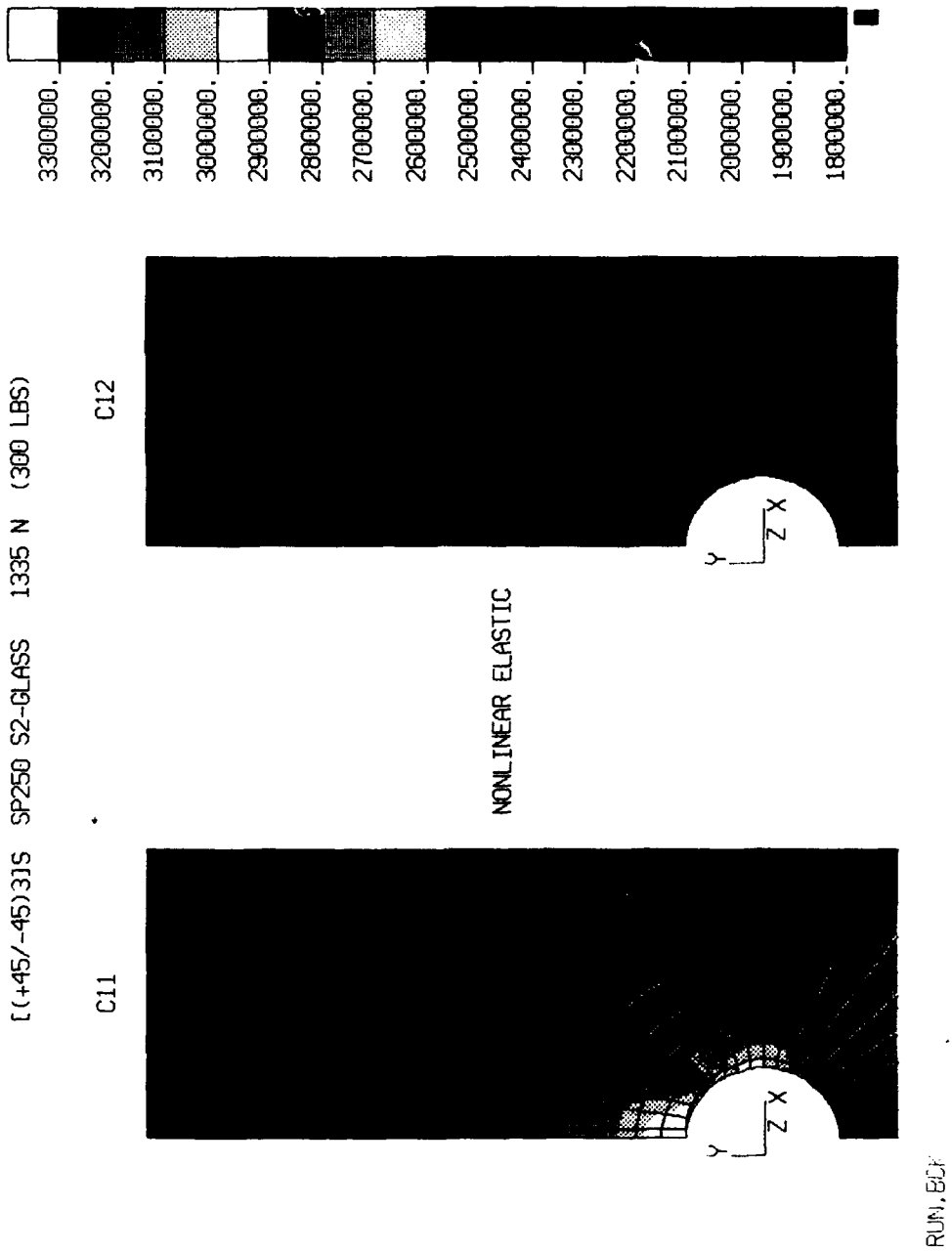

Figure 9.61 $[(+45/-45)_3]_s$ Nonlinear Elastic Coupon C_{11} and C_{12} Constitutive Equation Constants [300 lbs load level]

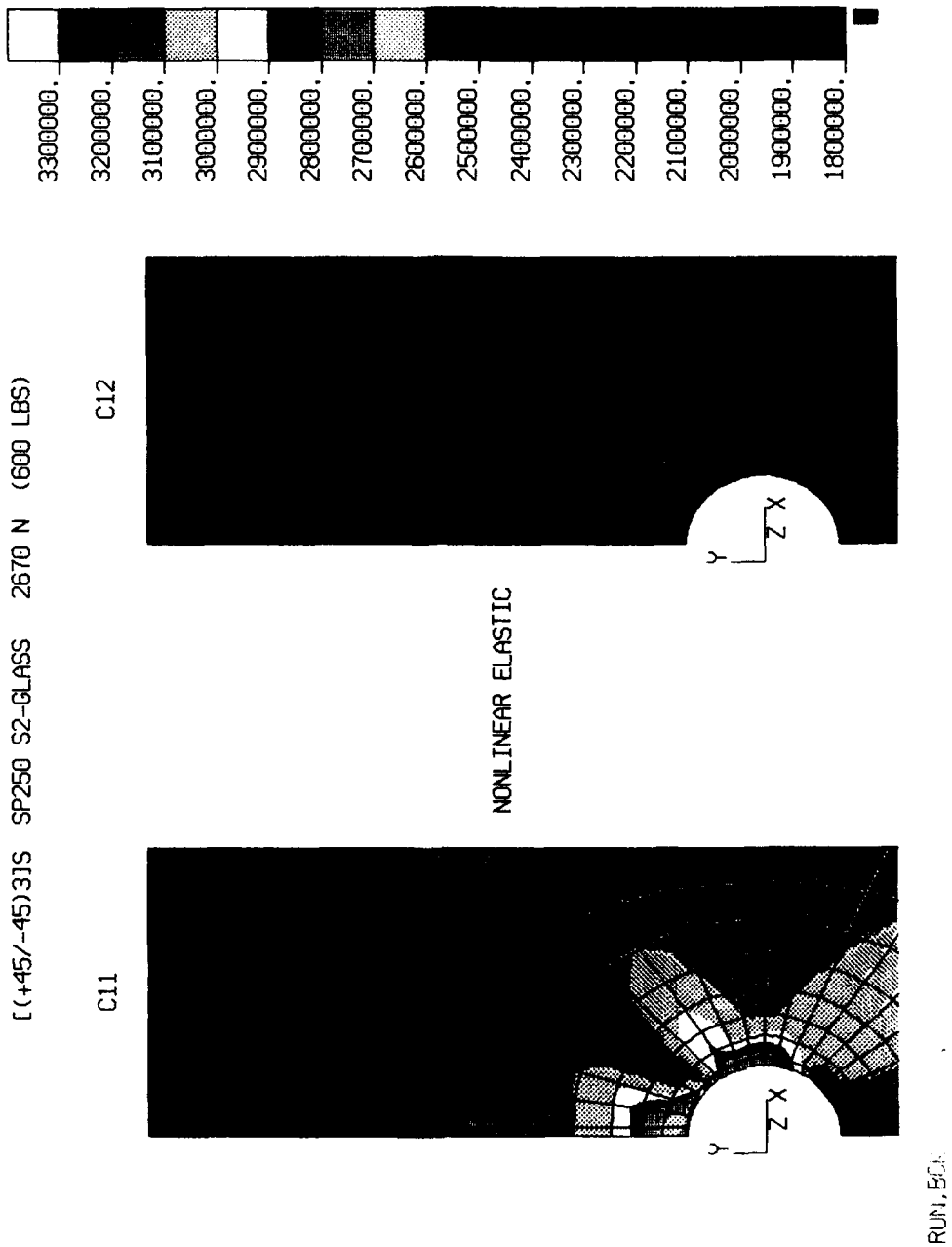

Figure 9.62 $[(+45/-45)_3]_s$ Nonlinear Elastic Coupon C_{11} and C_{12} Constitutive Equation Constants [600 lbs load level]

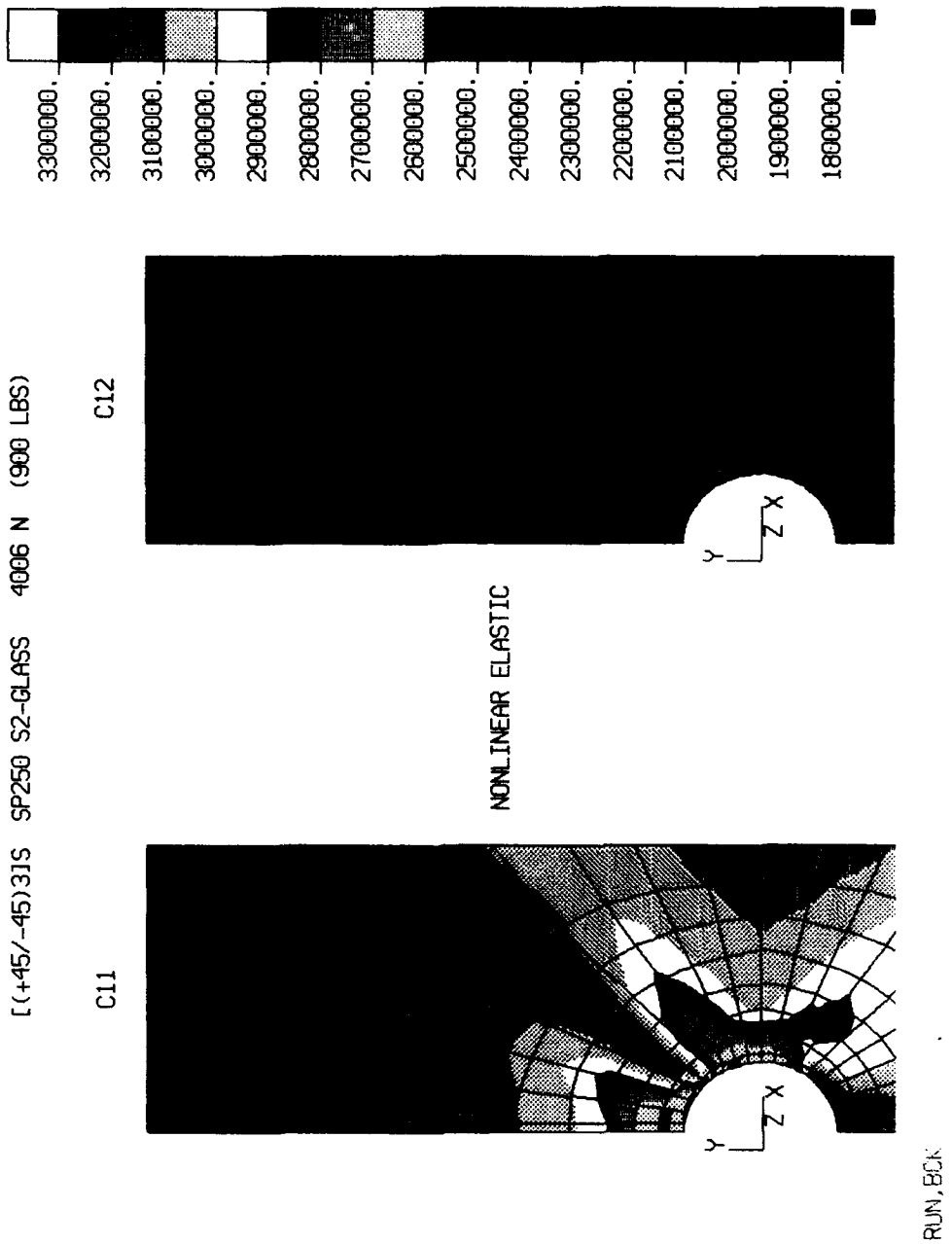

Figure 9.63 $[(+45/-45)_3]_s$ Nonlinear Elastic Coupon C_{11} and C_{12} Constitutive Equation Constants [900 lbs load level]

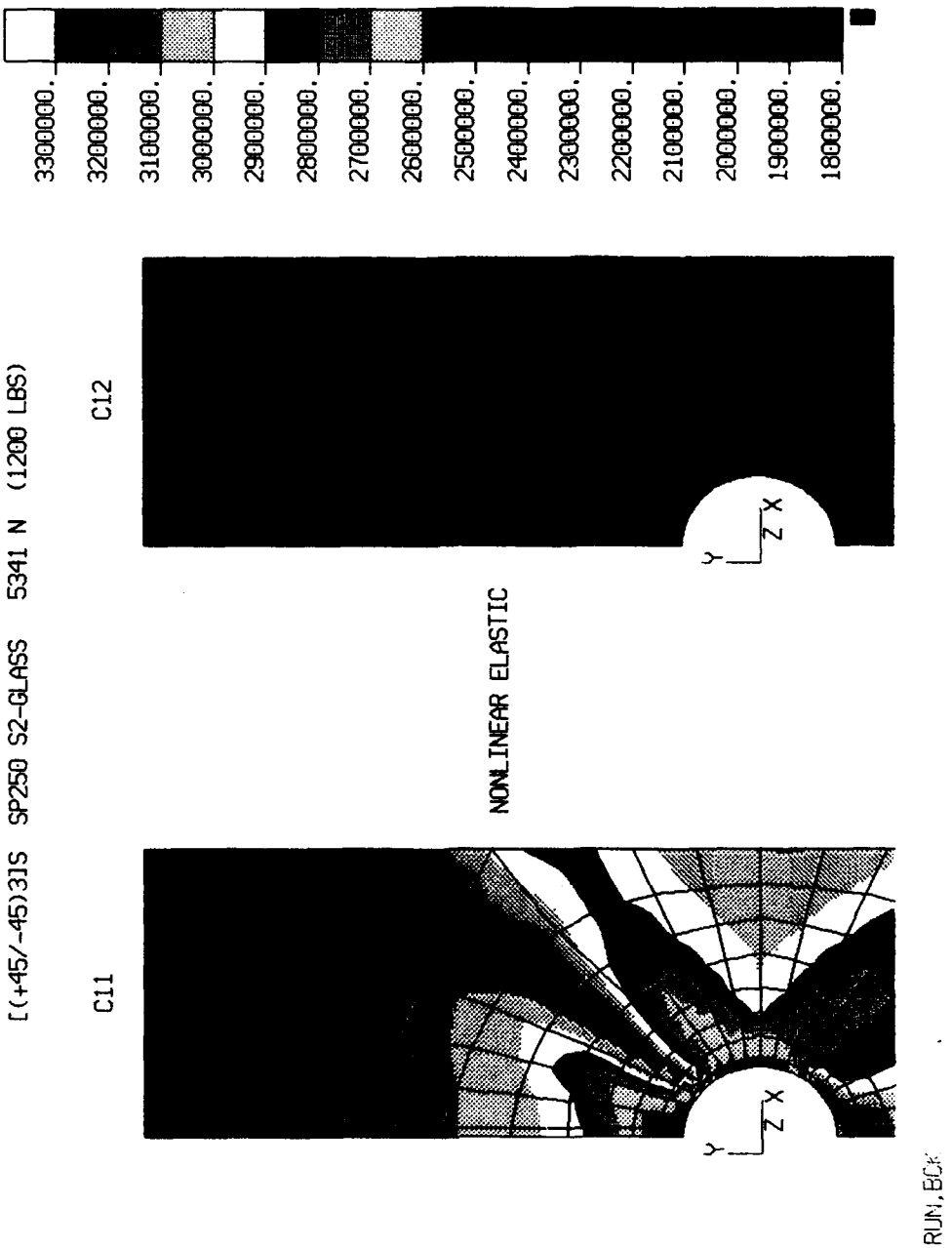

Figure 9.64 $[(+45/-45)_3]_s$ Nonlinear Elastic Coupon C_{11} and C_{12} Constitutive Equation Constants [1200 lbs load level]

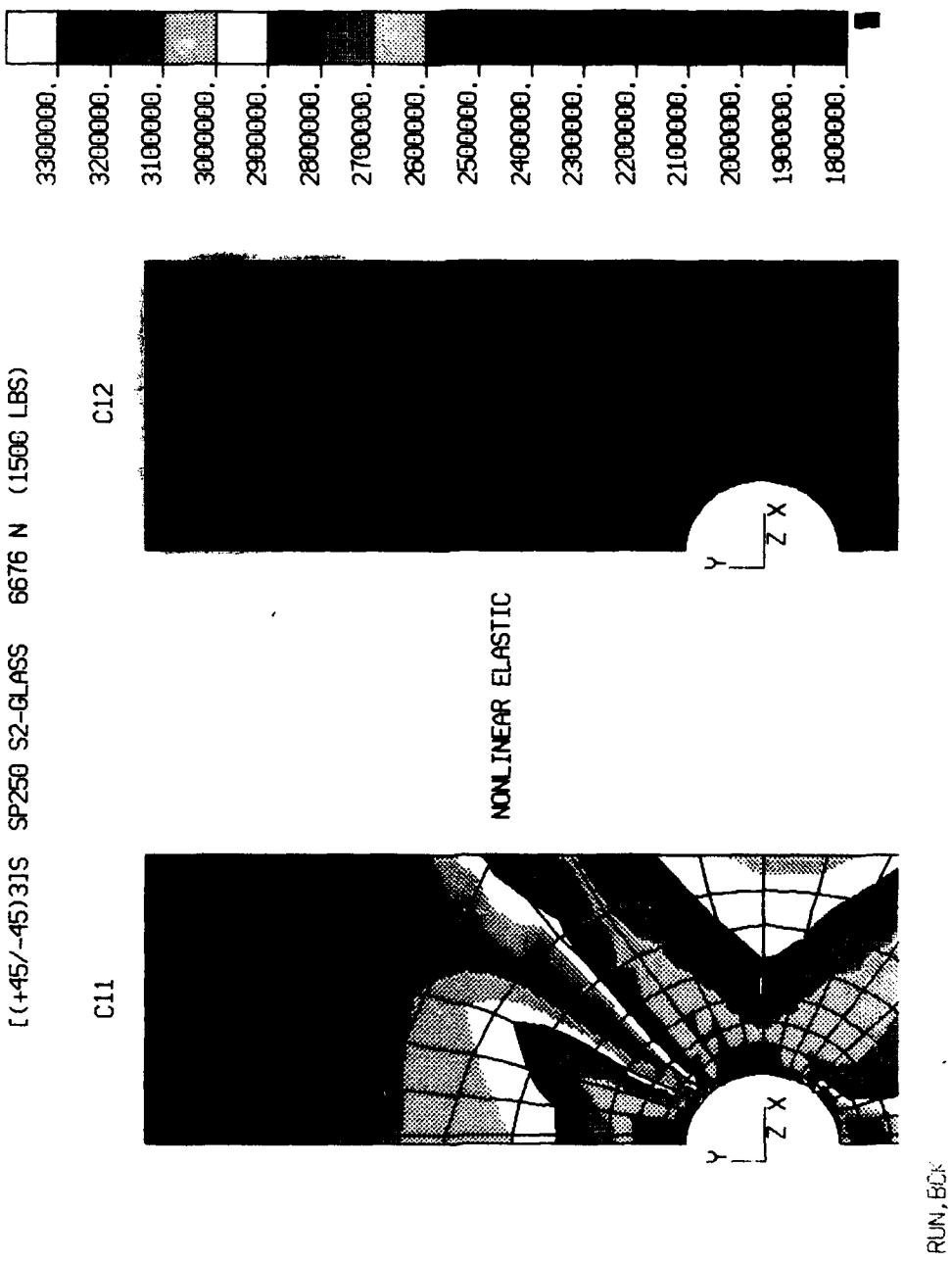

Figure 9.65 $[(+45/-45)_3]_s$ Nonlinear Elastic Coupon C_{11} and C_{12} Constitutive Equation Constants [1500 lbs load level]

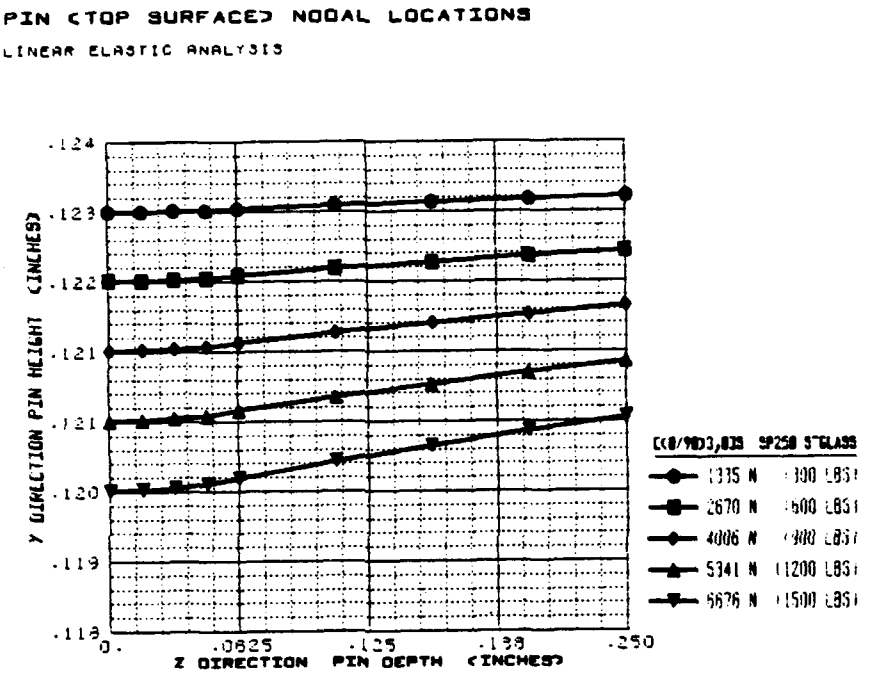

Figure 9.66 [(0/90)3,0]s Pin Top Surface Nodal Locations as a Function of Load Level [Linear Elastic Analysis]

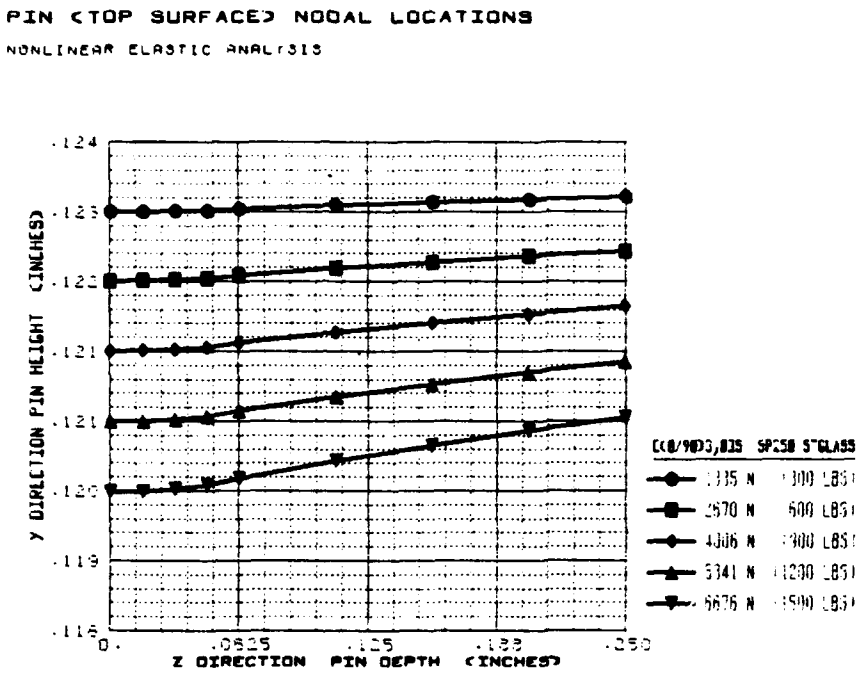

Figure 9.67 $[(0/90)_{3},0]_{s}$ Pin Top Surface Nodal Locations as a Function of Load Level [Nonlinear Elastic Analysis]

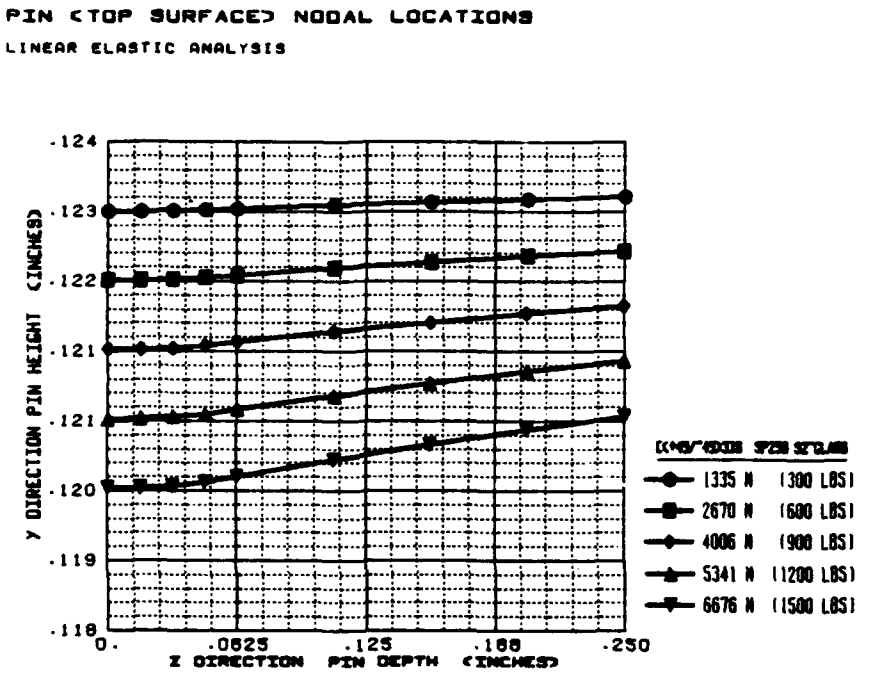

Figure 9.68 $[(+45/-45)_3]_s$ Pin Top Surface Nodal Locations as a Function of Load Level [Linear Elastic Analysis]

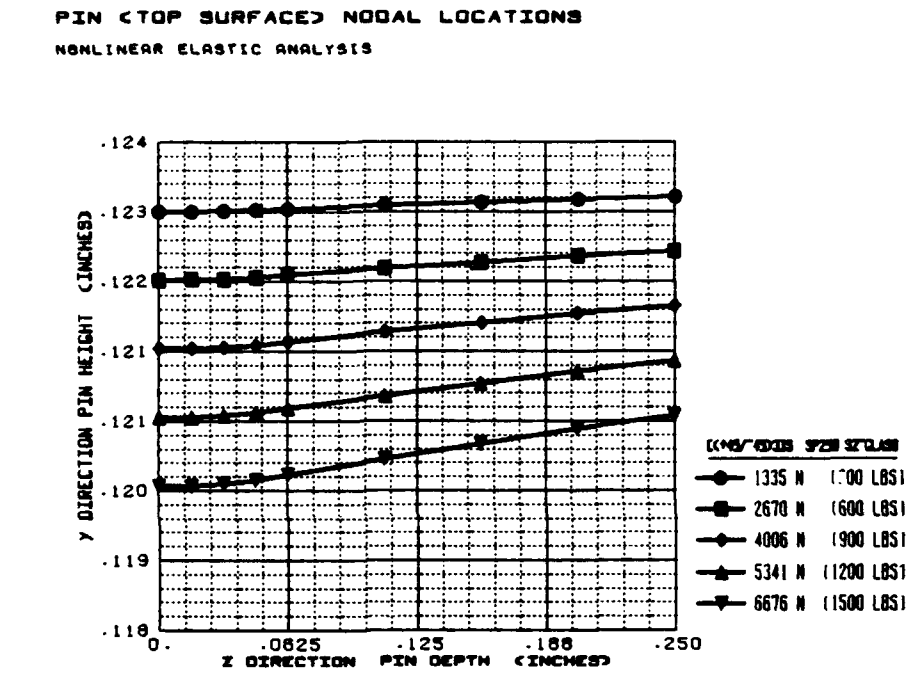

Figure 9.69 $[(+45/-45)_3]_s$ Pin Top Surface Nodal Locations as a Function of Load Level [Nonlinear Elastic Analysis]

CHAPTER 10. EXPERIMENTAL/NUMERICAL MODELING COMPARISONS

Post processing of the $[(+45/-45)_3]_s$ tensile and compressive mismatch moire displacement fields was undertaken along net and bearing section respectively to determine experimental ε_y strain values. Comparisons of these strains with three dimensional linear and nonlinear finite element approximations were made. Experimental and two dimensional linear elastic finite element $[(0/90)_3,0]_s$ intralaminar shear strains results [66] were compared to their respective values from three dimensional linear and nonlinear elastic finite element approximations.

10.1 Post Processing of Moire Displacement Contours

The $[(+45/-45)_3]_s$ experimental moire displacement contours were post processed using the moire fringe data acquisition system shown in Figure 10.1. The C1000-01 HAMAMATSU video camera was mounted at the end of the optical rail shown in Figure 5.13 to image the moire displacement fringe patterns within a CONRAC video monitor. Single light intensity scans were acquired with the HEWLETT-PACKARD 9845B computer through the C1000 HAMAMATSU digitizing unit. Light and dark fringe intensities of the 1024 pixel scan were digitized on a 256 grey level scale. Smoothing of these fringe intensity variations was done by slightly misfocusing the fringe pattern image. A typical scan line is shown in Figure 10.2. As can be seen, increased fringe density allowed a more accurate fringe center selection.

The $[(+45/-45)_3]_s$ moire fringe patterns with a compressive mismatch were used to obtain bearing section ε_y strains. Half order fringe locations of contour interval .0005" were obtained from a bearing section scan. Graphical differentiation of the resulting v displacement versus y location curve ($\partial v/\partial y$) and subtraction of mismatch pattern strains yielded bearing

section ε_y strains at ten section locations. This procedure was followed for all load levels with the exception of the 300 lb case which suffered from poor photographic quality.

The $[(+45/-45)_3]_s$ moire fringe patterns with a tensile mismatch were used to obtain net section ε_y strains. A total of ten vertical scans throughout the net section were made. Fringe shifting methods[1] were employed to straddle a light / dark fringe intensity variation over the net section for each scan. The .0005" displacement contour interval of this light / dark fringe pair divided by its measured fringe spacing yielded the net section ε_y strains for each scan. This procedure was followed for all load levels with the exception of the 300 lb case which suffered from poor photographic quality.

10.2 $[(0/90)_3,0]_s$ Laminate Comparisons

Maximum $[(0/90)_3,0]_s$ intralaminar shear strain values for both the linear and nonlinear elastic three dimensional finite element analysis were compared to those from the two dimensional linear elastic finite element and moire results from the authors earlier work [66]. These comparisons may be seen in Figures 10.3 through 10.7. The two dimensional linear elastic finite element results were slightly less than their three dimensional linear elastic counterparts. Moire intralaminar shear strain values appeared to be somewhat lower than these two dimensional results for the 300 lb load level. The 600 lb and 900 lb load levels showed an agreement with the two and three dimensional analysis respectively while the 1200 lb load level showed a closer agreement with the three dimensional nonlinear elastic analysis. However; the 300 lb, 600 lb, and 900 lb load level moire results were lower closer to the pin than their sectional trends suggested. Moire results for the 1500 lb load level were in good agreement with the three dimensional nonlinear elastic results away from the pin, but showed an increased tendency to exceed those values closer to the pin.

The observation of slightly higher γ_{xy} strain values for the three dimensional analysis in comparison to those of the two dimensional analysis was no doubt caused by pin elasticity effects. The simply supported pin

boundary conditions employed in the three dimensional analysis produced pin deflections that caused an uneven through thickness load transfer between the pin and the coupon. This may be seen in the pin deflections of Figures 9.65 - 9.68. In this instance, front surface strains were slightly higher than midsurface or rigid pin strains.

The increased tendency of the moire strain data to approach and surpass the three dimensional nonlinear elastic analysis results with increasing load level was caused by the unsymmetric experimental pin boundary conditions and the presence of a material shear failure mechanism. The clamped/simply supported boundary conditions of the respective rear and front pin surfaces employed during the experimental moire analysis resulted in unsymmetric pin deflections. This type of deflection caused the rear surface of the coupon to carry a higher percentage of the pin load than the front surface forcing initial front surface moire strains to be lower than those predicted by analysis. This is born out by the uneven front and rear surface coupon strain values observed in the author's earlier work [66] where a clamped/free (rear/front) pin boundary condition was initially investigated. Lower experimental moire shear strains near the pin in the 300 lb, 600 lb, and 900 lb load cases was caused by using only the $\partial v/\partial x$ component of shear strain in determining γ_{xy}. The $\partial u/\partial y$ component of shear strain could not be determined due to a lack of u field contouring sensitivity. The presence of a material shear failure mechanism no doubt acted to progressively increase the shear strain values for the higher load levels thus causing them to approach and surpass those of the nonlinear elastic analysis.

10.3 $[(+45/-45)_3]_s$ Laminate Comparisons

A comparison of three dimensional linear and nonlinear elastic analysis $[(+45/-45)_3]_s$ bearing section ε_y strains with those for the experimental moire analysis may be seen in Figures 10.8 through 10.11. Similar net section ε_y strain comparisons may be seen in Figures 10.12 through 10.15.

For the 600 lb load, moire and finite element bearing strains were inclose comparison far from the pin. However, moire strain values appeared

lower than the linear elastic results close to the pin. All other load levels indicated a good agreement between moire and three dimensional nonlinear elastic finite element bearing strains. However, slightly lower moire bearing strain values were seen close to the pin followed by slightly higher moire bearing strain values just beyond the pin. Far field bearing strains were in excellent agreement with finite element results.

The 600 lb moire net section strains were in excellent agreement with the three dimensional nonlinear elastic finite element results. At subsequent load levels, net section moire strains appeared to exhibit progressively higher values than those of the nonlinear elastic analysis at close pin proximity. This divergence spread deeper into the net section with higher load level until the 1350 lb load case where far field net section moire strains exceeded those of the nonlinear elastic analysis.

Bearing strain comparisons close to the pin for the $[(+45/-45)_3]_s$ laminate appear to be affected by the clamped/simply supported (rear/front) experimental pin boundary conditions in much the same fashion as the $[(0/90)_3,0]_s$ intralaminar shear strain comparisons. Higher experimental moire strains are expected if a symmetric simply supported pin boundary condition was used during the experiment. Net section strain comparisons did not appear to suffer from this experimental pin boundary condition effect. This seemed plausible in that the unsymmetric pin/coupon load transfer occured in the bearing region and not the net section. Variations in net section moire strains from those of the three dimensional nonlinear elastic analysis were highly suggestive of a tensile material failure mechanism.

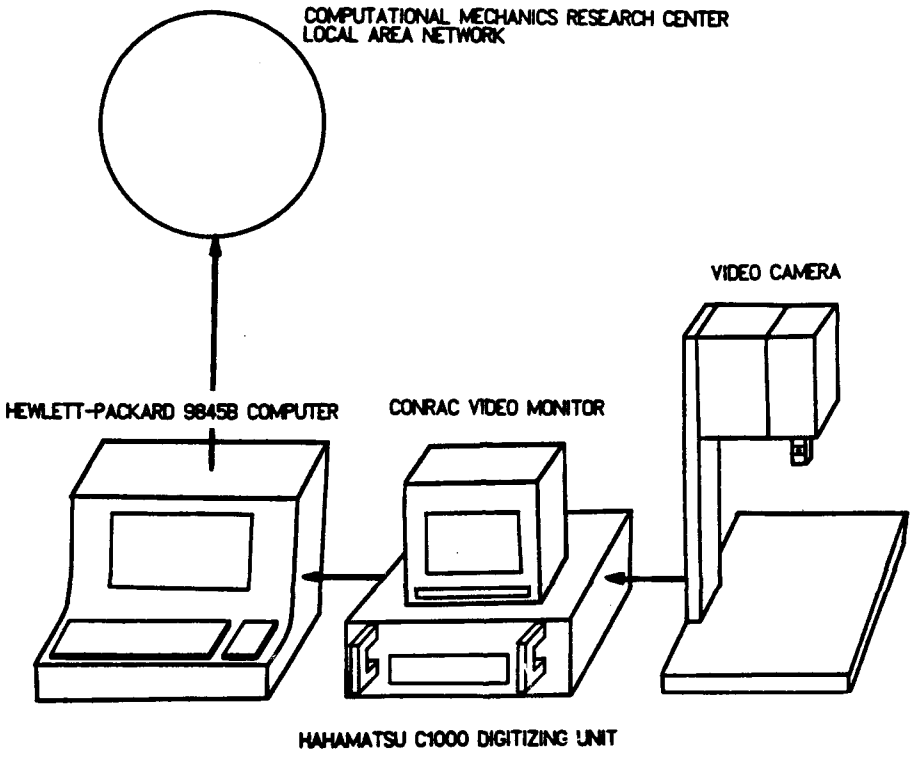

Figure 10.1 Moire Fringe Data Acquisition System

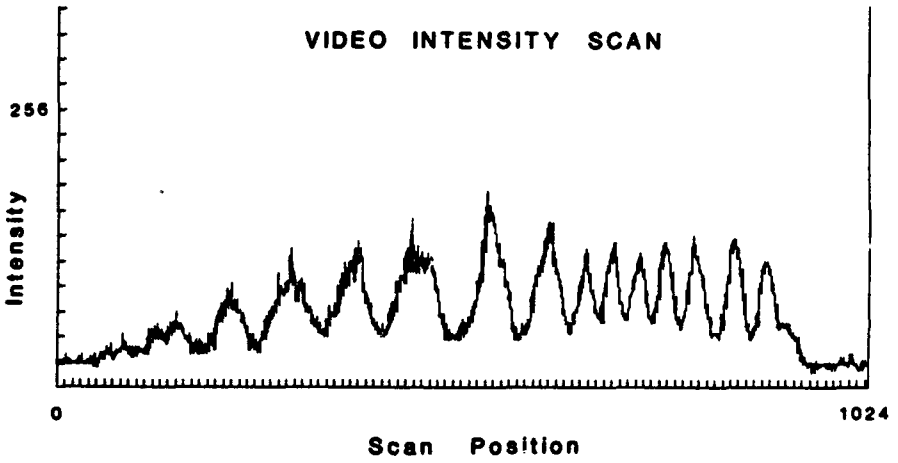

Figure 10.2 Typical Moire Fringe Pattern Video Intensity Scan

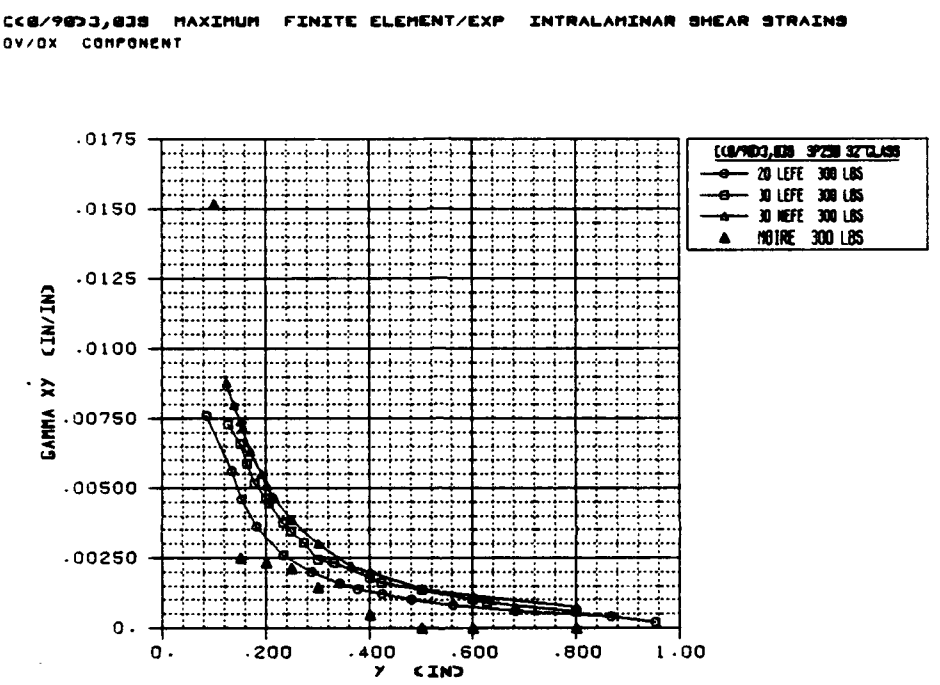

Figure 10.3 $[(0/90)_3,0]_s$ Finite Element and Moire Shearout Section γ_{xy} Strain Comparison [300 lbs]

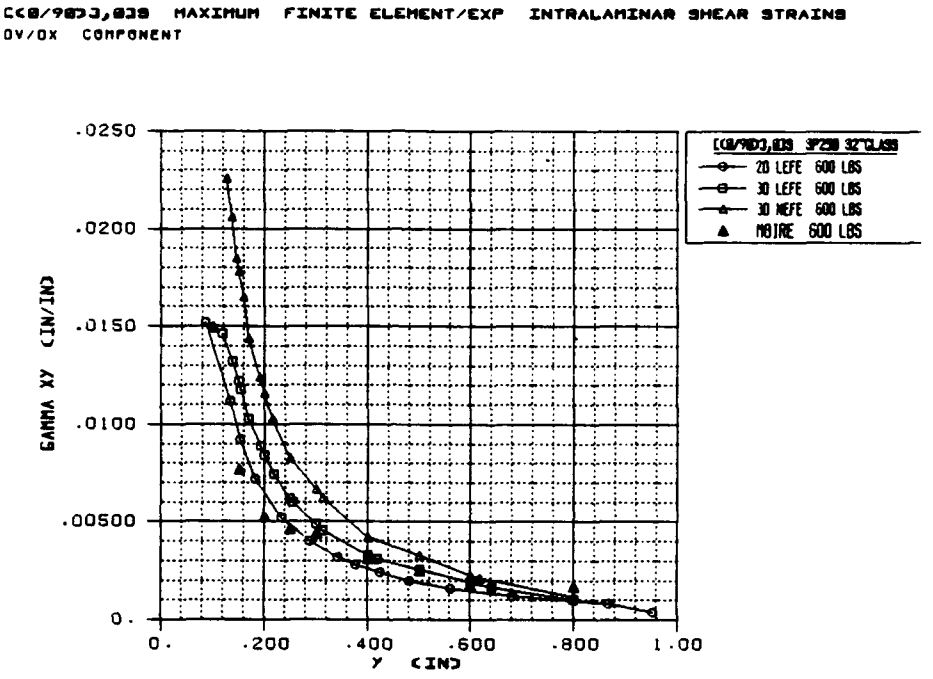

Figure 10.4 $[(0/90)_{3,0}]_S$ Finite Element and Moire Shearout Section γ_{xy} Strain Comparison [600 lbs]

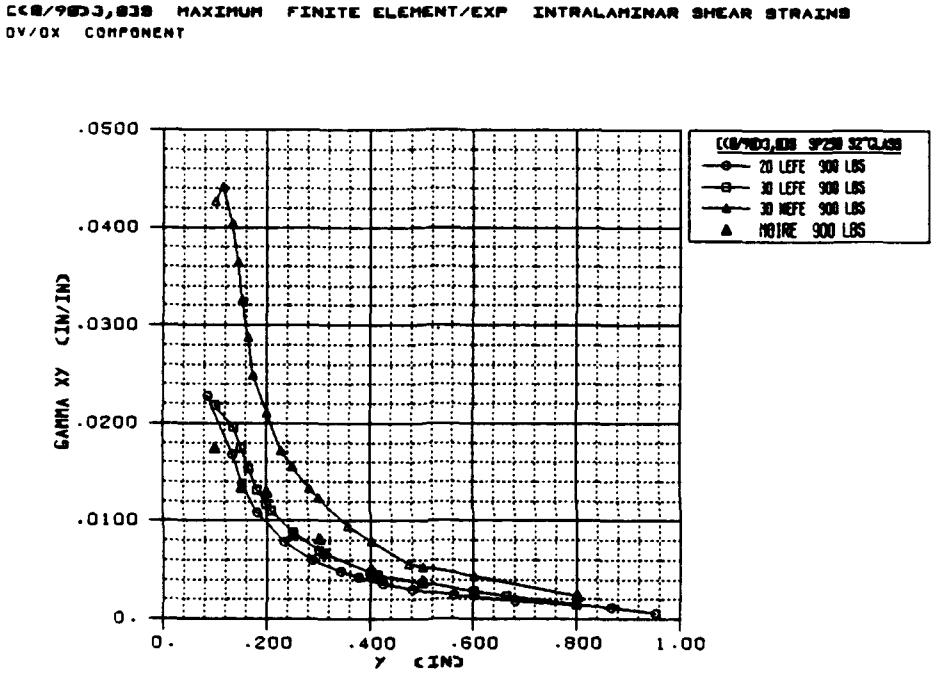

Figure 10.5 [(0/90)3,0]s Finite Element and Moire Shearout Section γ_{xy} Strain Comparison [900 lbs]

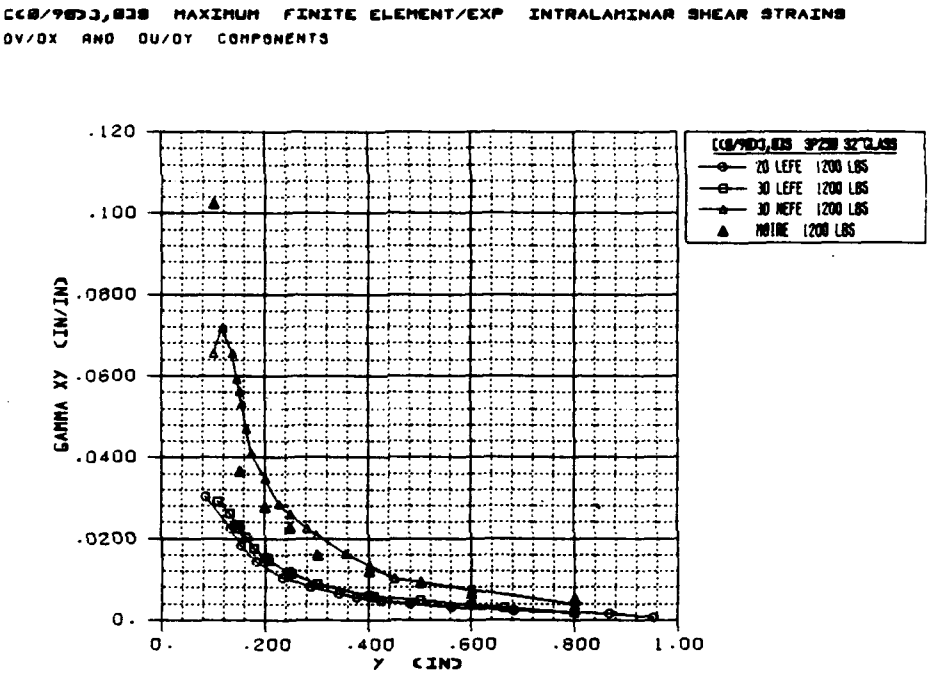

Figure 10.6 $[(0/90)_3,0]_s$ Finite Element and Moire Shearout Section γ_{xy} Strain Comparison [1200 lbs]

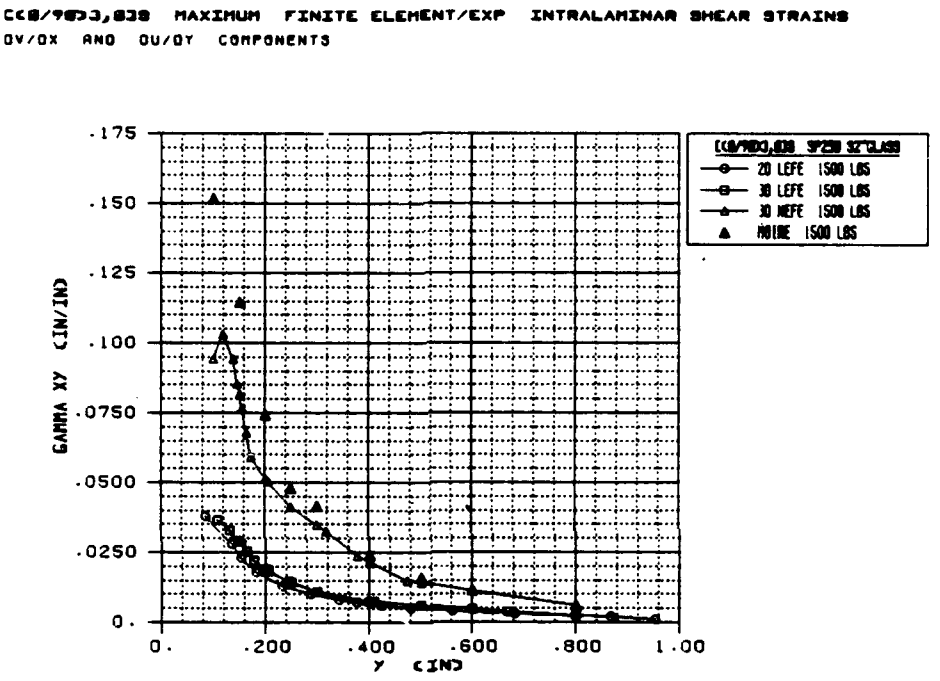

Figure 10.7 $[(0/90)_3,0]_s$ Finite Element and Moire Shearout Section γ_{xy} Strain Comparison [1500 lbs]

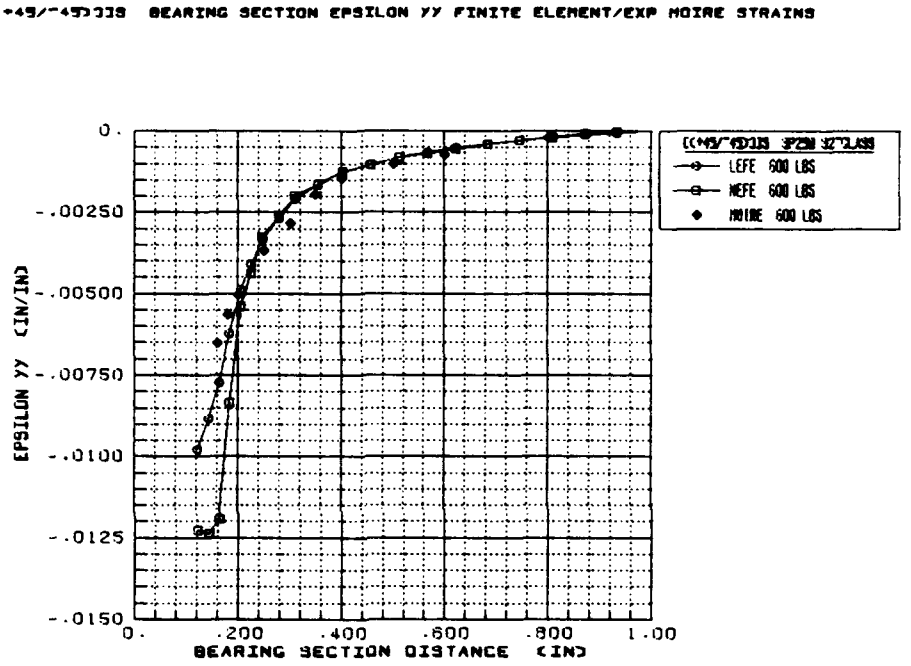

Figure 10.8 $[(+45/-45)_3]_s$ Finite Element and Moire Bearing Section ε_y Strain Comparison [600 lbs]

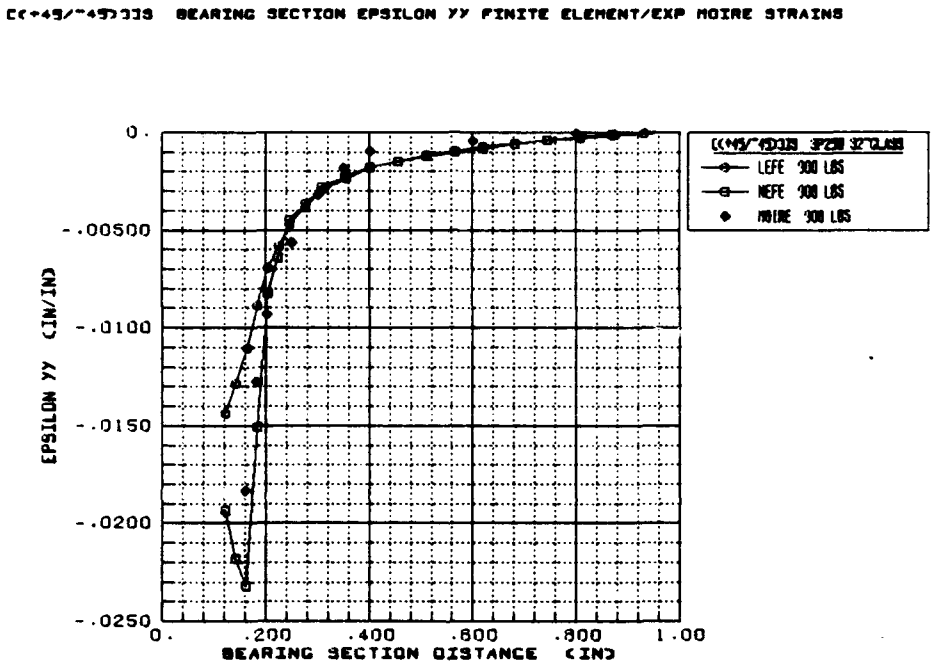

Figure 10.9 $[(+45/-45)_3]_s$ Finite Element and Moire Bearing Section ε_y Strain Comparison [900 lbs]

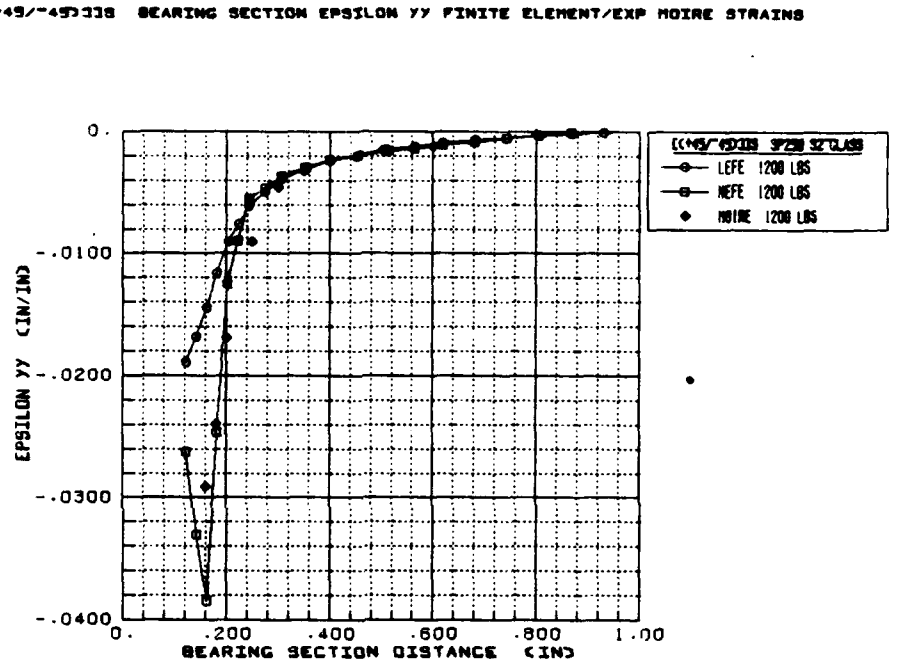

Figure 10.10 $[(+45/-45)_3]_s$ Finite Element and Moire Bearing Section ε_y Strain Comparison [1200 lbs]

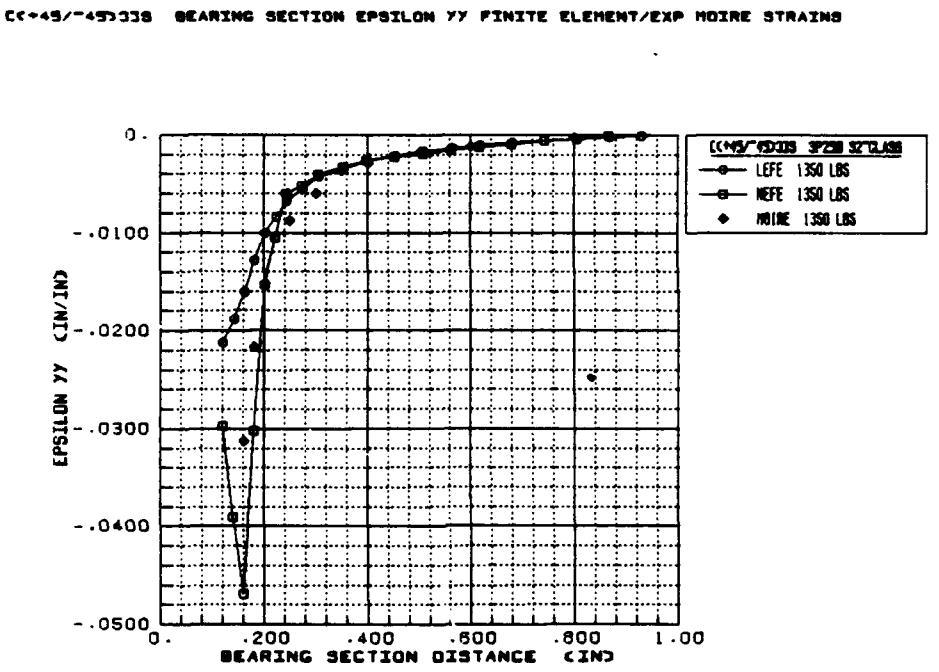

Figure 10.11 $[(+45/-45)_3]_s$ Finite Element and Moire Bearing Section ε_y Strain Comparison [1350 lbs]

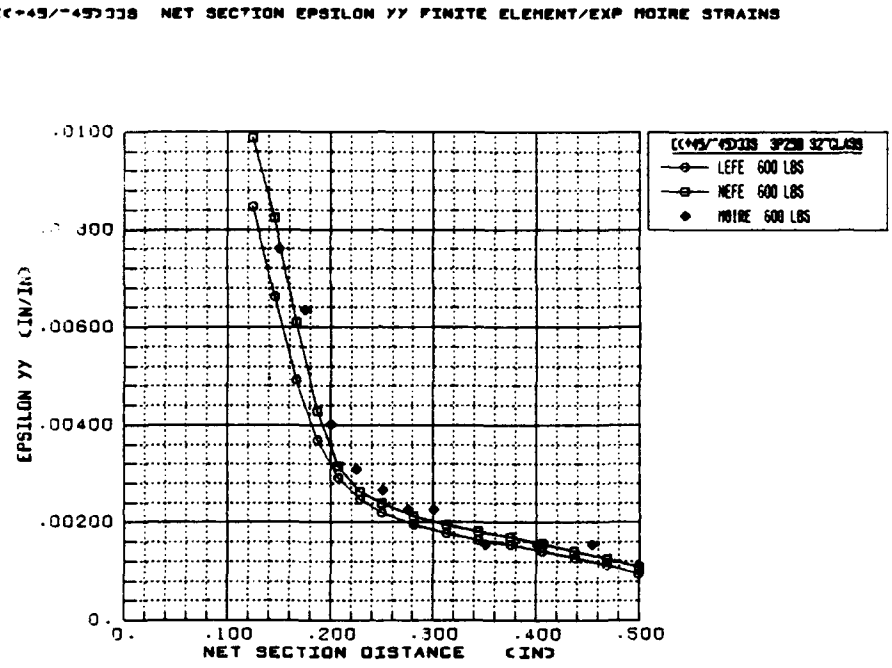

Figure 10.12 [(+45/-45)3]s Finite Element and Moire Net Section ε_y Strain Comparison [600 lbs]

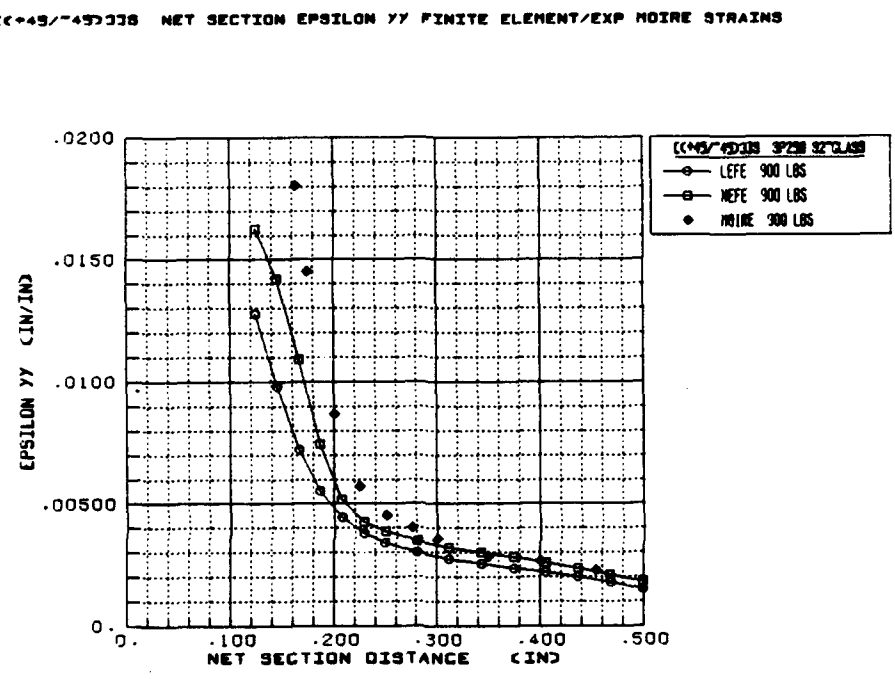

Figure 10.13 $[(+45/-45)_3]_s$ Finite Element and Moire Net Section ε_y Strain Comparison [900 lbs]

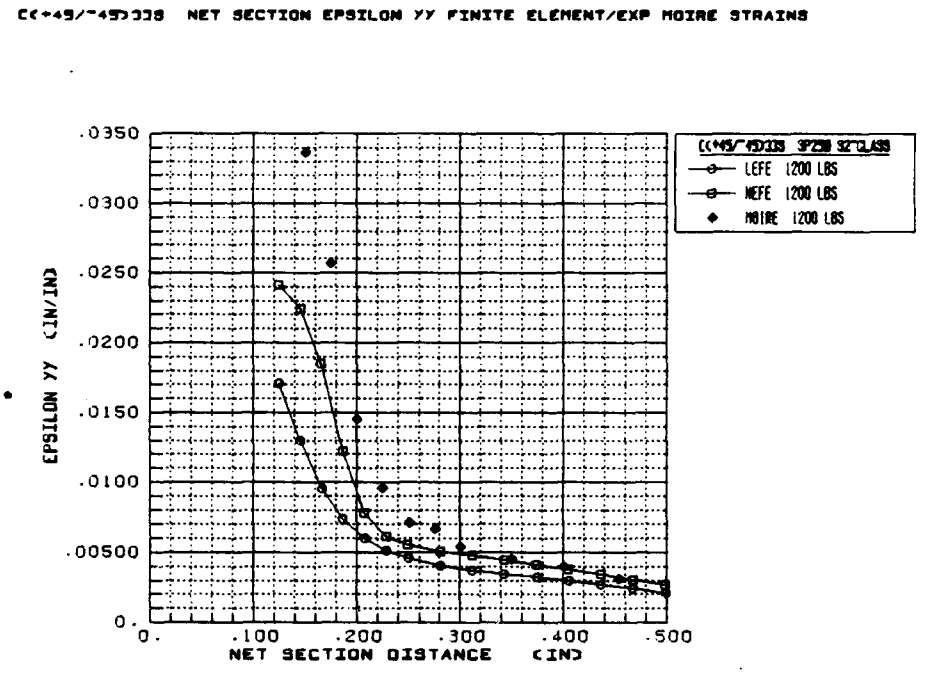

Figure 10.14 $[(+45/-45)_3]_s$ Finite Element and Moire Net Section ε_y Strain Comparison [1200 lbs]

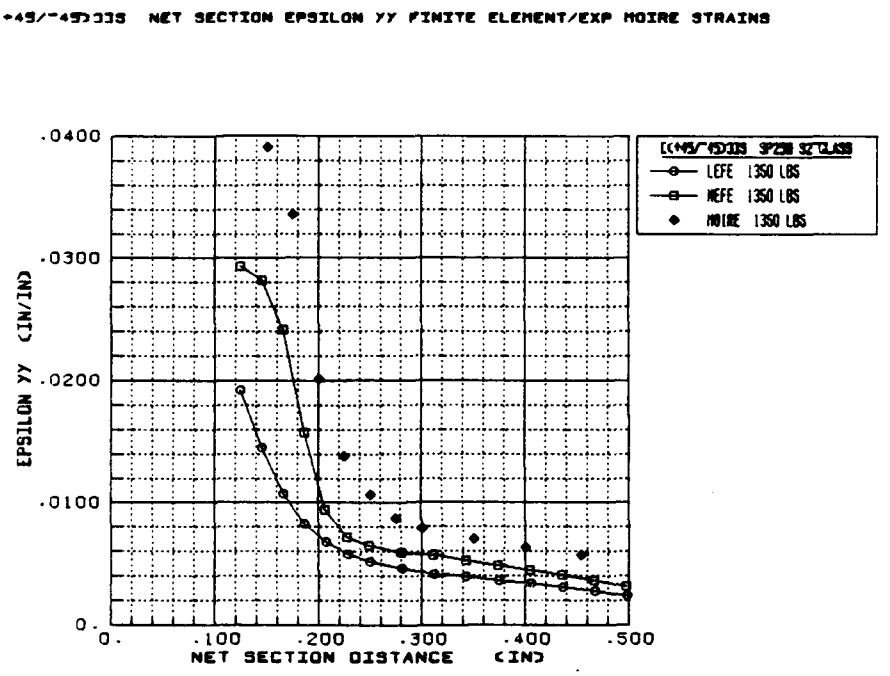

Figure 10.15 $[(+45/-45)_3]_s$ Finite Element and Moire Net Section ε_y Strain Comparison [1350 lbs]

CHAPTER 11. QUALITATIVE MATERIAL DAMAGE INVESTIGATION

Comparisons of sectional strains obtained from finite element approximations and those from the experimental moire results indicated possible material failure occurring within the net and bearing sections of the $[(+45/-45)_3]_s$ laminate and in the locus of maximum shear stress within the $[(0/90)_{3,}0]_s$ laminate respectively. A qualitative investigation of this observation was undertaken in the hope of providing insight. Use of the translucent nature of the SP250 S-2 fiber / resin system, liquid penetrant and a backlighting experimental arrangement were employed to provide a qualitative planer view of progressive coupon damage for each laminate type.

11.1 Experimental Damage Detection Technique

The experimental arrangement shown in Figure 11.1 was used in the qualitative damage detection study. A doubly simple supported pin arrangement of span length equivalent to that used in both the Moire and finite element analysis was used. The fixture was placed into a 20,000 lbs INSTRON mechanical testing machine with one mechanical wedge grip grabbing the top part of the fixture and the other grabbing the coupon itself. A NIKON 35 mm SLR camera with motor drive film advancing unit and 80-120 mm VIVITAR zoom lens was positioned to image the front surface of the pin-loaded portion of the coupon. A thick, black cardboard mask was placed around the coupon to eliminate stray light from overexposing the photographs. A quartz-iodine high intensity lamp was placed behind the coupon at such a distance to provide uniform front surface coupon illumination. KODAK Tri-X Panchromatic black and white film was used as a recording medium.

11.2 Test Procedures

A series of trial exposures were made to determine what shutter speed and appropriate *f* stop camera settings would yield optimum photographic results. After subsequent development and printing of all trial exposures, the camera settings were determined.

For both laminate arrangements, the coupon was placed within the experimental arrangement of figure 11.1. The coupons were subjected to 300 lbs loading increments to 900 lbs, 100 lbs loading increments to 1200 lbs, and 50 lbs loading increments till failure. In between each load increment, the coupon was removed from the experimental arrangement and submersed in MAGNAFLUX type SKL-HF liquid penetrant for approximately twenty minutes. The coupon was then wiped of front and rear surface excess penetrant with MAGNAFLUX type SKL-NF/ZC-7B cleaner and placed back into the experimental arrangement for photographing at the predetermined camera settings. Care was taken for proper specimen fixture alignment during its reinstallation. Both specimens were loaded until significant load reduction was observed upon reloading (ie failure).

11.3 Test Results

Figures 11.2 - 11.9 represent the experimental results for the $[(0/90)_3,0]_s$ coupon while Figures 11.10 - 11.15 represent those of the $[(+45/-45)_3]_s$ coupon.

A vertical crack was seen in the right side of the $[(0/90)_3,0]_s$ coupon at the locus of maximum shear strain at the 1000 lb load level. This crack grew in a vertical fashion with increased load level until the 1300 lb load level where several smaller vertical cracks were observed on the left side of the coupon in the vicinity of the locus of maximum shear strain. The existence of transverse cracks were seen in this location at the 1350 lb load level. With increased loading, both vertical and transverse cracks enlarged while the formation of transverse cracks were observed around the pin. Ply delamination or three dimensional "brooming" of the material was observed on the left coupon side near the initial site of transverse crack formation at

the 1400 lb load level. This delamination area grew until failure at just over 1600 lb load level where massive ply delamination occurred above the pin.

The $[(+45/-45)_3]_s$ coupon exhibited cracks along the -45° fiber direction in the net section at the 1000 lb load level. These cracks continued to grow in length and number at the net section with increasing load level. Cracks along the $+45^\circ$ fiber direction were initiated in the net section at the 1250 lb load level. The 1300 lb load load level saw the initiation of $+45^\circ$ and -45° cracks to the left and right of the bearing section respectively. These bearing section cracks grew in length and formed a "cone" like formation above the pin with increased load level. Ply delamination was observed in the net and bearing section crack initiation locations at the 1400 lb load level. Increased loading caused massive ply delamination above the pin.

The vertical cracks in the $[(0/90)_3,0]_s$ laminate suggested an initial matrix shear failure along the locus of maximum shear strain in the 90° ply layers. The ensuing observation of transverse cracks in the 0° layers is suggestive of a load transfer to and matrix failure of these plies. The existence of this shear failure mechanism and the lack of inelastic material behavior in the modeling effort caused experimental / finite element shear strain discrepancies along the locus of maximum shear strain. Similar experimental and finite element pin boundary conditions might have allowed a load level correlation between observable damage and shear strain discrepancies.

The observation of cracks along the fiber directions within the net and bearing sections of the $[(+45/-45)_3]_s$ laminate suggested a matrix / fiber interface failure. This type of failure manifested itself in a "scissoring" action of the $+45^\circ$ and -45° plies. Discrepancies between net section ε_y experimental / finite element strains exhibited a load level correlation with observable net section damage thus indicating the presence of inelastic material behavior. This same conclusion might have been drawn for bearing section ε_y strains had similar experimental and finite element pin boundary conditions prevailed.

Delaminations and resulting coupon failures were no doubt due to the unrestrained through thickness coupon boundary condition. A true double lap joint configuration would provide this through thickness restraint thus producing a delamination suppression mechanism. Since both shearout and net

section damage mechanisms were present prior to delamination formation within the $[(0/90)_3,0]_s$ and $[(+45/-45)_3]_s$ coupons respectively, delamination suppression most likely would have resulted in these coupon failure modes.

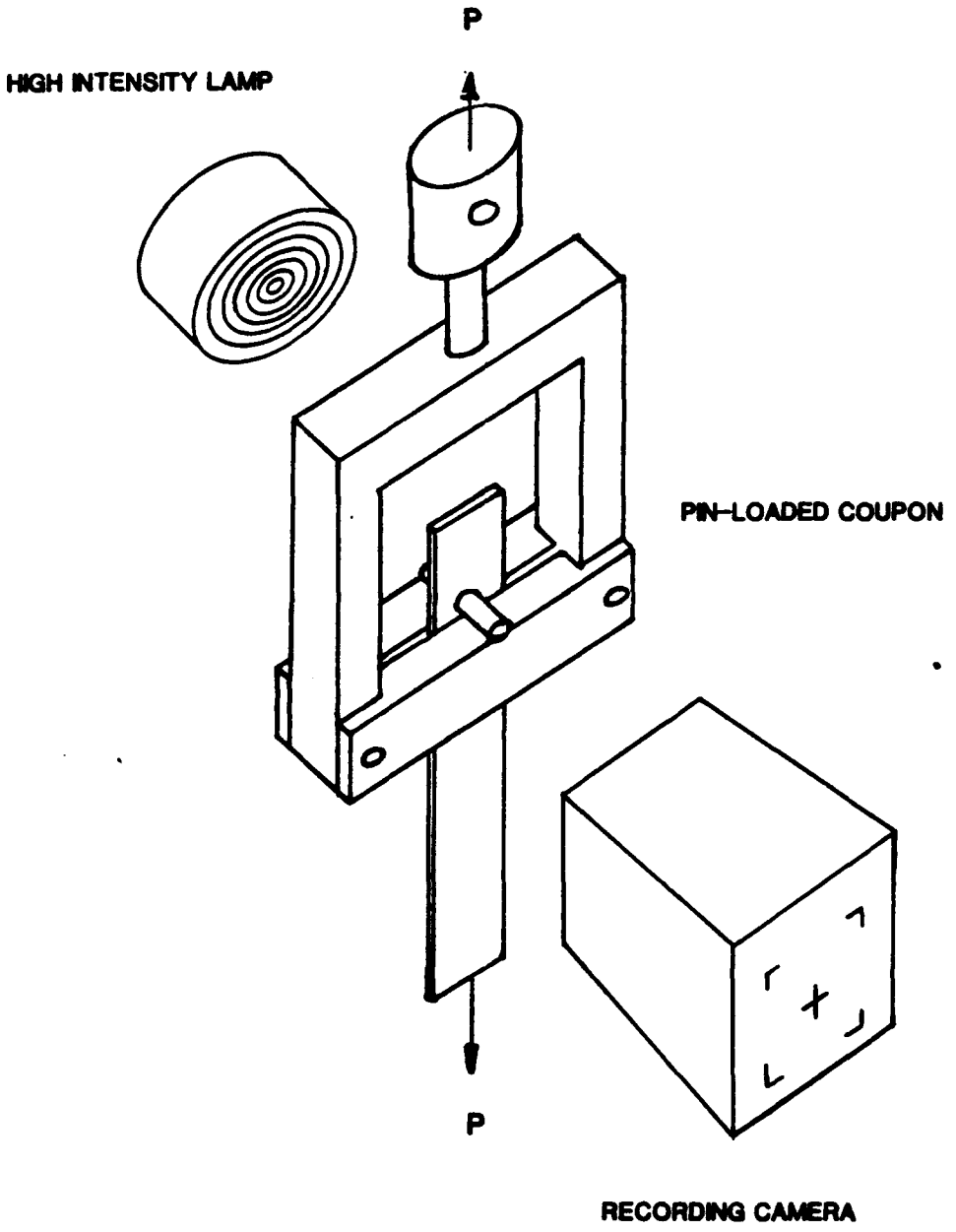

Figure 11.1 Qualitative Damage Detection Experimental Arrangement

0 N (0 lbs)

$((0/90)_3,\bar{0})_S$

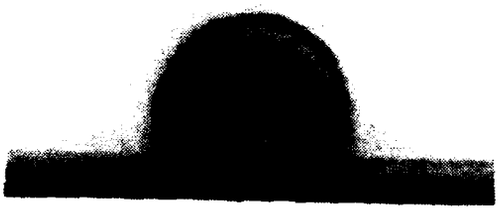

1334 N (300 lbs)

Figure 11.2 [(0/90)3,0]s Pin-loaded Coupon Damage [0 lbs 300 lbs]

2668 N (600 lbs)

$((0/90)_3,\bar{0})_S$

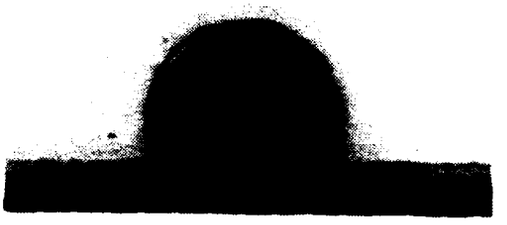

4003 N (900 lbs)

Figure 11.3 [(0/90)3,0]s Pin-loaded Coupon Damage [600 lbs 900 lbs]

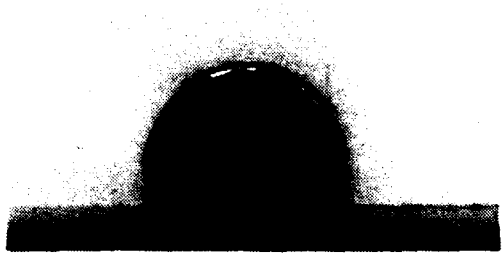

4448 N (1000 lbs)

$((0/90)_3,\bar{0})_S$

4893 N (1100 lbs)

Figure 11.4 [(0/90)3,0]s Pin-loaded Coupon Damage [1000 lbs 1100 lbs]

5338 N (1200 lbs)

$((0/90)_3,\bar{0})_S$

5560 N (1250 lbs)

Figure 11.5 [(0/90)3,0]s Pin-loaded Coupon Damage [1200 lbs 1250 lbs]

5783 N (1300 lbs)

$((0/90)_3,\bar{0})_S$

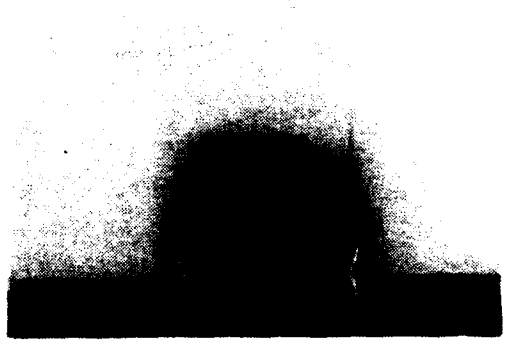

6005 N (1350 lbs)

Figure 11.6 $[(0/90)_3,0]_s$ Pin-loaded Coupon Damage [1300 lbs 1350 lbs]

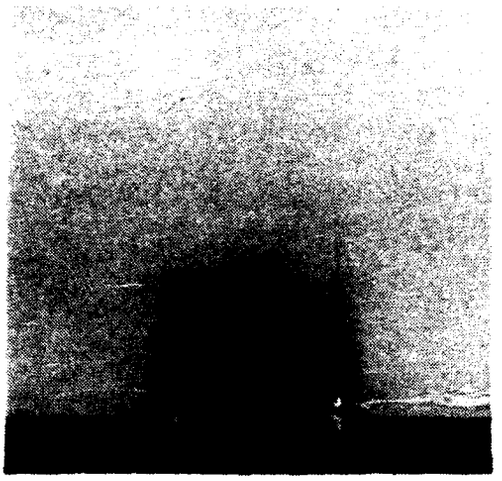

6227 N (1400 lbs)

$((0/90)_3,\bar{0})_S$

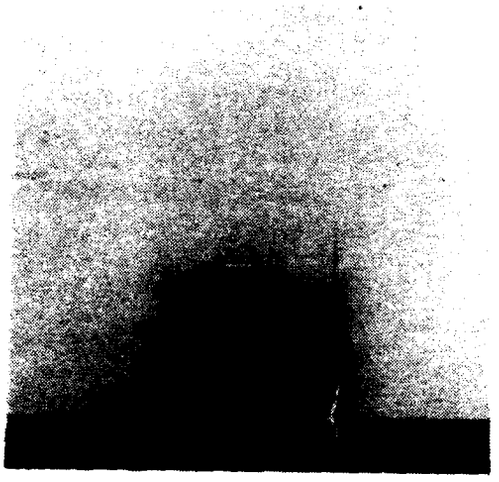

6450 N (1450 lbs)

Figure 11.7 [(0/90)3,0]s Pin-loaded Coupon Damage [1400 lbs 1450 lbs]

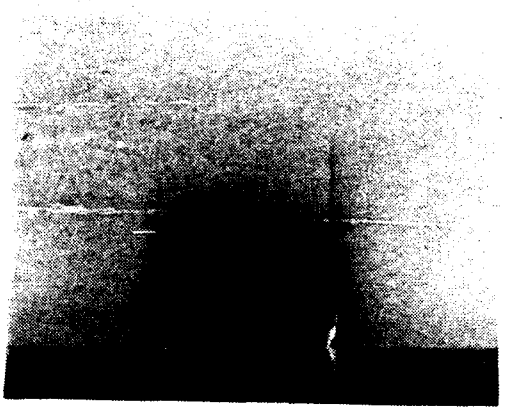

6672 N (1500 lbs)

$((0/90)_3,\bar{0})_S$

6895 N (1550 lbs)

Figure 11.8 [(0/90)3,0]s Pin-loaded Coupon Damage [1500 lbs 1550 lbs]

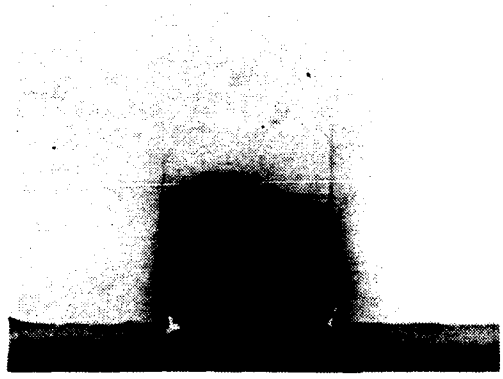

7117 N (1600 lbs)

$((0/90)_3,\bar{0})_S$

FAILURE

Figure 11.9 [(0/90)3,0]s Pin-loaded Coupon Damage [1600 lbs failure]

0 N (0 lbs)

$((45/-45)_3)_S$

1334 N (300 lbs)

Figure 11.10 [(+45/-45/)3]s Pin-loaded Coupon Damage [0 lbs 300 lbs]

2668 N (600 lbs)

$((45/-45)_3)_S$

4003 N (900 lbs)

Figure 11.11 $[(+45/-45/)_3]_s$ Pin-loaded Coupon Damage [600 lbs 900 lbs]

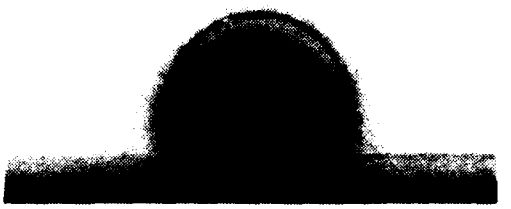

4448 N (1000 lbs)

$((45/-45)_3)_S$

4893 N (1100 lbs)

Figure 11.12 [(+45/-45/)3]s Pin-loaded Coupon Damage [1000 lbs 1100 lbs]

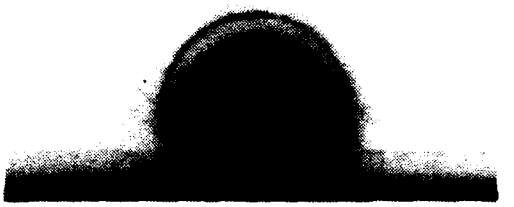

5338 N (1200 lbs)

$((45/-45)_3)_S$

5560 N (1250 lbs)

Figure 11.13 [(+45/-45/)3]s Pin-loaded Coupon Damage [1200 lbs 1250 lbs]

5783 N (1300 lbs)

$((45/-45)_3)_S$

6005 N (1350 lbs)

Figure 11.14 [(+45/-45/)3]s Pin-loaded Coupon Damage [1300 lbs 1350 lbs]

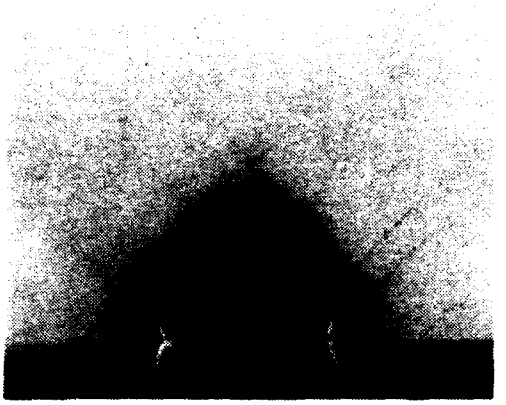

6227 N (1400 lbs)

$((45/-45)_3)_S$

FAILURE

Figure 11.15 [(+45/-45/)3]s Pin-loaded Coupon Damage [1400 lbs failure]

CHAPTER 12. CONCLUSIONS

The combined experimental and analytical nature of this dissertation has served to answer some crucial questions regarding the mechanical response and modeling assumptions of $[(0/90)_n]_s$ and $[(+45/-45)_n]_s$ pin-loaded laminates. Its interdisciplanary approach allowed for relevant experimental / analytical comparisons that led to validated conclusions.

Application of projection shadow moire clearly illustrated a significant through thickness mechanical response of both laminates at load levels considerably lower than failure. These observations led to a three dimensional finite element modeling approach.

Through thickness laminate mechanical property determinations produced fairly accurate estimation of these values for constitutive equation development. Transverse shear modulus determinations of both laminate orientations through a conventional three point bend test arrangement yielded highly inaccurate results. Application of calibrated beam deflection equations in the small span to depth ratio regime yielded a more accurate determination of laminate transverse moduli. Use of a displacement clip gage during laminate tension tests suffered from lack of measurement sensitivity, yet gave good approximations for laminate through thickness Poisson ratios. The $[(+45/-45)_3]_s$ through thickness Poisson ratio was extremely nonlinear in nature.

Use of effective in-plane laminate mechanical properties and the application of three dimensional orthotropic constitutive relations in conjunction with through thickness laminate mechanical properties provided a sound constitutive equation approach for laminate stress-strain behavior. Development of laminate constitutive equations including nonlinear crossply intralaminar shear behavior was successfully accomplished for both laminate orientations. The material axes transformation of the $[(0/90)_n]_s$ constitutive equations led to compact yet accurate expressions for $[(+45/-45)_n]_s$

constitutive equations. Uniaxial stress predictions for the $[(+45/-45)_n]_s$ laminate underscored the importance of including crossply based nonlinear intralaminar shear behavior within the constitutive expressions.

A sensitivity analysis showed that $[(0/90)_4]_s$ uniaxial stress predictions were insensitive to through thickness $[(0/90)_4]_s$ modulus and Poisson ratio value variations. However; uniaxial $[(+45/-45)_4]_s$ stress predictions were effected by $[(+45/-45)_4]_s$ through thickness modulus and crossply based Poisson ratio value variations. Assuminga through thickness modulus equal to that of pure resin reduced this sensitivity.

Both single and multi-element verifications of laminate ABAQUS user material subroutines were successful. The Newton-Raphson nonlinear solution technique employed by ABAQUS converged well when using the $[(0/90)_4]_s$ subroutine. However; the constrained nature of the $[(+45/-45)_4]_s$ subroutine required increased cycles for convergence. Effects of convergence tolerance upon solution accuracy and computation time were investigated proving the $[(+45/-45)_4]_s$ user subroutine to be computationally inefficient. It is not apparent if computational efficiency could have been acheived by use of a Modified Newton-Raphson approach in which global stiffness is not updated.

The linear and nonlinear three dimensional finite element approximations of $[(0/90)_{3,0}]_s$ and $[(+45/-45)_3]_s$ pin-loaded laminates analytically established the effects of nonlinear crossply intralaminar shear material behavior. Both radial and circumferential pin boundary coupon stresses were significantly affected by the inclusion of the material nonlinearity for both laminate orientations. An approximate threefold reduction of maximum τ_{xy} stresses was observed in the shearout section of the $[(0/90)_{3,0}]_s$ pin-loaded coupon. A similar reduction occured in the net section of the $[(+45/-45)_3]_s$ laminate. Nonlinear elastic predictions of $[(0/90)_{3,0}]_s$ γ_{xy} values along the coupon locus of maximum shear strain were observed to gradually increase over linear elastic predictions with increasing pin-load level. These variations increased closer to the pin. In a similar fashion, nonlinear elastic predictions of $[(+45/-45)_3]_s$ ε_y values in the coupon net and bearing sections was observed to gradually increase from those of the linear elastic prediction with increasing pin-load level. These variations also increased closer to the pin.

Through thickness σ_z finite element stresses were negligable in

comparison to in-plane laminate stresses. Larger values were observed closer to the midplane of the laminates than the front surface. The nonlinear material assumptions increased these σ_z stresses for both laminate arrangements.

Variations of nonlinear elastic constitutive equation constants were observed for both laminate configurations. These variations were seen at the lowest pin-load level of 300 lbs and became more pronounced at higher pin loads. A softening of the $[(0/90)_3,0]_s$ intralaminar shear modulus was seen along the locus of maximum shear stress. A similar effect was seen in C_{11} in the net and bearing sections of the $[(+45/-45)_3]_s$ laminate. Corresponding net and bearing section $[(+45/-45)_3]_s$ C_{12} values increased.

Application of geometric moire successfully generated in-plane displacement contours for the $[(+45/-45)_3]_s$ pin-loaded laminate. Application of Fourier filtering, mismatch methods, and semi-automated fringe digitization procedures allowed for accurate strain determinations in both the net and bearing sections of the coupon. Detailed displacement contouring around the circumference of the pin in order to observe frictional effects could not be made due to the lack of experimental displacement contouring sensitivity.

Comparisons of experimental and finite element strains in the shearout section of the $[(0/90)_3,0]_s$ coupon and in the net and bearing section of the $[(+45/-45)_3]_s$ coupon validated the importance of including nonlinear crossply intralaminar shear material behavior in numerical computations and highlighted the effects of material damage. Net section $[(+45/-45)_3]_s$ ε_y experimental strains were seen to follow nonlinear elastic finite element predictions at low pin-load levels. Increasingly higher experimental ε_y values were observed with increasing pin-load levels. This departure increased with closer pin proximity suggesting the presence of a net section tensile damage mechanism. Similar trends in $[(+45/-45)_3]_s$ bearing section ε_y and in $[(0/90)_3,0]_s$ shear out section γ_{xy} were observed, but were altered somewhat by unsymmetric experimental pin boundary conditions.

The qualitative material damage investigation effectively illustrated the role material damage plays in pin-loaded composite connectors. Load level comparisons with both linear and nonlinear finite element and experimental sectional strain values indicated the presence of tensile and shear damage mechanisms for the $[(+45/-45)_3]_s$ and $[(0/90)_3,0]_s$ laminate respectively. The

progressive nature of the damage was observed in both laminates at pin-load levels well under failure.

CHAPTER 13. RECOMMENDATIONS FOR FUTURE WORK

Recommendations for future work should include the following efforts.

1) Development of fixturing for symmetric experimental boundary conditions.

2) Use of a higher experimental displacement contouring sensitivity to determine pin/coupon frictional effects.

3) A better characterization of laminate through thickness modulus and Poisson ratio.

4) An accurate determination of free edge interlaminar stresses.

5) Development of a more computationally efficient $[(+45/-45)_3]_s$ constitutive equation subroutine.

6) Inclusion of validated statistically based failure theories.

7) Investigation of a front and rear surface restraint of a true double lap joint upon through thickness stresses and failure modes.

8) Investigation of residual stresses from laminate cure cycles and their possible effects upon pin-loaded response.

9) Full field comparison of experimental and finite element strains by the approach of Tessler *et al.* [72].

14. BIOGRAPHICAL SKETCH OF AUTHOR

The author was born in Schenectady, New York on February 18,1958. He attended Chelmsford High School in Chelmsford, Massachusetts until graduation in 1976. He entered the University of Lowell in the Fall of the same year and received his Bachelors in Mechanical Engineering in 1980.

In 1981 he joined the Mechanics of Advanced Structures and Materials Branch of the Mechanics and Structural Integrity Laboratory at the Army Materials Technology Laboratory (formerly AMMRC). The author became involved with structural testing, finite element modeling, and experimental stress techniques in support of departmental composite materials research efforts.

In the Fall of 1982, the author enrolled in the Mechanical Engineering Department of the University of Lowell while maintaining his position at the Army Materials Technology Center. His research work in bolted composite joints under the late Professor John McElman led to a Masters of Science Degree in the Fall of 1985.

15. APPENDIX

[(0/90)3.0]S LINEAR ELASTIC PINLOADED COUPON FINITE ELEMENT RUN RESULTS

LOAD(lbs)	STEP #	INC#	ITTER#	PTOL	MAX RESIDUAL	MAX RF (coupon)	% MAX RF	CPU(hrs)	CUMULATIVE CPU(hrs)
rbt	1	1	2	1.00E-03	-1.35E-13	-3.E-07 (531)	4.50E-07	0.47	00.47
300	2	1	6	2.00E-03	1.64E-04				
300	2	2	3	2.00E-03	3.34E-04				
300	2	3	2	2.00E-03	4.53E-04				
300	2	4	2	2.00E-03	7.73E-04				
300	2	5	2	2.00E-03	5.70E-03				
300	2	6	2	2.00E-03	-3.19E-04				
300	2	7	3	2.00E-03	-7.19E-04				
300	2	8	2	2.00E-03	1.39E-04				
300	2	9	2	2.00E-03	1.76E-04				
300	2	10	2	2.00E-03	1.27E-03	-2.18 (1202)	5.82E-04	8.22	08.69
600	3	1	2	4.00E-03	2.99E-04				
600	3	2	2	4.00E-03	3.08E-04				
600	3	3	2	4.00E-03	-1.55E-03				
600	3	4	2	4.00E-03	4.13E-04				
600	3	5	2	4.00E-03	4.74E-04				
600	3	6	2	4.00E-03	5.38E-04				
600	3	7	2	4.00E-03	6.08E-04				
600	3	8	2	4.00E-03	-1.59E-03	-4.45 (1248)	3.57E-04		
600	3	9	2	4.00E-03	7.54E-04				
600	3	10	2	4.00E-03	8.36E-04			6.80	15.49
900	4	1	2	6.90E-03	5.54E-04				
900	4	2	2	6.90E-03	5.89E-04				
900	4	3	2	6.90E-03	6.24E-04				
900	4	4	2	6.90E-03	6.59E-04				
900	4	5	2	6.90E-03	6.97E-04				
900	4	6	2	6.90E-03	7.33E-04				
900	4	7	2	6.90E-03	7.70E-04				
900	4	8	2	6.90E-03	8.10E-04				
900	4	9	2	6.90E-03	8.50E-04				
900	4	10	2	6.90E-03	8.92E-04				
900	4	11	2	6.90E-03	9.35E-04				
900	4	12	2	6.90E-03	9.79E-04				
900	4	13	2	6.90E-03	1.02E-03				
900	4	14	2	6.90E-03	1.07E-03				
900	4	15	2	6.90E-03	1.12E-03				
900	4	16	2	6.90E-03	1.17E-03	-8.21 (1248)	1.42e-04	10.65	26.14
1200	5	1	2	7.20E-03	1.21E-03				
1200	5	2	2	7.20E-03	1.26E-03				
1200	5	3	2	7.20E-03	1.32E-03				
1200	5	4	2	7.20E-03	1.37E-03				
1200	5	5	2	7.20E-03	1.42E-03				
1200	5	6	2	7.20E-03	1.48E-03				
1200	5	7	2	7.20E-03	1.53E-03				
1200	5	8	2	7.20E-03	1.59E-03				
1200	5	9	2	7.20E-03	1.64E-03				
1200	5	10	2	7.20E-03	1.70E-03				
1200	5	11	2	7.20E-03	1.76E-03				
1200	5	12	2	7.20E-03	1.82E-03				
1200	5	13	2	7.20E-03	1.88E-03				
1200	5	14	2	7.20E-03	1.94E-03				
1200	5	15	2	7.20E-03	2.01E-03				
1200	5	16	2	7.20E-03	2.07E-03	-12.02 (1248)	1.72E-04	10.52	36.66
1500	6	1	2	9.50E-03	2.14E-03				
1500	6	2	2	9.50E-03	2.20E-03				
1500	6	3	2	9.50E-03	2.27E-03				
1500	6	4	2	9.50E-03	2.34E-03				
1500	6	5	2	9.50E-03	2.41E-03				
1500	6	6	2	9.50E-03	2.48E-03				
1500	6	7	2	9.50E-03	2.55E-03				
1500	6	8	2	9.50E-03	2.62E-03				
1500	6	9	2	9.50E-03	2.69E-03				
1500	6	10	2	9.50E-03	2.77E-03				
1500	6	11	2	9.50E-03	2.84E-03				
1500	6	12	2	9.50E-03	2.91E-03				
1500	6	13	2	9.50E-03	3.00E-03				
1500	6	14	2	9.50E-03	3.08E-03				
1500	6	15	2	9.50E-03	3.16E-03				
1500	6	16	2	9.50E-03	3.24E-03	-15.93 (1248)	2.03E-04	10.27	46.93

Table A.1 $[(0/90)_{3},0]_{S}$ Pin-Loaded Coupon Linear Elastic Finite Element Computational Results

[(0/90)3,0]S NONLINEAR ELASTIC PINLOADED COUPON FINITE ELEMENT RUN RESULTS

LOAD(lbs)	STEP #	INC#	ITTER#	PTOL	MAX RESIDUAL	MAX RF (coupon)	% MAX RF	CPU(hrs)	CUMULATIVE CPU(hrs)
rst	1	1	2	1.00E-03	1.76E-13	-3.E-07 (531)	5.87E-07	0.51	00.51
300	2	1	7	2.00E-03	2.89E-04				
300	2	2	4	2.00E-03	1.94E-03	-2.30 (1202)	8.43E-04		
300	2	3	3	2.00E-03	1.79E-03				
300	2	4	4	2.00E-03	-1.41E-04				
300	2	5	3	2.00E-03	-1.52E-03				
300	2	6	4	2.00E-03	1.12E-04				
300	2	7	4	2.00E-03	1.35E-04				
300	2	8	3	2.00E-03	-1.52E-03				
300	2	9	3	2.00E-03	1.74E-04			12.40	12.91
300	2	10	4	2.00E-03	1.27E-03				
600	3	1	3	4.00E-03	-1.53E-03				
600	3	2	3	4.00E-03	1.97E-03				
600	3	3	3	4.00E-03	-1.53E-03				
600	3	4	3	4.00E-03	-1.53E-03				
600	3	5	3	4.00E-03	-1.53E-03				
600	3	6	3	4.00E-03	-1.53E-03				
600	3	7	3	4.00E-03	-1.54E-03				
600	3	8	3	4.00E-03	-1.54E-03				
600	3	9	3	4.00E-03	-1.54E-03				
600	3	10	3	4.00E-03	-1.54E-03	-4.61 (1202)	3.34E-04	9.75	22.66
900	4	1	3	6.90E-03	5.54E-04				
900	4	2	3	6.90E-03	5.89E-04				
900	4	3	3	6.90E-03	6.24E-04				
900	4	4	3	6.90E-03	6.59E-04				
900	4	5	3	6.90E-03	6.97E-04				
900	4	6	3	6.90E-03	7.33E-04				
900	4	7	3	6.90E-03	7.70E-04				
900	4	8	3	6.90E-03	8.10E-04				
900	4	9	3	6.90E-03	8.50E-04				
900	4	10	3	6.90E-03	8.92E-04				
900	4	11	3	6.90E-03	9.35E-04				
900	4	12	3	6.90E-03	9.79E-04				
900	4	13	4	6.90E-03	1.02E-03				
900	4	14	3	6.90E-03	1.07E-03				
900	4	15	3	6.90E-03	1.12E-03				
900	4	16	3	6.90E-03	1.17E-03	-7.42 (1202)	1.58E-04	15.42	38.08
1200	5	1	3	7.20E-03	-9.64E-04				
1200	5	2	3	7.20E-03	-9.65E-04				
1200	5	3	3	7.20E-03	-9.76E-04				
1200	5	4	3	7.20E-03	-9.87E-04				
1200	5	5	3	7.20E-03	-4.19E-03				
1200	5	6	3	7.20E-03	-1.01E-03				
1200	5	7	3	7.20E-03	-1.02E-03				
1200	5	8	11	7.20E-03	6.29E-03				
1200	5	9	3	7.20E-03	5.13E-03				
1200	5	10	3	7.20E-03	1.09E-03				
1200	5	11	3	7.20E-03	-1.06E-03				
1200	5	12	3	7.20E-03	4.49E-03				
1200	5	13	11	7.20E-03	1.22E-02	-10.97 (1202)	1.11E-03		
1200	5	14	3	7.20E-03	-1.10E-03				
1200	5	15	3	7.20E-03	-1.11E-03				
1200	5	16	3	7.20E-03	1.25E-03			19.12	57.20
1500	6	1	3	9.50E-03	-1.13E-03				
1500	6	2	3	9.50E-03	1.32E-03				
1500	6	3	3	9.50E-03	-1.15E-03				
1500	6	4	3	9.50E-03	1.33E-03				
1500	6	5	3	9.50E-03	1.37E-03				
1500	6	6	3	9.50E-03	-6.39E-03				
1500	6	7	3	9.50E-03	1.61E-03				
1500	6	8	3	9.50E-03	-9.72E-03				
1500	6	9	3	9.50E-03	1.57E-03				
1500	6	10	3	9.50E-03	1.79E-03				
1500	6	11	3	9.50E-03	4.49E-03				
1500	6	12	3	9.50E-03	1.99E-03				
1500	6	13	3	9.50E-03	2.04E-03				
1500	6	14	3	9.50E-03	2.28E-03				
1500	6	15	3	9.50E-03	2.63E-03				
1500	6	16	3	9.50E-03	3.24E-03	-15.31 (1202)	2.12E-04	15.06	72.26

Table A.2 $[(0/90)_{3},0]_{S}$ Pin-Loaded Coupon Nonlinear Elastic Finite Element Computational Results

[(+45/-45)3]S LINEAR ELASTIC PINLOADED COUPON FINITE ELEMENT RUN RESULTS

LOAD(lbs)	STEP #	INC#	ITTER#	PTOL	MAX RESIDUAL	MAX RF (coupon)		% MAX RF	CPU(hrs)	CUMULATIVE CPU(hrs)
rbt	1	1	2	1.00E-03	-1.44E-13	-3.0E-07	(531)	4.80E-07	0.53	00.51
300	2	1	5	2.00E-03	1.23E-04					
300	2	2	3	2.00E-03	5.44E-04					
300	2	3	3	2.00E-03	1.85E-04					
300	2	4	3	2.00E-03	1.90E-04					
300	2	5	2	2.00E-03	-3.42E-04					
300	2	6	2	2.00E-03	1.03E-04					
300	2	7	2	2.00E-03	1.53E-03	-2.96	(1227)	5.17E-04		
300	2	8	2	2.00E-03	1.77E-04					
300	2	9	2	2.00E-03	1.29E-03					
300	2	10	2	2.00E-03	2.73E-04				08.62	09.13
600	3	1	3	4.00E-03	1.79E-05					
600	3	2	2	4.00E-03	5.76E-04					
600	3	3	2	4.00E-03	4.53E-04					
600	3	4	2	4.00E-03	5.25E-04					
600	3	5	2	4.00E-03	6.03E-04					
600	3	6	2	4.00E-03	1.85E-03					
600	3	7	2	4.00E-03	7.68E-04					
600	3	8	2	4.00E-03	8.61E-04					
600	3	9	2	4.00E-03	9.59E-04					
600	3	10	2	4.00E-03	2.14E-03	-4.77	(1227)	4.49E-04	07.12	16.25
900	4	1	2	6.90E-03	7.00E-04					
900	4	2	2	6.90E-03	7.41E-04					
900	4	3	2	6.90E-03	7.86E-04					
900	4	4	2	6.90E-03	8.31E-04					
900	4	5	2	6.90E-03	8.78E-04					
900	4	6	2	6.90E-03	9.26E-04					
900	4	7	2	6.90E-03	9.75E-04					
900	4	8	2	6.90E-03	1.02E-03					
900	4	9	2	6.90E-03	1.08E-03					
900	4	10	2	6.90E-03	1.13E-03					
900	4	11	2	6.90E-03	1.18E-03					
900	4	12	2	6.90E-03	1.24E-03					
900	4	13	2	6.90E-03	1.30E-03					
900	4	14	2	6.90E-03	1.35E-03					
900	4	15	2	6.90E-03	1.42E-03					
900	4	16	2	6.90E-03	1.47E-03	-7.38	(1227)	1.99E-04	10.64	26.89
1200	5	1	2	7.20E-03	1.54E-03					
1200	5	2	2	7.20E-03	1.60E-03					
1200	5	3	2	7.20E-03	1.66E-03					
1200	5	4	2	7.20E-03	1.73E-03					
1200	5	5	2	7.20E-03	1.80E-03					
1200	5	6	2	7.20E-03	1.86E-03					
1200	5	7	2	7.20E-03	2.00E-03					
1200	5	8	2	7.20E-03	2.07E-03					
1200	5	9	2	7.20E-03	2.15E-03					
1200	5	10	2	7.20E-03	2.22E-03					
1200	5	11	2	7.20E-03	2.30E-03					
1200	5	12	2	7.20E-03	2.38E-03					
1200	5	13	2	7.20E-03	2.45E-03					
1200	5	14	2	7.20E-03	2.53E-03					
1200	5	15	2	7.20E-03	2.61E-03	-9.94	(1227)	2.62E-04		
1200	5	16	2	7.20E-03	1.54E-03				11.48	38.37
1500	6	1	2	1.50E-02	2.70E-03					
1500	6	2	2	1.50E-02	2.78E-03					
1500	6	3	2	1.50E-02	2.86E-03					
1500	6	4	2	1.50E-02	2.95E-03					
1500	6	5	2	1.50E-02	1.92E-04					
1500	6	6	2	1.50E-02	3.14E-03					
1500	6	7	2	1.50E-02	3.21E-03					
1500	6	8	2	1.50E-02	3.31E-03					
1500	6	9	2	1.50E-02	3.39E-03					
1500	6	10	2	1.50E-02	3.49E-03					
1500	6	11	2	1.50E-02	3.58E-03					
1500	6	12	2	1.50E-02	3.68E-03					
1500	6	13	2	1.50E-02	3.78E-03					
1500	6	14	2	1.50E-02	3.88E-03					
1500	6	15	2	1.50E-02	3.98E-03					
1500	6	16	2	1.50E-02	4.08E-03	-12.56	(1227)	3.25E-04	12.16	50.53

Table A.3 $[(\pm 45)_3]_s$ Pin-Loaded Coupon Linear Elastic Finite Element Computational Results

[(+45/-45)3]S NONLINEAR ELASTIC PINLOADED COUPON FINITE ELEMENT RUN RESULTS

LOAD(lbs)	STEP #	INC#	ITTER#	PTOL	MAX RESIDUAL	MAX RF (coupon)	% MAX RF	CPU(hrs)	CUMULATIVE CPU(hrs)
rbt	1	1	2	1.00E-03	-1.44E-13	-3.0E-07 (531)	4.80E-07	0.53	00.53
300	2	1	8	2.00E-03	8.79E-04				
300	2	2	7	2.00E-03	-8.96E-04				
300	2	3	7	2.00E-03	-9.61E-04				
300	2	4	7	2.00E-03	-1.03E-03				
300	2	5	7	2.00E-03	-1.10E-03				
300	2	6	7	2.00E-03	-1.17E-03				
300	2	7	7	2.00E-03	-1.25E-03				
300	2	8	7	2.00E-03	-1.34E-03				
300	2	9	7	2.00E-03	-1.44E-03				
300	2	10	7	2.00E-03	-1.54E-03	-2.40 (1227)	6.42E-04	21.13	21.66
600	3	1	3	4.00E-03	-3.60E-03				
600	3	2	3	4.00E-03	-3.85E-03	-5.24 (1227)	7.34E-04		
600	3	3	3	4.00E-03	-1.90E-03				
600	3	4	3	4.00E-03	2.31E-03				
600	3	5	3	4.00E-03	2.91E-03				
600	3	6	3	4.00E-03	3.61E-03				
600	3	7	3	4.00E-03	2.65E-03				
600	3	8	3	4.00E-03	3.30E-03				
600	3	9	3	4.00E-03	2.63E-03				
600	3	10	3	4.00E-03	3.24E-03			21.91	43.57
900	4	1	7	6.90E-03	5.53E-03				
900	4	2	7	6.90E-03	6.14E-03				
900	4	3	7	6.90E-03	6.64E-03				
900	4	4	8	6.90E-03	4.74E-03				
900	4	5	8	6.90E-03	4.94E-03				
900	4	6	8	6.90E-03	5.42E-03				
900	4	7	8	6.90E-03	6.44E-03				
900	4	8	8	6.90E-03	6.19E-03				
900	4	9	8	6.90E-03	6.90E-03	-8.55 (1227)	8.07E-04		
900	4	10	9	6.90E-03	5.91E-03				
900	4	11	9	6.90E-03	6.42E-03				
900	4	12	9	6.90E-03	6.88E-03				
900	4	13	9	6.90E-03	6.41E-03				
900	4	14	11	6.90E-03	3.62E-03				
900	4	15	10	6.90E-03	5.85E-03				
900	4	16	10	6.90E-03	6.20E-03			38.60	82.17
1200	5	1	11	7.20E-03	5.71E-03				
1200	5	2	10	7.20E-03	6.99E-03				
1200	5	3	11	7.20E-03	6.07E-03				
1200	5	4	11	7.20E-03	6.32E-03				
1200	5	5	11	7.20E-03	6.99E-03				
1200	5	6	11	7.20E-03	7.18E-03				
1200	5	7	12	7.20E-03	5.73E-03				
1200	5	8	12	7.20E-03	6.14E-03				
1200	5	9	13	7.20E-03	4.32E-03				
1200	5	10	13	7.20E-03	5.61E-03				
1200	5	11	12	7.20E-03	6.78E-03				
1200	5	12	14	7.20E-03	4.66E-03				
1200	5	13	12	7.20E-03	7.12E-03	-12.17 (1227)	9.85E-04		
1200	5	14	12	7.20E-03	7.17E-03				
1200	5	15	13	7.20E-03	6.52E-03				
1200	5	16	13	7.20E-03	6.63E-03			53.93	136.10
1500	6	1	10	1.50E-02	1.36E-02				
1500	6	2	10	1.50E-02	1.43E-02				
1500	6	3	10	1.50E-02	1.44E-02				
1500	6	4	10	1.50E-02	1.46E-02	-15.86 (1227)	9.20E-04		
1500	6	5	11	1.50E-02	1.34E-02				
1500	6	6	11	1.50E-02	1.43E-02				
1500	6	7	12	1.50E-02	1.42E-02				
1500	6	8	13	1.50E-02	1.25E-02				
1500	6	9	13	1.50E-02	1.34E-02				
1500	6	10	14	1.50E-02	1.24E-02				
1500	6	11	15	1.50E-02	-1.42E-02				
1500	6	12	15	1.50E-02	1.45E-02				
1500	6	13	16	1.50E-02	1.28E-02				
1500	6	14	17	1.50E-02	1.36E-02				
1500	6	15	18	1.50E-02	1.42E-02				
1500	6	16	19	1.50E-02	1.36E-02			60.68	196.78

Table A.4 $[(\pm 45)_3]_S$ Pin-Loaded Coupon Nonlinear Elastic Finite Element Computational Results

```
s0;11;30m120;60 G


**********************************************************************
** 3D nonlinear elastic [(0/90)]s intralaminar shear material subroutine ***
** Newton-Raphson formulation                          ABAQUS version 4.7 ***
**********************************************************************
C
C
C
*USER SUBROUTINE
      SUBROUTINE UMAT(STRESS,STATEV,DDSDDE,SSE,SPD,SCD,
     1 RPL,DDSDDT,DRPLDE,DRPLDT,STRAN,DSTRAN,TIME,DTIME,
     2 TEMP,DTEMP,PREDEF,DPRED,CMNAME,NDI,NSHR,NTENS,NSTATV,
     3 PROPS,NPROPS,COORDS,DROT)
C
C
       IMPLICIT REAL*8(A-H,O-Z)
C
       CHARACTER*8 CMNAME
       DIMENSION STRESS(NTENS),STATEV(NSTATV),DDSDDE(NTENS,NTENS),
     1 DDSDDT(NTENS),DRPLDE(NTENS),STRAN(NTENS),DSTRAN(NTENS),
     2 PREDEF(1),DPRED(1),PROPS(NPROPS),COORDS(3),DROT(3,3),TSTRAN(6)
C
C
C*********************  UPDATE STRAINS  ***********************************
C
       DO 5 I=1,6
        TSTRAN(I)=STRAN(I)+DSTRAN(I)
   5   CONTINUE
C
C*********************  UPDATE STRESSES  **********************************
C
        STRESS(1)=PROPS(1)*TSTRAN(1)+PROPS(2)*
     1   TSTRAN(2)+PROPS(3)*TSTRAN(3)
C
        STRESS(2)=PROPS(2)*TSTRAN(1)+PROPS(4)*
     1   TSTRAN(2)+PROPS(5)*TSTRAN(3)
C
        STRESS(3)=PROPS(3)*TSTRAN(1)+PROPS(5)*
     1   TSTRAN(2)+PROPS(6)*TSTRAN(3)
C
        ABSGALT=ABS(TSTRAN(4))
C
C------ obtain corresponding 0/90 shear stress from ASTM D3576-18 curve-----
C
        IF(ABSGALT .LE. .029904) THEN
        TAULT=(0.735113E+06*ABSGALT - 0.244057E+08*ABSGALT**2. +
     &         0.313738E+09*ABSGALT**3.)
C
         ELSE IF((ABSGALT.GT..029904).AND.(ABSGALT.LT..032178)) THEN
         TAULT=(0.848000E+04 + 70360.6*(ABSGALT - 0.0299040))
C
          ELSE IF(ABSGALT .GE. .032178) THEN
          TAULT=(0.731176E+04 + 0.465649E+05*ABSGALT -
     &           0.964921E+05*ABSGALT**2.)
C
        ENDIF
C
        STRESS(4)=TAULT
        IF(TSTRAN(4).LT. 0.) STRESS(4)=-TAULT
C
```

Listing A.1 $[(0/90)_3,0]_s$ Nonlinear Elastic ABAQUS User Material Subroutine [1 of 2]

```
      STRESS(5)=PROPS(8)*TSTRAN(5)
      STRESS(6)=PROPS(9)*TSTRAN(6)
C
C*************  FORM JACOBIAN OF CONSTITUITIVE MATRIX  ********************
C
      DO 20 I=1,6
      DO 30 J=1,6
       DDSDDE(I,J)=0.0
  30  CONTINUE
  20  CONTINUE
C
       DDSDDE(1,1)=PROPS(1)
       DDSDDE(1,2)=PROPS(2)
       DDSDDE(1,3)=PROPS(3)
       DDSDDE(2,2)=PROPS(4)
       DDSDDE(2,3)=PROPS(5)
       DDSDDE(3,3)=PROPS(6)
C
C------------------- calculate 0/90 tangent modulus -------------------------
C
       IF(ABSGALT .LE. .0379640) THEN
       DDSDDE(4,4)=(0.817047E+06 - 0.720163E+08*ABSGALT +
     & 0.301293E+10*ABSGALT**2. - 0.649077E+11*ABSGALT**3. +
     & 0.569318E+12*ABSGALT**4.)
C
        ELSE IF((ABSGALT .GT. .037964).AND.(ABSGALT .LT. .04167)) THEN
        DDSDDE(4,4)=(0.532406E+05 - 1.93861E+06*(ABSGALT - .037964))
C
         ELSE IF(ABSGALT .GE. .04167) THEN
         DDSDDE(4,4)=(0.346802E+06 - 0.165373E+08*ABSGALT     +
     &    0.327833E+09*ABSGALT**2. - 0.290658E+10*ABSGALT**3. +
     &    0.971387E+10 *ABSGALT**4.)
C
      END IF
C
       DDSDDE(5,5)=PROPS(8)
       DDSDDE(6,6)=PROPS(9)
C
C
       RETURN
       END
```

Listing A.1 $[(0/90)_3,0]_s$ Nonlinear Elastic ABAQUS User Material Subroutine [2 of 2]

```
s0;11;30m120;60 G

**********************************************************************
******** 3D nonlinear elastic [(+45/-45)]s material subroutine       **********
******** developed by material axis transformation of nonlinear      **********
******** elastic [(0/90)]s intralaminar shear material subroutine    **********
******** Newton-Raphson formulation          ABAQUS version 4.7      **********
**********************************************************************
C
C
*USER SUBROUTINE
      SUBROUTINE UMAT(STRESS,STATEV,DDSDDE,SSE,SPD,SCD,
     1 RPL,DDSDDT,DRPLDE,DRPLDT,STRAN,DSTRAN,TIME,DTIME,
     2 TEMP,DTEMP,PREDEF,DPRED,CMNAME,NDI,NSHR,NTENS,NSTATV,
     3 PROPS,NPROPS,COORDS,DROT)
C
C
      IMPLICIT REAL*8(A-H,O-Z)
C
      CHARACTER*8 CMNAME
      DIMENSION STRESS(NTENS),STATEV(NSTATV),DDSDDE(NTENS,NTENS),
     1 DDSDDT(NTENS),DRPLDE(NTENS),STRAN(NTENS),DSTRAN(NTENS),
     2 PREDEF(1),DPRED(1),PROPS(NPROPS),COORDS(3),DROT(3,3),TSTRAN(6)
C
C
C*****************************  UPDATE STRAINS  ***************************
C
      DO 5 I=1,6
       TSTRAN(I)=STRAN(I)+DSTRAN(I)
   5  CONTINUE
C
C
C*****************************  UPDATE STRESSES  **************************
C
C-------------------- calculate effective 0/90 shear strain ----------------
C
      GALT=TSTRAN(2)-TSTRAN(1)
C
C------ obtain corresponding 0/90 shear stress from ASTM D3576-18 curve--------
C
      ABSGALT=ABS(GALT)
C
      IF(ABSGALT .LE. .029904) THEN
      TAULT=(0.735113E+06*ABSGALT - 0.244057E+08*ABSGALT**2. +
     &       0.313738E+09*ABSGALT**3.)
C
       ELSE IF((ABSGALT.GT..029904).AND.(ABSGALT.LT..032178)) THEN
       TAULT=(0.848000E+04 + 70360.6*(ABSGALT - 0.0299040))
C
        ELSE IF(ABSGALT .GE. .032178) THEN
        TAULT=(0.731176E+04 + 0.465649E+05*ABSGALT -
     &          0.964921E+05*ABSGALT**2.)
C
       ENDIF
C
C-------------------- calculate 0/90 secant modulus ------------------------
C
      IF (ABSGALT .EQ. 0.) THEN
      SECMOD=0.0
      ELSE
      SECMOD=TAULT/ABSGALT
```

Listing A.2 $[(\pm 45)_3]_s$ Nonlinear Elastic ABAQUS User Material Subroutine [1 of 3]

```
      END IF
C
C- form +-45 constitutive matrix as a function of 0/90 constitutive constants -
C- 0/90 secant modulus will allow for "true" updated +-45 stress calculations -
C
      CPK1=2.984749E+06
      CPK2=1.081625E+06
      CPK3=1.898651E+06
C
      APC11=CPK1+SECMOD
      APC12=CPK1-SECMOD
      APC13=CPK2
      APC22=APC11
      APC23=CPK2
      APC33=PROPS(6)
      APC44=CPK3
      APC55=PROPS(8)
      APC66=PROPS(9)
C
      STRESS(1)=APC11*TSTRAN(1)+APC12*TSTRAN(2)+APC13*TSTRAN(3)
      STRESS(2)=APC12*TSTRAN(1)+APC22*TSTRAN(2)+APC23*TSTRAN(3)
      STRESS(3)=APC13*TSTRAN(1)+APC23*TSTRAN(2)+APC33*TSTRAN(3)
      STRESS(4)=APC44*TSTRAN(4)
      STRESS(5)=APC55*TSTRAN(5)
      STRESS(6)=APC66*TSTRAN(6)
C
C*************  FORM JACOBIAN OF CONSTITUITIVE MATRIX  **********************
C
       DO 20 I=1,6
       DO 30 J=1,6
        DDSDDE(I,J)=0.0
  30   CONTINUE
  20   CONTINUE
C
C------------------- calculate 0/90 tangent modulus --------------------------
C
      IF(ABSGALT .LE. .029904) THEN
      TANMOD=(7.35113E+05 - 4.88114E+07*ABSGALT +
     &        9.41214E+08*ABSGALT**2.)
C
       ELSE IF((ABSGALT.GT..029904).AND.(ABSGALT.LT..032178)) THEN
       TANMOD=70360.6
C
        ELSE IF(ABSGALT .GE. .032178) THEN
        TANMOD=(4.65649E+04 - 1.92984E+05*ABSGALT)
C
       ENDIF
C
C-- calculate jacobian of +-45 constitutive matrix as a function of 0/90 -----
C-- constitutive constants.  please note use of 0/90 tangent tangent mod -----
C
      DDSDDE(1,1)=CPK1+TANMOD
      DDSDDE(1,2)=CPK1-TANMOD
      DDSDDE(1,3)=APC13
      DDSDDE(2,2)=DDSDDE(1,1)
      DDSDDE(2,3)=APC23
      DDSDDE(3,3)=APC33
      DDSDDE(4,4)=APC44
      DDSDDE(5,5)=APC55
```

Listing A.2 $[(\pm 45)_3]_s$ Nonlinear Elastic ABAQUS User Material Subroutine [2 of 3]

```
      DDSDDE(6,6)=APC66
C
C
        RETURN
        END
```

Listing A.2 $[(\pm 45)_3]_s$ Nonlinear Elastic ABAQUS User Material Subroutine [3 of 3]

16 LITERATURE CITED

[1]NASA-DOD Advanced Composites Design Guide, Contract F33615-78-C-3202, Rockwell International Corporation, North American Aircraft Operations, July 1983.

[2]Bickley, W., G., "The Distribution of Stresses Around a Circular Hole in a Plate", *Phil. Trans. Royal Soc.*, London, Vol 227A, 383-415, July, 1928.

[3]Howland, R., C., "On Stresses in Flat Plates Containing Rivet Holes", *Proceedings of the 3rd International Congress of Applied Mechanics*, Vol. II, 1930, p. 74-79.

[4]Knight, R., C., "The Action of a Rivet in a Plate of Finite Breadth", *Phil. Mag.*, Series 7, Vol. 19, No. 127, March 1935, pp. 517-540.

[5]Theocaries, P. S., "The Stress Distribution in a Strip Loaded in Tension by Means of a Central Pin", *Transaction ASME, Journal of Applied Mechanics*, Vol. 23, No. 1, March 1956, pp. 85-90.

[6]Howland, R.C., "On Stresses in, Flat Plates Containing Rivet Holes", *Proceedings of 3rd International Congress of Applied Mechanics*, Vol II, 1930, pp. 74-79.

[7]Oplinger, D.W. and Gandhi, K.R., "Stresses in Mechanically Fastened Orthotropic Laminates", *2nd Conference on Fibrous Composites in Flight Vehicle Design*, pp. 813-841, May 1974, Dayton, OH, AFFDL Report # AFFDL-TR-74-103, September 1974, pp. 811-842 (AD-B00135L).

[8]Hoffman, O., "The Brittle Strength of Orthotropic Materials", *Journal of Composite Materials*, 1, 1967, pp. 200-206.

[9]Oplinger, D.W., and Gandhi, K.R., "Analytic Studies of Structural Performance in Mechanically Fastened Fiber Reinforced Plates", *Army Symposium on Solid Mechanics*, September 1974, pp. 211-240.

[10]de Jong, T., "Stresses Around Pin-Loaded Holes in Elastically Orthotropic and Isotropic Plates", *Journal of Composite Materials*, 11, 1977, pp. 313-331.

[11]de Jong, T., "The Influence of Friction on the Theoretical Strength of Pin-Loaded Holes in Orthotropic Plates", *Report #* LR-350, *Department of Aerospace Engineering, Delft University Tech.*, 1982.

[12]Garbo, S.P. and Ogonowski, J.M., "The Effects of Variances and Manufacturing tolerances on the Design Strength and Life of Mechanically Fastened Composite Joints", AFWAL-TR-81-3041, Vols. 1-3, 1981.

[13]Whitney, J.M. and Nuismer, R.J., "Stress Fracture Criteria for Laminated Composites Containing Stress Concentrations", *Journal of Composite Materials*, 8, July 1974, pp. 253.

[14]Zhang, K. and Ueng, C., "Stresses Around a Pin-Loaded Hole in Orthotropic Plates", *Journal of Composite Materials*, 18, September 1984, pp. 432-446.

[15]Mahajerin, E. and Sikarskie, D.L., "Boundary Element Study of a Loaded Hole in an Orthotropic Plate", *Journal of Composite Materials*, 20, July 1986, pp. 375-389.

[16]Hyer, M.H., Klang, E.C., and Cooper, D.E., "The Effects of Pin Elasticity, Clearance, and Friction on the Stresses in a Pin-Loaded Orthotropic Plate", *Journal of Composite Materials*, 21, March 1987, pp. 190-206.

[17]Smith, P.A., Ashby, M.F., and Pascoe, K.J., "Modeling Clamp-up Effects in Composite Bolted Joints", *Journal of Composites*, 21, October 1987, pp. 878-897.

[18]Waszczak, J.P. and Cruise, T.A., "Failure Modes and Strength Predictions of Anisotropic Bolt Bearing Specimens", *Journal of Composite Materials*, 5, July 1971, pp. 421-425.

[19]Tsai, S.W., "Mechanics of Composite Materials, Part II-Theoretical Aspects", *Air Force Materials Laboratory Technical Report* AFML-TR-66-149, 1966.

[20]Wong, C.M.S. and Matthews, F.L.' "A Finite Element Analysis of Single and Two-Hole Bolted Joints in Fiber Reinforced Plastics", *Journal of Composite Materials*, 15, September 1981, pp. 481-491.

[21]Chang, F.K., "The Effects of Pin Load Distribution on the Strength of Pin-Loaded Holes in Laminated Composites", *Journal of Composite Materials*, 20, July 1986, pp. 401-408.

[22]Yamada, S.E. and Sun, C.T., "Analysis of Laminate Strength and Its Distribution" *Journal of Composite Materials*, 12, 1987, pp. 275-284.

[23]Agarwal, B.L., "Static Strength Predictions of Bolted Joints in Composite Materials", *AIAA Journal*, 18, No. 11, November 1980, pp. 1371-1375.

[24]Grimes, G.C. and Whitney, J.M., "Degradation of Graphite/Epoxy Composite Materials Because of Load Induced Micromechanical Damage", *SAMPE Quarterly*, 5, July 1974, pp. 1-13.

[25]Whitney, J.M. and Nuismer, R.J., "Stress Fracture Criteria for Laminated Composites Containing Stress Concentrations", *Journal of Composite Materials*, 8, 1974, pp. 253-265.

[26]Soni, S.R., "Failure Analysis of Composite Laminates with a Fastener Hole", *ASTM-STP-749*, Keward, K.T., 1981, pp. 145-164.

[27]Pipes, R.B., York,J.L., and Wilson, D.W., "Analysis of Net Tension Failure Mode in Composite Bolted Joints". *Journal of Reinforced Plastics and Composites*, 1, April 1982, pp. 141-152.

[28]Tsai, S.W. and Wu, E.M., "A General Theory of Strength of Anisotropic Materials", *Journal of Composite Materials*, 5, 1971, pp. 58-80.

[29]Crews, J.H., Jr., Hong, C.S., and Raju, I.S., " Stress Concentration Factors in Finite Orthotropic Laminates With a Pin-Loaded Whole", *NASA Technical Paper* 1862, May 1981.

[30]Tsujimoto, Y. and Wilson, D., "Elasto-Plastic Failure Analysis of composite Bolted Joints", *Journal of Composite Materials*, 20, May 1986, pp. 236-252.

[31]Hill, R., "The Mathematical Theory of Plasticity", Oxford Press, 1950.

[32]Eriksson, L.I., "Contact Stresses in Bolted Joints of Composite Laminates", *Composite Structures*, 6, 1986, pp.57-75.

[33]Matthews, F.L., Wong, C.M., and Chryssafitis, S., "Stress Distribution Around a Single Bolt in Fiber Reinforced Plastic", *Composites*, July 1982, pp. 316-322.

[34]Rybicki, E.F. and Schmueser, D.W.' "Effects of Stacking Sequence and Lay-up Angle on Free Edge Stresses Around a Hole in a Laminated Plate in Tension", *Journal of Composites*, 12, July 1978, pp. 300-312.

[35]Raju, I.S. and Crews, J.H., "Three Dimensional Analysis of $(0/90)_s$ and $(90/0)_s$ Laminates With a Central Circular Hole", *Composites Technology Review*, 4, Winter 1982, pp. 116-124.

[36]Carlsson, L, "Interlaminar Stresses at a Hole in a Composite Member Subjected to In-Plane Loading", *Journal of Composites*, 17, May 1983, pp. 238-249.

[37]Lucking, W.M., Hoa, S.V., and Sankar, T.S., "The Effects of Geometry on Interlaminar Stresses of $(0/90)_s$ Composite Laminates With Circular Holes", *Journal of Composites*, 17, March 1984, pp. 188-198.

[38]Collings, T.A., "The Strength of Bolted Joints in Multi-Directional CRFP Laminates", *Composites*, January 1977, pp. 43-55.

[39]Stockdale, J.H. and Matthews, F.L., "The Effect of Clamping Pressure on Bolt Bearing Loads in Glass Fiber Reinforced Plastics", *Composites*, January 1976, pp. 34-38.

[40]Quinn, W.J. and Matthews, F.L., "The Effect of Stacking Sequence on the Pin Bearing Strength in Glass Fiber Reinforced Plastics", *Journal of Composite Materials*, 11, April 1987, pp. 139-145.

[41]Collings, T.A. and Beauchamp, M.J., "Bearing Deflection Behavior of a Loaded Hole in Carbon Fiber Reinforced Plastics", *Composites*, 15, January 1984, pp. 33-38.

[42]Johnson, M. and Matthews, F.L., "Determination of Safety Factors For Use When Designing Bolted Joints In Graphite Reinforced Plastics", *Composites*, April 1979, pp. 73-76.

[43]Matthews, F.L., Roshan, A.A., and Phillips, L.N., "The Bolt Bearing Strength of Glass/Carbon Hybrid Composites", *Composites*, July 1982, pp. 225-227.

[44]Collings, T.A., "On the Bearing Strength of Carbon Fiber Reinforced Laminates", *Composites*, July 1982, pp. 241-252.

[45]Collings, T.A., "The Strength of Bolted Joints in Multi-Directional Carbon Fiber Reinforced Plastic Laminates", *Composites*, January 1977, pp. 43-54.

[46]Pyner, G.R. and Matthews, F.L., "Comparisons of Single and Multi-Hole Bolted Joints in Glass Fiber Reinforced Plastic", *Journal of Composite Materials*, 13, July 1979, pp. 232-239.

[47]Nisida, M. and Saito, H., "Stress Distributions in a Semi-Infinite Plate Due to a Pin Determined by Interferometric Method", *Experimental Mechanics*, 6(5), May 1966, pp. 273-279.

[48]Prabhakaran, R., "Photoelastic Investigation of Bolted Joints in Composites", *Composites*, July 1982, pp. 253-256.

[49]Hyer, M.W. and Liu, D., "Stresses in a Quasi-isotropic Pin-loaded Connector Using Photoelasticity", *Experimental Mechanics,* 24(1), 1984, 48-53.

[50]Hyer, M.W. and Lui, D., "Stresses in Pin-Loaded Orthotropic Plates: Photoelastic Results", *Journal of Composite Materials,* 19, March 1985, pp. 138-153.

[51]Koshide, S., "Investigation of the Pin Joints in Composites by the Moire Method", *Experimental Mechanics,* June 1986, pp. 113-118.

[52]Prabhakaran, R. and Naik, N., "Investigation of Non-linear Contact for a Clearance-fit Bolt in a Graphite/Epoxy Laminate", *Composite Structures,* 6, 1986, pp. 77-85.

[53]Chang, F.K., Scott, R.A., and Springer, G.S., "Strength of Mechanically Fastened Composite Joints", *Journal of Composite Materials,* 16,1982, pp. 470-493.

[54]Yamada, S.E. and Sun, C.T., "Analysis of Laminate Strength and Its Distribution", *Journal of Composite Materials,* 18, 1978, pp. 275-284.

[55]Chang, F.K., Scott, R.A., and Springer, G.S., "Failure of Composite Laminates Containing Pin-Loaded Holes-Method of Solution", *Journal of Composite Materials,* 18, May 1984, pp.255-277.

[56]Chang, F.K., Scott, R.A., and Springer, G.S., "Design of Composite Laminates Containing Pin-Loaded Holes", *Journal of Composite Materials,* 18, May 1984, pp. 279-289.

[57]Chang, F.K., Scott, R.A., and Springer, G.S., "Failure Strength of Nonlinearly Elastic Composite Laminates Containing a Pin-Loaded Hole", *Journal of Composite Materials,* 18, September 1984, pp. 464-477.

[58]Chang, F. K, Scott, R.A., and Springer, G.S., "A Progressive Damage Model for Laminated Composites Containing Stress Concentrations", *Journal of Composite Materials,* 21, September 1987, pp. 843-855.

[59]Chang, F.K., Scott, R.A., and Springer, G.S., "Post-Failure Analysis of Bolted Composite Joints in Tension or Shear-Out Mode Failure", *Journal of Composite Materials,* 21, September 1987, pp. 809-833.

[60]Hashin, Z., "Failure Criterion for Unidirectional Fiber Composites", *Journal of Applied Mechanics,* 47, 1980, pp. 329-334.

[61]Tsiang, T.H. and Mandell, J.F., "Damage Development at Bolted Joints in Composites", AMTL Technical Report AMMRC TR 84-12, March 1984.

[62]Oplinger, D.W., "On the Structural Behavior of Mechanically Fastened Joints in Composite Structures", Fibrous Composites in Structural Design, Edited by E.M. Lenoe and J.J. Burke, Plenum Press, New York, 1980, pp. 575-602.

[63]Wilkinson, T.L. and Rowlands, R.E., "Analysis of Mechanical Joints in Wood", *Experimental Mechanics,* 21 (11), November 1981, pp. 408-414.

[64]Rowlands, R.E., Rahman, M.U., Wilkinson, T.L., and Chiang, Y.I., "Single and Multiple Bolted Joints In Orthotropic Materials", *Composites,* July 1982, pp. 273-278.

[65]Cloud, G., Sikarskie,S., Mahajerin, E., Herrera, P., "Theoretical and Experimental Investigation of Mechanically Fastened Composites", Contract # DAAE07-82-K-4002, U.S. Army Tank Automotive Command, Research and Development Center, Warren, Michigan.

[66]Serabian, S.M., "Comparisons of Finite Element Predictions and Experimental Results for $[0/90]_s$ Pin-Loaded Laminates", *Masters Thesis,* University of Lowell, Lowell,MA, Fall 1985.

[67]Serabian, S.M., "Experimental Verification of Analytic Bolted Joint Methodologies", *Proceedings of the Army Symposium on Solid Mechanics - Advances in Solid Mechanics For Design and Analysis*, Work in Progress Section, Newport, R.I., October 1984, pp. 369-373.

[68]Serabian, S.M. and Oplinger, D.W.' "An Experimental and Finite Element Investigation Into the Mechanical Response of $[0/90]_s$ Pin-Loaded Laminates", *Journal of Composite Materials,* 21, July 1987, pp. 462-478.

[69]Talreja,R.,"Transverse Cracking and Stiffness Reduction in Composite Laminates", *Journal of Composite Materials,*19, July 1985, pp. 355-375.

[70]Groves, S.E., Harris, A.L., Highsmith,D.H., Allen,D.H., and Norvell, R.G., "An Experimental and Analytical Treatment of Matrix Cracking in Cross-Ply Laminates", *Experimental Mechanics,* 27(1), 1987, pp. 73-79.

[71]Katz, A., "A Semi-Automated System For Moire Strain Analysis", *Proceedings of The Army Symposium on Solid Mechanics - Advances in Solid Mechanics For Design and Analysis*, Work in Progress Section, Newport, R.I., October 1984, pp. 365-367.

[72]Tessler, A., Freese, C., Anastasi, A., Serabian, S.M., Oplinger, D., and Katz, A., "Least Squares Penalty-Constraint Finite Element Method For Generating Strain Fields From Moire Fringe Patterns", *accepted for publication in Experimental Mechanics.*

[73]Serabian, S. M. and Anastasi, R. A., "Out-of Plane Deflections of Metallic and Composite Pin Loaded Coupons", *Experimental Mechanics, accepted for publication, October 1990.*

[74]Parks, V.J., "Manual on Experimental Stress Analysis", SESA, New York, 1989, Ch. 6.

[75]Rosen, B.W., "A Simple Procedure for Experimental Determination of the Longitudinal Shear Modulus of Unidirectional Composites", *Journal of Composite Materials,* 6, October, 1972, pp.552-554.

[76]Petit, P.H., "A Simplified Method of Determining the In-Plane Shear Stress-Strain Response of a Unidirectional Composite", *ASTM STP 460 (ASTM, 1969),* pp.83-93.

[77]Lee, S. and Munro, M. "Evaluation of In-Plane Shear Test Methods for Composite Materials by the Decision Analysis Technique", *Composites,* 17(1):13, January, 1986.

[78]Tarnopol'skii, T. and Kincis, T. "Static Test Methods for Composites", Van Nostrand Reinhold Inc, New York, N.Y., 1985, pp. 230-243.

[79]Fisher, S., Itzhak, R., Haret, H., Marom, G., and Wagner, H.D., "Simultaneous Determination of Shear and Young's Moduli in Composites", *Journal of Testing and Evaluation,* 1981, pp. 303-307.

[80]Jones, R.M., "Mechanics of Composite Materials", McGraw-Hill Book Company, New York, 1975.

[81]Herakovich, C.T, "Composite Laminates With Negative Through-the-Thickness Poisson Ratios", *Journal of Composite Materials*", 18, September, 1984, pp. 447-455.

[82]Hibbit, Carlson, and Sorenson, "ABAQUS User Maneral", Version 7.1, Hibbit, Carlson, and Sorenson, Providence, R.I., 1988.

[83]Chiang, F.P., Parks, V.J., and Durelli, A.J., "Moire Fringe Interpolation and Multiplication by Fringe Shifting", *Experimental Mechanics,* 8(12), 1968, pp.554-560.

DISTRIBUTION LIST

No. of Copies	To
1	Office of the Under Secretary of Defense for Research and Engineering, The Pentagon, Washington, DC 20301
	Commander, U.S. Army Laboratory Command, 2800 Powder Mill Road, Adelphi, MD 20783-1145
1	ATTN: AMSLC-IM-TL
1	AMSLC-CT
	Commander, Defense Technical Information Center, Cameron Station, Building 5, 5010 Duke Street, Alexandria, VA 22304-6145
2	ATTN: DTIC-FDAC
1	Metals and Ceramics Information Center, Battelle Columbus Laboratories, 505 King Avenue, Columbus, OH 43201
	Commander, Army Research Office, P.O. Box 12211, Research Triangle Park, NC 27709-2211
1	ATTN: Information Processing Office
	Commander, U.S. Army Materiel Command, 5001 Eisenhower Avenue, Alexandria, VA 22333
1	ATTN: AMCLD
	Commander, U.S. Army Materiel Systems Analysis Activity, Aberdeen Proving Ground, MD 21005
1	ATTN: AMXSY-MP, H. Cohen
	Commander, U.S. Army Missile Command, Redstone Scientific Information Center, Redstone Arsenal, AL 35898-5241
1	ATTN: AMSMI-RD-CS-R/Doc
1	AMSMI-RLM
	Commander, U.S. Army Armament, Munitions and Chemical Command, Dover, NJ 07801
2	ATTN: Technical Library
1	AMDAR-LCA, Mr. Harry E. Pebly, Jr., PLASTEC, Director
	Commander, U.S. Army Natick Research, Development and Engineering Center, Natick, MA 01760-5010
1	ATTN: Technical Library
	Commander, U.S. Army Satellite Communications Agency, Fort Monmouth, NJ 07703
1	ATTN: Technical Document Center
	Commander, U.S. Army Tank-Automotive Command, Warren, MI 48397-5000
1	ATTN: AMSTA-ZSK
2	AMSTA-TSL, Technical Library
	Commander, White Sands Missile Range, NM 88002
1	ATTN: STEWS-WS-VT
	President, Airborne, Electronics and Special Warfare Board, Fort Bragg, NC 28307
1	ATTN: Library
	Director, U.S. Army Ballistic Research Laboratory, Aberdeen Proving Ground, MD 21005
1	ATTN: SLCBR-TSB-S (STINFO)
	Commander, Dugway Proving Ground, Dugway, UT 84022
1	ATTN: Technical Library, Technical Information Division
	Commander, Harry Diamond Laboratories, 2800 Powder Mill Road, Adelphi, MD 20783
1	ATTN: Technical Information Office
	Director, Benet Weapons Laboratory, LCWSL, USA AMCCOM, Watervliet, NY 12189
1	ATTN: AMSMC-LCB-TL
1	AMSMC-LCB-R
1	AMSMC-LCB-RM
1	AMSMC-LCB-RP
	Commander, U.S. Army Foreign Science and Technology Center, 220 7th Street, N.E., Charlottesville, VA 22901-5396
3	ATTN: AIFRTC, Applied Technologies Branch, Gerald Schlesinger

No. of Copies	To
	Commander, U.S. Army Aeromedical Research Unit, P.O. Box 577, Fort Rucker, AL 36360
1	ATTN: Technical Library
	Commander, U.S. Army Aviation Systems Command, Aviation Research and Technology Activity, Aviation Applied Technology Directorate, Fort Eustis, VA 23604-5577
1	ATTN: SAVDL-E-MOS
	U.S. Army Aviation Training Library, Fort Rucker, AL 36360
1	ATTN: Building 5906-5907
	Commander, U.S. Army Agency for Aviation Safety, Fort Rucker, AL 36362
1	ATTN: Technical Library
	Commander, USACDC Air Defense Agency, Fort Bliss, TX 79916
1	ATTN: Technical Library
	Commander, U.S. Army Engineer School, Fort Belvoir, VA 22060
1	ATTN: Library
	Commander, U.S. Army Engineer Waterways Experiment Station, P. O. Box 631, Vicksburg, MS 39180
1	ATTN: Research Center Library
	Commandant, U.S. Army Quartermaster School, Fort Lee, VA 23801
1	ATTN: Quartermaster School Library
	Naval Research Laboratory, Washington, DC 20375
1	ATTN: Code 5830
2	Dr. G. R. Yoder - Code 6384
	Chief of Naval Research, Arlington, VA 22217
1	ATTN: Code 471
1	Edward J. Morrissey, WRDC/MLTE, Wright-Patterson Air Force, Base, OH 45433-6523
	Commander, U.S. Air Force Wright Research & Development Center, Wright-Patterson Air Force Base, OH 45433-6523
1	ATTN: WRDC/MLLP, M. Forney, Jr.
1	WRDC/MLBC, Mr. Stanley Schulman
	NASA - Marshall Space Flight Center, MSFC, AL 35812
1	ATTN: Mr. Paul Schuerer/EH01
	U.S. Department of Commerce, National Institute of Standards and Technology, Gaithersburg, MD 20899
1	ATTN: Stephen M. Hsu, Chief, Ceramics Division, Institute for Materials Science and Engineering
1	Committee on Marine Structures, Marine Board, National Research Council, 2101 Constitution Ave., N.W., Washington, DC 20418
1	Librarian, Materials Sciences Corporation, 930 Harvest Drive, Suite 300, Blue Bell, PA 19422
1	The Charles Stark Draper Laboratory, 68 Albany Street, Cambridge, MA 02139
	Wyman-Gordon Company, Worcester, MA 01601
1	ATTN: Technical Library
	Lockheed-Georgia Company, 86 South Cobb Drive, Marietta, GA 30063
1	ATTN: Materials and Processes Engineering Dept. 71-11, Zone 54
	General Dynamics, Convair Aerospace Division, P.O. Box 748, Fort Worth, TX 76101
1	ATTN: Mfg. Engineering Technical Library
1	Prof. F. K. Chang, Department of Aeronautics and Astronautics, Stanford University, Stanford, CA 94305
1	Dr. J. H. Crews, Jr., Mail Stop 188E, NASA Langley Research Center, Hampton, VA 23665-5225

No. of Copies	To
1	Prof. M. W. Hyer, Department of Engineering Science and Mechanics, Virginia Polytechnic Institute and State University, Blacksburg, VA 24060-0219
1	Prof. F. L. Mathews, Department of Aeronautics, Imperial College of Science & Technology, Prince Consort Road, London SW7 2BY
1	Prof. J. Morton, Department of Engineering Science and Mechanics, Virginia Polytechnic Institute and State University, Blacksburg, VA 24060-0219
1	Prof. R. E. Rowlands, Department of Engineering Mechanics, University of Wisconsin-Madison, Madison, WI 53706
1	Dr. J. R. Soderquist, Federal Aviation Administration, 800 Independence Avenue S.W., Washington, DC 20591
	Director, U.S. Army Materials Technology Laboratory, Watertown, MA 02172-0001
2	ATTN: SLCMT-TML
1	Author

U.S. Army Materials Technology Laboratory,
Watertown, Massachusetts 02172-0001
AN EXPERIMENTAL AND FINITE ELEMENT INVESTIGATION INTO
THE NONLINEAR MATERIAL BEHAVIOR OF PIN-LOADED
COMPOSITE LAMINATES -
Steven M. Serabian

Technical Report MTL TR 91-2, January 1991, 272 pp -
illus-tables, D/A Project: 1L162105AH84,
AMCMS Code: 612105.AH840011

AD_____
UNCLASSIFIED
UNLIMITED DISTRIBUTION

Key Words

Composite materials
Bolted joints
Finite element analysis

The effect of crossply nonlinear intralaminar shear behavior on the modeling accuracy of pin-loaded [(0/90)n]s and [(+45/-45)n]s composite laminates was quantitatively investigated. Both linear and nonlinear elastic three dimensional finite element approximations that included pin elasticity and contact angle formation were generated. These approximations were compared to both front surface in-plane and out-of-plane experimental moire displacement contours generated from geometric and projection shadow moire techniques. A modified three point bend test was used to obtain values of laminate transverse shear moduli while through thickness contraction measurements on laminate tension tests were employed to obtain estimates of the Poisson ratio values. Nonlinear crossply intralaminar shear behavior was determined from the ASTM D3518-76 specification. Three dimensional constitutive equations for the [(0/90)n]s laminate were developed from effective and actual lamina mechanical properties. A material axis transformation of these constitutive equations was employed to produce [(+45/-45)n]s laminate constitutive equations. The validity of these constitutive equations and the effects of nonlinear intralaminar shear behavior were experimentally investigated by a comparison with uniaxial tension tests of both laminates. A sensitivity analysis of through thickness modulus was also done in this comparison in hope of providing insight into the selection of its magnitude. Comparisons of linear and nonlinear elastic finite element results show significant stress level reductions and increased strain values in [(+45/-45)3]s laminate net and bearing sections. Similar results were observed in the [(0/90)3,0]s laminate shearout section. Both pin proximity and load level intensified these effects. Net section [(+45/-45)3]s experimental strains agreed well with nonlinear elastic finite element results at low pin load levels, but surpassed them at higher pin load levels. Closer pin proximity and increased load level intensified these results. Similar trends were observed in [(+45/-45)3]s bearing and [(0/90)3,0]s shearout sections, but were affected by unsymmetric experimental pin boundary conditions. A qualitative determination of material damage within the pin-loaded laminates indicated material failure in those regions where experimental and nonlinear elastic finite element results diverged.

U.S. Army Materials Technology Laboratory,
Watertown, Massachusetts 02172-0001
AN EXPERIMENTAL AND FINITE ELEMENT INVESTIGATION INTO
THE NONLINEAR MATERIAL BEHAVIOR OF PIN-LOADED
COMPOSITE LAMINATES -
Steven M. Serabian

Technical Report MTL TR 91-2, January 1991, 272 pp -
illus-tables, D/A Project: 1L162105AH84,
AMCMS Code: 612105.AH840011

AD_____
UNCLASSIFIED
UNLIMITED DISTRIBUTION

Key Words

Composite materials
Bolted joints
Finite element analysis

The effect of crossply nonlinear intralaminar shear behavior on the modeling accuracy of pin-loaded [(0/90)n]s and [(+45/-45)n]s composite laminates was quantitatively investigated. Both linear and nonlinear elastic three dimensional finite element approximations that included pin elasticity and contact angle formation were generated. These approximations were compared to both front surface in-plane and out-of-plane experimental moire displacement contours generated from geometric and projection shadow moire techniques. A modified three point bend test was used to obtain values of laminate transverse shear moduli while through thickness contraction measurements on laminate tension tests were employed to obtain estimates of the Poisson ratio values. Nonlinear crossply intralaminar shear behavior was determined from the ASTM D3518-76 specification. Three dimensional constitutive equations for the [(0/90)n]s laminate were developed from effective and actual lamina mechanical properties. A material axis transformation of these constitutive equations was employed to produce [(+45/-45)n]s laminate constitutive equations. The validity of these constitutive equations and the effects of nonlinear intralaminar shear behavior were experimentally investigated by a comparison with uniaxial tension tests of both laminates. A sensitivity analysis of through thickness modulus was also done in this comparison in hope of providing insight into the selection of its magnitude. Comparisons of linear and nonlinear elastic finite element results show significant stress level reductions and increased strain values in [(+45/-45)3]s laminate net and bearing sections. Similar results were observed in the [(0/90)3,0]s laminate shearout section. Both pin proximity and load level intensified these effects. Net section [(+45/-45)3]s experimental strains agreed well with nonlinear elastic finite element results at low pin load levels, but surpassed them at higher pin load levels. Closer pin proximity and increased load level intensified these results. Similar trends were observed in [(+45/-45)3]s bearing and [(0/90)3,0]s shearout sections, but were affected by unsymmetric experimental pin boundary conditions. A qualitative determination of material damage within the pin-loaded laminates indicated material failure in those regions where experimental and nonlinear elastic finite element results diverged.

U.S. Army Materials Technology Laboratory,
Watertown, Massachusetts 02172-0001
AN EXPERIMENTAL AND FINITE ELEMENT INVESTIGATION INTO
THE NONLINEAR MATERIAL BEHAVIOR OF PIN-LOADED
COMPOSITE LAMINATES -
Steven M. Serabian

Technical Report MTL TR 91-2, January 1991, 272 pp -
illus-tables, D/A Project: 1L162105AH84,
AMCMS Code: 612105.AH840011

AD_____
UNCLASSIFIED
UNLIMITED DISTRIBUTION

Key Words

Composite materials
Bolted joints
Finite element analysis

The effect of crossply nonlinear intralaminar shear behavior on the modeling accuracy of pin-loaded [(0/90)n]s and [(+45/-45)n]s composite laminates was quantitatively investigated. Both linear and nonlinear elastic three dimensional finite element approximations that included pin elasticity and contact angle formation were generated. These approximations were compared to both front surface in-plane and out-of-plane experimental moire displacement contours generated from geometric and projection shadow moire techniques. A modified three point bend test was used to obtain values of laminate transverse shear moduli while through thickness contraction measurements on laminate tension tests were employed to obtain estimates of the Poisson ratio values. Nonlinear crossply intralaminar shear behavior was determined from the ASTM D3518-76 specification. Three dimensional constitutive equations for the [(0/90)n]s laminate were developed from effective and actual lamina mechanical properties. A material axis transformation of these constitutive equations was employed to produce [(+45/-45)n]s laminate constitutive equations. The validity of these constitutive equations and the effects of nonlinear intralaminar shear behavior were experimentally investigated by a comparison with uniaxial tension tests of both laminates. A sensitivity analysis of through thickness modulus was also done in this comparison in hope of providing insight into the selection of its magnitude. Comparisons of linear and nonlinear elastic finite element results show significant stress level reductions and increased strain values in [(+45/-45)3]s laminate net and bearing sections. Similar results were observed in the [(0/90)3,0]s laminate shearout section. Both pin proximity and load level intensified these effects. Net section [(+45/-45)3]s experimental strains agreed well with nonlinear elastic finite element results at low pin load levels, but surpassed them at higher pin load levels. Closer pin proximity and increased load level intensified these results. Similar trends were observed in [(+45/-45)3]s bearing and [(0/90)3,0]s shearout sections, but were affected by unsymmetric experimental pin boundary conditions. A qualitative determination of material damage within the pin-loaded laminates indicated material failure in those regions where experimental and nonlinear elastic finite element results diverged.

U.S. Army Materials Technology Laboratory,
Watertown, Massachusetts 02172-0001
AN EXPERIMENTAL AND FINITE ELEMENT INVESTIGATION INTO
THE NONLINEAR MATERIAL BEHAVIOR OF PIN-LOADED
COMPOSITE LAMINATES -
Steven M. Serabian

Technical Report MTL TR 91-2, January 1991, 272 pp -
illus-tables, D/A Project: 1L162105AH84,
AMCMS Code: 612105.AH840011

AD_____
UNCLASSIFIED
UNLIMITED DISTRIBUTION

Key Words

Composite materials
Bolted joints
Finite element analysis

The effect of crossply nonlinear intralaminar shear behavior on the modeling accuracy of pin-loaded [(0/90)n]s and [(+45/-45)n]s composite laminates was quantitatively investigated. Both linear and nonlinear elastic three dimensional finite element approximations that included pin elasticity and contact angle formation were generated. These approximations were compared to both front surface in-plane and out-of-plane experimental moire displacement contours generated from geometric and projection shadow moire techniques. A modified three point bend test was used to obtain values of laminate transverse shear moduli while through thickness contraction measurements on laminate tension tests were employed to obtain estimates of the Poisson ratio values. Nonlinear crossply intralaminar shear behavior was determined from the ASTM D3518-76 specification. Three dimensional constitutive equations for the [(0/90)n]s laminate were developed from effective and actual lamina mechanical properties. A material axis transformation of these constitutive equations was employed to produce [(+45/-45)n]s laminate constitutive equations. The validity of these constitutive equations and the effects of nonlinear intralaminar shear behavior were experimentally investigated by a comparison with uniaxial tension tests of both laminates. A sensitivity analysis of through thickness modulus was also done in this comparison in hope of providing insight into the selection of its magnitude. Comparisons of linear and nonlinear elastic finite element results show significant stress level reductions and increased strain values in [(+45/-45)3]s laminate net and bearing sections. Similar results were observed in the [(0/90)3,0]s laminate shearout section. Both pin proximity and load level intensified these effects. Net section [(+45/-45)3]s experimental strains agreed well with nonlinear elastic finite element results at low pin load levels, but surpassed them at higher pin load levels. Closer pin proximity and increased load level intensified these results. Similar trends were observed in [(+45/-45)3]s bearing and [(0/90)3,0]s shearout sections, but were affected by unsymmetric experimental pin boundary conditions. A qualitative determination of material damage within the pin-loaded laminates indicated material failure in those regions where experimental and nonlinear elastic finite element results diverged.